2012-04-25

High Fidelity Simulation of Non-Synchronous Vibration for Aircraft Engine Fan/Compressor

Hong-Sik Im
University of Miami, sunny33156@gmail.com

UNIVERSITY OF MIAMI

HIGH FIDELITY SIMULATION OF NON-SYNCHRONOUS VIBRATION FOR AIRCRAFT ENGINE FAN/COMPRESSOR

By

Hong-Sik Im

A DISSERTATION

Submitted to the Faculty
of the University of Miami
in partial fulfillment of the requirements for
the degree of Doctor of Philosophy

Coral Gables, Florida

May 2012

UNIVERSITY OF MIAMI

A dissertation submitted in partial fulfillment of
the requirements for the degree of
Doctor of Philosophy

HIGH FIDELITY SIMULATION OF NON-SYNCHRONOUS VIBRATION FOR AIRCRAFT ENGINE FAN/COMPRESSOR

Hong-Sik Im

Approved:

Gecheng Zha, Ph.D. Associate Professor of Mechanical & Aerospace Engineering	Terri A. Scandura, Ph.D. Dean of the Graduate School
Hongtan Liu, Ph.D. Professor of Mechanical & Aerospace Engineering	Manuel A. Huerta, Ph.D. Professor of Physics
Weiyong Gu, Ph.D. Professor and Chairman of Mechanical & Aerospace Engineering	

IM, HONG-SIK (Ph.D., Mechanical & Aerospace Engineering)
High Fidelity Simulation of (May 2012)
Non-Synchronous Vibration for Aircraft Engine Fan/Compressor

Abstract of a dissertation at the University of Miami.

Dissertation supervised by Professor Gecheng Zha.
No. of pages in text. (368)

The objectives of this research are to develop a high fidelity simulation methodology for turbomachinery aeromechanical problems and to investigate the mechanism of non-synchronous vibration (NSV) of an aircraft engine axial compressor. A fully conservative rotor/stator sliding technique is developed to accurately capture the unsteadiness and interaction between adjacent blade rows. Phase lag boundary conditions (BC) based on the time shift (direct store) method and the Fourier series phase lag BC are implemented to take into account the effect of phase difference for a sector of annulus simulation. To resolve the nonlinear interaction between flow and vibrating blade structure, a fully coupled fluid-structure interaction (FSI) procedure that solves the structural modal equations and time accurate Navier-Stokes equations simultaneously is adopted. An advanced mesh deformation method that generates the blade tip block mesh moving with the blade displacement is developed to ensure the mesh quality. An efficient and low diffusion E-CUSP (LDE) scheme as a Riemann solver designed to minimize numerical dissipation is used with an improved hybrid RANS/LES turbulence strategy, delayed detached eddy simula-

tion (DDES). High order accuracy (3rd and 5th order) weighted essentially non-oscillatory (WENO) schemes for inviscid flux and a conservative 2nd and 4th order viscous flux differencing are employed.

Extensive validations are conducted to demonstrate high accuracy and robustness of the high fidelity FSI simulation methodology. The validated cases include: 1) DDES of NACA 0012 airfoil at high angle of attack with massive separation. The DDES accurately predicts the drag whereas the URANS model significantly over predicts the drag. 2) The AGARD Wing 445.6 flutter boundary is accurately predicted including the point at supersonic incoming flow. 3) NASA Rotor 67 validation for steady state speed line and radial profiles at peak efficiency point and near stall point. The calculated results agree excellently with the experiment. 4) NASA Stage 35 speed line and radial profiles to validate the steady state mixing plane BC for multistage computation. Excellent agreement is obtained between the computation and experiment. 5) NASA Rotor 67 full annulus and single passage FSI simulation at near peak condition to validate phase lag BC. The time shifted phase lag BC accurately predicts blade vibration responses that agrees better with the full annulus FSI simulation.

The DDES methodology is used to investigate the stall inception of NASA Rotor 67. The stall process begins with spike inception and develops to full stall. The whole process is simulated with full annulus of the rotor. The fully coupled FSI is then used to simulate the stall flutter of NASA Rotor 67.

The multistage simulations of a GE aircraft engine high pressure compressor (HPC) reveal for the first time that the travelling tornado vortex formed on the rotor blade tip region is the root cause for the NSV of the compressor. The rotor blades under NSV have

large torsional vibration due to the tornado vortex propagation in the opposite to the rotor rotation. The tornado vortex frequency passing the suction surface of each blade in the tip region agrees with the NSV frequency. The predicted NSV frequency based on URANS model with rigid blades agrees very well with the experimental measurement with only 3.3% under-predicted. The NSV prediction using FSI with vibrating blades also obtain the same frequency as the rigid blades. This is because that the NSV is primarily caused by the flow vortex instability and the no resonance occurs. The blade structures respond passively and the small amplitudes of the blade vibration do not have significant effect on the flow.

The predicted frequency using DDES with rigid blades is more deviated from the experiment and is 14.7% lower. The reason is that the DDES tends to predict the rotor stall earlier than the URANS and the NSV can be achieved only at higher mass flow rate, which generates a lower frequency. The possible reason for the DDES to predict the rotor stall early may be because DDES is more sensitive to wave reflection and a non-reflective boundary condition may be necessary.

Overall, the high fidelity FSI methodology developed in this thesis for aircraft engine fan/compressor aeromechanics simulation is demonstrated to be very successful and has advanced the forefront of the state of the art. Future work to continue to improve the accuracy and efficiency is discussed at the end of the thesis.

Dedicated to my family and to my parents

for their love, support, encouragement ...

Acknowledgment

I would like to give my sincere gratitude and deep respect to my academic advisor, Professor Gecheng Zha, for his invaluable guidance and support throughout my study at the University of Miami.

Dr. Xiangying Chen, Dr. Baoyuan Wang, Dr. Yiqing Shen and his family are greatly appreciated for their help and discussion on my research. I also would like to thank my dissertation committee members, Professor Hongtan Liu, Professor Manuel A. Huerta and Professor Weiyong Gu, for their insightful review and suggestions on my research work.

I appreciate Dr. Steve Manwaring and Dr. L.C. Colmenero at GE Aviation in Cincinnati for providing us the compressor geometry and data. The grants support from AFRL and the industrial partners of GUIde Consortium, 10-AFRL-1024 and 09-GUIDE-1010, are acknowledged. The numerical simulations are conducted at the Center for Computational Sciences at the University of Miami and Air Force Research Lab DoD Super-computing Resource Centers.

Contents

List of Figures

List of Tables

List of Symbols

a, c	speed of sound, $\sqrt{\gamma p/\rho}$
A, B, C	Jacobian matrix of inviscid flux $\mathbf{E}, \mathbf{F}, \mathbf{G}$ in ξ, η, ζ direction
C	speed of sound in generalized coordinates, $c\sqrt{l_\xi^2 + l_\eta^2 + l_\zeta^2}$
$\mathbf{C}$	absolute velocity vector
C_{DES}	DES coefficient, 0.65
C_m	meridional absolute velocity, $\sqrt{C_x^2 + C_r^2}$
C_p	specific heat capacity at constant pressure
C_x, C_θ, C_r	absolute velocities in x, θ, r direction
C_t	tip chord of the compressor rotor
d	distance from the closest wall
$\tilde{d}$	length scale of DES, $min(d, C_{DES}\Delta)$
dQ	head added to system
dW	total work done of the system
dE	change in total energy of system
D	source term of Navier-Stokes equations in generalized coordinates
$\mathbf{E}, \mathbf{F}, \mathbf{G}$	inviscid flux vectors in ξ, η, ζ direction
e	total energy per unit mass
$\mathbf{e}_x, \mathbf{e}_y, \mathbf{e}_z$	unit normal vector in reference xyz
$\mathbf{F}$	sum of fluid force acting on the structure or on a finite control volmue
$\mathbf{F}_b$	body force acting on a finite control volmue
$\mathbf{F}_s$	surface force acting on a finite control volmue

H	blade active length or wing span
I	identity matrix
I_o	rothalpy
J	Jacobian of the coordinate transformation, $\frac{\partial(\xi,\eta,\zeta)}{\partial(x,y,z)}$
L	reference or characteristic length
$\mathbf{l},\mathbf{m},\mathbf{n}$	normal vector on ξ,η,ζ surface with its magnitude equal to the elemental surface area and pointing to the direction of increasing ξ,η,ζ
l_t	grid moving velocity
L,M,N	Jacobian matrix of viscous flux $\mathbf{R},\mathbf{S},\mathbf{T}$ in ξ,η,ζ
$\mathbf{M},\mathbf{C},\mathbf{K}$	vibration mass, damping, stiffness matrices
m	pseudo time marching step
M_∞	reference Mach number, $\frac{V_\infty}{a_\infty}$
M_ξ	contravariant Mach number in ξ direction, $M_\xi = \frac{U}{C}$
n	physical time marching step
N_B	number of blade
N_D	number of nodal diameter
p,P	static pressure
p_o,P_o	total pressure
$\bar{p}_o,\bar{P}_o$	pitchwise mass averaged total pressure
Pr	Prandtl number
Pr_t	turbulent Prandtl number
$\mathbf{Q}$	conservative variable vector

q_k	total heat flux in Cartesian coordinates
R	gas constant
$\mathbf{R}, \mathbf{S}, \mathbf{T}$	viscous flux vectors in ξ, η, ζ direction
r	radius of computational domain with rotating axis of x, $\sqrt{y^2+z^2}$
$\mathbf{r}$	position vector in reference XYZ
R_e	Reynolds number, $\frac{\rho_\infty V_\infty L_\infty}{\mu_\infty}$
R_o	Rossby number, $\frac{\Omega L_\infty}{V_\infty}$
S_v	S-A turbulence model source term
T	static temperature, or period
$\mathbf{T}$	surface stress vector, $\sigma \cdot \mathbf{n}$
T_o	total temperature
t	time
U, V, W	contravariant velocities in ξ, η, ζ direction
$V_\infty (= C_\infty)$	inlet absolute total velocity as reference velocity, $\sqrt{C_m^2 + C_\theta^2}$
u, v, w	relative velocities in x, y, z direction
u^+	dimensionless velocity, u/u_τ
u_τ	friction velocity, $\sqrt{\tau_w/\rho}$
$\mathbf{V}$	relative velocity vector
V	cell volume
V_x, V_θ, V_r	relative velocities in x, θ, r direction
x, y, z	cartesian coordinates in moving frame of reference
X, Y, Z	cartesian coordinates in fixed frame of reference

y^+ dimensionless wall normal distance, $\frac{u_\tau y}{\nu}$

- **Greek Symbols** -

θ, r, x Cylindrical coordinates

α swirl angle, $tan^{-1}(C_\theta / C_m)$

β pitch angle, $tan^{-1}(C_r / C_x)$

ΔS Change of entropy, $C_p ln\frac{To}{To_\infty} - Rln\frac{Po}{Po_\infty}$

Δt physical time step

δ_{ik} Kronecker delta function

ε convergence criterion taken by FSI solver

γ specific heat ratio

λ_j structure eigenvalue of the jth mode

μ viscosity

μ_{DES} turbulent eddy viscosity determined by DES

ν kinematic viscosity

ϕ structure mode shape

$\tilde{\phi}$ structure mass normalized mode shape

$\tilde{\nu}$ working variable of the S-A model related to turbulent eddy viscosity

Ω rotor angular velocity in rad/s

ρ fluid density

τ_{ik} shear stress in Cartesian coordinates

τ_w fluid shear stress at the wall surface

φ position vector in reference xyz

ξ, η, ζ generalized coordinates

- **Flutter parameters** -

b_s bade (or wing) root semi-chord

$\bar{m}$ blade (or wing panel) mass

$\bar{V}$ frustum volume

V^* reduced velocity, $\frac{U_\infty}{b_s \omega_\alpha}$

V_f flutter speed index, $\frac{V^*}{\bar{\mu}}$

ω_α 1st torsional mode natural frequency (=ω_2)

ω_{ij} fluid particle angular velocity tensor, $\frac{1}{2}(\frac{\partial u_i}{\partial x_j} - \frac{\partial u_j}{\partial x_i})$

ω_j blade (or wing) angular eigenfrequency

$\bar{\mu}$ mass ratio, $\frac{\bar{m}}{\bar{V}\rho_\infty}$

- **Subscripts** -

b computational domain outer boundary

i computational domain inner boundary

i, j, k indices

∞ reference point

- **Abbreviations** -

AOA Angle of Attack

BC Boundary Condition

BPF Blade Passing Frequency

BTW Backward Travelling Wave

CFD Computational Fluid Dynamics

CFL	Courant-Friedrichs-Lewy number
CSD	Computational Structural Dynamics
CUSP	Convective Upwind and Split Pressure
DDES	Delayed Detached Eddy Simulation
DES	Detached Eddy Simulation
DNS	Direct Numerical Simulation
DOF	Degree of Freedom
FSI	Fluid-Structural Interaction
FSPL	Fourier Series Phase Lag
FTW	Forward Travelling Wave
FVS	Flux Vector Splitting
GCF	Greatest Common Factor
HCF	High Cycle Fatigue
IGV	Inlet Guide Vane
LCO	Limit Cycle Oscillation
LDE	Low Diffusion E-CUSP scheme
LES	Large Eddy Simulation
LHS	Left Hand Side
MSD	Modeled-Stress Depletion
MUSCL	Monotone Upstream-centered Schemes for Conservation Laws
NSV	Non-Synchronous Vibration
RANS	Reynolds Averaged Navier-Stokes equations

RHS	Right Hand Side
$S-A$	Spalart-Allmaras (S-A) one equation turbulence model
$TSPL$	Time Shifted Phase Lag
$URANS$	Unsteady Reynolds Averaged Navier-Stokes equations
$WENO$	Weighted Essentially Non-Oscillatory scheme

Chapter 1

Introduction

1.1 Background

As a core component of an aircraft engine, fan/compressor is designed to deliver the high pressure air to the engine and to control the mass flow. There are two types of aircraft engine compressor named as axial flow compressor and radial flow compressor. Axial flow compressor is designed to have air flow parallel to the rotating axis, while radial or centrifugal compressor is designed to have air flow axially at entrance but turn to the radial direction. As presented in Fig. 1.1, axial compressors have been widely used in aircraft engines due to high efficiency and large mass flow capacity.

Over the past several decades, there has been a strong motivation for engine manufacturers to improve engine compressor efficiency due to the increase in fuel cost and the need of high-speed high-pressure ratio compressors. Increase in compression ratio of aircraft engines leads to increase in fuel efficiency. The flow inside fan/compressor at a high pressure stage reaches supersonic speed at the rotor blade tip region, which results in increased aero-

Figure 1.1: GE90 jet engine with high pressure axial compressor

dynamic loss as well as aerodynamic excitation and forcing to the blade structure. Therefore, modern transonic fan/compressor blades are designed in more sophisticated manner by applying 3D techniques such as blade lean and sweep to maximize aerodynamic efficiency.

With the fan/compressor aerodynamic loading continues to increase and the structure and material weight continue to decrease, designing of fans/compressors with high structure stability becomes more challenging. Modern fans/compressors can undergo serious aeromechanical problems such as flutter, forced vibration and non-synchronous vibration(NSV). These aeromechanical problems are very difficult to predict since they involve both aerodynamics and structural vibration and they can not be solved without considering fluid-structure interaction.

Aeromechanical phenomena due to forced response and flutter have been studied for decades with the progress of improving turbomachinery efficiency and reliability. Flutter is an aeroelastic self-excited instability at or close to blade natural frequency, but flutter frequencies are in general not an integer multiple of the engine speed [1]. Flutter occurs if

vibration induced by the aerodynamic force acting on the structure exceeds a condition of dynamic equilibrium. The shock instabilities, rotating stall and even choking are know as main sources that trigger flutter in a transonic fan/compressor of aircraft engines [6–12].

To clarify blade vibration terms used in aircraft engine, the terminology of engine order vibration is adopted. If a frequency coincides with an integer multiple of the rotational speed, it is called engine order vibration or synchronous vibration to the engine. Flutter is usually low frequency close to the 1st eigenfrequency of the blade structure and non-synchronous to the engine order [13].

Blade forced vibration occurs when a engine blade eigenfrequency coincides with the blade passing frequency (BPF) [1]. It may result in catastrophic mechanical failures of the engine because BPF is an engine order frequency as a function of the number of blades and engine rotor speed. A harmonic wave usually forms in the circumferential direction due to the rotor rotation. The blade forced vibration is called as engine resonance and occurs at an integer multiple of the rotational speed. The Campbell diagram is used to identify the engine speed at which the forced vibration is likely to occur. In the Campbell diagram, the frequencies at different running conditions are plotted as a function of rotor speed.

Recently, a new aeromechanic problem in axial compressors of aircraft engines, namely non-synchronous vibration(NSV), whose blade vibration frequency is away from harmonics of rotor shaft frequency, has attracted a lot of attention [1, 2, 14–18]. NSV is a non-engine order vibration and is usually locked-on between two engine order lines with high frequency and amplitude enough to cause high cycle fatigue (HCF), in which the stress level is over the material endurance limit due to unsteady aerodynamic excitation forces acting on the blades. NSV is usually observed on the first stage rotor of a multistage high

pressure compressor [1, 16]. Unlike stall flutter, NSV can occur in a stable compressor operating region. Since lack of understanding on NSV will increase cost and development time, many efforts have been made by major engine manufacturers to investigate the mechanism behind NSV. Investigation of the NSV mechanism is thus the major purpose of this thesis. Although the design technologies related to turbomachinery in aircraft engines have been advanced in recent years with the development of numerical methods such as computational fluid dynamics (CFD) and computational structural dynamics (CSD), it is still a great challenge to accurately predict these fluid/structure interaction (FSI) phenomena such as flutter, forced vibration, and NSV because of strong nonlinearities of the flow and structure interaction and lack of high fidelity methods to adequately resolve turbulence, shock/turbulent boundary layer and fluid-structure interaction.

In nature the interaction between fluid and structure occurs at the same instant. Hence, governing equations for the flow and structure need to be solved simultaneously such that the flow and structure always respond without time lag. However, most of the studies on fluid-structural interaction uses a loosely coupled procedure [19–23], in which the information is exchanged between the flow and structural solver with a time difference after partial or complete convergence of individual solvers. Therefore, a tool that can capture the simultaneous fluid/structure interaction is crucial in the design and analysis of aircraft engine fans/compressors. In this thesis, the fully coupled FSI strategy [17, 24–27] is developed for turbomachinery.

For FSI, computational mesh used for aerodynamics simulation is regenerated in each iteration following the structure motion. Hence, the mesh deformation is one of the requisites for simulating the fluid/structure interaction. For turbomachinery, one moving mesh

technique is to regenerate the inside domain mesh with fixed outer boundaries. However, this may cause significant numerical problems due to poor mesh quality in particular in the blade tip region. A typical tip clearance is less than 1% tip chord, the tip surface of the blade is therefore very close to casing wall boundary. It may cause difficulties for FSI simulation because of the mesh skewness of blade tip region.

To facilitate turbomachinery FSI, an advanced deforming mesh technique that makes the mesh slide with the blade motion to ensure high mesh quality at the tip clearance is developed in this study [7].

A numerical method to achieve conservation of flux is very important for an aircraft engine multistage axial compressor. This is because that compressor stage matching is based on the fundamental law of flow physics with the conservation of mass and energy, and the Newton's second law. In other words, if a numerical method can not achieve an accurate conservation of fluxes, the stage loading calculation will be inaccurate, so is the FSI calculation including blade flutter, forced response, and NSV.

In this thesis, two sliding BCs are implemented: 1) a fully conservative BC with the grid point one-to-one connected to avoid interpolation [28]; 2) an interpolation BC between the two sides of the grids. This method is convenient to use and the mesh can be any type, but is not ensured to be fully conservative.

For multistage simulation, use of full annulus simulation is still rare due to excessive computer resources required. A full annulus simulation is sometimes used for rotating stall simulation [29] since the symmetry of the flow field in the annulus is completely lost. Rotating stall is a major concern since the compressor may surge the engine and the flow instability can cause blade failures [30]. As the compressor approaches to stall, an

increased incidence caused by a minor non-uniformity or disturbance of the incoming flow can trigger rotating stall [31]. Since the rotor rotates, the stall cell propagates to the next blade. In this way the rotating stall develops usually up to the length scale of several blade pitches [32] and eventually breaks the flow symmetry in the circumference, hence the full annulus is necessary to simulate rotating stall. In this thesis, a full annulus simulation is conducted to investigate the stall inception of Rotor 67.

However, NSV typically occurs before a fan/compressor stalls [2, 15, 18], so use of single or multi-blade passage for NSV simulation is highly desirable. The phase-lagged boundary conditions at the circumferential boundaries should be employed in order to reflect the influence of the phase difference on a sector of annulus simulation according to the number of nodal diameters. The phase angle difference is important in aeromechanical problems because it has a large effect on the aerodynamic damping. The method to impose inter blade phase angle is necessary since the fan/compressor flutter usually occurs with a travelling wave. In this thesis, two phase lag BCs are implemented, the time shift phase lag BC [33] and the one suggested by He and Denton [28, 34] based on Fourier series. A method to impose inter-blade phase angle for each blade in order to obtain travelling wave is developed.

Simulation of turbulent flows is critical for accurate prediction of NSV since flow separation, tip leakage vortex, and their interaction with main flow can play a key role in creating the instability that causes NSV. The flow instability simulation has many difficulties if using Reynolds-averaged Navier-Strokes (RANS) methods since RANS cannot predict unsteady vortical flows well [35]. RANS methods intend to model the large scale eddies using a universal model. Large scale turbulence is affected by flow geometries and

boundary conditions and a universal model does not exist. Large Eddy Simulation (LES) is promising to overcome the disadvantages of the RANS model. However, for high Reynolds number flows such as those of transonic wings and turbomachinery blades, to resolve wall boundary layer, LES needs the CPU resource not much less than the Direct Numerical Simulation(DNS). This makes the LES too expensive for fluid-structural interaction unsteady calculations.

The Detached Eddy Simulation(DES) suggested by Spalart et al. [36] is a sound compromise between the accuracy and CPU cost. DES is a hybrid RANS and LES method. Near the solid surface within the wall boundary layer, the unsteady RANS model is realized. Away from the wall surface boundary layer, the model is automatically converted to LES. By using the RANS model near walls, the mesh size as well as the CPU time can be tremendously reduced. However, a defect of the first generation DES model [36], DES97, has been also exposed. DES97 may behave incorrectly and cause modeled stress depletion (MSD) in the regions of thick boundary layers and shallow separation regions due to the grid spacing dependence [37]. Delayed detached-eddy simulation (DDES) by Spalart [37] is an improved version of the DES97 model. With DDES, a blending function similar to the one used by Menter and Kuntz [38] for the SST model is introduced to limit the length scale of DES97 to ensure the transition of RANS to LES be independent of grid spacing. DDES is employed in this thesis

So far, the effects of blade aeroelasticity due to FSI of NSV have not been simulated and rigid blades are used without blade vibration. The reason is that simulation of fluid-structural interaction is not straightforward and the methodology is not well established yet in particular for multistage turbomachinery. The goal of present NSV simulation is to

let engineers avoid NSV or to decide if the vibration amplitudes are within the limits of structural strength and fatigue. A simulation with realistic fluid structural interaction (FSI) for a multistage must be adopted to guide the rotor blade design. Such simulation will not only shed more light to reveal the flow physics of NSV, but also provide the blade structural response for blade mechanical design. This research is to make the first effort to solve NSV of aircraft engine multistage compressor using high fidelity fully coupled FSI simulation strategy.

1.2 The Objectives

The objectives of this research are to develop a high fidelity numerical methodology for multistage fan/compressor and to investigate NSV mechanism of a GE axial compressor. In order to fulfill the primary goal of this research, the following tasks are achieved in this thesis:

- Conservative rotor/stator interaction sliding BC for multistage turbomachinery
- Fully coupled FSI interaction for turbomachinery aeroelasticity
- Efficient phase lag BC for a sector of annulus turbomachinery simulation
- Advanced LES/RANS hybrid turbulence, delayed detached eddy simulation (DDES) for turbomachinery
- Intensive validation of the high fidelity turbomachinery FSI methodology
- Investigation of the NSV mechanism for a GE aircraft engine compressor

1.3 The Strategy of This Research

To achieve the objectives of this research, a high fidelity numerical strategy for turbomachinery aeroelasticity is developed based on the following novel numerical methods.

1) An accurate rotor/stator sliding BC is developed for multistage turbomachinery simulation in order to resolve the wake propagation between blade rows. The flux at the interface is fully conserved by using one-to-one grid point connected mesh topology since no interpolation is needed for data exchange between rotor/stator domains. The rotor side mesh rotates and at the same time connects the nearest corresponding cell at the stator side to exchange the conservative variables. A rotor/stator sliding BC based on linear interpolation is also developed in this study. In addition, a mixing plane approach based on circumferential averaging to conserve the mass flow and radial profiles at rotor/stator interface is developed for steady state multistage simulation.

2) To make use of a sector of annulus turbomachinery simulation, efficient and accurate circumferential boundary conditions are implemented to consider the effect of phase angle difference using a time shifted phase lag (TSPL) approach and the Fourier series approach.

3) Simulation capability for turbomachinery aeroelasticity is established by using a fully coupled fluid/structure interaction approach and by developing an advanced deforming mesh that can facilitate a large displacement of vibrating blade by removing mesh skewness over the blade tip. For the fully coupled FSI, the time accurate 3D Navier-Stokes equations in a rotating frame of reference are solved with a system of 5 decoupled structure modal equations until both the flow and structure solutions are fully converged via a successive iteration within each physical time step.

4) Advanced numerical algorithms are adopted for high speed axial fan/compressor simulations. An efficient and low diffusion E-CUSP (LDE) scheme is used as a shock capturing Riemann solver to resolve discontinuities with minimal numerical dissipation. An implicit high order accuracy weighted essentially non-oscillatory (WENO) scheme for the inviscid flux is employed with a set of fully conservative high order central differencing for the viscous terms to accurately capture the nonlinear interaction of vibrating blades with the flow.

5) An advanced LES/RANS hybrid turbulence model, DDES suggested by Spalart et al. [37] is employed for high fidelity NSV simulation. DDES is devised to overcome the modeled stress depletion (MSD) problem of the original DES97 when the mesh is very thin compared to the boundary layer thickness. With DDES, a blending function is introduced to limit the length scale of DES97 to ensure the transition of RANS to LES be independent of grid spacing.

6) An efficient wall boundary condition based on the wall function is used to save mesh size. When y^+ is over 11, no-slip condition is replaced by using the wall function. The law of the wall approach is based on the assumption that the boundary layer is attached. The rational that the law of the wall BC is used for all the conditions including near stall is that the vortices in the tip and hub region are mostly large structures and the inconsistency is minimized by using the local velocity direction at the boundary layer edge.

Finally, intensive validation of the high fidelity turbomachinery numerical methodology developed is achieved for series of aeromechanical benchmark cases with analytical or experimental results including the MSD in a 3D flat plate, NACA0012 stall, AGARD wing flutter, rotating stall and flutter for NASA Rotor 67, and NASA Stage 35.

1.4 Outline of the Thesis

The state-of-art technologies employed for high fidelity turbomachinery FSI simulation are reviewed in chapter 2.

Noninertial reference frame is adopted for both flow and structure governing equations. The time accurate Navier-Stokes equations are derived in a rotating frame as the flow governing equations in chapter 3. For the structure governing equations, the decoupled modal equations are derived in the same rotating frame in chapter 4.

In chapter 5, the numerical methods including the implicit discretization of the Navier-Stokes equations, the low diffusion E-cusp scheme as an accurate approximate Riemann solver, and the high order inviscid and viscous flux reconstruction schemes are described.

Turbomachinery boundary conditions developed in this thesis including the steady mixing plane, the fully conservative rotor/stator sliding interface, the sliding BC using interpolation, the Fourier series phase lag, and the time-shifted phase lag are given with great details in chapter 6. Advanced blade deforming mesh is described in chapter 7.

Validation studies on the high fidelity FSI methodology including the flat plate modeled stress depletion (MSD), NACA0012 stall flows, NASA Rotor 67 rotating stall and flutter, AGARD Wing supersonic flutter, NASA Stage 35, and a GE axial compressor are demonstrated in chapter 8.

In chapter 9, 10 and 11, investigation of non-synchronous vibration mechanism of a GE aircraft engine axial compressor is conducted using the high fidelity FSI methodology developed in this thesis.

Chapter 2

Overview of FSI Methodology

This chapter describes the current research status on axial fan/compressor non-synchronous vibration, turbomachinery flutter, turbulence simulation, rotating stall, rotor/stator interaction, phase lag BC, and high order shock capturing scheme.

2.1 Non-synchronous Vibration

Rotating instability (RI) is considered as one cause for NSV [1, 2, 14, 15]. The experiment for the 10 stage high pressure axial compressor by Baumgartner et al. [1] seen in Fig. 2.1 shows a NSV event with high amplitude vibration on the 1st stage rotor blades. A rotating flow instability revolves relative to the rotor similar to rotating stall. The measured pressure at various blade heights near the rotor leading edge show the radial dependency of this rotating instability. The measured frequencies show high coherence levels of the NSV above 74% span, which are decaying away from the RI center and eventually at 65% blade span the NSV due to RI is no more detectable as shown in Fig. 2.2.

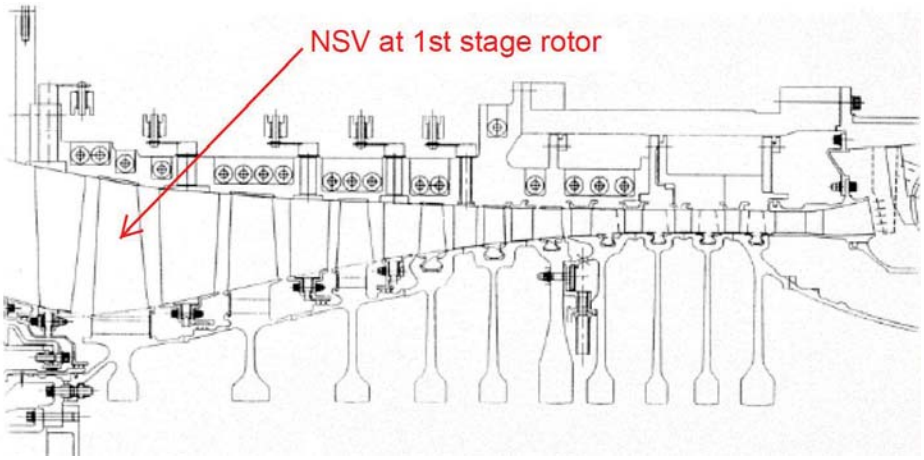

Figure 2.1: The 10 stage high pressure axial compressor with a NSV at the 1st stage rotor blades [1]

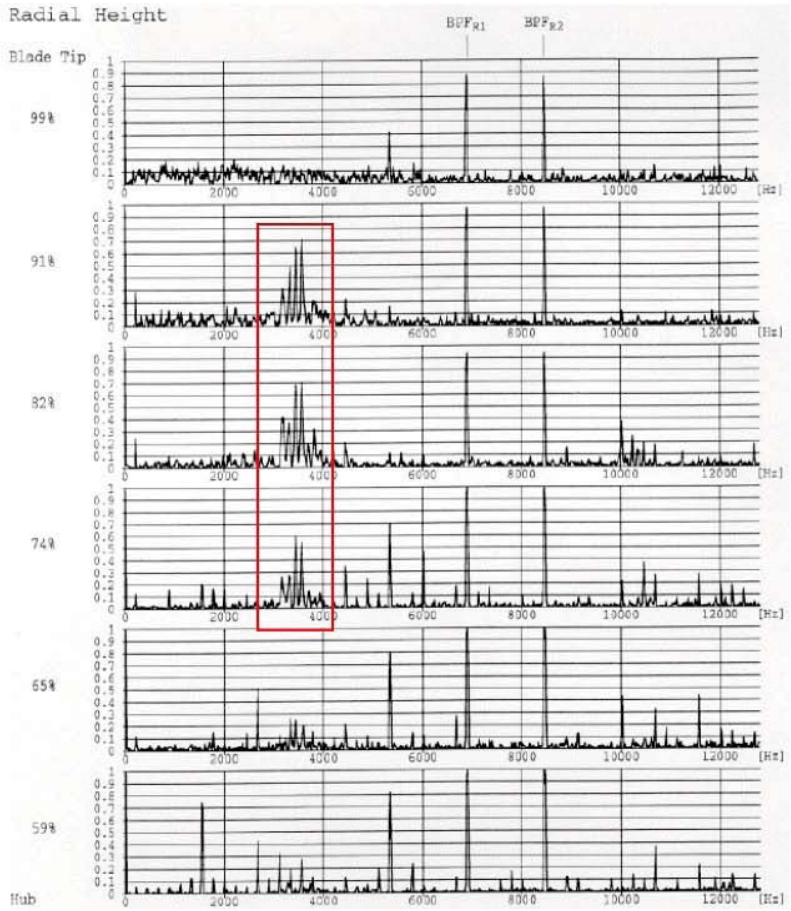

Figure 2.2: The frequencies of the measured pressure acquired on the rotor leading edge of the 10 stage high pressure axial compressor [1]

Kielb et al. [14] conducted an experimental and numerical investigation for a full size compressor rig where blade-mounted strain gages and case-mounted unsteady pressure transducers are devised to measure the NSV. The experimental strain gage data show step change in frequency as the compressor operating condition varies. This is another feature of the NSV. The 1st stage rotor blades experience a significant non-engine order vibration of 2661 Hz at 12700 RPM near 1st torsional mode (or 2nd mode natural frequency) and exhibit the NSV frequency shift from 2661 to 2600 Hz at 12800 RPM. At the casing, the NSV frequencies of 3516 Hz and 3662 Hz are measured in the non-rotating reference frame. Their numerical results for the 1/7th rotor annulus rotor indicate a suction side vortex shedding and a tip flow instability near 75% span as the excitation source of the NSV.

The work of Marz et al. [2] also shows a rotating instability as a main source for NSV. A low speed single stage fan with outlet guide vanes is used for their experimental and numerical study on NSV. The rotor design speed is 3000 RPM and has the blade passing frequency (BPF) of 560Hz. They tested four different tip clearances of 0.7%, 1.4%, 2.8%, and 5.6% tip axial chord at near the maximum fan loading condition. The measured wall pressure spectrum shows a NSV frequency at roughly half of BPF. The time-lapse plots of casing wall pressure seen in Fig. 2.3 indicate that the flow intensity varies from blade to blade with the presence of a high fluctuating flow instability in the rotor entry plane for tip clearances of 2.8% and 5.6%. Their experiment turns out that the blade sensor signal near the rotating instability has a strong periodic content. A vortex structure moving from the suction side to the pressure side is observed in the middle of the blade passage by the full annulus simulation for 2.8% tip clearance, which is the main causes of unsteadiness when

the rotating instability develops. The numerical study shows no tip spillage flow even with the rotating instability.

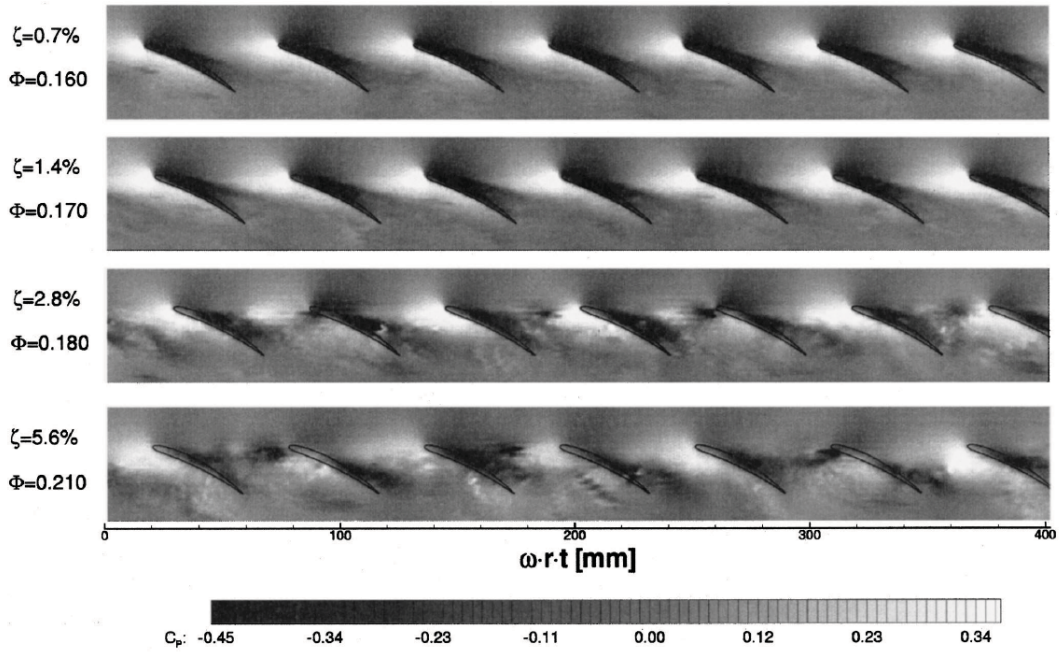

Figure 2.3: The time-lapse plots of casing wall pressure at different tip clearances [2]

Mailach et al. [15] carried out an experimental study of a low speed research compressor to investigate influence of tip clearance and operating point on rotating instability. Rotating instability have been found at a tip clearance of 3% tip axial chord. At a larger tip clearance of 4.3%, the rotating instability is fully developed for all the rotor speeds including 50%, 80%, and 100% design speed. The formation of rotating instability is limited to a narrow operating range near the stall boundary. The measurement at the casing wall shows a narrow band increase of the amplitudes in the frequency spectrum at about 30% of BPF. When the compressor approaches the stall boundary, the rotating instability shifts to slightly lower frequencies while amplitude of the perturbation grows. Measurements on the rotor blades show that the rotating instability is limited to the blade tip region. Maximum

amplitudes appear at 92% of the blade height and 20% to 30% of chord length. For a large tip clearance a strong blade tip vortex is observed in the rotor tip region. The fluctuating blade tip vortices propagate in rotor circumferential direction. Tip clearance size is shown as the main influence parameter on the rotating instability.

Thomassin, et al. [3, 16] suggested a theory different from the rotating instability to explain the NSV of the 1st stage rotor blades of a PWC multistage high pressure compressor illustrated by Fig. 2.4 based on the resonance of a impinging jet vortex structure and the acoustic feedback of a vibrating plate. The jet core feedback theory has been proved by an experiment conducted in [3, 16]. It shows that when the acoustic reflection wave length equals to the jet-to-plate distance, the jet vortical structures lock-on to the acoustic wave frequency and significant amplification of the pressure fluctuation and vibration of the flexible plate are observed. They suggest a simple model to predict the critical tip velocity based on their impinging jet experiment. Vo's simulation [39] shows a tip clearance flow instability for an isolated subsonic axial compressor rotor. In the blade tip region the trailing edge backflow causes flow impingement on the pressure side that leads to the flow unsteadiness associated with the NSV.

A NSV phenomenon for a low aspect ratio fan stage stator with a large amplitude is identified by the experiment of Sanders [40]. The rotor blades ahead the stators experience flutter, not NSV. Strain gage measurements on selected vanes at various locations around the annulus show that the highest response occurs on the vicinity of low static pressure(high Mach number) regions of the fan stator assembly. The high amplitude frequencies observed along the nominal operating line during the fan engine test is a narrow band and non-synchronous with the 1st bending mode approximately 25% below. The URANS

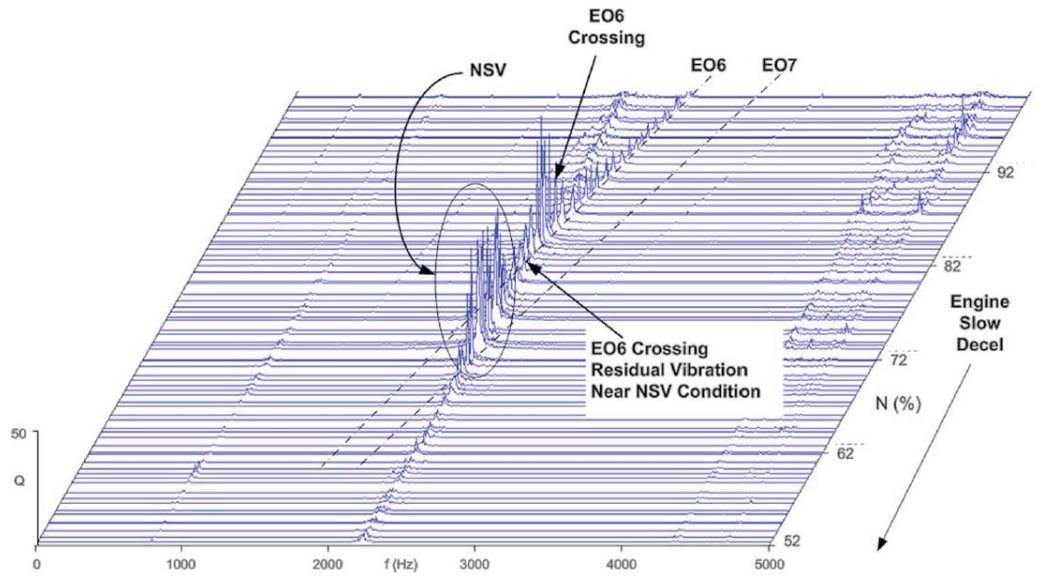

Figure 2.4: The frequencies obtained by the actual engine blade strain gage response during the NSV [3]

simulation demonstrates that the NSV is driven by dynamic stalling of the fan stator due to unsteady shock-boundary layer interaction.

In this thesis, the mechanism of NSV of a GE axial compressor is investigated using the high fidelity FSI methodology achieved based on a fully conservative rotor/stator sliding BC, the time-shifted phase lag BC, the fully coupled fluid/structure interaction with advanced blade tip deforming mesh, and an advanced hybrid RANS/LES turbulence, DDES with the Low Diffusion E-CUSP scheme. It is demonstrated for the first time that the tornado vortex propagates at the speed of a non-engine order frequency in the opposite to the rotor rotation and causes the NSV of the high speed axial compressor. The rotor blades under NSV is not damped out similar to a limited cycle oscillation (LCO) and is not divergent unlike turbomachinery flutter. NSV of the high-speed axial compressor is a torsional blade vibration coupled with highly oscillating aerodynamic pressure acting on the blades due to the tornado vortex instability.

2.2 Turbomachinery Flutter

Flutter of turbomachinery blades is an aeroelastic self-excited instability at or close to the eigenfrequency of the blades [1]. It may occur in several ways including subsonic/supersonic stall flutter, supersonic unstalled flutter, choking flutter and acoustic flutter [11, 41–43].

Stall flutter occurs when some blades are stalled and it often causes mechanical failure due to the resonance of the blade frequency with the stall cell propagation [41]. It is noted that the flutter frequency is virtually identical with the blade natural frequency owing to the large mass ratio of the blade to the fluid [44]. Frequency of flutter is usually not synchronized with integer multiples of engine rotational frequency [13]. Sanders [6] shows stall-side flutter with resonance at the first bending mode in a modern transonic shroudless low-aspect ratio fan blisk by the experiment. The present authors [7] numerically demonstrate stall flutter of a transonic rotor occurs when the shock is fully detached from the rotor blade with flow separation, and it shows resonance at the first mode of blade natural frequencies using the fully coupled fluid/structure interaction model.

Flutter observed in modern fans/compressors has been predicted by using different methodlogies [6–12]. Srivastava et al. [8] shows influence of shock wave on a transonic forward swept fan with supersonic tip using the energy method, in which the aerodynamic damping is used to determine flutter instability. As a fan approaches to stall, the predicted aerodynamic damping rapidly drops to the stability limit due to the shock induced flow separation on the suction surface, and the flutter occurs. Vahdati et al. [11] uses a strongly coupled fluid/strcuture interaction to simulate a wide-chord transonic fan flutter. They indicate that the flow separation behind the shock on the suction surface is the key driver of

the fan flutter. Chew et al. [12] used inviscid linearized model to capture stall flutter(or referred to as part-speed flutter) of a civil wide chord fan and a low aspect ratio military fan engine. Due to some shortcomings such as neglecting viscous terms, endwall boundary layers and tip clearance, their computation fails to show any signs of flutter instability. It is demonstrated by Gruber and Carstens [45] that viscous effects can cause a significant difference in aerodynamic damping.

To accurately resolve nonlinearities of FSI, the governing equations of structural and fluid motion need to be simultaneously integrated in time. However, due to high CPU cost, many of the fluid-structural interaction simulations are implemented by a loosely coupled procedure, i.e., the structural response lags behind the flow solution by one or a few time steps. The information is exchanged after partial or complete convergence of individual solvers [19]. For example, Gnesin et al. [21] solved the unsteady Euler equations with the modal approach for the structure analysis in the partially coupled manner. Doi et al. [20] weakly coupled an explicit Runge-Kutta multigrid flow solver with a FEM structure solver to predict aeroelastic responses of NASA Rotor 67 blade. Carstens eta al. [22] and Sayma et al. [23] loosely integrate the equations of motion using Newmark scheme at each time step.

The fully coupled fluid-structure interaction used in this NSV study [7] is extended for turbomachinery based on the aerodynamic wing flutter approach suggested by Chen and Zha [24, 46]. In their study, time accurate Navier-Stokes equations are solved with a system of N-decoupled structure modal equations in a fully coupled manner. To decouple the equation of motion, transformation of the structural equations to the modal coordinates are applied. The flow field and structure always respond simultaneously by exchanging the

unsteady aerodynamic force and structural displacement within each physical time step via successive iterations on the pseudo-time step.

For validation study, 3D AGARD wing flutter boundary at a supersonic condition is conducted. Even though the mass ratio of structure to fluid does not tend to be same, a high speed fan/compressor blade can flutter because of the instability caused by a strong shock/boundary layer interaction in the passages. Most of the studies on fluid-structural interaction [47–52] of 3D wing has been implemented by a staggered or loosely coupled procedure. In this way the information is exchanged after partial or complete convergence of individual solvers with time lag. For example, Liu et al. [50] used a loosely coupled approach for AGARD 445.6 wing flutter calculations. The equations governing the flow and the displacement of the structure are solved separately by two distinct solvers. Deformed grid is obtained by an energy conservative interpolation procedure between two different grid systems.

Alonso and Jameson [53] used a tightly coupled approach for 2D Euler aeroelastic simulations with explicit Runge-Kutta time marching method. At time level n, the pseudo-time calculation is conducted, and the flow information is sent to the structural solver. Then, the new position is taken into account by the flow solver which repeats the process. The two systems exchange information after every pseudo-time step. In general, about 100 pseudo-time steps are needed for the explicit schemes to ensure adequate convergence [49, 50]. Yang et al. [54] also presented an implicit coupled fluid-structure coupling based on the Runge-Kutta time integration scheme. The combined systems of fluid and structural equations are solved in a strongly coupled manner to eliminate time lag between the flow and the structure solution at each physical time step.

Prediction of supersonic flutter is particularly challenging since the flow involves complicated nonlinear phenomena such as shock wave/boundary layer interaction and flow separation. So far, the flutter boundary prediction for AGARD wing can agree with the experimental measurement fairly well at subsonic Mach number including the sonic dip.

However, currently the flutter boundary predictions for AGARD Wing at supersonic incoming flow agree poorly with the experimental measurement. For example, for the AGARD wing 445.6 at Mach number of 1.141, Liu et al. [50] used Jameson's explicit Runge-Kutta scheme and overpredicted the flutter velocity index by 61.74%. Rausch et al. [47] also overpredicted the flutter boundary by about 20% using the upwind flux vector splitting scheme with Baldwin-Lomax turbulence model. Xiao et al. [48] overpredicted the flutter boundary by 34% using a loosely coupled FSI procedure with Menter's $k-\omega$ turbulence model. Yang et al. [54] overpredicted by 58.7% using Baldwin-Lomax turbulence model. Chen et al. [24] overpredicted by 14% using a RANS Baldwin-Lomax model. In general, almost all the current CFD simulations for supersonic flutter boundary overpredict the flutter boundary with a large discrepancy.

In this thesis, the high fidelity simulation capability for turbomachinery aeroelasticity is established by using a fully coupled fluid/structure interaction approach and by developing an advanced deforming mesh that can facilitate a large displacement of vibrating blade by removing mesh skewness over the blade tip. Validation of supersonic flutter of a 3D wing at free stream Mach number of 1.141 demonstrates excellency of the fully coupled higher order FSI methodology with DDES in the prediction of the flutter boundary. NASA Rotor 67 FSI simulation using 4 blade passages with the DES of turbulence indicates the transonic rotor flutters as rotating stall develops. In addition, the traveling wave BC is

implemented to consider BTW (backward travelling wave) and FTW (forward travelling wave) effect on blade flutter. FSI simulations of a Honeywell fan rotor is conducted to investigate the mechanism of a transonic fan blade flutter. A half annulus FSI simulation with FTW (forward travelling wave) at N_D of 2 is in progress using the high order fully coupled FSI with the travelling BC. This case study is not included in this thesis because of the time limitation and will be presented in other publications.

2.3 Phase Lag BC

The phase-lagged technique for periodic boundary can dramatically reduce the computational efforts since it makes use of a reduced sector model instead of full annulus simulation. The phase-lagged methods can be used as long as the phase shifted periodicity exits. When a single blade passage or a sector of the annulus is used for unsteady aerodynamic simulation of turbomachinery, the effect of the phase difference needs to be considered due to the inter blade phase angle (IBPA). Without considering phase angle difference, an approach such as in-phase condition may not capture the unsteadiness and nonlinearity in turbomachinery flutter.

The numerical methods to treat phase angle difference at the periodic boundaries have been proposed by several researchers [33, 34, 55–57]. The TSPL, known as the direct store method suggested by Erodes et al. [33], requires large computational memory since all flow variables are stored over a complete oscillation period. Those stored data are then used to update the current solutions at the corresponding upper/lower periodic boundaries. Instead of using frequency information such as blade passing frequency or blade natural frequency,

the time shifted conditions at the boundaries are determined based on the stored data for an oscillation cycle. With the direct store approach, no other assumption except for the phase-shifted condition itself is made.

An efficient FSPL BC so called the shape correction method was proposed by He and Denton [34, 55]. The basic idea is to approximate the timewise variations of the flow variables in the Fourier series, and then store the Fourier components instead of the variables at each time step. Using these coefficients, the flow variables at the boundaries are regenerated. For most flow conditions of interest, the first few orders of Fourier coefficients are sufficient to predict the unsteady characteristics [34, 55, 56]. In consequence only minor additional computer memory is needed.

Srivastava et al. [56] compared the direct store method and the Fourier phase lag BC for a turbine cascade, and shows that once convergence is achieved, basically similar results are obtained. However, there is a disadvantage that it needs to input the primary perturbation or vibration frequencies required by the Fourier phase lag BC although such frequencies are not known *a priori*. In other words, the TSPL BC is more general than the Fourier phase lag BC, but still limited to the temporal periodicity assumption, which does not exist when a rotating stall occurs.

In this thesis, the-time shifted phase-lagged BC (TSPL) and the Fourier series phase lag BC (FSPL) are implemented to facilitate a sector of annulus FSI by considering the effect of inter-blade phase angle difference. These phase-lagged boundary conditions are validated using NASA Rotor 67. The fully coupled FSI flutter simulations for the full annulus and single blade passage with phase lag methods indicate that TSPL predicts blade vibration level closer to the full annulus FSI simulation than the Fourier series phase lag BC.

2.4 Rotor/Stator Interaction

The interaction between rotating and stationary blades introduces inherent unsteadiness to the flow of multistage turbomachinery. There are typically two approaches to treat two adjacent blade rows in relative rotation frame; mixing plane and sliding interface.

Mixing plane method has been widely used due to its simplicity. Denton [58], Dawes [59], Singh [60], and Chen [61] used mixing plane approach to calculate multistage machines. In this approach the circumferential-averaging is typically used in order to achieve the radial profiles and conserve the mass flow. Most researchers [58–61] exchange the flow data between two blade rows using less than two cells for the mixing BC. Gerolymos et al. [62] overlapped multiple phantom cells where the averaged quantities of the opposite domain are stored. There are two major disadvantages that arise with mixing plane. First, mixing plane generates artificial mixing loss [63] due to averaging the non-uniform flow at the mixed-out and mixed-in plane. Second, the effects of unsteady interaction between inter-blade rows could not be taken into account. Barter et al. [61] presented an effect of unsteady interaction that changes the blade loading of the upstream blade in a multistage transonic turbine.

Sliding interface methods are often used for multi-stage unsteady rotor-stator interaction. For instance, the shock wave interaction between the inter blade rows as well as rotating instabilities such as NSV(Non-Synchronous Vibration) and rotating stall can be predicted not by the steady approach, but only by the conservative unsteady approach. Numerous studies on the unsteady rotor/stator interaction has been developed [64–67] based on interpolation on the rotor-stator interface. Rai [64] used the patched and overlaid grid

system based on interpolation to solve an axial turbine with a rotor-stator configuration. Chen et al. [68] pointed out that lack of flux conservation can significantly affect the solution accuracy where shock interaction exists between the blade rows. The fact is the methods of rotor/stator interaction using any type of interpolation methods can not satisfy the conservation of the flux across the interface.

For transonic multistage simulations, low diffusion and shock capturing capability have large impacts on the accuracy due to the shock wave interaction with boundary layer and tip vortices and, wake propagation. For example, Gerolymos et al. [62] applied the MUSCL Van Leer flux vector splitting with Van Albada limiters to solve a four stage axial turbine at a off-design point where strong coupling of the flow field between the blade rows is dominant. Comparison of CFD and experiment shows that the mixing plane overestimated efficiency by about 2%, and the predicted radial profiles such as total pressure, total temperature, and flow angle shows large discrepancy compared to the experiment.

In this thesis, a fully conservative sliding BC based on one-to-one interface mesh is developed with high order shock capturing schemes to accurately capture the unsteady interaction between rotor and stationary blades. A sliding BC using interpolation is also implemented to be used in more convenient way. The unsteady multistage simulation for a 1/7th annulus of a GE axial compressor with TSPL shows that the fully conservative sliding BC captures wake propagation very well in the interaction between blade rows. The sliding BC using interpolation also performs very well for unsteady rotor/stator interaction even though a full conservation of the fluxes across the sliding BC is not ensured. The numerical experiments indicate the error is very small and acceptable. The mixing plane method cuts off the shock propagation upstream, tip vortex and propagation downstream. However, it is

an efficient and convenient methodology for multi-stage compressor calculation. Numerical experiments indicate that an excellent agreement with experiment for the steady state speedline and radial profiles can be achieved.

2.5 Rotating stall

When rotating stall occurs in axial compressors, two different stall inception patterns exist [31, 69–75], known as modal and spike. Modal stall inception is a form of pre-stall disturbance with a wavelength equal to the rotor circumference. In the experiments [31,69,70] of low-speed compressors, modal inception is observed prior to stall. The rotating stall through modal inception is smoothly developed without an abrupt change in amplitude or speed. The speed of stall cell rotation is observed to have up to 50% of the rotor speed. The work of Camp and Day [69] shows that modal disturbance only occurs at the peak total-to-static pressure rise characteristic.

Spike stall inception was first discovered by Day [31]. In his experiment, the low speed compressor stalled via the growth of a small localized disturbance with a few notable features. First, the unstable sharp peaks found in a limited area of rotor tip passages rapidly destroys the axial symmetry of the flow. Consequently, a part of annulus has the stalled blades whereas the remainder has the unstalled blades. Second, the speed of rotation of the disturbance was dramatically decreased from 72% at onset to 45% when fully developed. Silkowski's experiment [72] of the GE low-speed four stage compressor shows the downward spike for about three blade passages in the measured axial velocity of the tip span. Inoue [73]'s experiment shows that the stall inception characterized by a spiky short length-

scale disturbance turns into a deep stall cell with growth of a long length scale disturbance. All these stall inception observations are limited to low speed compressors.

For the high-speed compressors, the type of flow breakdown through stall or surge is not well understood due to the effects of compressibility, difficulties in detailed measurement, shaft speed, and geometry. Recently Reuss et al. [74] tested a jet engine high pressure compressor to investigate the effects of inlet total pressure distortions on rotating stall. Their experiment shows that the spike type stall cell moves at approximately 60% of the compressor speed. After two to three more revolutions, rotating stall has been established. The speed of the cell is reduced to about 45% of the compressor speed and its length scale is roughly 50% of the annulus. Hah et al. [75] numerically and experimentally studied the inception of a high speed compressor, which is an isolated rotor designed to have a pressure ratio of 1.5, the supersonic tip speed of Mach number 1.35, and the shaft speed of 20,000 RPM. The measured casing pressure shows the rotor stalls quickly at about two rotor revolutions with spike inception, and more than two blade passages are disturbed at the onset. The short length scale stall cell rotates at roughly half of the rotor speed in the opposite direction to the rotor during the stall inception.

Mina et al. [76] carried out numerical simulation of rotating stall inception for NASA stage 35 using a single passage. It is observed that at near stall, the tip vortex is larger in size and its trajectory becomes perpendicular to the main axial flow. A low-momentum area near rotor tip leading edge causes the flow spillage and leads to stall inception. L. He [77] simulated a rotating stall using a 2D multi-blade passage and showed rotating stall pattern during its inception is sensitive to external disturbances. A long length scale single cell rotates at about 50% blade speed, while two-cell pattern with a shorter length scale

has an absolute rotating speed of about 60% blade speed. Davis and Yao [78] also used NASA stage 35 single blade passage to investigate stall inception. Their finding agrees with Hoying et al. [79] who shows that the circulation of tip clearance vortex plays an important role in stall inception development. Vo [80] conducted rotating stall simulation for a low speed rotor with relative tip Mach number of 0.2 and the transonic NASA stage 35 rotor using six blade passages. It is shown that leading edge tip clearance flow spillage below blade tip and backflow at the trailing-edge plane occur at the onset of spike.

A full annulus approach is essential to accurately capture rotating stall due to the non-periodicity of the disturbance and the length scale of the stall cells. For instance, the developed stall cell induced by spike inception can have the length scale equal to the rotor circumference [32]. Hah et al. [75] used full annulus large eddy simulation (LES) and captured the spike type stall inception triggered by tip clearance vortex in high-speed rotor. Khaleghi et al. [81] carried out a full annulus simulation of NASA Rotor 67 by considering the blade surface roughness effect as a source to trigger rotating stall. They also investigated the effects of injection on rotating stall stability [82]. The casing injection pushes the shock backward in the passages and reduces the region of negative axial velocity near the tip of the blades. Chen et al. [83,84] conducted a full annulus simulation of NASA Stage 35 at the full speed using an unsteady RANS (URANS) model. Their simulation shows that a disturbance first travels at the rotor speed, then changes to a spike disturbance of 84% rotor speed consisting of multiple stall cells. The disturbance eventually forms a single rotating stall cell of 43% rotor speed [83]. In case of a long length disturbance followed by a spike type inception, the study shows no evidence of flow separation linked to stall [84]. Lin et al. [85] demonstrated the flow structure of short length scale disturbances for a low-speed

axial compressor rotor. A full annulus with a coarse grid is used to simulate spike type rotating stall process with an inlet distortion. It is shown that the complex flow interaction of main flow, tip leakage flow, and reversed flow is the key to the formation of the spike type rotating stall and it extends deeply into the blade span. A horn-shaped tip leakage vortex that generates a pressure dip near the casing is detected during the spike type rotating stall. The spike rotates at about 50% of the rotor speed.

In this thesis, detached eddy simulation (DES) of a full annulus rotor is conducted for the first time to investigate stall inception for an axial transonic rotor - NASA Rotor 67. An inflow total pressure perturbation BC is implemented to consider background disturbance on rotating stall. It is observed that the rotating stall is initiated by the local spike flow disturbance, which quickly induces the rotor to stall roughly over 2 rotor revolutions. The stall cell covering more than 6 blade tip passages propagates at 48% of rotor speed in the counter rotor rotation direction. The process of rotating stall is captured by the full annulus DES, which indicates that the blockage created by the low energy vortical flow structure pushes the tip leakage flow to the adjacent blade behind the detached sonic boundary.

2.6 Turbulence Simulation

Simulation of turbulent flows is critical for accurate prediction of such aeromechanical phenomena since flow separation and vortical flows play a key role in formation of rotating instabilities, which is considered as the root cause of blade faiulre [6, 7, 42]. For example, rotating stall characteristics such as the number of cells and propagating speed in an annulus determines the frequency of the stall cells passing each blade. If such a frequency is near

the natural frequency of the blades, resonance may occur and result in mechanical failure of the blades.

Stall flow simulation has many difficulties in using Reynolds-averaged Navier-Strokes (RANS) methods since RANS cannot predict unsteady vortical flows well. RANS methods intend to model the large scale eddies using a universal model. Large scale turbulence is affected by flow geometries and boundary conditions and a universal model does not exist.

Large Eddy Simulation (LES) is an intermediate approach between the direct numerical simulation (DNS) of turbulence flows and the solution of RANS, hence LES is promising to overcome the disadvantages of the RANS model. DNS has largely been limited to simple geometries at low Reynolds number since it requires grid points $\simeq Re^{9/4}$ and times steps $\simeq Re^{3/4}$ to resolve all scales of turbulence [86].

In LES, the governing equations are spatially filtered on the scale of the numerical grid. The large energy containing scales are directly simulated, and the small scale eddies, which are generally more homogeneous and universal, are modeled. The large eddies are strongly affected by the flow field geometry boundaries. Therefore the direct computation of large eddies by LES is more accurate than the modeling of the large eddies by RANS. However, for high Reynolds number flows such as those of transonic wings and turbomachinery blades, to resolve wall boundary layer, LES needs the CPU resource not much less than the Direct Numerical Simulation(DNS). This makes the LES too expensive for full annulus unsteady calculations. For engineering applications, it is not hopeful for LES to be rigorously used until in another 4 decades [36]. LES has been used for airfoil stall flows [87–89]. For example, Moreau et al. [89] employed LES to simulate the trailing edge flow and noise of NACA0012 airfoil at near stall. It is pointed out that RANS fails to capture the stall

point, while LES provides a more realistic behavior and qualitatively resolves better the shea-layer and the von Karman instabilities [89].

To overcome the intensive CPU requirement for LES, Spalart et al. developed the detached eddy simulation (DES) strategy [36], which is a hybrid RANS and LES method. Near the solid surface within the wall boundary layer, the unsteady RANS model is realized. Away from the wall surface, the model automatically converts to LES. By using the RANS model near walls, the mesh size as well as the CPU time can be tremendously reduced. The motivation of DES is that the LES is powerful in regions of massive separation and other free shear flows such as jets, but much too costly in the large area of thin wall boundary layers.

However, a defect of the first generation DES model [36], DES97, has been also exposed. DES97 may behave incorrectly and cause modeled stress depletion (MSD) in the regions of thick boundary layers and shallow separation regions due to the grid spacing dependence [37]. Delayed detached-eddy simulation (DDES) by Spalart [37] is an improved version of the DES97 model. With DDES, a blending function similar to the one used by Menter and Kuntz [38] for the SST model is introduced to limit the length scale of DES97 to ensure the transition of RANS to LES be independent of grid spacing. Spalart et al. [37] validated DDES for a flat plate turbulent boundary layer with the wall-parallel grid spacing about 1/10th of the boundary layer thickness (severe grid or ambiguous grid defined by Spalart).

Numerical studies on airfoil stall flows have been conducted by other researchers [89–92]. For example, Morton et al. [90] applied DES97 to simulate a full F/A-18E aircraft experiencing massively separated flows. The simulation demonstrates the ability of DES to

accurately predict transonic nonlinear aerodynamic phenomena of abrupt wing stall, which is created by a shock-vortex-boundary layer interaction. Travin et al. [92] indicate that for massively separated flows over NACA0021 airfoil at 60 degrees angle of attack, DDES performs quite the same as the original DES97 using a coarse grid of $141 \times 101 \times 31$ nodes in the streamwise, wall-normal and spanwise directions respectively.

For DES, the majority of the flow field with the large vortex structure of separation is resolved by LES. The requirement for DES numerical schemes hence should be as stringent as LES. To achieve high accuracy DES solution, the high order (higher than 2nd order) scheme is desirable. Travin et al. [92] has employed a high order biased upwind scheme and central differencing scheme for DES. However, the scheme is not aimed at shock capturing and has difficulty in dealing with shock boundary layer interaction of high speed flows.

It is shown [36, 93, 94] that the use of hybrid RANS/LES approaches is very effective for stalled flow predictions. The validation of current DES methodology for the stalled flow over NACA0012 airfoil at 45° angle of attack was accomplished by the present authors [35]. The DES predicts the drag accurately compared to the experiment, whereas the URANS model overpredicts the drag by about 33%.

In this thesis, an advanced hybrid RANS/LES turbulence model DDES(delayed detached eddy simulation) with high order schemes is validated for a 3D flat plate turbulent boundary layer using a severe grid designed to generate Modeled-Stress Depletion of DES97. The DES shows 75% reduction of the eddy viscosity in the wall boundary layer, whereas the DDES preserves the eddy viscosity at the same level as the URANS. Simulations using the DDES with the 3rd order and 5th order WENO schemes are also conducted to investigate the dynamic stall flows over NACA0012 airfoil at 17°, 26°, 45° and 60° angle

of attack (AOA). Both the 3rd order and 5th order WENO schemes predict the stalled flow similarly with little difference in the predicted lift and drag less than AOA of 45°, while at AOA of 60°, the 5th order WENO scheme shows better agreement with the experiment than the 3rd order WENO scheme. In addition, DDES and DES97 predict the drag and lift accurately, whereas URANS overpredicts the drag and lift by about 32% at 45° AOA.

2.7 High Order Shock Capturing Scheme

Developing accurate and efficient numerical schemes is one of the most important tasks of the CFD researchers and engineers. It is particularly important when a high fidelity numerical simulation, such as detached-eddy simulation (DES) and large eddy simulation (LES) is performed for a unsteady flow problem, which is usually very CPU intensive. For aerospace engineering applications with shock waves or contact surfaces, the essentially non-oscillatory (ENO) or weighted essentially non-oscillatory (WENO) schemes are attractive for their capability to capture discontinuities and achieve the consistent high order accuracy in smooth regions. By using a convex combination of all candidate stencils to replace the smoothest one in the ENO scheme, a WENO scheme has more advantages over its ENO counterpart. For example, it approaches certain high order accuracy in smooth regions and has better convergence rate due to the smoother numerical flux used. From its appearance [95, 96] to present, the WENO schemes have been extensively applied to different flow problems in many areas.

In a WENO scheme, a Riemann solver is needed to capture the discontinuities. There are two ways to evaluate the Riemann solver fluxes. For WENO finite difference schemes,

Shu suggested that the WENO reconstruction be directly applied to the split fluxes from left or right [97]. In this research, we employ a different method, which is to evaluate the conservative variables with WENO scheme and then use the conservative variables to calculate the fluxes based on the Riemann solvers. This is similar to the MUSCL method of Van Leer [98].

Zhang and Shu [99] found that, when a 5th order WENO scheme combined with a Runge-Kutta time discretization is used to achieve steady state solutions, the residual stops dropping at the truncation error level of the scheme, which is far above the machine zero. They noticed that the original smoothness indicator of Jiang and Shu [96] results in a small oscillation near a steady shock wave. The oscillation propagates to the smooth region and causes the residual to hang at the truncation error level rather than to approach machine zero. They proposed a modified smoothness indicator near the shock region for the fifth order WENO scheme, which can drive the residual to machine zero for some 1D and 2D problems without the influence from the boundary conditions. But for the other examples, the residuals still fluctuate at the level of ($10^{-2} \sim 10^{-4}$). Zhang and Shu [99] attribute the convergence difficulty to the influence of boundary conditions. At a critical point (the first derivative is zero), the first term in the Taylor series expansion of the IS_k of Zhang and Shu does not satisfy the requirement of $IS_k = D(1 + O(\Delta x^{r-1}))$ to achieve 5th order accuracy. Thus the accuracy of the scheme of Zhang and Shu [99] is only 3rd order at a critical point.

Henrick et al. [100] proposed a mapped WENO scheme to achieve the optimal accuracy order at the critical point of a smooth function and discussed the choice of ε value for the 5th order WENO scheme. When ε is dominant in magnitude, the preconditions of WENO5 scheme approaches those of a central difference scheme. Furthermore, the oscillation on

the order of ε^2 may exist near discontinuities. Hence if the ε is too large, it will mitigate the ENO behavior of the method. Henrick et al. suggested that ε can be slightly larger than the square root of the smallest positive number allowed for a particular machine. But they didn't study the convergence behavior for computing steady state solutions.

In this research, the 5th order finite differencing WENO scheme [101, 102] is used to evaluate the inviscid fluxes, and the 4th order central differencing scheme [103] is used to calculate the viscous fluxes. The WENO scheme adopted uses an optimized ε value and is able to remove the weights oscillation, maintain the sensitivity to shock and contact surface discontinuities, achieve optimal weights and thus the minimal dissipation, and obtain solid convergence to machine zero.

An upwind scheme is required as a Riemann solver when a high order WENO scheme is used. The upwind schemes are designed to make the flux computation based on the flow characteristics. The upwind schemes have inherent numerical dissipation, which makes the artificial dissipation unnecessary. The approximate Riemann solver scheme developed by Roe [104] is one of the most famous upwind schemes. By introducing the Jacobian and Roe's average for the variables, the Roe scheme exactly satisfies the Rankine-Hugonoit relations and directly capture the discontinuities. The Roe scheme was considered as the most accurate scheme among the available differencing schemes in 1987 [105]. But the Roe scheme uses matrix dissipation and hence it is time consuming.

To achieve the purpose of efficiency, accuracy and simplicity to use, many efforts have been made to develop upwind schemes only using scalar dissipation instead of matrix dissipation such as that of the Roe's flux difference splitting (FDS) scheme [104]. Pioneered by Liou and Steffen [106], the researchers seeking the scalar dissipation primarily follow the

guideline that the velocity and pressure should be separated to consider their characteristics representing the physics of the convection and waves. Liou and his colleagues termed their schemes as advection upstream splitting method(AUSM) schemes, and Jameson gave the name of convective upwind and split pressure (CUSP) schemes [107, 108].

Zha et al. recently suggested a Low Diffusion E-CUSP (LDE) scheme [109] using the Mach number splitting of Edwards's LDFSS schemes [110, 111] for the convective flux. The LDE scheme has low diffusion and can capture crisp shock wave profiles and exact contact discontinuities [109]. The scheme is consistent with the characteristic directions due to the nature of E-CUSP scheme. The solutions calculated by the new scheme is smooth and the scheme can capture crisp shock profile and exact contact discontinuity.

In this thesis, the LDE scheme is used for all cases studied. It is shown by extensive turbomachinery validations that the LDE scheme accurately predicts turbomachinery flows with strong shock/boundary layer interactions and shows its robustness for turbomachinery aeromechanical applications as well.

Chapter 3

The Fluid Flow Governing Equations

In this chapter, the equations of motion of fluid flow for turbomachinery are derived in a moving frame of reference in order to take into account the effects of Coriolis force $(2\Omega\times\mathbf{W})$ and the centrifugal force$(\Omega\times\Omega\times\mathbf{r})$. To improve computational efficiency and accuracy, the Navier-Stokes equations are transformed from the physical space to the computational space.

3.1 Motion in Moving Frame

The motion of a particle A in a relative frame *xyz* to the fixed frame *XYZ* can be depicted in Fig. 3.1. The vector $\mathbf{r}$ is defined in the *XYZ* reference as

$$\mathbf{r} = \mathbf{R} + \varphi \tag{3.1}$$

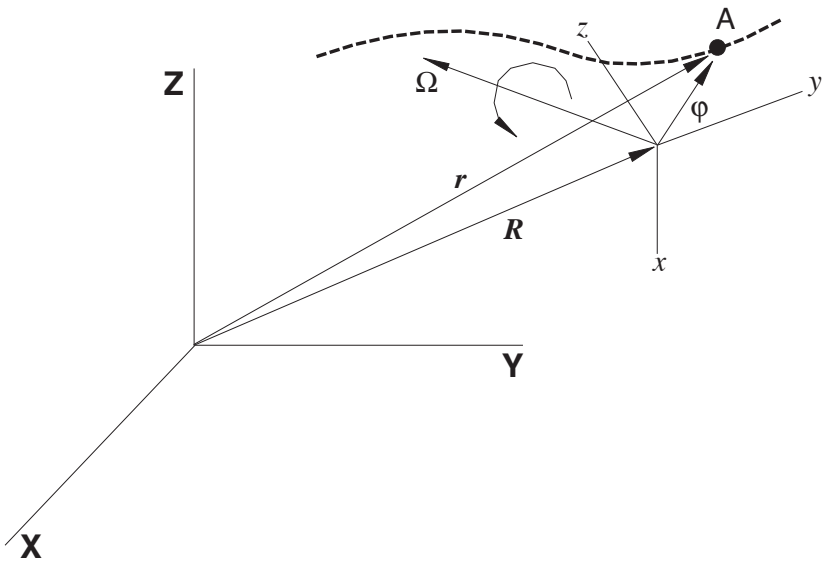

Figure 3.1: Motion of a moving frame of *xyz* relative to the fixed frame of *XYZ*

where **R** is the vector of the reference *xyz* relative to the fixed coordinates *XYZ* and φ a position vector in reference *xyz*.

Applying the material(or Lagrangian) derivative of the vector **r** with respect to time for the *XYZ* reference, then we have

$$\mathbf{V}_{XYZ} = \mathbf{W}_{xyz} + \dot{\mathbf{R}} + \Omega \times \varphi \tag{3.2}$$

where Ω is the angular velocity vector with unit normal vector **e** in a moving frame of *xyz*. **V** is the absolute velocity vector in the *XYZ* reference and **W** is the relative velocity vector in the *xyz* reference.

$$\Omega = \Omega_x \mathbf{e}_x + \Omega_y \mathbf{e}_y + \Omega_z \mathbf{e}_z \tag{3.3}$$

The acceleration of a particle A for different references can be obtained [112] by carrying out the derivative of the velocity vector $\mathbf{V}_{XYZ}$ with respect to time for the XYZ reference as

$$\begin{aligned}\mathbf{a}_{XYZ} = \tfrac{D\mathbf{V}}{Dt})_{XYZ} = \tfrac{D\mathbf{W}}{Dt})_{xyz} + \Omega \times \mathbf{W} + \ddot{\mathbf{R}} + \Omega \times \tfrac{D\varphi}{Dt})_{xyz} + \Omega \times \Omega \times \varphi \\ + \tfrac{D\Omega}{Dt})_{XYZ} \times \varphi\end{aligned} \tag{3.4}$$

The superscript $\dot{}$ and $\ddot{}$ stand for first and second order derivative with respect to time. Since the rotating axis of turbomachinery with the constant angular velocity of Ω used in this study has no translational motion($\dot{R} = 0$) to the fixed or absolute frame(X, Y, Z), in above equation $\ddot{R} = 0$, $D\Omega/Dt = 0$, $\varphi = \mathbf{r}$ and $D\varphi/Dt_{xyz} = \mathbf{W}$. Eq. (3.4) is then rewritten in a rotating cartesian coordinate(x, y, z) as presented in Fig. 3.2.

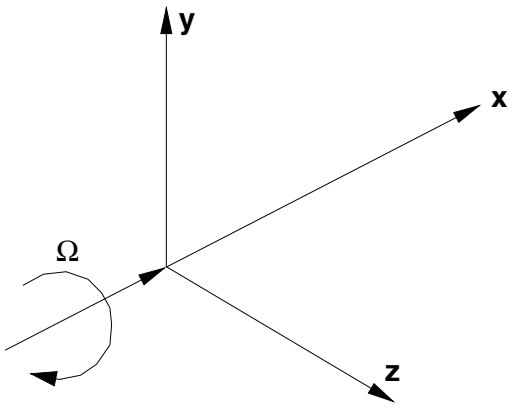

Figure 3.2: The rotating frame in cartesian coordinates for turbomachinery

$$\tfrac{D\mathbf{V}}{Dt})_{XYZ} = \tfrac{D\mathbf{W}}{Dt}_{xyz} + 2\Omega \times \mathbf{W} + \Omega \times \Omega \times \mathbf{r} \tag{3.5}$$

The relationship given by Eq. (3.5) can be used to derive both the aerodynamic and structure model equations. In the Eq. (3.5), $2\Omega \times \mathbf{W}$ is called the Coriolis acceleration vector and $\Omega \times \Omega \times \mathbf{r}$ is the Centrifugal acceleration vector.

3.2 Control Volume Approach

Using the control volume approach known as the Reynolds' transport theorem, the basic conservation equations of mass, momentum, and energy for turbomachinery are derived in a convenient way. Consider the flow quantity $q(t)$ enclosed in a finite control volume $V(t)$ containing the specified mass of fluid. The rate of change of q for the system at any instant t with outward unit normal vector $\mathbf{n}$ and local boundary velocity $\mathbf{u}$ can be expressed as

$$\frac{D}{Dt}\int_{V(t)} qdV = \int_S q(\mathbf{u}\bullet\mathbf{n})dS + \int_V \frac{\partial q}{\partial t}dV \tag{3.6}$$

where S is the control surface. The surface integral can be converted to a volume integral by use of Gauss' divergence theorem as

$$\int_S q(\mathbf{u}\bullet\mathbf{n})dS = \int_V \nabla\bullet(q\mathbf{u})dV \tag{3.7}$$

Then, Eq. (3.6) is written as

$$\frac{D}{Dt}\int_V qdV = \int_V [\frac{\partial q}{\partial t} + \nabla\bullet(q\mathbf{u})]dV \tag{3.8}$$

Or, alternatively,

$$\frac{D}{Dt}\int_V qdV = \int_V [\frac{\partial q}{\partial t} + \frac{\partial}{\partial x_k}(qu_k)]dV \tag{3.9}$$

Eq. (3.8) relates the Lagrangian derivative of a volume integral of a given mass to a volume integral in which the integrand has the Eulerian derivatives only. Conservation of the mass, momentum, and total energy are derived based on Eq. (3.8) in the following sections.

3.3 Conservation of Mass

The property of q in the Reynolds' transport theorem is the mass, m.

$$\frac{D}{Dt}\int_{V(t)} \rho dV = 0 \tag{3.10}$$

where ρ stands for the fluid density. Then, Eq. (3.8) becomes

$$\int_V [\frac{\partial \rho}{\partial t} + \nabla \bullet (\rho \mathbf{u})]dV = 0 \tag{3.11}$$

3.4 Momentum Equation

The property of q in the linear momentum is $\rho \mathbf{V}$, then

$$\mathbf{F} = \frac{D}{Dt}(m\mathbf{V}) = \int_V \nabla \bullet (\rho \mathbf{u}\mathbf{V})dV + \int_V \frac{\partial \rho \mathbf{V}}{\partial t}dV \tag{3.12}$$

Note this relation holds only for an inertial (or fixed) control volume. If the control volume is in a moving frame, $D\mathbf{V}/Dt$ must be replaced by the moving frame equivalent as defined in Eq. (3.5).

$$\mathbf{F} = \int_V \nabla \bullet (\rho \mathbf{u}\mathbf{W}) dV + \int_V \frac{\partial \rho \mathbf{W}}{\partial t} dV + \int_V [2\Omega \times \mathbf{W} + \Omega \times \Omega \times \mathbf{r}] \rho dV \tag{3.13}$$

where $\mathbf{F}$ is the sum of all forces acting on the fluid within the control volume including the surface force $\mathbf{F}_s$ and the body force $\mathbf{F}_b$.

$$\mathbf{F}_s + \mathbf{F}_b = \int_S \mathbf{T} dS + \int_V \rho \mathbf{f}_b dV \tag{3.14}$$

where $\mathbf{T}(= \sigma \bullet \mathbf{n})$ is the surface stress vector. If we neglect the body force which is usually the gravity acceleration, apply Gauss' theorem to the surface integral of the stress vector, and take the Coriolis and the centrifugal force term in the left hand side to the right hand side as additional source terms, then Eq. (3.13) becomes

$$\int_V \frac{\partial \rho \mathbf{W}}{\partial t} dV + \int_V \nabla \bullet (\rho \mathbf{u}\mathbf{W}) dV = \int_V \nabla \bullet \sigma dV - \int_V [2\Omega \times \mathbf{W} + \Omega \times \Omega \times \mathbf{r}] \rho dV \tag{3.15}$$

Using the assumptions made by Stokes for a Newtonian fluid, the stress tensor σ_{ij} can given as follows;

$$\sigma_{ij} = -p\delta_{ij} + \tau_{ij} = -p\delta_{ij} + \mu [\frac{\partial u_i}{\partial x_j} + \frac{\partial u_j}{\partial x_i} - \frac{2}{3} \frac{\partial u_k}{\partial x_k} \delta_{ij}] \tag{3.16}$$

where δ_{ij} is the Kronecker's delta and μ is the molecular viscosity of the working fluid.

3.5 Conservation of Energy

Based on the 1st law of thermodynamics, the control volume approach is used to derive conservation of energy.

$$\frac{DQ}{Dt} + \frac{DW}{Dt} = \frac{DE}{Dt} \tag{3.17}$$

where DQ is the heat added, DW is the total work done, and DE is the change in total energy of the system. The derivative DE/Dt is commonly modified only by use of the control volume approach and can be expressed in terms of the total energy(e) per unit mass. Then, the 1st law of thermodynamics becomes

$$\frac{DQ}{Dt} + \frac{DW}{Dt} = \int_V \nabla \bullet (\rho \mathbf{u} e) dV + \int_V \frac{\partial \rho e}{\partial t} dV \tag{3.18}$$

where the total energy e is defined by the sum of the internal energy per unit mass e_i and the kinetic energy per unit mass $\frac{1}{2}\mathbf{W} \bullet \mathbf{W}$.

$$e = \frac{DE}{Dm} = e_i + \frac{1}{2}\mathbf{W} \bullet \mathbf{W} \tag{3.19}$$

The total work done on the system typically includes the work by the surface stress vector $\mathbf{T}$ on the control surface boundaries by neglecting the work due to the body force and any shaft work added.

$$\frac{DW}{Dt} = \int_S (\mathbf{u} \bullet \sigma) \bullet \mathbf{n} dS = \int_V \nabla \bullet (\mathbf{u} \bullet \sigma) dV \tag{3.20}$$

Let consider the heat transfer by the conduction through the control surface only and

neglect the rate of volumetric energy addition by other heat sources such as radiation, then the net flux of heat added on the system can be expressed as

$$\frac{DQ}{Dt} = -\int_S q \bullet \mathbf{n} dS \tag{3.21}$$

where the heat conduction q by the Fourier, law is

$$q = -k\nabla T \tag{3.22}$$

Then, the energy conservation becomes

$$\int_V \frac{\partial \rho e}{\partial t} dV + \int_V \nabla \bullet (\rho \mathbf{u} e) dV = \int_V \nabla \bullet (\mathbf{u} \bullet \sigma) dV + \int_V \nabla \bullet (k \nabla T) dV \tag{3.23}$$

where T is the static temperature of the fluid and k is the thermal conductivity.

Sutherland, law is used to model the molecular viscosity μ.

$$\frac{\mu}{\mu_\infty} = (\frac{T}{T_\infty})^{1.5} \frac{T + 110K}{T + T_\infty} \tag{3.24}$$

where the subscript ∞ represents the condition at a reference point. A constant Prandtl number is given to determine thermal conductivity k.

In the Navier-Stokes (NS) equations, Eq. (3.11), Eq. (3.15) and Eq. (3.23) need to be supplemented with the equations of the state, Eq. (3.28) and Eq. (3.29). Applying the Einstein summation convention to repeated indices, the Navier-Stokes equations can be rewritten in a conservative form in a rotating frame as follows;

$$\frac{\partial \rho}{\partial t} + \frac{\partial \rho u_k}{\partial x_k} = 0 \tag{3.25}$$

$$\frac{\partial \rho u_i}{\partial t} + \frac{\partial \rho u_i u_k}{\partial x_k} = -\frac{\partial p}{\partial x_i} + \frac{\partial \tau_{ik}}{\partial x_k} + S_i \tag{3.26}$$

$$\frac{\partial \rho e}{\partial t} + \frac{\partial (\rho e + p) u_k}{\partial x_k} = \frac{\partial (\tau_{ik} u_i + q_k)}{\partial x_k} \tag{3.27}$$

$$p = \rho RT \tag{3.28}$$

$$\rho e = \frac{p}{\gamma - 1} + \frac{1}{2}\rho (W^2 - \Omega^2 r^2) \tag{3.29}$$

where R is the gas constant and γ is the specific heat ratio of the working fluid. S_i is the source term added due to the rotor rotation and can be given as

$$\begin{pmatrix} S_x \\ S_y \\ S_z \end{pmatrix} = \begin{pmatrix} 0 \\ \rho\Omega^2 y + 2\rho\Omega w \\ \rho\Omega^2 z - 2\rho\Omega v \end{pmatrix} \tag{3.30}$$

3.6 Spatially Filtered NS Equations in Rotating Frame

The Navier-Stokes equations through Eq. (3.25) - Eq. (3.29) are considered to be able to directly solve engineering turbulent flows. However, such a direct numerical simulation has largely been limited to simple geometries at low Reynolds number since in general it requires a tremendous mesh and very small temporal scale, for example grid points $\simeq Re^{9/4}$ and times steps $\simeq Re^{3/4}$ to resolve all scales of turbulence [86].

Since turbulence consists of random fluctuations of the various flow properties, the statistical approach such as time, spatial or ensemble averaging is usually more meaningful

in engineering practice. The spatial filtering eliminates the small scale high frequency components of the fluid motion, while keeping the unsteadiness associated with the large scale turbulent motion [113]. For an arbitrary function $u(x_i,t)$, the filtered variable $\bar{u}(x_i,t)$ is defined as:

$$\bar{u}(x_i,t) = \int_D G(x_i - \xi_i, \Delta) u(\xi_i, t) d\xi_i \tag{3.31}$$

where G is the filter function and Δ is the filter width and is associated with the mesh size. Similar to the case of RANS, for compressible flows, it is convenient to introduce the Favre-filtered variable $\tilde{u}(x_i,t)$ as:

$$\tilde{u}(x_i,t) = \frac{\overline{\rho u}}{\bar{\rho}} \tag{3.32}$$

A variable can be thus decomposed into its Favre-filtered component and fluctuating component as:

$$u(x_i,t) = \tilde{u}(x_i,t) + u''(x_i,t) \tag{3.33}$$

The molecular viscous stress tensor, $\bar{\tau}$ is estimated as:

$$\bar{\tau}_{ij} = \frac{2}{3}\tilde{\mu}\frac{\partial \tilde{u}_k}{\partial x}_k \delta_{ij} + \mu(\frac{\partial \tilde{u}_i}{\partial x_j} + \frac{\partial \tilde{u}_j}{\partial x_i}), \qquad i,j = 1,2,3 \tag{3.34}$$

The above equation is in the tensor form, where the subscript 1, 2, 3 represent the coordinates, x, y, z and the Einstein summation convention is used. The molecular viscosity $\tilde{\mu} = \tilde{\mu}(\tilde{T})$ is determined by Sutherland law.

The σ is the subgrid scale stress tensor due to the filtering process and is expressed as:

$$\sigma_{ij} = -\bar{\rho}(\widetilde{u_i u_j} - \tilde{u}_i \tilde{u}_j) \tag{3.35}$$

The energy flux Q is expressed as:

$$Q_i = \tilde{u}_j(\bar{\tau}_{ij} + \sigma_{ij}) - \bar{q}_i + \Phi_i \tag{3.36}$$

where Φ is the subscale heat flux:

$$\Phi_i = -C_p \bar{\rho}(\widetilde{u_i T} - \tilde{u}_i \tilde{T}) \tag{3.37}$$

The $\bar{q}_i$ is the molecular heat flux:

$$\bar{q}_i = -\frac{C_p \tilde{\mu}}{Pr} \frac{\partial \tilde{T}}{\partial x_i} \tag{3.38}$$

$$\bar{\rho}\tilde{e} = \frac{\bar{p}}{(\gamma - 1)} + \frac{1}{2}\bar{\rho}(\tilde{u}^2 + \tilde{v}^2 + \tilde{w}^2 - \Omega^2 r^2) + \rho k \tag{3.39}$$

where γ is the ratio of specific heats, ρk is the subscale kinetic energy per unit volume.

$$\rho k = \frac{1}{2}\bar{\rho}(\widetilde{u_i u_i} - \tilde{u}_i \tilde{u}_i) = -\frac{1}{2}\sigma_{ii} \tag{3.40}$$

In the current simulations, the ρk in Eq.(3.39) is omitted based on the assumption that the effect is small.

Applying above definitions for the Navier-Stokes equations through Eq. (3.25) - Eq.

(3.29) and using the eddy viscosity concept, then the shear stress $\bar{\tau}_{ik}$ and total heat flux $\bar{q}_k$ can be expressed in Cartesian coordinates as follows:

$$\bar{\tau}_{ik} = (\mu + \mu_{DES}) \left[\left(\frac{\partial \tilde{u}_i}{\partial x_k} + \frac{\partial \tilde{u}_k}{\partial x_i} \right) - \frac{2}{3} \delta_{ik} \frac{\partial \tilde{u}_j}{\partial x_j} \right] \tag{3.41}$$

$$\bar{q}_k = - \left(\frac{\mu}{Pr} + \frac{\mu_{DES}}{Pr_t} \right) \frac{\partial \tilde{T}}{\partial x_k} \tag{3.42}$$

Note that μ_{DES} is obtained by high fidelity delayed detached eddy simulation (DDES) of turbulence [36,37] in this study. For simplicity, all the bar and tilde in above equations will be dropped for the rest of the thesis.

3.7 Nondimensionalization of the Governing Equations

The flow governing equations are normalized by a characteristic dimension L and freestream conditions.

$$\begin{gathered} t^* = \frac{tV_\infty}{L}, \quad x^* = \frac{x}{L}, \quad y^* = \frac{y}{L}, \quad z^* = \frac{z}{L} \\ \mu^* = \frac{\mu}{\mu_\infty}, \quad u^* = \frac{u}{V_\infty}, \quad v^* = \frac{v}{V_\infty}, \quad w^* = \frac{w}{V_\infty} \\ \rho^* = \frac{\rho}{\rho_\infty}, \quad T^* = \frac{T}{T_\infty}, \quad p^* = \frac{p}{\rho_\infty V_\infty^2}, \quad e^* = \frac{e}{V_\infty^2} \end{gathered} \tag{3.43}$$

As the nondimensional numbers introduced in this study, Reynolds number Re, Mach number M, and Rossby number R_o are defined as

$$Re = \frac{\rho_\infty L V_\infty}{\mu_\infty} \tag{3.44}$$

$$M_\infty = \frac{V_\infty}{\sqrt{\gamma R T_\infty}} \tag{3.45}$$

$$R_o = \frac{\Omega L}{V_\infty} \tag{3.46}$$

Above normalization results in

$$\mu^* = \frac{\mu}{\mu_\infty} = \frac{\mu Re}{\rho_\infty L V_\infty} \tag{3.47}$$

$$\mu^* = (T^*)^{1.5} \frac{T^* + 110/T_\infty}{T^* + 1} \tag{3.48}$$

$$p^* = \frac{\rho^* T^*}{\gamma M_\infty^2} \tag{3.49}$$

$$\rho^* e^* = \frac{P^*}{\gamma - 1} + \frac{1}{2}\rho^*(u^{*2} + v^{*2} + w^{*2} - {R_o}^2 r^{*2}) \tag{3.50}$$

For simplicity, the superscript asterisk will be dropped for the rest of the thesis. The normalized filtered compressible Navier-Stokes(NS) equations in Cartesian coordinates in a rotating frame can be expressed in a conservative flux vector form as

$$\frac{\partial \mathbf{Q}}{\partial t} + \frac{\partial \mathbf{E}}{\partial x} + \frac{\partial \mathbf{F}}{\partial y} + \frac{\partial \mathbf{G}}{\partial z} = \frac{1}{Re}\left(\frac{\partial \mathbf{E_v}}{\partial x} + \frac{\partial \mathbf{F_v}}{\partial y} + \frac{\partial \mathbf{G_v}}{\partial z}\right) + S_R \tag{3.51}$$

where S_R is the source term appeared due to the rotor rotation. The variable vector $\mathbf{Q}$, inviscid flux vectors $\mathbf{E}$, $\mathbf{F}$, $\mathbf{G}$, and the viscous fluxes $\mathbf{E_v}$, $\mathbf{F_v}$, $\mathbf{G_v}$ are given as the following.

$$\mathbf{Q} = \begin{pmatrix} \rho \\ \rho u \\ \rho v \\ \rho w \\ \rho e \end{pmatrix} \tag{3.52}$$

$$\mathbf{E} = \begin{pmatrix} \rho u \\ \rho u^2 + p \\ \rho uv \\ \rho uw \\ (\rho e + p)u \end{pmatrix}, \mathbf{F} = \begin{pmatrix} \rho v \\ \rho vu \\ \rho v^2 + p \\ \rho vw \\ (\rho e + p)v \end{pmatrix}, \mathbf{G} = \begin{pmatrix} \rho w \\ \rho wu \\ \rho wv \\ \rho w^2 + p \\ (\rho e + p)w \end{pmatrix} \tag{3.53}$$

$$\mathbf{E_v} = \begin{pmatrix} 0 \\ \tau_{xx} \\ \tau_{xy} \\ \tau_{xz} \\ u_k \tau_{xk} - q_x \end{pmatrix}, \mathbf{F_v} = \begin{pmatrix} 0 \\ \tau_{yx} \\ \tau_{yy} \\ \tau_{yz} \\ u_k \tau_{yk} - q_y \end{pmatrix}, \mathbf{G_v} = \begin{pmatrix} 0 \\ \tau_{zx} \\ \tau_{zy} \\ \tau_{zz} \\ u_k \tau_{zk} - q_z \end{pmatrix} \tag{3.54}$$

$$S_R = \begin{pmatrix} 0 \\ 0 \\ \rho R_o^2 y + 2\rho R_o w \\ \rho R_o^2 z - 2\rho R_o v \\ 0 \end{pmatrix} \tag{3.55}$$

where

$$\tau_{ik} = (\mu + \mu_{DES} Re)[\frac{\partial u_i}{\partial x_k} + \frac{\partial u_k}{\partial x_i} - \frac{2}{3}\delta_{ik}\frac{\partial u_j}{\partial x_j}] \tag{3.56}$$

$$q_j = -\frac{1}{(\gamma-1)M_\infty^2}(\frac{\mu}{Pr} + \frac{\mu_{DES} Re}{Pr_t})\frac{\partial T}{\partial x_j} \tag{3.57}$$

3.8 Transformation of the Navier-Stokes Equations

A transformation of the governing equations from the physical space(x, y, z) to the computational space(ξ, η, ζ) is performed to have the computational domain as equally spaced rectangular grid system, which can improve numerical accuracy and simplify implementation.

Using the chain rule, the metric equations for transformation can be derived as

$$\begin{bmatrix} dt \\ dx \\ dy \\ dz \end{bmatrix} = \begin{bmatrix} 1 & 0 & 0 & 0 \\ x_\tau & x_\xi & x_\eta & x_\zeta \\ y_\tau & y_\xi & y_\eta & y_\zeta \\ z_\tau & z_\xi & z_\eta & z_\zeta \end{bmatrix} \begin{bmatrix} d\tau \\ d\xi \\ d\eta \\ d\zeta \end{bmatrix} \tag{3.58}$$

$$\begin{bmatrix} 1 & 0 & 0 & 0 \\ \xi_t & \xi_x & \xi_y & \xi_z \\ \eta_t & \eta_x & \eta_y & \eta_z \\ \zeta_t & \zeta_x & \zeta_y & \zeta_z \end{bmatrix} = \begin{bmatrix} 1 & 0 & 0 & 0 \\ x_\tau & x_\xi & x_\eta & x_\zeta \\ y_\tau & y_\xi & y_\eta & y_\zeta \\ z_\tau & z_\xi & z_\eta & z_\zeta \end{bmatrix}^{-1} \tag{3.59}$$

$$\begin{aligned}
\xi_x &= J(y_\eta z_\zeta - y_\zeta z_\eta), \xi_y = J(x_\zeta z_\eta - x_\eta z_\zeta), \xi_z = J(x_\eta y_\zeta - x_\zeta y_\eta) \\
\eta_x &= J(y_\eta z_\xi - y_\xi z_\eta), \eta_y = J(x_\xi z_\zeta - x_\zeta z_\xi), \eta_z = J(x_\zeta y_\xi - x_\xi y_\zeta) \\
\zeta_x &= J(y_\xi z_\eta - y_\eta z_\xi), \zeta_y = J(x_\eta z_\xi - x_\xi z_\eta), \zeta_z = J(x_\xi y_\eta - x_\eta y_\xi)
\end{aligned} \tag{3.60}$$

$$\begin{aligned}
\xi_t &= -(x_\tau \xi_x + y_\tau \xi_y + z_\tau \xi_z) \\
\eta_t &= -(x_\tau \eta_x + y_\tau \eta_y + z_\tau \eta_z) \\
\zeta_t &= -(x_\tau \zeta_x + y_\tau \zeta_y + z_\tau \zeta_z)
\end{aligned} \tag{3.61}$$

where J is the transformation Jacobian.

$$J = \frac{\partial(\xi,\eta,\zeta)}{\partial(x,y,z)} = \frac{1}{x_\xi(y_\eta z_\zeta - y_\zeta z_\eta) - x_\eta(y_\xi z_\zeta - y_\zeta z_\xi) + x_\zeta(y_\xi z_\eta - y_\eta z_\xi)} \tag{3.62}$$

In generalized coordinates, Eq.(3.51) can be expressed as the following:

$$\frac{\partial \mathbf{Q}'}{\partial t} + \frac{\partial \mathbf{E}'}{\partial \xi} + \frac{\partial \mathbf{F}'}{\partial \eta} + \frac{\partial \mathbf{G}'}{\partial \zeta} = \frac{1}{\mathrm{Re}}\left(\frac{\partial \mathbf{E}'_\mathbf{v}}{\partial \xi} + \frac{\partial \mathbf{F}'_\mathbf{v}}{\partial \eta} + \frac{\partial \mathbf{G}'_\mathbf{v}}{\partial \zeta}\right) + \mathbf{S}'_\mathbf{R} \tag{3.63}$$

where

$$\mathbf{Q}' = \frac{\mathbf{Q}}{J} \tag{3.64}$$

$$\mathbf{E}' = \frac{1}{J}(\xi_t \mathbf{Q} + \xi_x \mathbf{E} + \xi_y \mathbf{F} + \xi_z \mathbf{G}) \tag{3.65}$$

$$\mathbf{F}' = \frac{1}{J}(\eta_t \mathbf{Q} + \eta_x \mathbf{E} + \eta_y \mathbf{F} + \eta_z \mathbf{G}) \tag{3.66}$$

$$\mathbf{G}' = \frac{1}{J}(\zeta_t \mathbf{Q} + \zeta_x \mathbf{E} + \zeta_y \mathbf{F} + \zeta_z \mathbf{G}) \tag{3.67}$$

$$\mathbf{E}'_\mathbf{v} = \frac{1}{J}(\xi_x \mathbf{E}_\mathbf{v} + \xi_y \mathbf{F}_\mathbf{v} + \xi_z \mathbf{G}_\mathbf{v}) \tag{3.68}$$

$$\mathbf{F}'_{\mathbf{v}} = \frac{1}{J}(\eta_x \mathbf{E}_{\mathbf{v}} + \eta_y \mathbf{F}_{\mathbf{v}} + \eta_z \mathbf{G}_{\mathbf{v}}) \tag{3.69}$$

$$\mathbf{G}'_{\mathbf{v}} = \frac{1}{J}(\zeta_x \mathbf{E}_{\mathbf{v}} + \zeta_y \mathbf{F}_{\mathbf{v}} + \zeta_z \mathbf{G}_{\mathbf{v}}) \tag{3.70}$$

$$\mathbf{S}'_{\mathbf{R}} = \frac{S_R}{J} \tag{3.71}$$

The inviscid fluxes in generalized coordinate system are expressed as:

$$\mathbf{E}' = \begin{bmatrix} \rho U \\ \rho u U + l_x p \\ \rho v U + l_y p \\ \rho w U + l_z p \\ (\rho e + p) U - l_t p \end{bmatrix}, \mathbf{F}' = \begin{bmatrix} \rho V \\ \rho u V + m_x p \\ \rho v V + m_y p \\ \rho w V + m_z p \\ (\rho e + p) V - m_t p \end{bmatrix}, \mathbf{G}' = \begin{bmatrix} \rho W \\ \rho u W + n_x p \\ \rho v W + n_y p \\ \rho w W + n_z p \\ (\rho e + p) W - n_t p \end{bmatrix} \tag{3.72}$$

where U, V and W are the contravariant velocities in ξ, η and ζ directions.

$$\begin{aligned} U &= l_t + \mathbf{l} \bullet \mathbf{V} = l_t + l_x u + l_y v + l_z w \\ V &= m_t + \mathbf{m} \bullet \mathbf{V} = m_t + m_x u + m_y v + m_z w \\ W &= n_t + \mathbf{n} \bullet \mathbf{V} = n_t + n_x u + n_y v + n_z w \end{aligned} \tag{3.73}$$

where $\mathbf{l}$, $\mathbf{m}$, $\mathbf{n}$ are the normal vectors on ξ, η, ζ surfaces with their magnitudes equal to the elemental surface area and pointing to the directions of increasing ξ, η, ζ.

$$\mathbf{l} = \frac{\nabla \xi}{J} d\eta d\zeta,\ \mathbf{m} = \frac{\nabla \eta}{J} d\xi d\zeta,\ \mathbf{n} = \frac{\nabla \zeta}{J} d\xi d\eta \tag{3.74}$$

$$l_t = \frac{\xi_t}{J} d\eta d\zeta,\ m_t = \frac{\eta_t}{J} d\xi d\zeta,\ n_t = \frac{\zeta_t}{J} d\xi d\eta \tag{3.75}$$

where $d\xi = d\eta = d\zeta = 1$ in the current discretization. When the gird is stationary, $l_t = m_t = n_t = 0$.

3.9 Delayed Detached Eddy Simulation

In 1997 Spalart et al. [36] suggested a hybrid RANS/LES turbulence, the detached eddy simulation (DES), based on the Spalart-Allmaras (S-A) one equation model [114] which solves a transport equation for the working variable $\tilde{\nu}$ related to the turbulent eddy ν and LES subgrid-scale (SGS) viscosity. Using the normalization given in Eq. (3.43), the nondimensionalized S-A model including closure coefficients and damping functions is written in terms of eddy viscosity ν_t as follows.

Turbulent Eddy Viscosity:

$$\mu_{DES} = \rho \nu_t = \rho \tilde{\nu} f_{v1} \tag{3.76}$$

Eddy Viscosity Equation:

$$\begin{aligned} \frac{\partial \bar{\rho}\bar{\tilde{\nu}}}{\partial \bar{t}} + \bar{\nabla}\cdot\left(\bar{\rho}\bar{\tilde{\nu}}\bar{\vec{V}}\right) &= \frac{1}{Re}\bar{\nabla}\cdot\left[\frac{\bar{\rho}}{\sigma}(\bar{\nu}+\bar{\tilde{\nu}})\bar{\nabla}\bar{\tilde{\nu}}\right] + \bar{\rho}c_{b1}(1-f_{t2})\left(\bar{S}+\frac{1}{Re}\frac{\bar{\tilde{\nu}}}{\kappa^2\bar{d}^2}f_{v2}\right)\bar{\tilde{\nu}} - \\ &\frac{1}{Re}\bar{\rho}\left(c_{w1}f_w - \frac{c_{b1}}{\kappa^2}f_{t2}\right)\left(\frac{\bar{\tilde{\nu}}}{\bar{d}}\right)^2 - \frac{1}{Re}\frac{1}{\sigma}\left(\bar{\nu}+\bar{\tilde{\nu}}\right)\bar{\nabla}\bar{\tilde{\nu}}\cdot\bar{\nabla}\bar{\rho} + \\ &\frac{1}{Re}\frac{\bar{\rho}}{\sigma}c_{b2}\left(\bar{\nabla}\bar{\tilde{\nu}}\right)^2 + Re\bar{\rho}f_{t1}(\Delta\bar{q})^2 \end{aligned} \tag{3.77}$$

Closure Coefficients:

$$\begin{gathered} c_{b1} = 0.1355, c_{b2} = 0.622, \sigma = \tfrac{2}{3}, c_{w1} = \tfrac{c_{b1}}{k^2} + \tfrac{1+c_{b2}}{\sigma} \\ c_{w2} = 0.3, c_{w3} = 2, k = 0.41, c_{v1} = 7.1, c_{t1} = 1.0, c_{t2} = 2.0, c_{t3} = 1.1, c_{t4} = 2.0 \end{gathered} \tag{3.78}$$

Auxiliary Relations:

$$\chi = \frac{\tilde{\nu}}{\nu}, \quad g = r + c_{w2}(r^6 - r), \quad r = \frac{\tilde{\nu}}{Re\tilde{S}k^2d^2} \tag{3.79}$$

$$f_{v1} = \frac{\chi^3}{\chi^3 + c_{v1}^3}, \quad f_{v2} = 1 - \frac{\chi}{1 + \chi f_{v1}}, \quad f_w = g(\frac{1 + c_{w3}^6}{g^6 + c_{w3}^6})^{1/6} \tag{3.80}$$

$$\tilde{S} = S + \frac{\tilde{\nu}}{Rek^2d^2} f_{v2}, \quad S = \sqrt{2\omega_{ij}\omega_{ij}}, \quad g_t = min\left(0.1, \frac{\Delta q}{\omega_t \Delta x_t}\right) \tag{3.81}$$

$$f_{t2} = c_{t3} exp\left(-c_{t4}\chi^2\right), \quad f_{t1} = c_{t1} g_t exp\left[-c_{t2}\frac{\omega_t^2}{\Delta U^2}\left(d^2 + g_t^2 d_t^2\right)\right] \tag{3.82}$$

Where $\omega_{ij} = \frac{1}{2}\left(\frac{\partial u_i}{\partial x_j} - \frac{\partial u_j}{\partial x_i}\right)$ is the fluid particle angular velocity tensor. ω_t is the wall vorticity at the wall boundary layer trip location, d is the distance to the closest wall, d_t is the distance of the field point to the trip location, Δq is the difference of the velocities between the field point and the trip location, Δx_t is the grid spacing along the wall at the trip location.

In DES, the coefficients c_{t1} and c_{t3} in the S-A model are set to zero and the distance to the nearest wall, d, is replaced by $\tilde{d}$ as

$$\tilde{d} = min(d, C_{DES}\Delta) \tag{3.83}$$

where Δ is the largest spacing of the grid cell in all the directions. Within the boundary layer close to the wall, $\tilde{d} = d$, hence the turbulence is simulated by RANS mode of Spalart-

Allmaras [114]. Outside of a wall the boundary layer, $\tilde{d} = C_{DES}\Delta$ is most of the cases. When the production and destruction terms of the model are balanced, the length scale $\tilde{d}$ will yield a Smagorinsky-like eddy viscosity and the turbulence is simulated by the LES model. The coefficient $C_{DES} = 0.65$ is used as set in the homogeneous turbulence [93]. The Pr_t may take the value of 0.9 within the boundary layer for RANS mode and 0.5 for LES mode away from the wall surface.

To overcome the modeled stress depletion problem and make the DES limiter independent of grid spacing, the DDES model suggested by Spalart et al. [37] switches the subgrid scale formulation in the S-A model by redefining the distance to the nearest wall $\tilde{d}$ as

$$\tilde{d} = d - f_d max(0, d - C_{DES}\Delta) \tag{3.84}$$

where

$$f_d = 1 - tanh([8r_d]^3) \tag{3.85}$$

$$r_d = \frac{\nu_t + \nu}{(U_{i,j}U_{i,j})^{0.5}k^2d^2R_e} \tag{3.86}$$

$$U_{i,j} = \frac{\partial u_i}{\partial x_j} \tag{3.87}$$

where Δ is the largest spacing of the grid cell in all the directions, $U_{i,j}$ represents the velocity gradient, and k denotes the Karmann constant. Within the boundary layer close to walls, $\tilde{d} = d$, and away from the boundary layer, $\tilde{d} = d - f_d(d - C_{DES}\Delta)$ is most of the case. This

mechanism enables DDES to behave as a RANS model in the near-wall region, and LES away from walls. This modification in $\tilde{d}$ reduces the grey transition area between RANS and LES.

To couple the SA based DES/DDES with Eq. (3.63), the eddy viscosity equation (3.77) is also transformed to the computational space and can be expressed in the generalized coordinate system as

$$\frac{\partial \frac{1}{J}\rho\tilde{\nu}}{\partial t}+\frac{\partial \rho\tilde{\nu}U}{\partial \xi}+\frac{\partial \rho\tilde{\nu}V}{\partial \eta}+\frac{\partial \rho\tilde{\nu}W}{\partial \zeta}=\frac{1}{Re}\left(\frac{\partial \frac{\rho}{\sigma}(\nu+\tilde{\nu})(\mathbf{l}\bullet\nabla\tilde{\nu})}{\partial \xi}\right.$$
$$\left.+\frac{\partial \frac{\rho}{\sigma}(\nu+\tilde{\nu})(\mathbf{m}\bullet\nabla\tilde{\nu})}{\partial \eta}+\frac{\partial \frac{\rho}{\sigma}(\nu+\tilde{\nu})(\mathbf{n}\bullet\nabla\tilde{\nu})}{\partial \zeta}+\frac{1}{J}S_{\nu}\right) \tag{3.88}$$

where

$$\begin{aligned} S_{\nu} &= \rho c_{b1}(1-f_{t2})\tilde{S}\tilde{\nu}+\tfrac{1}{Re}\left[-\rho\left(c_{w1}f_{w}-\tfrac{c_{b1}}{\kappa^{2}}f_{t2}\right)\left(\tfrac{\tilde{\nu}}{d}\right)^{2}\right. \\ &\left.+\tfrac{\rho}{\sigma}c_{b2}(\nabla\tilde{\nu})^{2}-\tfrac{1}{\sigma}(\nu+\tilde{\nu})\nabla\tilde{\nu}\bullet\nabla\rho\right]+Re\left[\rho f_{t1}(\Delta q)^{2}\right] \end{aligned} \tag{3.89}$$

In summary, the spatially filtered Navier-Stokes equations with the improved DES turbulence closure in a rotating frame of reference in the generalized coordinates(ξ,η,ζ) can be written in a conservative form as the following:

$$\frac{\partial \mathbf{Q}}{\partial t}+\frac{\partial \mathbf{E}}{\partial \xi}+\frac{\partial \mathbf{F}}{\partial \eta}+\frac{\partial \mathbf{G}}{\partial \zeta}=\frac{1}{Re}\left(\frac{\partial \mathbf{R}}{\partial \xi}+\frac{\partial \mathbf{S}}{\partial \eta}+\frac{\partial \mathbf{T}}{\partial \zeta}\right)+\mathbf{D} \tag{3.90}$$

where

$$\mathbf{Q} = \frac{1}{J}\begin{bmatrix} \rho \\ \rho u \\ \rho v \\ \rho w \\ \rho e \\ \rho \tilde{\nu} \end{bmatrix} \tag{3.91}$$

$$\mathbf{E} = \begin{bmatrix} \rho U \\ \rho u U + l_x p \\ \rho v U + l_y p \\ \rho w U + l_z p \\ (\rho e + p) U - l_t p \\ \rho \tilde{\nu} U \end{bmatrix}, \mathbf{F} = \begin{bmatrix} \rho V \\ \rho u V + m_x p \\ \rho v V + m_y p \\ \rho w V + m_z p \\ (\rho e + p) V - m_t p \\ \rho \tilde{\nu} V \end{bmatrix}, \mathbf{G} = \begin{bmatrix} \rho W \\ \rho u W + n_x p \\ \rho v W + n_y p \\ \rho w W + n_z p \\ (\rho e + p) W - n_t p \\ \rho \tilde{\nu} W \end{bmatrix} \tag{3.92}$$

$$\mathbf{R} = \begin{bmatrix} 0 \\ l_k \tau_{xk} \\ l_k \tau_{yk} \\ l_k \tau_{zk} \\ l_k (u_i \tau_{ik} - q_k) \\ \frac{\rho}{\sigma} (\nu + \tilde{\nu}) (\mathbf{l} \bullet \nabla \tilde{\nu}) \end{bmatrix}, \mathbf{S} = \begin{bmatrix} 0 \\ m_k \tau_{xk} \\ m_k \tau_{yk} \\ m_k \tau_{zk} \\ m_k (u_i \tau_{ik} - q_k) \\ \frac{\rho}{\sigma} (\nu + \tilde{\nu}) (\mathbf{m} \bullet \nabla \tilde{\nu}) \end{bmatrix}, \mathbf{T} = \begin{bmatrix} 0 \\ n_k \tau_{xk} \\ n_k \tau_{yk} \\ n_k \tau_{zk} \\ n_k (u_i \tau_{ik} - q_k) \\ \frac{\rho}{\sigma} (\nu + \tilde{\nu}) (\mathbf{n} \bullet \nabla \tilde{\nu}) \end{bmatrix} \tag{3.93}$$

$$\mathbf{D} = \frac{1}{J}\begin{bmatrix} 0 \\ 0 \\ \rho R_o^2 y + 2\rho R_o w \\ \rho R_o^2 z - 2\rho R_o v \\ 0 \\ \frac{S_v}{Re} \end{bmatrix} \tag{3.94}$$

where

$$\tau_{ik} = (\mu + \mu_{DES} Re)[\frac{\partial u_i}{\partial x_k} + \frac{\partial u_k}{\partial x_i} - \frac{2}{3}\delta_{ik}\frac{\partial u_j}{\partial x_j}] \tag{3.95}$$

$$q_k = -\frac{1}{(\gamma - 1)M_\infty^2}(\frac{\mu}{Pr} + \frac{\mu_{DES} Re}{Pr_t})\frac{\partial T}{\partial x_k} \tag{3.96}$$

Chapter 4

The Structure Governing Equations

To be consistent with the fluid flow governing equations, the structural governing equations for turbomachinery fluid/structure interaction in the rotating frame are derived with the coriolis force and centrifugal force. Forced vibration equations are decoupled using the modal coordinates. Both the pressure and shear force are included in the aerodynamic excitation force acting on the structure. The effect of rotor disk vibration is neglected in this study since stiffness of rotor disk is much larger than that of fan/compressor blade and blade vibration characteristics is in general dominant for the aeromechanical phenomena such as flutter, non-synchronous blade vibration.

4.1 Blade Forced Vibration in Rotating Frame

The equation of motion for the rotating blade structure can be derived based on Eq. (3.4) in the same manner of motion of a fluid particle in a rotating reference of frame. The blade structure is modeled as the fixed root on the rotor disk as sketched in Fig. 4.1. The

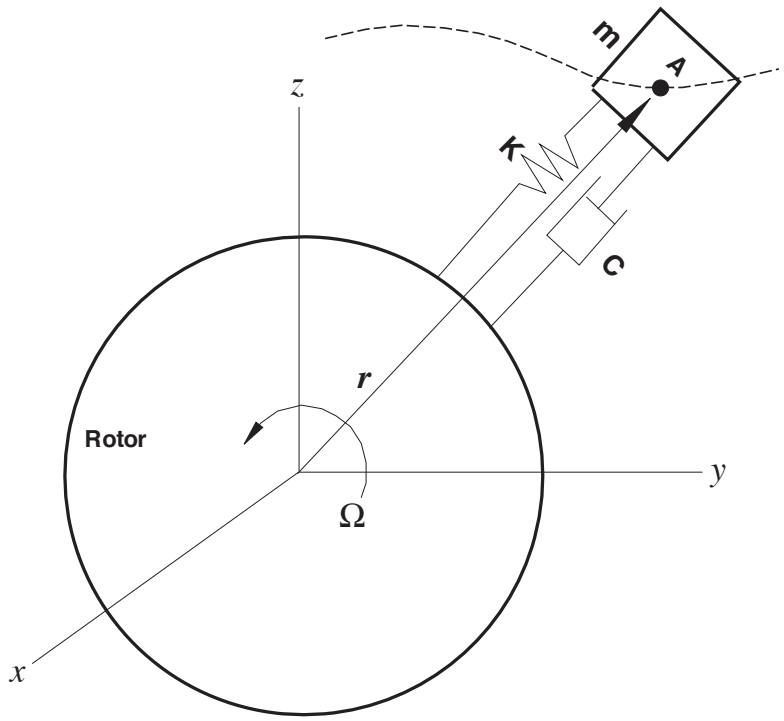

Figure 4.1: Sketch of blade motion in a rotating frame

rotor rotates at the constant angular velocity of Ω and has no translational motion. The acceleration of the particle A yields

$$\frac{D\mathbf{V}}{Dt})_{XYZ} = \frac{D\mathbf{W}}{Dt}_{xyz} + 2\Omega \times \mathbf{W} + \Omega \times \Omega \times \mathbf{r} \tag{4.1}$$

where $\mathbf{r}(= x\mathbf{i} + y\mathbf{j} + z\mathbf{k})$ is the displacement vector and $\mathbf{W}(= \dot{\mathbf{r}})$ is the velocity of the structure element A. In the present study the angular velocity vector is defined as

$$\Omega = \Omega_x \mathbf{i} + 0\mathbf{j} + 0\mathbf{k} \tag{4.2}$$

The acceleration vector in the fixed frame can be obtained as the following.

$$\begin{Bmatrix} a_X \\ a_Y \\ a_Z \end{Bmatrix} = \begin{bmatrix} \ddot{x} & 0 & 0 \\ 0 & (\ddot{y} - 2\dot{z}\Omega_x - \Omega_x^2 y) & 0 \\ 0 & 0 & (\ddot{z} + 2\dot{y}\Omega_x - \Omega_x^2 z) \end{bmatrix} \begin{Bmatrix} \mathbf{i} \\ \mathbf{j} \\ \mathbf{k} \end{Bmatrix} \tag{4.3}$$

Apply Newton's 2nd law for a particle A with mass m, stiffness k, and damping coefficient c. Then, the forced vibration equations in a rotating frame can be written in the matrix form. For simplicity, let $\Omega = \Omega_x$ hereafter.

$$\begin{bmatrix} m & 0 & 0 \\ 0 & m & 0 \\ 0 & 0 & m \end{bmatrix} \begin{Bmatrix} \ddot{x} \\ \ddot{y} \\ \ddot{z} \end{Bmatrix} + \begin{bmatrix} c & 0 & 0 \\ 0 & c & -2m \\ 0 & 2m & c \end{bmatrix} \begin{Bmatrix} \dot{x} \\ \dot{y} \\ \dot{z} \end{Bmatrix} + \begin{bmatrix} k & 0 & 0 \\ 0 & k - m\Omega^2 & 0 \\ 0 & 0 & k - m\Omega^2 \end{bmatrix} \begin{Bmatrix} x \\ y \\ z \end{Bmatrix} = \begin{Bmatrix} F_x \\ F_y \\ F_z \end{Bmatrix} \tag{4.4}$$

It is shown that the forced vibration equations in Eq. (4.4) is nonlinearly coupled system of equations due to additional terms in the damping and stiffness matrix caused by rotation. In order to decouple these equations, transformation of the structural equations to the modal coordinates are employed in the present study. Eq. (4.4) also indicates that the effect of centrifugal force must be taken into account in the FE mode analysis by the fact that the centrifugal terms $-m\Omega^2$ are added to the global stiffness matrix(K) in the direction of two

axes perpendicular to the axis of rotation [115]. Therefore, use of the blade mode shapes obtained by the FE mode analysis for the rotating blade can simplify the modal analysis without additional efforts regarding these terms [116].

4.2 Decoupling Forced Vibration Equations

Eq. (4.4) can be extended to the equation of motion of an N-DOF (degree of freedom) system with the mechanical damping and the aerodynamic loading as the excitation force, and which can be expressed as the following:

$$[\mathbf{M}]\{\ddot{\mathbf{X}}\} + [\mathbf{C}]\{\dot{\mathbf{X}}\} + [\mathbf{K}]\{\mathbf{X}\} = \{\mathbf{F}\} \tag{4.5}$$

where, **M**, **C**, **K** are the global mass, structural damping and stiffness matrices. **F** is total aerodynamic force acting on the blade surface.

Total aerodynamic force can be defined as follows:

$$\mathbf{F} = -\oint P \cdot \hat{n} dA + \oint \tau_{\mathbf{w}} \cdot \hat{t} dA \tag{4.6}$$

where, $\hat{n}$ is the unit normal vector to the blade surface and $\hat{t}$ is the unit tangent vector to the blade surface. P is the fluid static pressure and $\tau_{\mathbf{w}}$ is the fluid wall shear stress acting on the blade surface. The effects of viscosity can not be neglected for the highly loaded transonic rotor because rotating stall with large structure of flow separation may occur in/near stall conditions.

To obtain the solution of forced vibration in terms of the normal coordinates of the

system, first a finite number of mode shapes(ϕ_j) are obtained by solving the characteristic equation of motion.

$$\mathbf{K}\phi_j = \lambda_j \mathbf{M}\phi_j \tag{4.7}$$

where $\lambda_j (= \omega_j^2)$ is the eigenvalue of the j-th mode and ω_j is the corresponding natural frequency. Note that $\mathbf{K}$ is the global stiffness matrix of Eq. (4.4), in which the centrifugal force term is added in the perpendicular directions of rotating axis. It is desirable to use the mass normalized mode shape($\tilde{\phi}$) defined as the normal modes divided by square root of the the generalized mass($\sqrt{\phi^T m \phi}$) since the orthogonality in terms of the orthogonal modes becomes

$$\tilde{\phi}_j^T M \tilde{\phi}_j = 1 \tag{4.8}$$

To decouple Eq. (4.5), let the displacement vector as

$$\{\mathbf{X}\} = [\tilde{\Phi}]\{\mathbf{q}\} \tag{4.9}$$

and premultiply Eq. (4.5) by the transpose $[\tilde{\Phi}]^T$

$$\begin{aligned} [\tilde{\Phi}]^T[\mathbf{M}][\tilde{\Phi}]\{\ddot{\mathbf{q}}\} + [\tilde{\Phi}]^T[\mathbf{C}][\tilde{\Phi}]\{\dot{\mathbf{q}}\} + [\tilde{\Phi}]^T[\mathbf{K}][\tilde{\Phi}]\{\mathbf{q}\} \\ = [\tilde{\Phi}]^T\{\mathbf{F}\} \end{aligned} \tag{4.10}$$

where $\mathbf{q}$ is the vector of the principal coordinates. Apply the orthogonality of eigenvectors of the system defined as

$$\phi_j^T M \phi_i = 0; i \neq j \tag{4.11}$$

$$\phi_j^T K \phi_i = 0; i \neq j \tag{4.12}$$

$$\phi_i^T M \phi_i = M_{ii} \tag{4.13}$$

$$\phi_i^T K \phi_i = K_{ii} \tag{4.14}$$

where M_{ii} and K_{ii} are called the generalized mass and the generalized stiffness. Assume damping matrix to be a linear combination of the mass and stiffness matrices as

$$\mathbf{C} = \alpha \mathbf{M} + \beta \mathbf{K} \tag{4.15}$$

and define the modal damping ratio by

$$2\varsigma_j \omega_j = \alpha + \beta \omega_j^2 \tag{4.16}$$

Eq. (A.28) is then completely decoupled and the *j*th equation will have the form as

$$\ddot{q}_j + 2\zeta_j \omega_j \dot{q}_j + \omega_j^2 q_j = \frac{\tilde{\phi}_j^T}{m_j} \mathbf{F} \tag{4.17}$$

where $[\tilde{\Phi}]^T = [\tilde{\phi}_1, \cdots, \tilde{\phi}, \cdots, \tilde{\phi}_N]^T$. N is the number of modal coordinates. ω_j and ζ_j are natural frequency and modal damping ratio for mode *j*. m_j denotes the *j*th diagonal element of the generalized mass matrix and is unity, resulting in

$$\ddot{q}_j + 2\zeta_j \omega_j \dot{q}_j + \omega_j^2 q_j = \tilde{\phi}_j^T \mathbf{F} \tag{4.18}$$

In the current study, the structural system may be reduced to only five mode shapes,

since a few bending and torsional frequencies are usually sufficient to determine aeromechanical phenomena of turbomachinery such as flutter and non-synchronous vibration.

4.3 Normalization of Modal Equation

The modal equation (4.18) is further normalized to be consistent with the aerodynamic model for the fully coupled fluid/structure interaction procedure. The following dimensionless parameters are introduced.

$$x^* = \frac{x}{L} \tag{4.19}$$

$$q^* = \frac{q}{L} \tag{4.20}$$

$$t^* = t\omega_\alpha \tag{4.21}$$

$$\mathbf{F}^* = \frac{\mathbf{F}}{\rho_\infty U_\infty^2 L^2} \tag{4.22}$$

where t is structural time, ω_α is the characteristic frequency of the system (or in general the first torsional mode natural frequency), and L is the characteristic length used in the normalization of the aerodynamic model. ρ_∞ and U_∞ are the fluid density and velocity at a point of reference. Apply above normalization to Eq. (4.18), then we have

$$\frac{d^2 q_j^*}{dt^{*2}} + 2\varsigma_j \left(\frac{\omega_j}{\omega_\alpha}\right) \frac{dq_j^*}{dt^*} + \left(\frac{\omega_j}{\omega_\alpha}\right)^2 q_j^* = \tilde{\phi}_j^T \cdot \mathbf{F}^* \cdot \frac{\rho_\infty U_\infty^2 L}{{\omega_\alpha}^2} \tag{4.23}$$

To reflect the effects of three wing flutter control parameters: mass ratio $\bar{\mu} = \frac{\bar{m}}{\bar{V}\rho_\infty}$, reduced velocity $V^* = \frac{U_\infty}{b_s \omega_\alpha}$ and flutter speed index $V_f = \frac{V^*}{\bar{\mu}}$, the modal force term on the right hand side of the normalized modal equation (4.23) can be expressed as [24].

$$\ddot{q}_j + 2\zeta_j(\frac{\omega_j}{\omega_\alpha})\dot{q}_j + (\frac{\omega_j}{\omega_\alpha})^2 q_j = \frac{\tilde{\phi}_j^T}{m_j^*} \cdot \mathbf{F}^* \cdot {V_f}^2 \cdot \frac{b_s^2 L}{\bar{V}} \cdot \bar{m} \tag{4.24}$$

where the dimensionless quantities are denoted by an asterisk. $\bar{m}$ is the measured blade mass (or wing panel mass), $\bar{V}$ represents the conical frustum volume as illustrated in Fig. 4.2.

$$\bar{V} = \frac{\pi H}{3}(b_s^2 + b_s b_t + b_t^2) \tag{4.25}$$

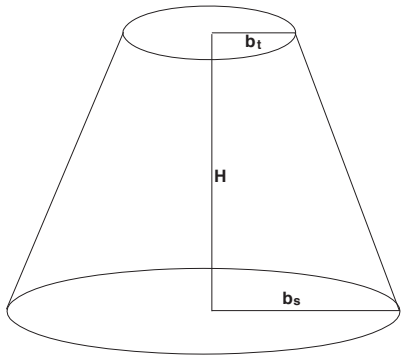

Figure 4.2: Frustrum volume

where b_s is the streamwise root semi chord (or blade semi root chord), b_t is the streamwise tip semi chord(or blade semi tip chord), and H is the blade active length or the wing span. L is the reference length and ω_α is the angular frequency of the first torsional mode in units $radians/sec$. $\bar{\mu}$ stands for the mass ratio, i.e. the ratio between the structural mass and the mass of the equivalent volume of fluid at reference density. It is noticed that m_j^* should be equal to one when the mass normalized mode shapes are used. Note that the structural

dimensionless time t^* may be calculated based on the dimensionless time(t^*_{fluid}) used in the normalized flow governing equation Eq. (3.90) as follows.

$$t^* = t^*_{fluid} \cdot \frac{L}{V^* b_s} \tag{4.26}$$

In order to use the time accurate FSI solver developed for the fluid flow [117], the equations are then transformed to a state form as follows:

$$[\mathbf{M}]\frac{\partial \mathbf{S}}{\partial t} + [\mathbf{K}]\{\mathbf{S}\} = \mathbf{q} \tag{4.27}$$

where

$$\mathbf{S} = \begin{pmatrix} q_j \\ \dot{q}_j \end{pmatrix}, \mathbf{M} = [I], \mathbf{K} = \begin{pmatrix} 0 & -1 \\ (\frac{\omega_j}{\omega_\alpha})^2 & 2\zeta_j(\frac{\omega_j}{\omega_\alpha}) \end{pmatrix}$$

$$\mathbf{q} = \begin{pmatrix} 0 \\ \phi_j^T \cdot \mathbf{F}^* \cdot V_f \cdot \frac{b_s^2 L}{V} \cdot \bar{m} \end{pmatrix}$$

4.4 Parameters for Flutter Control

There are in general three wing flutter control(or input) parameters: mass ratio $\bar{\mu} = \frac{\bar{m}}{\bar{V}\rho_\infty}$, reduced velocity $V^* = \frac{U_\infty}{b_s \omega_\alpha}$, and flutter speed index $V_f = \frac{V^*}{\bar{\mu}}$. The mass ratio $\bar{\mu}$ takes into account the effect of stiffness in flutter. It represents the ratio between the structural mass and the mass of the equivalent volume of fluid at reference density. Typically flutter speed index V_f is selected as the main parameter in flutter boundary prediction because V_f reflects the effects of both dynamic pressure of the surrounding flow and stiffness of the

structure. The effect of aircraft altitude in wind tunnel tests [4, 118] is obtained based on variation of dynamic pressure(varying the density) at constant Mach number. Liu [50] and Chen [24] used V_f, whereas Bakhle [119] used V^* to find the flutter boundary at a given Mach number. In this study, either V_f or V^* can be used explicitly as shown in Eq. (4.24). The V_f is selected for the wing flutter simulation.

Several iterations are usually needed for a given freestream Mach number to search the neutrally stable point, which is treated as the flutter boundary. Most of the computations only need to calculate a few periods to see whether the responses are divergent or damped with time. The flutter velocity index V_f is iterated to find the flutter boundary, all other variables such as inlet total pressure, inlet total temperature, and the static pressure at outlet are not varied. The Reynolds number, $R_e = \frac{\rho_\infty V_\infty L}{\mu_\infty}$ varies with the freestream velocity. In the wing flutter experiment [118], dynamic pressure $q = \frac{1}{2}\rho_\infty V_\infty^2$ is the main fluid quantity to adjust flutter level. The way to control the dynamic pressure is either by varying the free stream density using the real gas such as freon-12 or by changing the velocity instead of density. In this paper, we vary the freestream velocity, V_∞, which has direct relation with the reduced velocity V^*, and hence the flutter velocity index V_f.

For turbomachinery, the flutter boundary is typically determined along the speedline at a given rotor speed instead of varying the freestream Mach number unlike wing flutter because the change in the back pressure of fan/compressor controls the flow at inlet, resulting in the change in the mass flow and total pressure ratio.

Chapter 5

Numerical Methodology

In this chapter, an implicit finite difference discretization for the flow governing equations is described. The inviscid fluxes are discretized using a low diffusion E-CUSP scheme [109]. The fifth-order WENO scheme [101, 102] is used to reconstruct the conservative variables at volume interfaces. A set of fully conservative fourth-order accurate finite central differencing schemes for the viscous terms is employed in this research [103, 120]. The structure governing equations are discretized and solved implicitly in the same manner to be consistent with the flow governing equations.

5.1 Implicit Discretization

Let $J = \frac{1}{\Delta V}$, then 3D Navier-Stokes equations (3.90) is rewritten in a conservative flux vector form as

$$\frac{\partial \Delta V \mathbf{Q}}{\partial t} + \frac{\partial (\mathbf{E} - \mathbf{R}')}{\partial \xi} + \frac{\partial (\mathbf{F} - \mathbf{S}')}{\partial \eta} + \frac{\partial (\mathbf{G} - \mathbf{T}')}{\partial \zeta} = \Delta V \mathbf{D} \tag{5.1}$$

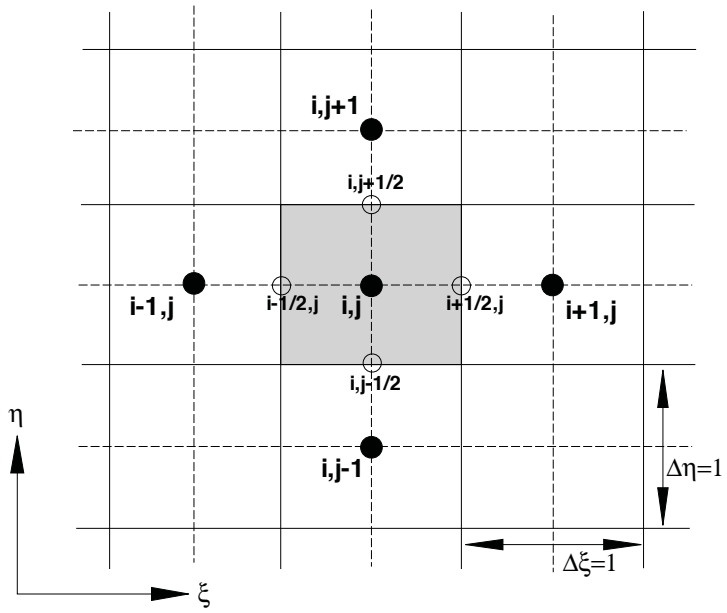

Figure 5.1: Discretization domain indicating the cell center(i,j)

where ΔV denotes the volume of the cell and $\mathbf{R}' = \mathbf{R}/Re$, $\mathbf{S}' = \mathbf{S}/Re$, $\mathbf{T}' = \mathbf{T}/Re$. For steady state solutions, the governing equation will be elliptic type at subsonic and hyperbolic at supersonic. This will make it difficult to discretize the Navier-Stokes equations using a consistent scheme. The temporal term is thus included for steady state solutions to keep the governing equations to have the same hyperbolic type across Mach number 1. For steady state solution, the accuracy of the temporal term is irrelevant since it must be zero when it is converged. Hence, the temporal term is discretized using first order Euler method for its simplicity. The discretized temporal term becomes

$$\frac{\Delta V(\mathbf{Q}^{n+1}-\mathbf{Q}^{n})}{\Delta t}+[\frac{\partial(\mathbf{E}-\mathbf{R}')}{\partial\xi}]^{n+1}+[\frac{\partial(\mathbf{F}-\mathbf{S}')}{\partial\eta}]^{n+1}+[\frac{\partial(\mathbf{G}-\mathbf{T}')}{\partial\zeta}]^{n+1}=\Delta V\mathbf{D}^{n+1} \quad (5.2)$$

where n and $n+1$ are two sequential time levels, which have a time interval of Δt. Eq. (5.2) can be further discretized in space using a conservative differencing as the following:

$$\begin{aligned}
&\frac{\Delta V_{ijk}(\mathbf{Q}_{ijk}^{n+1}-\mathbf{Q}_{ijk}^{n})}{\Delta t} \\
&+(\mathbf{E}_{i+\frac{1}{2}}-\mathbf{E}_{i-\frac{1}{2}})^{n+1}-(\mathbf{R}'_{i+\frac{1}{2}}-\mathbf{R}'_{i-\frac{1}{2}})^{n+1} \\
&+(\mathbf{F}_{j+\frac{1}{2}}-\mathbf{F}_{j-\frac{1}{2}})^{n+1}-(\mathbf{S}'_{j+\frac{1}{2}}-\mathbf{S}'_{j-\frac{1}{2}})^{n+1} \\
&+(\mathbf{G}_{k+\frac{1}{2}}-\mathbf{G}_{k-\frac{1}{2}})^{n+1}-(\mathbf{T}'_{k+\frac{1}{2}}-\mathbf{T}'_{k-\frac{1}{2}})^{n+1} \\
&=\Delta V_{ijk}\mathbf{D}_{ijk}^{n+1}
\end{aligned} \tag{5.3}$$

To evaluate the inviscid fluxes at the cell interface $\mathbf{E},\mathbf{F},\mathbf{G}$, the characteristic based upwind schemes are usually employed due to importance of capturing strong shocks and careful treatment of discontinuity, while the central differencing is used for the viscous fluxes $\mathbf{R},\mathbf{S},\mathbf{T}$. For implicit methods, a Jacobian must be introduced at time level $n+1$ for linearization. This Jacobian is formed by the derivatives of the flux values with respect to each conservative variables at a cell center point.

The implicit matrices will result in 9 elements around the diagonal element for 3D with first order upwind for inviscid fluxes and second order central differencing scheme. The first order upwind scheme for the implicit matrix will have the diagonal dominance required by Gauss-Seidel iteration [121]. Using Gauss-Seidel line relaxation, a block tri-diagonal matrix is inversed along each mesh line.

With an upwind scheme, the numerical flux is split into its left(L) and right(R) side fluxes. For example, the inviscid flux $\mathbf{E}$ at $i+\frac{1}{2}$ can be expressed as

$$\mathbf{E}_{i+\frac{1}{2}} = \mathbf{E}_L + \mathbf{E}_R = \mathbf{E}^+_{i+\frac{1}{2}} + \mathbf{E}^-_{i+\frac{1}{2}} \tag{5.4}$$

Since Eq. (5.1) is nonlinear, a linearization procedure is necessary. Let us apply a Taylor series expansion to the flux vectors at time level $n+1$ as

$$\mathbf{E}^{n+1} \cong \mathbf{E}^n + \frac{\partial \mathbf{E}}{\partial t}\Delta t + O[(\Delta t)^2] \tag{5.5}$$

$$\frac{\partial \mathbf{E}}{\partial t} = \frac{\partial \mathbf{E}}{\partial \mathbf{Q}}\frac{\partial \mathbf{Q}}{\partial t} \cong \frac{\partial \mathbf{E}}{\partial \mathbf{Q}}\frac{\Delta \mathbf{Q}}{\Delta t} \tag{5.6}$$

$$\mathbf{E}^{n+1} \cong \mathbf{E}^n + A \bullet \Delta \mathbf{Q} \tag{5.7}$$

where $A(= \frac{\partial \mathbf{E}}{\partial \mathbf{Q}})$ is the inviscid flux Jacobian matrix and the change in the conservative variable vector, $\Delta\mathbf{Q}$, is defined by

$$\Delta \mathbf{Q} = \mathbf{Q}^{n+1} - \mathbf{Q}^n \tag{5.8}$$

The inviscid flux $\mathbf{E}$ at the cell interface $i+\frac{1}{2}$ can be given as

$$\mathbf{E}^{n+1}_{i+\frac{1}{2}} = \mathbf{E}^n_{i+\frac{1}{2}} + (\frac{\partial \mathbf{E}^+}{\partial \mathbf{Q}})_L \bullet \Delta \mathbf{Q}_L + (\frac{\partial \mathbf{E}^-}{\partial \mathbf{Q}})_R \bullet \Delta \mathbf{Q}_R \tag{5.9}$$

where $\Delta\mathbf{Q}$ approaches zero when it is converged. Hence the accuracy order for $\Delta\mathbf{Q}$ is not important. The first order accuracy is used to evaluate $\Delta\mathbf{Q}$.

$$\Delta \mathbf{Q}_L = \Delta \mathbf{Q}_i, \quad \Delta \mathbf{Q}_R = \Delta \mathbf{Q}_{i+1} \tag{5.10}$$

Let

$$A^L_{i+\frac{1}{2}} = (\frac{\partial \mathbf{E}^+}{\partial \mathbf{Q}})_L, \quad A^R_{i+\frac{1}{2}} = (\frac{\partial \mathbf{E}^-}{\partial \mathbf{Q}})_R \tag{5.11}$$

Then,

$$\mathbf{E}^{n+1}_{i+\frac{1}{2}} = \mathbf{E}^n_{i+\frac{1}{2}} + A^L_{i+\frac{1}{2}}\Delta\mathbf{Q}_i + A^R_{i+\frac{1}{2}}\Delta\mathbf{Q}_{i+1} \tag{5.12}$$

Thus,

$$\begin{gathered}\mathbf{E}^{n+1}_{i+\frac{1}{2}} - \mathbf{E}^{n+1}_{i-\frac{1}{2}} = \\ (\mathbf{E}^n_{i+\frac{1}{2}} - \mathbf{E}^n_{i-\frac{1}{2}}) + A^R_{i+\frac{1}{2}}\Delta\mathbf{Q}_{i+1} + (A^L_{i+\frac{1}{2}} - A^R_{i-\frac{1}{2}})\Delta\mathbf{Q}_i - A^L_{i-\frac{1}{2}}\Delta\mathbf{Q}_{i-1}\end{gathered} \tag{5.13}$$

The viscous fluxes are linearized using central differencing.

$$\begin{aligned}(\mathbf{R}'_{i+\frac{1}{2}})^{n+1} &= (\mathbf{R}'_{i+\frac{1}{2}})^n + \frac{\partial \mathbf{R}'_{i+\frac{1}{2}}}{\partial \mathbf{Q}_{i+1}}\Delta\mathbf{Q}_{i+1} + \frac{\partial \mathbf{R}'_{i+\frac{1}{2}}}{\partial \mathbf{Q}_i}\Delta\mathbf{Q}_i \\ &= (\mathbf{R}'_{i+\frac{1}{2}})^n + L^R_{i+\frac{1}{2}}\Delta\mathbf{Q}_{i+1} + L^L_{i+\frac{1}{2}}\Delta\mathbf{Q}_i\end{aligned} \tag{5.14}$$

Thus,

$$\begin{gathered}(\mathbf{R}'_{i+\frac{1}{2}})^{n+1} - (\mathbf{R}'_{i-\frac{1}{2}})^{n+1} = \\ (\mathbf{R}'_{i+\frac{1}{2}})^n - (\mathbf{R}'_{i-\frac{1}{2}})^n + L^R_{i+\frac{1}{2}}\Delta\mathbf{Q}_{i+1} + (L^L_{i+\frac{1}{2}} - L^R_{i-\frac{1}{2}})\Delta\mathbf{Q}_i - L^L_{i-\frac{1}{2}}\Delta\mathbf{Q}_{i-1}\end{gathered} \tag{5.15}$$

The source term can be linearized by

$$\mathbf{D}^{n+1}_{i,j,k} \cong \mathbf{D}^n_{i,j,k} + (\frac{\partial \mathbf{D}}{\partial \mathbf{Q}})_{i,j,k} \bullet \Delta\mathbf{Q}_{i,j,k} \tag{5.16}$$

To apply above linearization to the fluxes in η and ζ direction, then the integrated governing equations are written as

$$
\begin{aligned}
&(I-\Theta)\Delta\mathbf{Q}_{i,j,k}+\hat{A}^{+}\Delta\mathbf{Q}_{i+1,j,k}+\hat{A}\Delta\mathbf{Q}_{i,j,k}+\hat{A}^{-}\Delta\mathbf{Q}_{i-1,j,k}\\
&+\hat{B}^{+}\Delta\mathbf{Q}_{i,j+1,k}+\hat{B}\Delta\mathbf{Q}_{i,j,k}+\hat{B}^{-}\Delta\mathbf{Q}_{i,j-1,k}\\
&+\hat{C}^{+}\Delta\mathbf{Q}_{i,j,k+1}+\hat{C}\Delta\mathbf{Q}_{i,j,k}+\hat{C}^{-}\Delta\mathbf{Q}_{i,j,k-1}=\mathbf{RHS}^{n}
\end{aligned}
\tag{5.17}
$$

where $\Theta=\Delta t\bullet(\frac{\partial\mathbf{D}}{\partial\mathbf{Q}})^{n}_{i,j,k}$. The coefficients A,A^{+},A^{-}, B,B^{+},B^{-}, and C,C^{+},C^{-} are called the left hand side (LHS) coefficient matrices and given as

$$
\begin{aligned}
\hat{A}^{+} &= \tfrac{\Delta t}{\Delta V}(A^{R}_{i+\frac{1}{2}}-L^{R}_{i+\frac{1}{2}})\\
\hat{A} &= \tfrac{\Delta t}{\Delta V}(A^{L}_{i+\frac{1}{2}}-L^{L}_{i+\frac{1}{2}}-A^{R}_{i-\frac{1}{2}}+L^{R}_{i-\frac{1}{2}})\\
\hat{A}^{-} &= -\tfrac{\Delta t}{\Delta V}(A^{L}_{i-\frac{1}{2}}-L^{L}_{i-\frac{1}{2}})\\
\hat{B}^{+} &= \tfrac{\Delta t}{\Delta V}(B^{R}_{j+\frac{1}{2}}-M^{R}_{j+\frac{1}{2}})\\
\hat{B} &= \tfrac{\Delta t}{\Delta V}(B^{L}_{j+\frac{1}{2}}-M^{L}_{j+\frac{1}{2}}-B^{R}_{j-\frac{1}{2}}+M^{R}_{j-\frac{1}{2}})\\
\hat{B}^{-} &= -\tfrac{\Delta t}{\Delta V}(B^{L}_{j-\frac{1}{2}}-M^{L}_{j-\frac{1}{2}})\\
\hat{C}^{+} &= \tfrac{\Delta t}{\Delta V}(C^{R}_{k+\frac{1}{2}}-N^{R}_{k+\frac{1}{2}})\\
\hat{C} &= \tfrac{\Delta t}{\Delta V}(C^{L}_{k+\frac{1}{2}}-N^{L}_{k+\frac{1}{2}}-C^{R}_{k-\frac{1}{2}}+N^{R}_{k-\frac{1}{2}})\\
\hat{C}^{-} &= -\tfrac{\Delta t}{\Delta V}(C^{L}_{k-\frac{1}{2}}-N^{L}_{k-\frac{1}{2}})
\end{aligned}
\tag{5.18}
$$

In Eq. (5.17), $\mathbf{RHS}^{n}$ is the summation of all terms on the right hand side (RHS) of the discretized equation and written as

$$
\begin{aligned}
\mathbf{RHS}^{n}=-\tfrac{\Delta t}{\Delta V}[&(\mathbf{E}_{i+\frac{1}{2}}-\mathbf{E}_{i-\frac{1}{2}})^{n}+(\mathbf{F}_{i+\frac{1}{2}}-\mathbf{F}_{i-\frac{1}{2}})^{n}+(\mathbf{G}_{i+\frac{1}{2}}-\mathbf{G}_{i-\frac{1}{2}})^{n}\\
&-(\mathbf{R}'_{i+\frac{1}{2}}-\mathbf{R}'_{i-\frac{1}{2}})^{n}-(\mathbf{S}'_{i+\frac{1}{2}}-\mathbf{S}'_{i-\frac{1}{2}})^{n}-(\mathbf{T}'_{i+\frac{1}{2}}-\mathbf{T}'_{i-\frac{1}{2}})^{n}]+\Delta t\bullet\mathbf{D}^{n}
\end{aligned}
\tag{5.19}
$$

Since the delta formulation($\Delta\mathbf{Q}$), the left hand side (LHS) in Eq. (5.17) constructed by employing 1st order scheme, does not affect the final solution, the accuracy of the converged solution relies on the accuracy of $\mathbf{RHS}^n$. The 5th order WENO scheme with an efficient upwind Riemann solver, so called the low diffusion E-CUSP (LDE) scheme [109], is used to evaluate the interface inviscid fluxes in $\mathbf{RHS}^n$. A fully conservative 4th order central differencing scheme [103] is used to evaluate the viscous fluxes. The unfactored Gauss-Seidel line iteration method is adopted to solve the Eq. (5.17) because the diagonal dominance is achieved through the 1st order implicit discretization and it is shown to be the most efficient relaxation method for transonic flow simulation [122].

5.2 Upwind Characteristics

Upwind schemes are designed to resolve the flow physics reasonably by accounting for the wave propagation, in which the flux vector is decomposed into a negative and a positive contributions according to the signs of the eigenvalues of the Jacobian matrices. Forward difference is then applied for the negative flux and backward difference for the positive flux. In the present study the Van Leer scheme [123] as a family of CUSP scheme is used for the LHS side in Eq. (5.17) and the LDE scheme [109] is applied for the RHS side in Eq. (5.17), which is described in detail in the following sections.

Before the upwind schemes are proposed to solve the LHS coefficients and RHS fluxes shown in Eq. (5.17), the characteristics of hyperbolic system as basis of the upwind schemes are explored. For example, the inviscid Jacobian matrix in ξ-direction can be computed as

$$\begin{aligned}\frac{\partial \mathbf{E}}{\partial \mathbf{Q}} &= \frac{\partial(E_1,E_2,E_3,E_4,E_5)}{\partial(Q_1,Q_2,Q_3,Q_4,Q_5)} \\ &= \begin{bmatrix} \frac{\partial E_1}{\partial Q_1} & \frac{\partial E_1}{\partial Q_2} & \frac{\partial E_1}{\partial Q_3} & \frac{\partial E_1}{\partial Q_4} & \frac{\partial E_1}{\partial Q_5} \\ \frac{\partial E_2}{\partial Q_1} & \frac{\partial E_2}{\partial Q_2} & \frac{\partial E_2}{\partial Q_3} & \frac{\partial E_2}{\partial Q_4} & \frac{\partial E_2}{\partial Q_5} \\ \frac{\partial E_3}{\partial Q_1} & \frac{\partial E_3}{\partial Q_2} & \frac{\partial E_3}{\partial Q_3} & \frac{\partial E_3}{\partial Q_4} & \frac{\partial E_3}{\partial Q_5} \\ \frac{\partial E_4}{\partial Q_1} & \frac{\partial E_4}{\partial Q_2} & \frac{\partial E_4}{\partial Q_3} & \frac{\partial E_4}{\partial Q_4} & \frac{\partial E_4}{\partial Q_5} \\ \frac{\partial E_5}{\partial Q_1} & \frac{\partial E_5}{\partial Q_2} & \frac{\partial E_5}{\partial Q_3} & \frac{\partial E_5}{\partial Q_4} & \frac{\partial E_5}{\partial Q_5} \end{bmatrix} \end{aligned} \tag{5.20}$$

$$\mathbf{Q} = \frac{1}{J}\begin{bmatrix} \rho & \rho u & \rho v & \rho w & \rho e \end{bmatrix} = \begin{bmatrix} Q_1 & Q_2 & Q_3 & Q_4 & Q_5 \end{bmatrix} \tag{5.21}$$

$$\mathbf{E} = \begin{bmatrix} \rho\bar{U} \\ \rho u\bar{U} + l_x P \\ \rho v\bar{U} + l_y P \\ \rho w\bar{U} + l_z P \\ (\rho e + P)\bar{U} \end{bmatrix} = \begin{bmatrix} \rho(l_x u + l_y v + l_z w) \\ \rho u(l_x u + l_y v + l_z w) + l_x P \\ \rho v(l_x u + l_y v + l_z w) + l_y P \\ \rho w(l_x u + l_y v + l_z w) + l_z P \\ (\rho e + P)(l_x u + l_y v + l_z w) \end{bmatrix} = \begin{bmatrix} E_1 \\ E_2 \\ E_3 \\ E_4 \\ E_5 \end{bmatrix} \tag{5.22}$$

where $\bar{U} = U - l_t$ and the static pressure for a perfect gas can be stated as

$$P = (\gamma - 1)[\rho e - \rho\frac{1}{2}(u^2 + v^2 + w^2 - \Omega^2 r^2)] \tag{5.23}$$

then, Eq. (5.22) and Eq. (5.23) can be reconstructed using the conservative variable vector **Q** as

$$E_1 = l_x Q_2 + l_y Q_3 + l_z Q_4 \tag{5.24}$$

$$E_2 = \frac{Q_2}{Q_1}(l_x Q_2 + l_y Q_3 + l_z Q_4) + l_x(\gamma - 1)(Q_5 - q) \tag{5.25}$$

$$E_3 = \frac{Q_3}{Q_1}(l_x Q_2 + l_y Q_3 + l_z Q_4) + l_y(\gamma - 1)(Q_5 - q) \tag{5.26}$$

$$E_4 = \frac{Q_4}{Q_1}(l_x Q_2 + l_y Q_3 + l_z Q_4) + l_z(\gamma - 1)(Q_5 - q) \tag{5.27}$$

$$E_5 = [\gamma Q_5 - (\gamma - 1)q](l_x \frac{Q_2}{Q_1} + l_y \frac{Q_3}{Q_1} + l_z \frac{Q_4}{Q_1}) \tag{5.28}$$

where

$$q = \frac{1}{2}(\frac{Q_2^2}{Q_1} + \frac{Q_3^2}{Q_1} + \frac{Q_4^2}{Q_1} - Q_1 \Omega^2 r^2) \tag{5.29}$$

The resulting Jacobian matrix A is

$$A = \frac{\partial \mathbf{E}}{\partial \mathbf{Q}} =$$

$$J \begin{pmatrix} 0 & l_x & l_y & l_z & 0 \\ -u\bar{U} + (\gamma-1)l_x e_k & \bar{U} + (2-\gamma)l_x u & l_y u + (1-\gamma)l_x v & l_z u + (1-\gamma)l_x w & (\gamma-1)l_x \\ -v\bar{U} + (\gamma-1)l_y e_k & l_x v + (1-\gamma)l_y u & \bar{U} + (2-\gamma)l_y v & l_z v + (1-\gamma)l_y w & (\gamma-1)l_y \\ -w\bar{U} + (\gamma-1)l_z e_k & l_x w + (1-\gamma)l_z u & l_y w + (1-\gamma)l_z v & \bar{U} + (2-\gamma)l_z w & (\gamma-1)l_z \\ a_{51} & (1-\gamma)\bar{U}u + I_o l_x & (1-\gamma)\bar{U}v + I_o l_y & (1-\gamma)\bar{U}w + I_o l_z & \gamma\bar{U} \end{pmatrix} \tag{5.30}$$

$$a_{51} = \bar{U}[(\gamma - 1) * (e_k + \Omega^2 r^2) - I_o] \tag{5.31}$$

where rothalpy I_o is defined as

$$I_o = \frac{\gamma}{\gamma-1}\frac{P}{\rho} + e_k = \frac{a^2}{\gamma-1} + e_k \tag{5.32}$$

$$e_k = \frac{1}{2}(u^2 + v^2 + w^2 - \Omega^2 r^2) \tag{5.33}$$

The eigenvalues($\lambda_{1,2,3,4,5}$) of the Jacobian matrix A that represent the characteristic direction of propagation are determined by

$$A = X_A \Lambda_A X_A^{-1} \tag{5.34}$$

$$\Lambda_A = \begin{bmatrix} \lambda_1 & 0 & 0 & 0 & 0 \\ 0 & \lambda_2 & 0 & 0 & 0 \\ 0 & 0 & \lambda_3 & 0 & 0 \\ 0 & 0 & 0 & \lambda_4 & 0 \\ 0 & 0 & 0 & 0 & \lambda_5 \end{bmatrix} = \begin{bmatrix} \bar{U} & 0 & 0 & 0 & 0 \\ 0 & \bar{U} & 0 & 0 & 0 \\ 0 & 0 & \bar{U} & 0 & 0 \\ 0 & 0 & 0 & \bar{U}+C & 0 \\ 0 & 0 & 0 & 0 & \bar{U}-C \end{bmatrix} \tag{5.35}$$

where Λ_A is a diagonal matrix with its element being the eigenvalues of A, X_A is the eigenvector matrix. C is the contravariant speed of sound given as

$$C = c\sqrt{l_x^2 + l_y^2 + l_z^2} \tag{5.36}$$

The eigenvector X_A is

$$X_A = [\vec{X}_1 \quad \vec{X}_2 \quad \vec{X}_3 \quad \vec{X}_4 \quad \vec{X}_5]$$

$$= \begin{pmatrix} 0 & 1 & 0 & 1 & 1 \\ -\frac{l_y}{l_x} & \frac{\bar{U}}{l_x} & -\frac{l_z}{l_x} & u + c\hat{l}_x & u - c\hat{l}_x \\ 1 & 0 & 0 & v + c\hat{l}_y & v - c\hat{l}_y \\ 0 & 0 & 1 & w + c\hat{l}_z & w - c\hat{l}_z \\ \frac{l_y u - l x v}{l x} & \frac{2u(l_y v + l_z w) - (v^2 + w^2 - u^2) l_x}{2 l_x} & \frac{l_x w - l_z u}{l_x} & I_o + \frac{c\bar{U}}{\sqrt{l_x^2 + l_y^2 + l_z^2}} & I_o - \frac{c\bar{U}}{\sqrt{l_x^2 + l_y^2 + l_z^2}} \end{pmatrix} \tag{5.37}$$

where

$$\hat{l}_x = \frac{l_x}{\sqrt{l_x^2 + l_y^2 + l_z^2}}$$

$$\hat{l}_y = \frac{l_y}{\sqrt{l_x^2 + l_y^2 + l_z^2}} \tag{5.38}$$

$$\hat{l}_z = \frac{l_z}{\sqrt{l_x^2 + l_y^2 + l_z^2}}$$

X_A^{-1} is the inverse eigenvector matrix of X_A such that

$$X_A^{-1} X_A = I \tag{5.39}$$

Note that the flux vector $\mathbf{E}$ equals $A\mathbf{Q}$ and is homogeneous function of degree one. The eigenvalues are real and consist of positive and negative eigenvalues. The signs of the eigenvalues indicate the direction of wave propagation, hence the flux vector can be split into positive or negative characteristics.

For example, for the subsonic flow where $M_\xi (= \frac{U}{C}) < 1$, the eigenvalues U, U, U and

$U+C$ are positive, and $U-C$ is negative. If the Steger-Warming flux vector splitting (FVS) scheme [124] is taken into account, then the Jacobian matrix A can be split as the following.

$$A = A^+ + A^- \tag{5.40}$$

where

$$A^+ = X_A \Lambda_A^+ X_A^{-1} \tag{5.41}$$

$$A^- = X_A \Lambda_A^- X_A^{-1} \tag{5.42}$$

Λ_A^+ is a diagonal matrix whose elements are the positive eigenvalues of A and Λ_A^- is a diagonal matrix whose elements are the negative eigenvalues of A. For example, if $\lambda_1 (= U)$ is positive, then

$$\Lambda_A^+ = \begin{bmatrix} \bar{U} & 0 & 0 & 0 & 0 \\ 0 & \bar{U} & 0 & 0 & 0 \\ 0 & 0 & \bar{U} & 0 & 0 \\ 0 & 0 & 0 & \bar{U}+C & 0 \\ 0 & 0 & 0 & 0 & 0 \end{bmatrix} \tag{5.43}$$

where $\Lambda_A^- = \Lambda_A - \Lambda_A^+$. Then, the flux vector $\mathbf{E}$ can be split as

$$\mathbf{E}^+ = A^+ \mathbf{Q} \tag{5.44}$$

$$\mathbf{E}^- = A^- \mathbf{Q} \tag{5.45}$$

The other inviscid coefficients matrices, B and C are determined in the same manner as the matrix A. For the supersonic flow ($M_\xi > 1$), all five eigenvalues are positive and which results in

$$A^+ = A \tag{5.46}$$

$$A^- = 0 \tag{5.47}$$

5.3 The VanLeer Scheme

A drawback of Steger-Warming scheme [124] is non-smoothness in the vicinity of sonic because the split fluxes are not continuously differentiable at sonic points. The Van Leer scheme [123] introduces both zero and 1st order continuity through sonic and stagnation points to correct the disadvantage of Steger-Warming scheme.

The Van Leer scheme is given in terms of the local contravariant Mach number(M_ξ). In generalized coordinates, take example of the splitting of $\mathbf{E}^\pm$ in ξ-direction. Let

$$M_\xi = \frac{\hat{U}}{a} = \frac{\bar{U}}{a\sqrt{l_\xi^2 + l_\eta^2 + l_\zeta^2}} \tag{5.48}$$

For a supersonic flow,

$$\mathbf{E}^+ = \mathbf{E} \qquad \mathbf{E}^- = 0 \qquad for \quad M_\xi > 1 \tag{5.49}$$

$$\mathbf{E}^+ = 0 \qquad \mathbf{E}^- = \mathbf{E} \qquad for \quad M_\xi < -1 \tag{5.50}$$

Note that the Van Leer scheme only splits mass flux($\rho \bar{U}$). For a subsonic flow, $|M_\xi| < 1$,

$$\mathbf{E}^\pm = \sqrt{l_\xi^2 + l_\eta^2 + l_\zeta^2} \begin{pmatrix} e^\pm \\ e^\pm \left[\hat{l_\xi} \frac{-\hat{U} \pm 2a}{\gamma} + u \right] \\ e^\pm \left[\hat{l_\eta} \frac{-\hat{U} \pm 2a}{\gamma} + v \right] \\ e^\pm \left[\hat{l_\zeta} \frac{-\hat{U} \pm 2a}{\gamma} + w \right] \\ e^\pm \left[\frac{-(\gamma-1)\hat{U}^2 \pm 2(\gamma-1)a\hat{U} + 2a^2}{\gamma^2-1} + \frac{u^2+v^2+w^2-\Omega^2 r^2}{2} \right] \end{pmatrix} \tag{5.51}$$

where

$$e^\pm = \pm \frac{1}{4} \rho a (M_\xi \pm 1)^2 \tag{5.52}$$

The flux vector $\mathbf{F}^\pm$ and $\mathbf{G}^\pm$ can be split into the same form as $\mathbf{E}^\pm$ by replacing ξ with η and ζ.

5.4 The Low Diffusion E-CUSP (LDE) Scheme

The Low Diffusion E-CUSP (LDE) Scheme [109] is used to evaluate the inviscid fluxes. The basic idea of the LDE scheme is to split the inviscid flux into the convective flux E^c and the pressure flux E^p based on the upwind characteristics. In generalized coordinate system, the flux $\mathbf{E}$ can be split as the following:

$$\mathbf{E}' = E^c + E^p = \begin{pmatrix} \rho U \\ \rho uU \\ \rho vU \\ \rho wU \\ \rho eU \\ \rho \tilde{\nu} U \end{pmatrix} + \begin{pmatrix} 0 \\ l_x p \\ l_y p \\ l_z p \\ p\overline{U} \\ 0 \end{pmatrix} \tag{5.53}$$

where, U is the contravariant velocity in ξ direction and is defined as the following:

$$U = l_t + l_x u + l_y v + l_z w \tag{5.54}$$

$\overline{U}$ is defined as:

$$\overline{U} = l_x u + l_y v + l_z w \tag{5.55}$$

The convective term, E^c is evaluated by

$$E^c = \rho U \begin{pmatrix} 1 \\ u \\ v \\ w \\ e \\ \tilde{\nu} \end{pmatrix} = \rho U f^c,\ f^c = \begin{pmatrix} 1 \\ u \\ v \\ w \\ e \\ \tilde{\nu} \end{pmatrix} \tag{5.56}$$

let

$$C = c\left(l_x^2 + l_y^2 + l_z^2\right)^{\frac{1}{2}} \tag{5.57}$$

where $c = \sqrt{\gamma RT}$ is the speed of sound.

Then the convective flux at interface $i+\frac{1}{2}$ is evaluated as:

$$E^c_{i+\frac{1}{2}} = C_{\frac{1}{2}}\left[\rho_L C^+ f^c_L + \rho_R C^- f^c_R\right] \tag{5.58}$$

where, the subscripts L and R represent the left and right hand sides of the interface. The Mach number splitting of Edwards [111] is borrowed to determine C^+ and C^- as the following:

$$C_{\frac{1}{2}} = \frac{1}{2}\left(C_L + C_R\right) \tag{5.59}$$

$$C^+ = \alpha^+_L\left(1+\beta_L\right)M_L - \beta_L M^+_L - M^+_{\frac{1}{2}} \tag{5.60}$$

$$C^- = \alpha^-_R\left(1+\beta_R\right)M_R - \beta_R M^-_R + M^-_{\frac{1}{2}} \tag{5.61}$$

$$M_L = \frac{U_L}{C_{\frac{1}{2}}},\ M_R = \frac{U_R}{C_{\frac{1}{2}}} \tag{5.62}$$

$$\alpha_{L,R} = \frac{1}{2}\left[1 \pm sign\left(M_{L,R}\right)\right] \tag{5.63}$$

$$\beta_{L,R} = -max\left[0, 1 - int\left(|M_{L,R}|\right)\right] \tag{5.64}$$

$$M^{+}_{\frac{1}{2}} = M_{\frac{1}{2}} \frac{C_R + C_L\Phi}{C_R + C_L},\ M^{-}_{\frac{1}{2}} = M_{\frac{1}{2}} \frac{C_L + C_R\Phi^{-1}}{C_R + C_L} \tag{5.65}$$

$$\Phi = \frac{\left(\rho C^2\right)_R}{\left(\rho C^2\right)_L} \tag{5.66}$$

$$M_{\frac{1}{2}} = \beta_L \delta^{+} M^{-}_{L} - \beta_R \delta^{-} M^{+}_{R} \tag{5.67}$$

$$M^{\pm}_{L,R} = \pm\tfrac{1}{4}\left(M_{L,R} \pm 1\right)^2 \tag{5.68}$$

$$\delta^{\pm} = \tfrac{1}{2}\left\{1 \pm sign\left[\tfrac{1}{2}\left(M_L + M_R\right)\right]\right\} \tag{5.69}$$

The pressure flux, E^p is evaluated as the following

$$E^{p}_{i+\frac{1}{2}} = \begin{pmatrix} 0 \\ \mathscr{P}^{+} p\, l_x \\ \mathscr{P}^{+} p\, l_y \\ \mathscr{P}^{+} p\, l_z \\ \frac{1}{2} p \left[\overline{U} + \overline{C}_{\frac{1}{2}}\right] \\ 0 \end{pmatrix}_L + \begin{pmatrix} 0 \\ \mathscr{P}^{-} p\, l_x \\ \mathscr{P}^{-} p\, l_y \\ \mathscr{P}^{-} p\, l_z \\ \frac{1}{2} p \left[\overline{U} - \overline{C}_{\frac{1}{2}}\right] \\ 0 \end{pmatrix}_R \tag{5.70}$$

The contravariant speed of sound $\overline{C}$ in the pressure vector is consistent with $\overline{U}$. It is computed based on C as the following,

$$\overline{C} = C - l_t \tag{5.71}$$

The use of $\overline{U}$ and $\overline{C}$ instead of U and C in the pressure vector is to take into account of the grid speed so that the flux will transit from subsonic to supersonic smoothly. When the grid is stationary, $l_t = 0, \overline{C} = C, \overline{U} = U$.

The pressure splitting coefficient is:

$$\mathscr{P}^{\pm}_{L,R} = \frac{1}{4}\left(M_{L,R} \pm 1\right)^2 \left(2 \mp M_L\right) \tag{5.72}$$

The LDE scheme can capture crisp shock profile and exact contact surface discontinuities as accurately as the Roe scheme [125]. With an extra equation from the DES, the splitting is basically the same as the original scheme for the Euler equation. This is an advantage over the Roe scheme [104], for which the eigenvectors need to be derived when any extra equation is added to the governing equations. In addition, it is simpler and more CPU efficient than the Roe scheme due to no matrix operation.

5.5 The 5th Order WENO Scheme

The interface flux, $E_{i+\frac{1}{2}} = E(Q_L, Q_R)$, is evaluated by determining the conservative variables Q_L and Q_R using fifth-order WENO scheme [101, 102]. For example,

$$(Q_L)_{i+\frac{1}{2}} = \omega_0 q_0 + \omega_1 q_1 + \omega_2 q_2 \tag{5.73}$$

where

$$\begin{aligned} q_0 &= \tfrac{1}{3}Q_{i-2} - \tfrac{7}{6}Q_{i-1} + \tfrac{11}{6}Q_i \\ q_1 &= -\tfrac{1}{6}Q_{i-1} + \tfrac{5}{6}Q_i + \tfrac{1}{3}Q_{i+1} \\ q_2 &= \tfrac{1}{3}Q_i + \tfrac{5}{6}Q_{i+1} - \tfrac{1}{6}Q_{i+2} \end{aligned} \tag{5.74}$$

$$\omega_k = \frac{\alpha_k}{\alpha_0 + \ldots + \alpha_{r-1}} \tag{5.75}$$

$$\begin{aligned} &\alpha_k = \tfrac{C_k}{\varepsilon + IS_k},\ k = 0, \ldots, r-1 \\ &C_0 = 0.1,\ C_1 = 0.6,\ C_2 = 0.3 \\ &IS_0 = \tfrac{13}{12}\left(Q_{i-2} - 2Q_{i-1} + Q_i\right)^2 + \tfrac{1}{4}\left(Q_{i-2} - 4Q_{i-1} + 3Q_i\right)^2 \\ &IS_1 = \tfrac{13}{12}\left(Q_{i-1} - 2Q_i + Q_{i+1}\right)^2 + \tfrac{1}{4}\left(Q_{i-1} - Q_{i+1}\right)^2 \\ &IS_2 = \tfrac{13}{12}\left(Q_i - 2Q_{i+1} + Q_{i+2}\right)^2 + \tfrac{1}{4}\left(3Q_i - 4Q_{i+1} + Q_{i+2}\right)^2 \end{aligned} \tag{5.76}$$

where, ε is originally introduced to avoid the denominator becoming zero and is supposed to be a very small number. In [102], it is observed that IS_k will oscillate if ε is small and also shift the weights away from the optimum values in the smooth region. The higher the ε values, the closer the weights approach the optimum weights, C_k, which will give the symmetric evaluation of the interface flux with minimum numerical dissipation. When there are shocks in the flow field, ε can not be too large to maintain the sensitivity to shocks. In [102], the optimized value of $\varepsilon = 10^{-2}$ is recommended for the transonic flow with shock waves.

5.6 The 4th Order Central Differencing for Viscous Terms

A set of conservative fourth-order accurate finite central differencing schemes for the viscous terms is suggested [103]. These central differencing schemes are constructed so that the stencil widths are within the WENO scheme stencil. This requires that the central differencing achieves their maximum order accuracy in the WENO stencil.

We take the viscous flux derivative in ξ-direction as the example to explain how the schemes are constructed. To conservatively discretize the viscous derivative term in Navier-Stokes equations Eq. (3.90), we have

$$\frac{\partial R}{\partial \xi}|_i = \frac{\tilde{R}_{i+1/2} - \tilde{R}_{i-1/2}}{\Delta \xi} \tag{5.77}$$

To obtain 4th order accuracy, $\tilde{R}$ needs to be reconstructed as

$$\tilde{R}_{i-1/2} = \sum_{I=i-3/2}^{i+1/2} \alpha_I R_I \tag{5.78}$$

where

$$\alpha_{i-3/2} = -\frac{1}{24},\ \alpha_{i-1/2} = \frac{26}{24},\ \alpha_{i+1/2} = -\frac{1}{24}$$

$$R_{i-1/2} = \left[(\xi_x \tau_{xx}) + (\eta_y \tau_{xy}) + (\zeta_z \tau_{xz})\right]_{i-1/2}$$

$$\begin{aligned}(\tau_{xx}) = \quad & \mu\{\tfrac{4}{3}\left[(\xi_x \tfrac{\partial u}{\partial \xi}) + (\eta_x \tfrac{\partial u}{\partial \eta}) + (\zeta_x \tfrac{\partial u}{\partial \zeta})\right] \\ & -\tfrac{2}{3}[(\xi_y \tfrac{\partial v}{\partial \xi}) + (\eta_y \tfrac{\partial v}{\partial \eta}) + (\zeta_y \tfrac{\partial v}{\partial \zeta}) \\ & (\xi_z \tfrac{\partial w}{\partial \xi}) + (\eta_z \tfrac{\partial w}{\partial \eta}) + (\zeta_z \tfrac{\partial w}{\partial \zeta})]\}\end{aligned} \tag{5.79}$$

If R in Eq. (5.78) can be approximated with the accuracy order not lower than 4th order, the Taylor series expansion analysis of (5.77) and (5.78) will give

$$\frac{1}{\Delta\xi}(\tilde{R}_{i+1/2}-\tilde{R}_{i-1/2}) = R^{'}(\xi_i) + O(\Delta\xi^4) \tag{5.80}$$

and the 4th order accuracy is achieved (to be proved later). It needs to point out that in Eq. (5.77), $\tilde{R}_{i-1/2}$ can not be replaced by $R_{i-1/2}$. Otherwise, the 4th order accuracy can not be achieved even though the high order approximation of $R_{i-1/2}$ is used. The 4th order accuracy from Eq. (5.77)-(5.80) is also based on the uniform spacing $\Delta\xi = C$.

In order to achieve the highest order accuracy of R_I with $I = i-3/2, i-1/2, i+1/2$, the approximation of each term in Eq. (5.78) using the same points is given below:

$$\mu_I = \sum_{l=m}^{n} C_l^I \mu_{i+l}, \tag{5.81}$$

$$\frac{\partial u}{\partial \xi}|_I = \frac{1}{\Delta\xi}\sum_{l=r}^{s} D_l^I u_{i+l}, \tag{5.82}$$

$$\frac{\partial u}{\partial \eta}|_I = \sum_{l=m}^{n} C_l^I \frac{\partial u}{\partial \eta}|_{i+l,j} \tag{5.83}$$

where

$$\frac{\partial u}{\partial \eta}|_{i,j} = \frac{1}{\Delta\eta}\sum_{l=p}^{q} C_l^c u_{i,j+l}, \tag{5.84}$$

By choosing different ranges for $(m,n),(r,s),(p,q)$ and different coefficients C_l^I, D_l^I, C_l^c,

one can obtain different order accuracy approximation to the viscous terms. The principle of choosing $(m,n),(r,s),(p,q)$ is to ensure that the approximation of $\frac{\partial R}{\partial \xi}|_i$ in Eq. (5.77) is a central differencing. For example, let $(m,n)=(-2,1),(r,s)=(-3,2),and\ (p,q)=(-2,2)$, and they give

$$\mu_I = \sum_{l=m}^{n} C_l^I \mu_{i+l} + O(\Delta\xi^4), \tag{5.85}$$

$$\frac{\partial u}{\partial \xi}|_I = \frac{1}{\Delta\xi}\sum_{l=r}^{s} D_l^I u_{i+l} + O(\Delta\xi^5), \tag{5.86}$$

$$\frac{\partial u}{\partial \eta}|_I = \sum_{l=m}^{n} C_l^I \frac{\partial u}{\partial \eta}|_{i+l,j} + O(\Delta\xi^4,\Delta\eta^4), \tag{5.87}$$

where

$$\frac{\partial u}{\partial \eta}|_{i,j} = \frac{1}{\Delta\eta}\sum_{l=p}^{q} C_l^c u_{i,j+l} + O(\Delta\eta^4) \tag{5.88}$$

the coefficients C_l^I, D_l^I, C_l^c can be obtained by Taylor's series expansion and are given in Tables 5.1-5.3. For example,

$$\begin{cases} \mu_{i-3/2} = \frac{1}{16}(5\mu_{i-2} + 15\mu_{i-1} - 5\mu_i + \mu_{i+1}) + O(\Delta\xi^4) \\ \mu_{i-1/2} = \frac{1}{16}(-\mu_{i-2} + 9\mu_{i-1} + 9\mu_i - \mu_{i+1}) + O(\Delta\xi^4) \\ \mu_{i+1/2} = \frac{1}{16}(\mu_{i-2} - 5\mu_{i-1} + 15\mu_i + 5\mu_{i+1}) + O(\Delta\xi^4) \end{cases} \tag{5.89}$$

$$\begin{cases} \frac{\partial u}{\partial \xi}|_{i-3/2} = \frac{1}{\Delta\xi}(\frac{71}{1920}u_{i-3} - \frac{141}{128}u_{i-2} + \frac{69}{64}u_{i-1} + \frac{1}{192}u_i - \frac{3}{128}u_{i+1} + \frac{3}{640}u_{i+2}) + O(\Delta\xi^5) \\ \frac{\partial u}{\partial \xi}|_{i-1/2} = \frac{1}{\Delta\xi}(-\frac{3}{640}u_{i-3} + \frac{25}{384}u_{i-2} - \frac{75}{64}u_{i-1} + \frac{75}{64}u_i - \frac{25}{384}u_{i+1} + \frac{3}{640}u_{i+2}) + O(\Delta\xi^5) \\ \frac{\partial u}{\partial \xi}|_{i+1/2} = \frac{1}{\Delta\xi}(-\frac{3}{640}u_{i-3} + \frac{3}{128}u_{i-2} - \frac{1}{192}u_{i-1} - \frac{69}{64}u_i + \frac{141}{128}u_{i+1} - \frac{71}{1920}u_{i+2}) + O(\Delta\xi^5) \end{cases} \tag{5.90}$$

The other terms are determined similarly. For comparison, the terms used in Ref. [126, 127] by De Rango and Zingg et al. are given as the following,

$$\begin{cases} \mu_{i-3/2} = \frac{1}{16}(-\mu_{i-3} + 9\mu_{i-2} + 9\mu_{i-1} - \mu_i) + O(\Delta\xi^4) \\ \mu_{i-1/2} = \frac{1}{16}(\mu_{i-2} + 9\mu_{i-1} + 9\mu_i - \mu_{i+1}) + O(\Delta\xi^4) \\ \mu_{i+1/2} = \frac{1}{16}(\mu_{i-1} + 9\mu_i + 9\mu_{i+1} - \mu_{i+2}) + O(\Delta\xi^4) \end{cases} \tag{5.91}$$

$$\begin{cases} \frac{\partial u}{\partial \xi}|_{i-3/2} = \frac{1}{24\Delta\xi}(-u_{i-3} - 27u_{i-2} + 27u_{i-1} - u_i) + O(\Delta\xi^4) \\ \frac{\partial u}{\partial \xi}|_{i-1/2} = \frac{1}{24\Delta\xi}(-u_{i-2} - 27u_{i-1} + 27u_i - u_{i+1}) + O(\Delta\xi^4) \\ \frac{\partial u}{\partial \xi}|_{i+1/2} = \frac{1}{24\Delta\xi}(-u_{i-1} - 27u_i + 27u_{i+1} - u_{i+2}) + O(\Delta\xi^4) \end{cases} \tag{5.92}$$

Compare Eqs. (5.89),(5.90) and Eqs. (5.91),(5.92), it can be seen that μ_I in present paper has the same accuracy order, as that of De Rango and Zingg et al., but has small stencil width $(i-2,\cdots,i+1)$, $\frac{\partial u}{\partial \xi}|_I$ has the same stencil width, but obtains one accuracy order higher than that in Ref. [126, 127].

Table 5.1: The coefficients of C_l^I

I	C_{-2}^I	C_{-1}^I	C_0^I	C_1^I
$i-3/2$	5/16	15/16	-5/16	1/16
$i-1/2$	-1/16	9/16	9/16	-1/16
$i+1/2$	1/16	-5/16	15/16	5/16

Table 5.2: The coefficients of D_l^I

I	D^I_{-3}	D^I_{-2}	D^I_{-1}	D^I_0	D^I_1	D^I_2
$i-3/2$	71/1920	-141/128	69/64	1/192	-3/128	3/640
$i-1/2$	-3/640	25/384	-75/64	75/64	-25/384	3/640
$i+1/2$	-3/640	3/128	-1/192	-69/64	141/128	-71/1920

Table 5.3: The coefficients of C_l^c

C^c_{-2}	C^c_{-1}	C^c_0	C^c_1	C^c_2
1/12	-8/12	0	8/12	-1/12

It can be proved that the scheme Eq. (5.77) is symmetric with respect to cell i. For example, the coefficients of $\mu_{i-2}u_{i-3}$, $\mu_{i+2}u_{i+3}$, $\mu_{i-1}u_{i-2}$, and $\mu_{i+1}u_{i+2}$ can be found as (in the following formula, $\tilde{C}_l^I$ and $\tilde{D}_l^I$ are the coefficients of μ_{i+l}, u_{i+l} in R_I for $\tilde{R}_{i+1/2}$, respectively. It's clear that there are $\tilde{C}_l^I = C_{l-1}^{I-1}$ and $\tilde{D}_l^I = D_{l-1}^{I-1}$, $\tilde{\alpha}_I = \alpha_{I-1}$, $I = i-1/2, i+1/2, i+3/2$):

$$
\begin{aligned}
C_{i-2,i-3} &= -\sum_{I=i-3/2}^{i+1/2} \alpha_I C^I_{-2} D^I_{-3} \\
&= -\left[(\tfrac{-1}{24})\cdot\tfrac{5}{16}\cdot\tfrac{71}{1920} + \tfrac{26}{24}\cdot(\tfrac{-1}{16})\cdot(\tfrac{-3}{640}) + (\tfrac{-1}{24})\cdot\tfrac{1}{16}\cdot(\tfrac{-3}{640})\right] \\
&= \tfrac{7}{46080}
\end{aligned}
$$

$$
\begin{aligned}
C_{i+2,i+3} &= \sum_{I=i-1/2}^{i+3/2} \tilde{\alpha}_I \tilde{C}^I_2 \tilde{D}^I_3 \\
&= (\tfrac{-1}{24})\cdot\tfrac{1}{16}\cdot\tfrac{3}{640} + \tfrac{26}{24}\cdot(\tfrac{-1}{16})\cdot\tfrac{3}{640} + (\tfrac{-1}{24})\cdot\tfrac{5}{16}\cdot(\tfrac{-71}{1920}) \\
&= \tfrac{7}{46080}
\end{aligned}
$$

$$
\begin{aligned}
C_{i-1,i-2} &= \sum_{I=i-1/2}^{i+3/2} \tilde{\alpha}_I \tilde{C}_{-1}^I \tilde{D}_{-2}^I - \sum_{I=i-3/2}^{i+1/2} \alpha_I C_{-1}^I D_{-2}^I \\
&= (\tfrac{-1}{24}) \cdot \tfrac{5}{16} \cdot \tfrac{71}{1920} + \tfrac{26}{24} \cdot (\tfrac{-1}{16}) \cdot (\tfrac{-3}{640}) + (\tfrac{-1}{24}) \cdot \tfrac{1}{16} \cdot (\tfrac{-3}{640}) \\
&\quad - \left[(\tfrac{-1}{24}) \cdot \tfrac{15}{16} \cdot (\tfrac{-141}{128}) + \tfrac{26}{24} \cdot \tfrac{9}{16} \cdot \tfrac{25}{384} + (\tfrac{-1}{24}) \cdot (\tfrac{-5}{16}) \cdot \tfrac{3}{128} \right] \\
&= -\tfrac{479}{5760}
\end{aligned}
$$

$$
\begin{aligned}
C_{i+1,i+2} &= \sum_{I=i-1/2}^{i+3/2} \tilde{\alpha}_I \tilde{C}_1^I \tilde{D}_2^I - \sum_{I=i-3/2}^{i+1/2} \alpha_I C_1^I D_2^I \\
&= (\tfrac{-1}{24}) \cdot (\tfrac{-5}{16}) \cdot (\tfrac{-3}{128}) + \tfrac{26}{24} \cdot \tfrac{9}{16} \cdot (\tfrac{-25}{384}) + (\tfrac{-1}{24}) \cdot \tfrac{15}{16} \cdot \tfrac{141}{128} \\
&\quad - \left[(\tfrac{-1}{24}) \cdot \tfrac{1}{16} \cdot \tfrac{3}{640} + \tfrac{26}{24} \cdot (\tfrac{-1}{16}) \cdot \tfrac{3}{640} + (\tfrac{-1}{24}) \cdot \tfrac{5}{16} \cdot (\tfrac{-71}{1920}) \right] \\
&= -\tfrac{479}{5760}
\end{aligned}
$$

So we have $C_{i-2,i-3} = C_{i+2,i+3}$, $C_{i-1,i-2} = C_{i+1,i+2}$, and so on. Hence the scheme Eq. (5.77) is symmetric with respect to grid node i. The symmetry of central differencing for Eq. (5.77) satisfies the diffusion property of the viscous flux.

Next, we prove that the order of accuracy given by Eq.(5.80) is satisfied. Take the term $T^- = \mu \partial u / \partial \xi$ in Eq.(5.80) as the example,

In $\tilde{R}_{i-1/2}$, at $I = i - 3/2$, based on Taylor's series expansion

$$
\begin{aligned}
T_{i-3/2}^- &= \sum_{l=m}^{n} C_l^I \mu_{i+l} (\tfrac{1}{\Delta\xi} \sum_{l=r}^{s} D_l^I u_{i+l}) \\
&= \left[\mu_{i-3/2} + A_I \mu_{i-3/2}^{(4)} \Delta\xi^4 + O(\Delta\xi^5) \right] \left[\tfrac{\partial u}{\partial \xi}|_{i-3/2} + O(\Delta\xi^5) \right] \\
&= \mu_{i-3/2} \tfrac{\partial u}{\partial \xi}|_{i-3/2} + A_I \mu_{i-3/2}^{(4)} \tfrac{\partial u}{\partial \xi}|_{i-3/2} \Delta\xi^4 + O(\Delta\xi^5)
\end{aligned}
$$

A_I is the coefficient of Taylor's series expansion.

The corresponding term T^+ in $\tilde{R}_{i+1/2}$ is at $I = i - 1/2$, and

$$\begin{aligned} T^+_{i-1/2} &= \Sigma_{l=m}^{n} \tilde{C}_l^I \mu_{i+1+l} (\tfrac{1}{\Delta\xi} \Sigma_{l=r}^{s} \tilde{D}_l^I u_{i+1+l}) \\ &= \left[\mu_{i-1/2} + \tilde{A}_I \mu^{(4)}_{i-1/2} \Delta\xi^4 + O(\Delta\xi^5) \right] \left[\tfrac{\partial u}{\partial \xi}|_{i-1/2} + O(\Delta\xi^5) \right] \\ &= \mu_{i-1/2} \tfrac{\partial u}{\partial \xi}|_{i-1/2} + \tilde{A}_I \mu^{(4)}_{i-1/2} \tfrac{\partial u}{\partial \xi}|_{i-1/2} \Delta\xi^4 + O(\Delta\xi^5) \end{aligned}$$

Note that $A_I = \tilde{A}_I$, hence

$$T^+_{i-1/2} - T^-_{i-3/2} = \mu_{i-1/2} \frac{\partial u}{\partial \xi}|_{i-1/2} - \mu_{i-3/2} \frac{\partial u}{\partial \xi}|_{i-3/2} + O(\Delta\xi^5)$$

The other two terms can be analyzed similarly as above, then Eq.(5.80)

$$\frac{1}{\Delta\xi} (\tilde{R}_{i+1/2} - \tilde{R}_{i-1/2}) = R^{'}(\xi_i) + O(\Delta\xi^4)$$

is proved, i.e. the constructed schemes are formally 4th order accuracy.

5.7 Implicit Time Integration

When a unsteady solution is considered, higher order approximation for the time derivative is desirable. For unsteady flow, Jameson formulated so called the 2nd order dual time stepping scheme [128]. By introducing a pseudo time term, the unsteady problem at each physical time step is treated as a steady state problem for pseudo time. Without losing time accuracy, the dual time stepping scheme can greatly improve the computation efficiency by enhancing diagonal dominance [129].

5.7.1 Implicit Time Accurate Flow Solver

The time accurate governing equations are solved using dual time stepping method suggested by Jameson [128]. To achieve high convergence rate, the implicit pseudo time marching scheme is used with the unfactored Gauss-Seidel line relaxation [117]. The physical temporal term is discretized implicitly using a three point, backward differencing as the following:

$$\frac{\partial Q}{\partial t} = \frac{3Q^{n+1} - 4Q^n + Q^{n-1}}{2\Delta t} \tag{5.93}$$

where $n-1$, n and $n+1$ are three sequential time levels, which have a time interval of Δt. The first-order Euler scheme is used to discretize the pseudo temporal term to enhance diagonal dominance. The semi-discretized equations of the governing equations are finally given as the following:

$$\begin{aligned} &\left[\left(\tfrac{1}{\Delta\tau} + \tfrac{1.5}{\Delta t}\right) I - \left(\tfrac{\partial R}{\partial Q}\right)^{n+1,m}\right] \delta Q^{n+1,m+1} \\ &= R^{n+1,m} - \tfrac{3Q^{n+1,m} - 4Q^n + Q^{n-1}}{2\Delta t} \end{aligned} \tag{5.94}$$

where the $\Delta\tau$ is the pseudo time step, R is the net flux evaluated on a grid point using the fifth-order WENO scheme.

5.7.2 Implicit Structural Solver

To solve the structural equations with the present CFD solver [109] in a fully coupled manner [24], the decoupled structural equations are integrated using the same method as the flow governing equations(5.94) within each physical time step:

$$\begin{aligned}&\left(\tfrac{1}{\Delta\tau}I+\tfrac{1.5}{\Delta t}M+K\right)\delta S^{n+1,m+1}\\&=q^{n+1,m+1}-M\tfrac{3S^{n+1,m}-4S^{n}+S^{n-1}}{2\Delta t}-KS^{n+1,m}\end{aligned}\tag{5.95}$$

5.7.3 Flow-Structure Coupling

The fully coupled procedure for fluid-structure interaction (FSI) simulation is achieved by removing time lag between the fluid flow and the structure as sketched in Fig. 5.2. Within each physical time step(m), the flow and structural governing equations are solved without time lag via every successive pseudo time step until the net flux residual R given by Eq. (5.94) satisfies the prescribed convergence criteria(ε). Note the residual q for the structure equation (4.27) gets converged quickly within a few steps. Therefore, the convergence of FSI is determined according to R. After the convergence criteria is reached, the fluid-structural interaction goes to next physical time step, $n+1$.

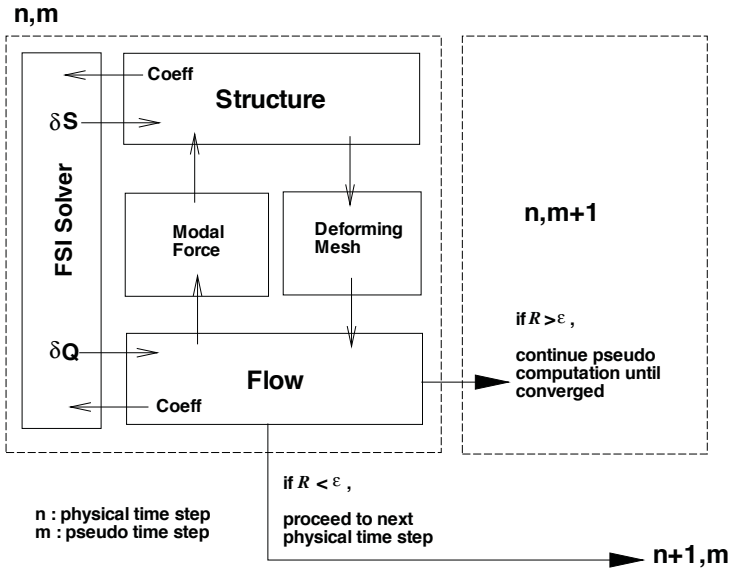

Figure 5.2: Procedure of fully coupled fluid-structure interaction

Chapter 6

Turbomachinery Boundary Conditions

The newly implemented and developed boundary conditions for 3D multistage fan/compressor simulation are described in this chapter. Inlet boundary condition(BC), outlet BC, wall BC, steady mixing plane BC at rotor/stator interface, unsteady rotor/stator sliding BC, two phase-lagged BC including the Fourier series phase lag (FSPL) and time shifted phase lag (TSPL) are given in detail. Since the present numerical discretization is carried out at the cell center using higher order schemes, the number of phantom cells (or ghost cells), which will vary depending on the scheme order of accuracy, are used to define the boundaries to match the accuracy of the inner points.

6.1 Cartesian and Cylindrical System Coordinate Mapping

It is convenient for turbomachinery to express the boundary conditions in Cylindrical system. Fig. 6.1 shows the relationship between the Cartesian and cylindrical coordinate system. Besides x, let θ and r denote the other two directions of the cylindrical system,

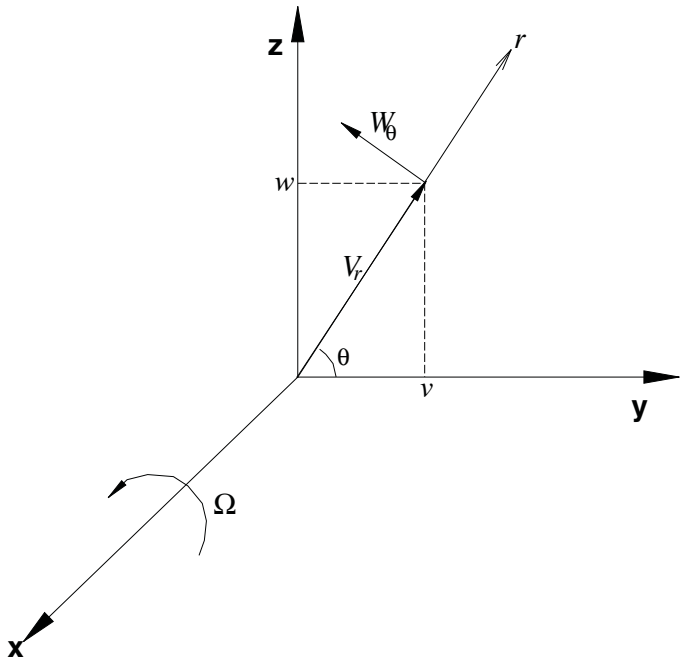

Figure 6.1: Relationship between the Cartesian to cylindrical coordinate

then

$$\theta = tan^{-1}(\frac{z}{y}) \tag{6.1}$$

$$r = \sqrt{y^2 + z^2} \tag{6.2}$$

Coordinates mapping between the Cartesian (x, y, z) and Cylindrical system(x, θ, r) can be given as

$$\begin{pmatrix} V_x \\ V_\theta \\ V_r \end{pmatrix} = \begin{pmatrix} u \\ -v \cdot sin\theta + w \cdot cos\theta \\ v \cdot cos\theta + w \cdot sin\theta \end{pmatrix} = \begin{pmatrix} u \\ \frac{-v \cdot z + w \cdot y}{r} \\ \frac{v \cdot y + w \cdot z}{r} \end{pmatrix} \tag{6.3}$$

where u, v, and w are the relative velocity components in the x, y, and z coordinate directions respectively.

The absolute velocity components in Cylindrical coordinates (C_x, C_θ, C_r) are related to the relative velocity components(V_x, V_θ, V_r) via the rotor wheel speed$(r\Omega)$ as

$$\begin{pmatrix} C_x \\ C_\theta \\ C_r \end{pmatrix} = \begin{pmatrix} V_x \\ V_\theta + rR_o \\ V_r \end{pmatrix} \tag{6.4}$$

6.2 Rotor Inlet BC

At the rotor inlet, the radial distributions of total pressure P_o, total temperature T_o, swirl angle α and pitch angle β are specified. The velocity is taken from the computational domain by the extrapolation in order to determine the rest of variables. First, we assume that the speed of sound a is constant at the inlet boundary. Then, the static temperature is obtained by

$$T_b = T_o[1 - \frac{\gamma - 1}{2}(\frac{C_i}{a_o})^2] \tag{6.5}$$

where the subscripts i represents the first interior cell and subscripts b indicates the first ghost cell of the boundary. C_i is the absolute velocity of the first interior cell and a_o is the total speed of sound defined by

$$\frac{a_o^2}{\gamma - 1} = \frac{a_i^2}{\gamma - 1} + \frac{C_i^2}{2} \tag{6.6}$$

Using the isentropic relations, the absolute velocity(C_b), the static pressure(p_b) and density(ρ_b) are determined by

$$|C_b| = \frac{1}{M_\infty}\sqrt{\frac{2}{\gamma-1}(T_o - T_b)} \tag{6.7}$$

$$p_b = P_o\left(\frac{T_b}{T_o}\right)^{\frac{\gamma}{\gamma-1}} \tag{6.8}$$

$$\rho_b = \frac{p_b\gamma}{a_b^2} \tag{6.9}$$

Then, the velocity components are decoupled and the conservative variables are found as the following:

$$\begin{pmatrix} \rho \\ \rho V_x \\ \rho V_r \\ \rho V_\theta \\ \rho e \end{pmatrix}_b = \begin{pmatrix} \rho_b \\ \rho_b C_m cos\beta \\ \rho_b C_m sin\beta \\ \rho_b(C_m tan\alpha - rR_o) \\ \frac{p_b}{(\gamma-1)} + \frac{\rho_b}{2}(V_x^2 + V_r^2 + V_\theta^2 - r^2R_o^2) \end{pmatrix} \tag{6.10}$$

6.3 Rotor Outlet BC

At the rotor outlet, the static pressure(p_b) is specified. The components of velocity(u, v, w) are extrapolated from the computational domain. If we neglect the viscosity and constant density, the radial momentum equation can be written as

$$\frac{\partial V_r}{\partial t} + V_r \frac{\partial V_r}{\partial t} + \frac{V_\theta}{r}\frac{\partial V_r}{\partial \theta} + u\frac{\partial V_r}{\partial z} - \frac{V_\theta^2}{r} = -\frac{1}{\rho}\frac{\partial p}{\partial r} \tag{6.11}$$

The change in the radial velocity can be usually negligible($\partial V_r \cong 0$) in axial turbomachinery and for the steady state, known as the radial equilibrium equation is obtained.

$$\frac{1}{\rho}\frac{\partial p}{\partial r} = \frac{V_\theta^2}{r} \tag{6.12}$$

Using the radial equilibrium equation(6.12) that can reflect the nonuniform variations of the static pressure in the annulus, the radial distributions of the back pressure are determined. If radial distributions of the static pressure are available from the experiment like NASA Rotor 67 [130], then the measured radial profile is directly given instead of solving the equation. The density(ρ_b) is calculated by using the following isentropic relation.

$$\rho_b = \left(\frac{p_b}{p_i}\right)^{\frac{1}{\gamma}} \rho_i \tag{6.13}$$

where p_i is the static pressure and ρ_i is the density at the first interior cell of the outlet boundary. Using the velocity, pressure and density at outlet boundary determined, the total energy given by Eq. (3.50) is updated.

6.4 Rotor Wall BC

On the solid wall, the non-slip boundary condition is applied to enforce mass flux going through the wall to be zero. The velocity components of the ghost cells are obtained by the extrapolation between the moving wall velocity and interior cells as follows:

$$\vec{V}_b = 2\vec{V}_w - \vec{V}_i \tag{6.14}$$

where $\vec{V}_b$ denotes the ghost cell velocity, $\vec{V}_i$ stands for the velocity of $1st$ interior cell close to the wall, and $\vec{V}_w$ is wall moving velocity given by $\vec{\Omega} \times \vec{r}$. Another option to save mesh size in our computation is to use the law of the wall. When y^+ is between 11 and 300, the no slip condition is replaced by using the wall function.

$$u^+ = \frac{1}{k} ln y^+ + B \tag{6.15}$$

where k denotes Von K*árm*á*n* constant taken as 0.41, and B denotes a dimensionless constant corresponding to the wall roughness taken as 5.0. The law of the wall approach is based on the assumption that the boundary layer is attached.

The rational that the law of the wall BC is used for all the conditions including near stall is that the vortices in the tip and hub region are mostly large structures and the inconsistency is minimized by using the local velocity direction at the boundary layer edge. The numerical results at the near stall conditions of NASA Rotor 67 by the present authors [29] indicate that the radial profiles at hub and tip agree very well with the measurement at the near stall conditions. It means that such treatment is acceptable and predicts reasonable

results. The same BC is also widely used by other research groups to reduce the excessive mesh and CPU time in the rotor tip region [39, 77, 79–81, 131–134].

Eq. (6.12) is used to determine the casing/hub wall static pressure, whereas zero pressure gradient condition is used on the blade surface. For the density, the perfect gas law is used to impose zero heat flux through the wall.

$$T_b = T_i : \qquad \rho_b = \frac{P_b}{P_i}\rho_i \tag{6.16}$$

6.5 Rotor Inflow Perturbation BC

In reality the flow at fan/compressor intake can be distorted under extreme flow conditions such as rotating stall and might be represented by using inlet total pressure perturbation [74]. As pointed out by He [77], a perturbation to the inlet total pressure is necessary for rotating simulation because the background noise driven by computer error is much smaller than typical background noise observed in the experiment. To consider the effect of background disturbances in the full annulus simulation of stall inception, the following total pressure(p_o) perturbation is applied at the inlet.

$$p_o = \bar{p_o}\left[1 + \frac{A}{2}sin\left(\frac{2\pi nL}{b}\right) + \frac{A}{2}cos\left(\frac{2\pi nL}{b}\right)\right] \tag{6.17}$$

where A is the amplitude of inlet total pressure perturbation set as 1%, which is in the order of experimental uncertainty. b represents the rotor circumference of the full annulus, L is the circumferential length of the coordinates at the inlet domain and n defines the spatial

length scale of the disturbance. In the current study, only the first mode disturbance(n=1) with its wavelength of one circumference was used.

6.6 Steady Mixing Plane

A mixing plane technique is implemented using the halo cell approach as sketched in Fig. 6.2. The conservative variables are averaged and stored to corresponding halo cell layers of the adjacent domain using the following relations between the moving (or rotating relative frame) and the fixed frame. For example, the flow quantities of the cell $n-1$, and n in the fixed domain are volume averaged circumferentially, and then stored to the halo cell $m+2$, and $m+1$ in the moving domain. This method couples two domains and facilitates higher order spatial schemes at the interface.

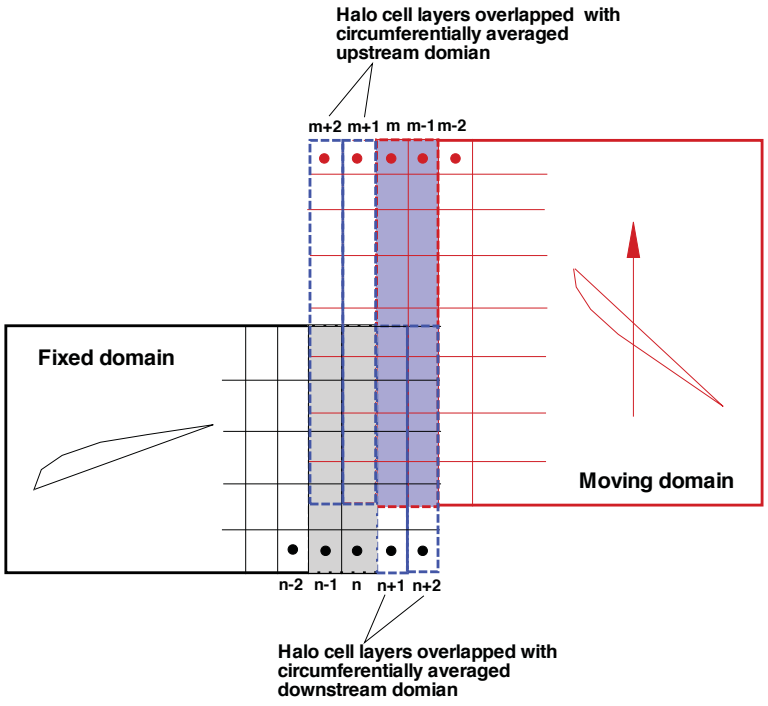

Figure 6.2: Halo cell approach for mixing plane

$$\begin{pmatrix} \bar{\rho} \\ \bar{\rho}\bar{U} \\ \bar{\rho}\bar{V}_r \\ \bar{\rho}(\bar{V}_\theta + rR_o) \\ \bar{\rho}\bar{e} + \bar{\rho}\bar{C}_\theta rR_o \\ \bar{\rho}\bar{\tilde{\nu}} \end{pmatrix}_{Fixed} \rightleftharpoons \begin{pmatrix} \bar{\rho} \\ \bar{\rho}\bar{U} \\ \bar{\rho}\bar{V}_r \\ \bar{\rho}\bar{V}_\theta \\ \bar{\rho}\bar{e} \\ \bar{\rho}\bar{\tilde{\nu}} \end{pmatrix}_{rotating\ relative\ frame} \tag{6.18}$$

where the overbar denotes volume-averaged variables and the cell volume V can be calculated by given Eq. (B.1) in Appendix A.

$$\bar{\Phi} = \frac{1}{V}\int\int\int \Phi dV \tag{6.19}$$

As aforementioned, the circumferential average cut off the wake propagation and add artificial mixing loss to the calculation. However, the mixing plane method is convenient to couple multi-stage computation.

6.7 Fully Conservative Rotor/Stator Sliding BC

The interaction between rotating and stationary blades introduces inherent unsteadiness to the flow of multistage turbomachinery. For instance, the shock wave interaction between the inter blade rows as well as rotating instabilities as a main driver of NSV can be predicted not by the steady approach, but only by the conservative unsteady approach. Numerous studies on the unsteady rotor/stator interaction has been developed [64–67] based

on interpolation on the rotor-stator interface. Rai [64] used the patched and overlaid grid system based on interpolation to solve an axial turbine with a rotor-stator configuration. Chen et al. [68] pointed out that lack of flux conservation can significantly affect the solution accuracy where shock interaction exists between the blade rows. In fact, the methods of rotor/stator interaction using any type of interpolation methods can not satisfy the conservation of the flux across the interface.

To rigorously resolve wake propagation, shocks interaction and rotating instabilities, a fully conservative sliding BC without interpolation is developed to solve the moving rotor in the rotating relative frame and the stator blades in the fixed frame. The following relations between the rotating relative frame and the fixed frame are used for variable exchange.

$$\begin{pmatrix} \rho \\ \rho U \\ \rho V_r \\ \rho(V_\theta + rR_o) \\ \rho e + \rho C_\theta r R_o \\ \rho \tilde{\nu} \end{pmatrix}_{Fixed} \rightleftharpoons \begin{pmatrix} \rho \\ \rho U \\ \rho V_r \\ \rho V_\theta \\ \rho e \\ \rho \tilde{\nu} \end{pmatrix}_{rotating\ relative\ frame} \tag{6.20}$$

The conservative variables in cylindrical rotating coordinates $(\rho, \rho U, \rho V_r, \rho V_\theta, \rho e, \rho \tilde{\nu})$ are exchanged when the moving domains slide and are updated in every pseudo time step. Since the sliding BC with the hallo cells ensure the sliding boundary to be solved in the same manner as the inner domain, it hence can capture the interactive effects between the rotor and the stator.

The condition for this sliding BC to avoid interpolation across the sliding BC is to use

one-to-one matched grid points at the interface [28]. The two domains at the interface need to have the same mesh size and the grid point coordinates, which should be also evenly distributed circumferentially. This condition can be always satisfied if it is a full annulus calculation. If it is for a sector of the annulus, a geometrically periodic sector should be used first if possible. In this case, the grid size of the interface disk in the rotor circumferential direction can be found by the greatest common factor (GCF). For example, if we have a compressor with the number of IGV 56 and the number of rotor 35, on can reduce the full annulus to 1/7th annulus with 8 IGV blades and 5 rotor blades that satisfies the geometry periodicity. Then, the GCF is 40 as 5 multiples per IGV blade and 8 multiples per rotor blade can meet the matching condition for both domains. In case a geometric periodicity for a sector of the full annulus does not exist, a sector being closest to a geometric periodicity may be used based on the best judgement.

When the rotor blades are rotating, their meshes are moving with the blades. If the circumferential distance of the grid moved is small such as less than half of the circumferential grid interval, the one-to-one connected grids will remain connected to the same grid points. When the circumferential distance of the grid moved is large such as greater than half of the grid interval, the connection will switch to the next grid point that is closer so that all the grid points remain one-to-one connected without high mesh skewness as illustrated in Fig. 6.3. In this way, one-to-one mesh system can completely avoid interpolation error in a conservative manner. This process keeps being repeated in the rotor-stator sliding interface during the calculation.

Even though this method allows us to choose arbitrary physical time step (Δt) that determines the circumferential moving distance during rotor mesh sliding, it is desirable

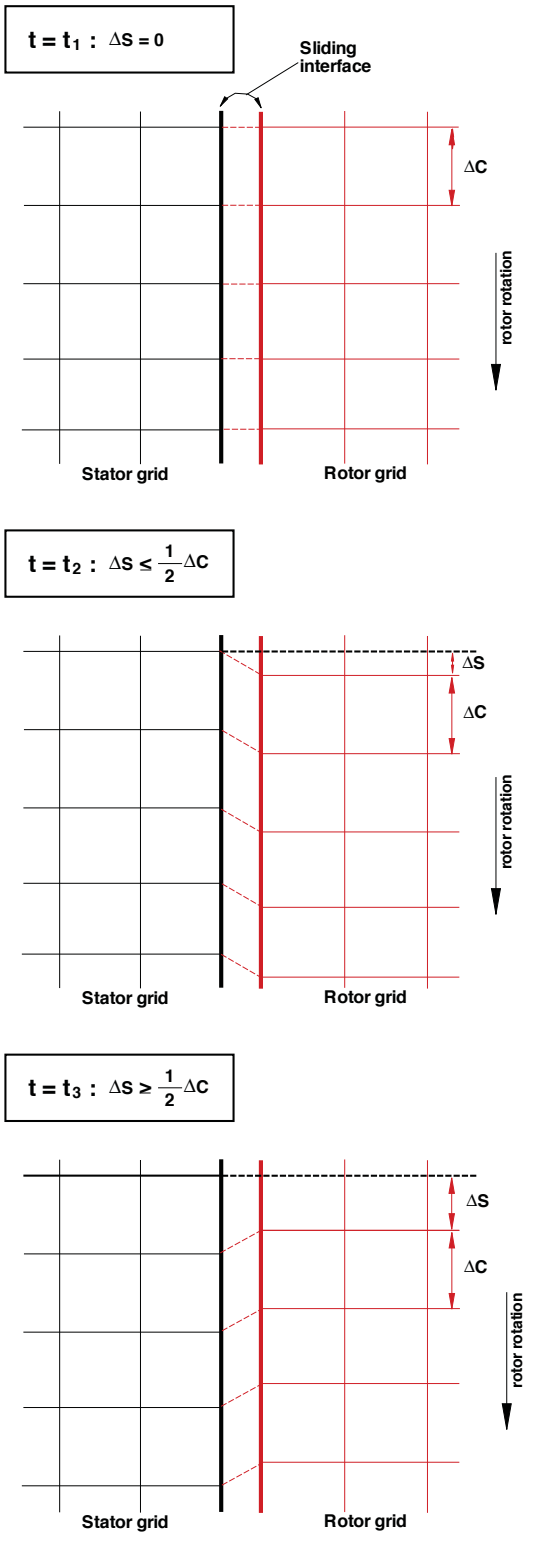

Figure 6.3: Exchange rule for one-to-one mesh based rotor/stator sliding BC, where ΔC is the half mesh interval in circumferential direction

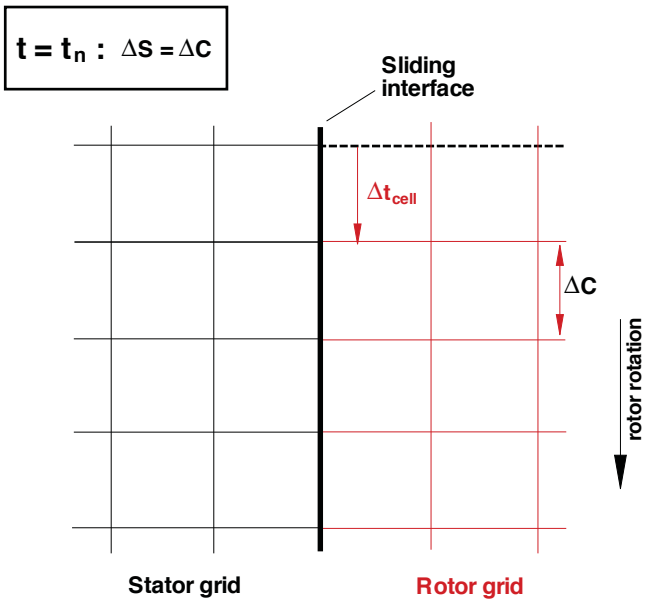

Figure 6.4: Perfectly matched one-to-one mesh sliding system like rubik's cube due to use of Δt_{cell} as unsteady physical time step

to use a physical time step (Δt_{cell}) that moves the rotor a distance exactly equal to the circumferential grid interval. This will ensure the mesh always slides in a perfectly matched system like rubik's cube as depicted in Fig.6.4. Δt_{cell} can be calculated as

$$\Delta t_{cell} = \frac{60}{RPM \times N_M} \frac{V_\infty}{L} = \frac{2\pi}{R_o \times N_M} \tag{6.21}$$

where R_o is Rossby number and N_M denotes total number of grid cells in the rotor rotational direction.

As illustrated in Fig. 6.5, assuming the rotor domain is rotated by two cells from the initial position, then cell 3 to 11 on the rotor side and cell 1 to 9 on the stator side are matched and exchanged. However, cell 1 and 2 of the rotor domain and cell 10 and 11 of the stator domain will have no halo cells for data exchange. Therefore, we define the exchange array

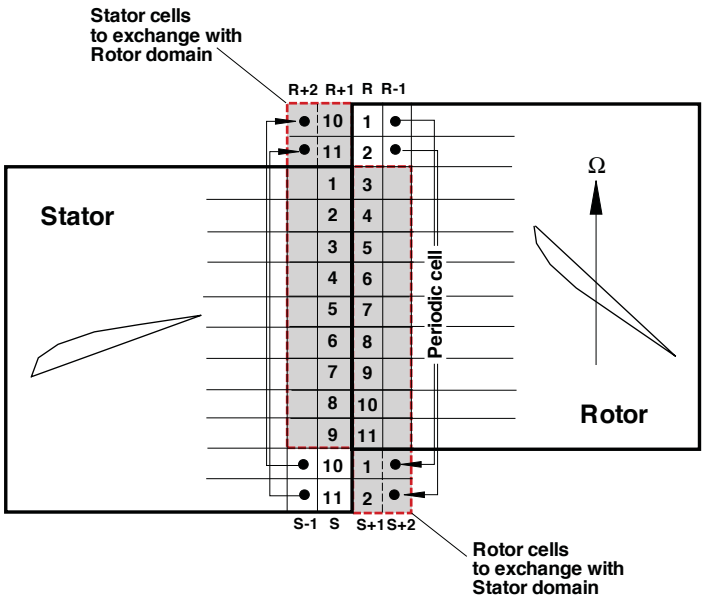

Figure 6.5: Rotor/stator interface exchange algorithm

of those cells using a periodic rotation rule under the condition that the circumferential boundaries are a nodal diameter boundary. For instance, rotor cell 1 and 2 are rotated by an angle(ϕ) and are exchanged with the stator cell 10 and 11. We employ the conservative cell exchange technique to reduce the computational efforts and to fully conserve the fluxes across the sliding interface. When Δt is large and the rotor mesh sliding distance is hence also large, more pseudo time steps are usually needed to reduce the residual.

Conservation of mass flux through the sliding interface is inspected for a GE axial compressor study in this thesis. Fig. 6.6 shows instant spanwise distributions of circumferentially averaged mass flux ρV_x at sliding interfaces. Fig. 6.7 instant circumferential distributions of mass flux ρV_x at 50% span of sliding interfaces. The present sliding BC fully satisfies mass flux conservation at the IGV/rotor and the rotor/stator interface.

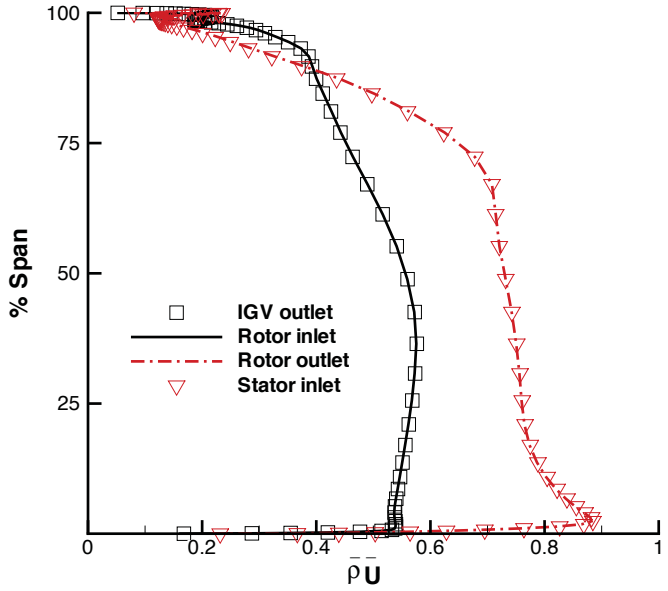

Figure 6.6: Instantaneous spanwise distributions of circumferentially averaged normalized mass flux $\bar{\rho}\bar{U}$ at sliding interfaces of a GE axial compressor predicted by fully conservative sliding BC

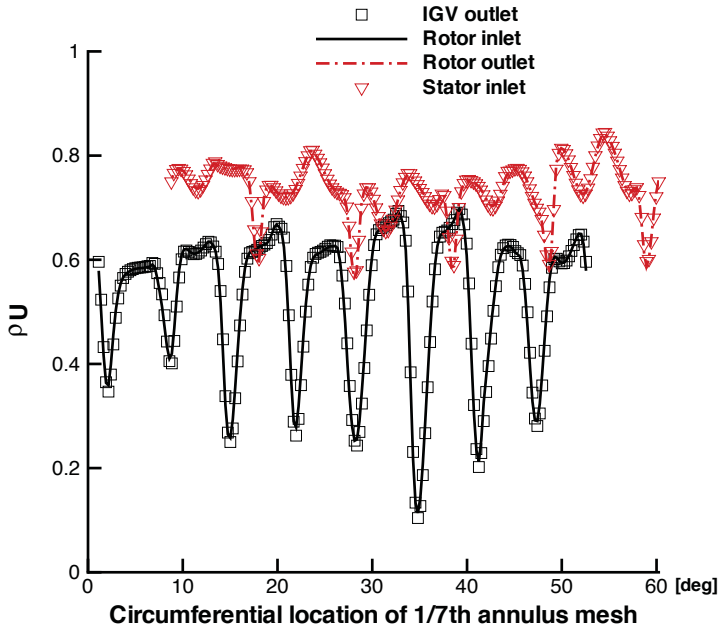

Figure 6.7: Instantaneous circumferential distributions of normalized mass flux ρU at 50% span of sliding interfaces of a GE axial compressor predicted by fully conservative sliding BC

6.8 Rotor/Stator Sliding BC Using Interpolation

To reduce the restriction of the mesh generation with one-to-one point connected at the sliding boundary for the conservative sliding boundary of unsteady multistage simulation, an interpolation rotor/stator sliding BC is developed to handle the arbitrary mesh on the two sides of the sliding boundary in the circumferential direction only. To minimize the flux losses due to interpolation, increase in the mesh size in the θ-direction is desirable and use of matched mesh in the radial direction adopted in this thesis is also highly desirable.

Fig. 6.8 shows a computational mesh for unsteady rotor/stator sliding CFD where the mesh points at the interface are not one-to-one point connected. Linear interpolation is used to obtain the data between the rotor/stator as illustrated in Fig .6.9. In practice this method can be a good option for engineers for its simplicity to use. However, the computation will suffer a small penalty since the fluxes across the sliding BC will not be conservative. The loss of accuracy is usually very small and acceptable as to be shown below. Note that linear interpolation is used instead of spline interpolation since the latter can create large oscillation at discontinuities such as shock waves. More accurate interpolation should employ the WENO technique to avoid crossing the shock discontinuities.

The algorithm developed for the rotor/stator sliding BC is sketched in Fig. 6.10. The block S1, S2 and S3 are the stator side domains and R1 and R2 are the rotor side domains. Block S1 consists of S1-A and S1-B. S1-B is located at the overlap zone ($\varphi - \alpha$) when the rotor is rotated by α. Block R2 also consists of R2-A and R2-B. R2-A is within the overlap zone.

The detailed procedure of the interpolation sliding BC is given as follows;

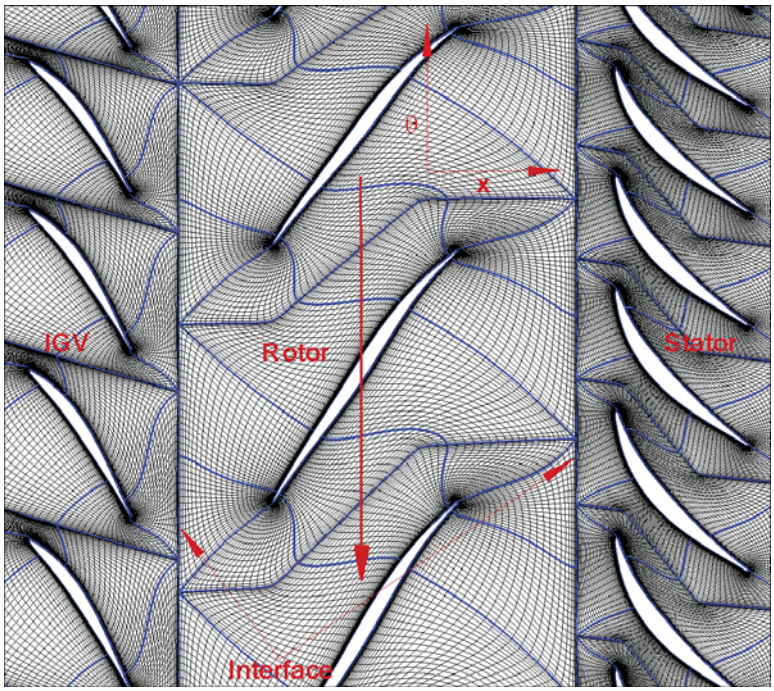

Figure 6.8: Non matching grid multi-block mesh for rotor/stator sliding simulation

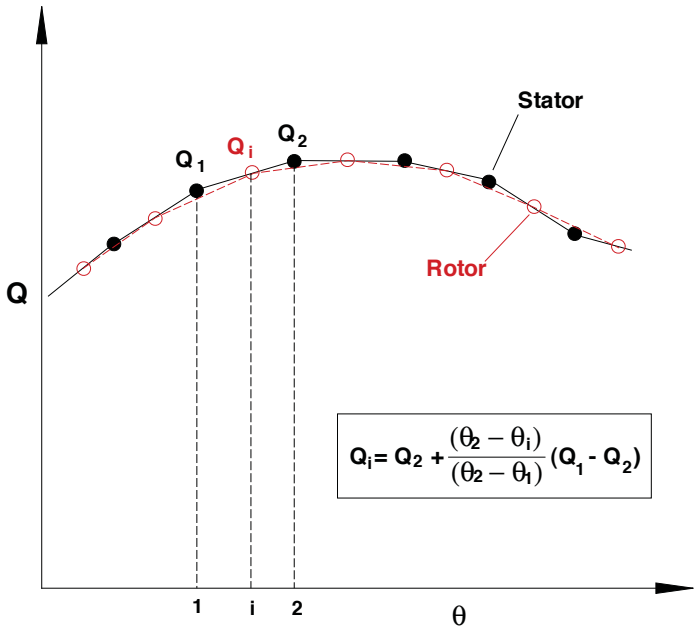

Figure 6.9: Linear interpolation between rotor/stator sliding interface

1) To find the overlap zone boundary between S1-A and S1-B and between R2-A and R2-B using interpolation according to an angle, α.

2) To apply the exchange relations given in Eq. (6.20) prior to MPI (Message Passing Interface) process such that the constructed halo cell layers are in the same frame of reference.

3) To construct the rotor/stator hallo cell layers using interpolation. Note that the number of exchange halo cell layers are determined by the spatial order of the schemes used. For example, two layers are needed for 5th order WENO scheme. Since S1-A in stator domain and R2-B in rotor domain will have no halo cells for interpolation, the stator/rotor inner domain blocks in non-overlapped zone are exchanged using the periodic rotation rule under the condition that the circumferential boundaries are a nodal diameter boundary. For example, the data of stator block S1-A is exchanged with rotor block R2-B.

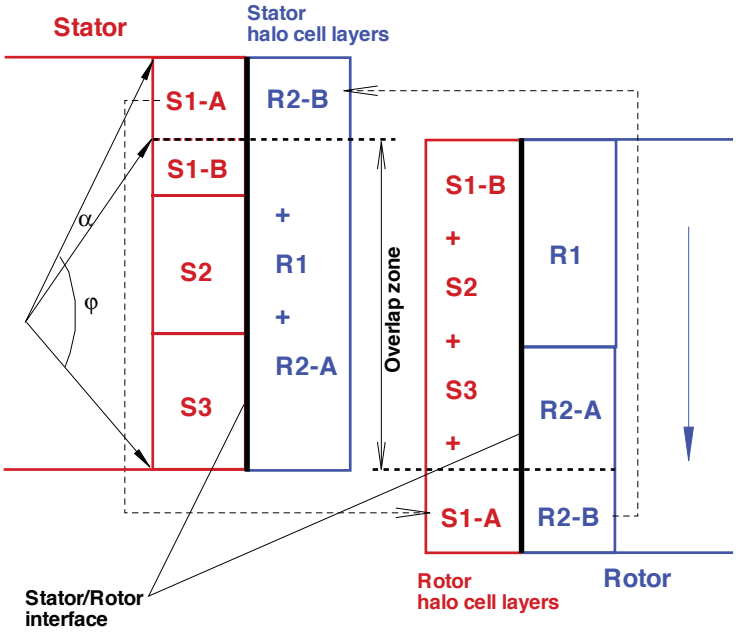

Figure 6.10: Rotor/stator interface exchange algorithm using interpolation

Fig. 6.11 shows instantaneous spanwise distributions of circumferentially averaged mass flux ρV_x at the IGV/rotor interface predicted by interpolation sliding BC. Fig. 6.12 instant circumferential distributions of mass flux ρV_x at 50% and 90% span of the IGV/rotor interface predicted by interpolation sliding BC. The mass flux is not fully conserved at the interfaces. The circumferential mesh size at the IGV side is total 160 and at the rotor side is total 200. The interpolation error can be reduced by either using similar circumferential mesh size at interface or applying high order interpolation techniques that can avoid crossing the shock discontinuities. Fig. 6.13 show entropy contour of mid span of GE 1-1/2 stage compressor predicted by interpolation sliding BC. Despite of small flux deviation at interface, the wakes at the IGV/rotor and rotor/stator travel interface without cut-off.

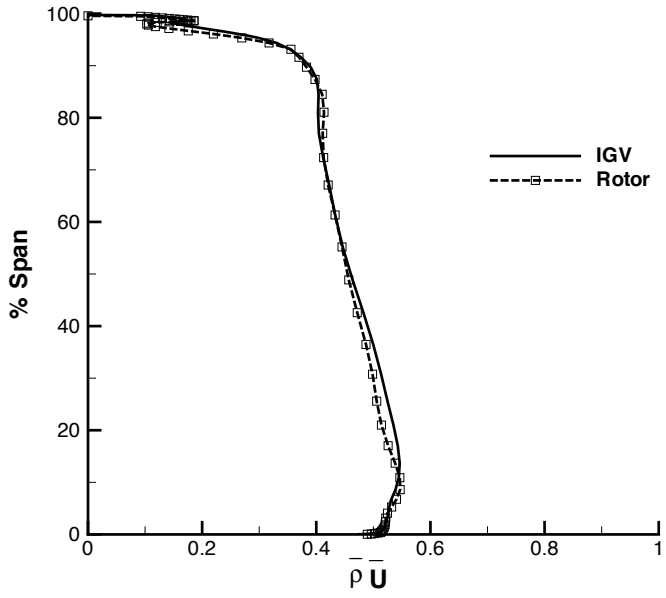

Figure 6.11: Instantaneous spanwise distributions of circumferentially averaged normalized mass flux $\bar{\rho}\bar{U}$ at sliding interfaces of a GE axial compressor predicted by interpolation sliding BC

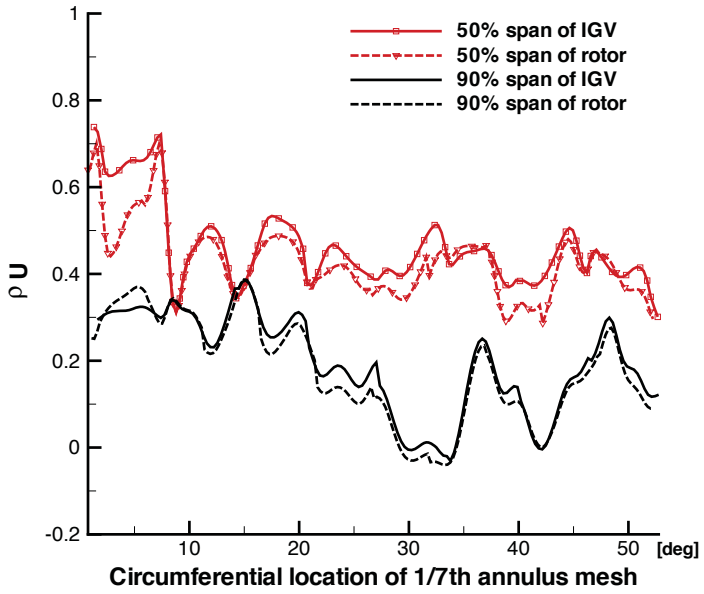

Figure 6.12: Instantaneous circumferential distributions of normalized mass flux ρU at 50% and 90% span of sliding interfaces of a GE axial compressor predicted by interpolation sliding BC

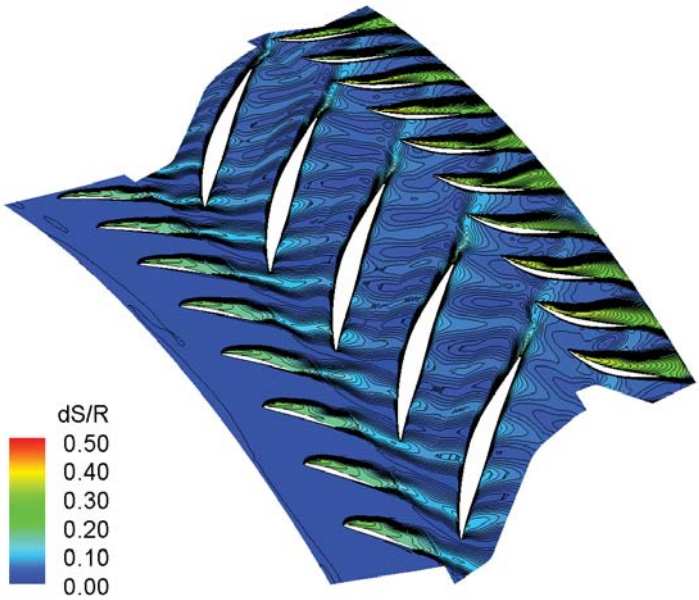

Figure 6.13: Entropy of 50% span predicted by the interpolation rotor/stator sliding BC

6.9 Phase-lagged Boundary Conditions

For turbomachinery, each blade is subjected to unsteadiness due to the phase difference. Hence, a boundary condition needs to be setup on the circumferential boundaries of a sector of the annulus in order to avoid calculation of full annulus. Two phase-lagged boundary conditions, the Fourier series phase lag (FSPL) and time shifted phase lag (TSPL), are implemented by assuming that the phase-shifted periodicity exits at upper and lower circumferential boundaries.

6.9.1 Fourier Series Phase Lag - FSPL

For the Fourier phase lag BC for a sector of annulus simulation, the variation in fluid properties over an oscillation cycle is decomposed into its Fourier coefficients and only the coefficients are stored to update the variables. Since the present solver uses the ghost cell approach at boundaries as sketched in Fig.6.14, the Cell *GL*(ghost cell of the lower periodic boundary) corresponds to the cell *IU*(inner cell of the upper periodic boundary), and vice versa for the cell *GU* and the cell *IL*. Nodal diameter N_D represents the radial lines with zero displacements.

To apply high order schemes in the same manner as inner computational domain, at leat two ghost cells are used for both Fourier and time shifted phase lag boundary conditions. One can write a N^{th} order timewise Fourier series for the conservative variable vector(Q) if the rotor rotates from the lower to the upper boundary with the inter blade phase angle(φ)

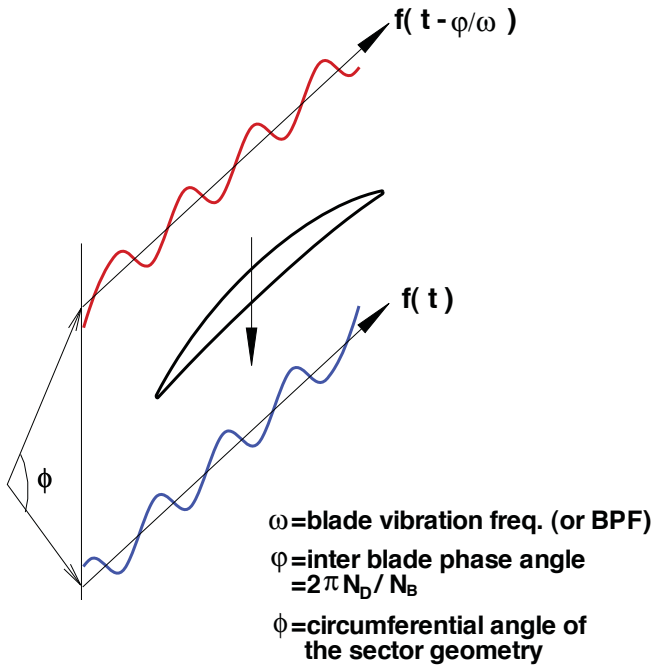

Figure 6.14: Sketch of the blade phase angle difference

as

$$Q_{GL(x,t)} = \bar{Q}_{IU(x)} + \sum_{n=1}^{N} [An_{IU} \cdot sin[n(\omega t + \varphi)] + Bn_{IU} \cdot cos[n(\omega t + \varphi)]] \tag{6.22}$$

$$Q_{GU(x,t)} = \bar{Q}_{IL(x)} + \sum_{n=1}^{N} [An_{IL} \cdot sin[n(\omega t - \varphi)] + Bn_{IL} \cdot cos[n(\omega t - \varphi)]] \tag{6.23}$$

where

$$\bar{Q}_{IL(x)} = \frac{1}{T} \sum_{j=1}^{NP} Q(t)_{IL} \Delta t \tag{6.24}$$

$$\bar{Q}_{IU(x)} = \frac{1}{T} \sum_{j=1}^{NP} Q(t)_{IU} \Delta t \tag{6.25}$$

$$An_{IL} = \frac{\omega}{2\pi} \sum_{j=1}^{NP} Q(t)_{IL} \cdot sin(n\omega t)\Delta t \tag{6.26}$$

$$An_{IU} = \frac{\omega}{2\pi} \sum_{j=1}^{NP} Q(t)_{IU} \cdot sin(n\omega t)\Delta t \tag{6.27}$$

$$Bn_{IL} = \frac{\omega}{2\pi} \sum_{j=1}^{NP} Q(t)_{IL} \cdot cos(n\omega t)\Delta t \tag{6.28}$$

$$Bn_{IU} = \frac{\omega}{2\pi} \sum_{j=1}^{NP} Q(t)_{IU} \cdot cos(n\omega t)\Delta t \tag{6.29}$$

where $\bar{}$ denotes a time-averaged variables, $\omega(=2\pi/T)$ is the blade vibration frequency(or blade passing frequency), T is the oscillation period, n is the harmonic number, N is the total number of the harmonics used in the phase lag BC, and $NP(=T/\Delta t)$ is the number of steps taken over one oscillation cycle.

The Fourier coefficients are calculated over one time period using an approximate integral technique, the trapezoidal rule. This means these coefficients are lagged by one cycle and no coefficient is available for the first cycle. For the first vibration cycle the upper and lower boundaries are considered periodic, and hence one can update the Fourier coefficients every period after the second cycle. Note that this phase lag BC implemented includes inherently the nonlinear interactions between the time-averaged flow and the unsteady disturbances [55].

6.9.2 Time Shifted Phase Lag - TSPL

The time shifted phase lag (TSPL) BC, also called direct store phase lag BC, suggested by Erods et al. [33] and Srivastava et al. [56] based on phase periodicity with the period

as nodal diameter is utilized. The TSPL BC is selected for this study for its advantage that it does not need to input the primary perturbation or vibration frequencies required by the Fourier phase lag BC [135]. Such frequencies are not known *a priori*. In other words, the TSPL BC is more general than the Fourier phase lag BC, but still limited to the circumferential periodicity assumption, which does not exist when a rotating stall occurs.

As sketched in Fig. 6.15, let us assume that the rotor rotates from the upper circumferential boundary to the lower circumferential boundary such that information at the upper side is delayed by time δt. T is the period of one nodal diameter (N_D). To update the upper/lower circumferential boundaries, first the conservative variables of the upper inner cells(Q_{IU}) and the lower inner cells(Q_{IL}) are stored for δt and $T-\delta t$ respectively. Then, these stored values are rotated by the circumferential angle of the sector geometry (ϕ) to update the boundary ghost cells of the other side. The upper ghost cell Q_{GU} at time t can be updated using Q_{IL} at time $T-\delta t$. However, the lower ghost cell Q_{GL} at time t can not be updated using the upper ghost cell values since Q_{IU} at time $t+\delta t$ is not available. The way to update Q_{GL} is to take one cycle-lagged value, Q_{IU} at time $T-t+\delta t$, by assuming phase periodicity as depicted in Fig. 6.15. Note that the boundaries are treated as in-phase condition for the first cycle since the stored Q at both sides are not available.

$$Q_{GL}(t) = Q_{IU}(t+\delta t) = Q_{IU}(t-T+\delta t) \tag{6.30}$$

$$Q_{GU}(t) = Q_{IL}(t-\delta t) \tag{6.31}$$

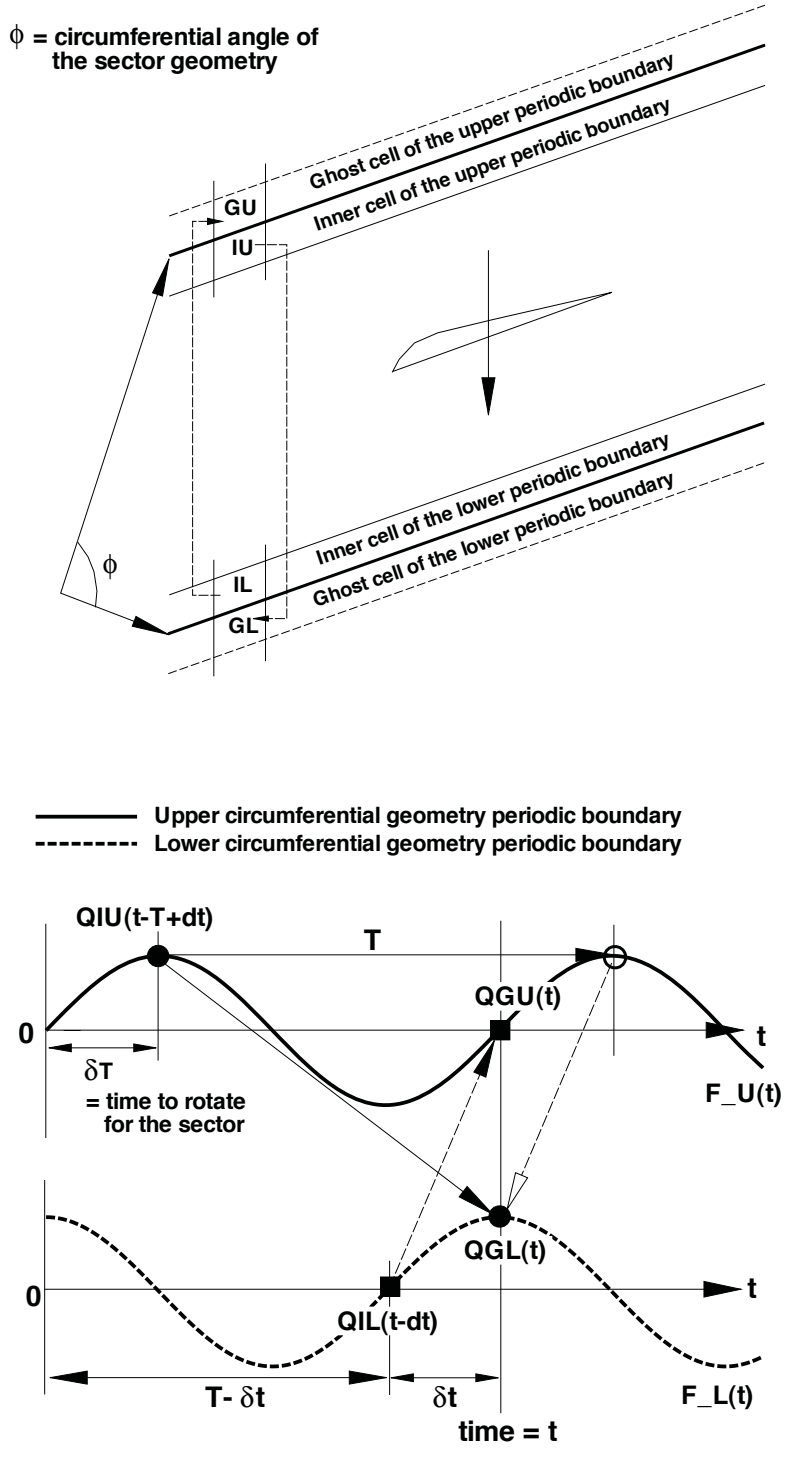

Figure 6.15: Sketch of the time shift phase lag BC showing how to define upper periodic ghost cell, Q_{GU}

Chapter 7

Deforming Mesh Generation

With the fully coupled fluid/structure interaction, a CPU efficient deforming mesh technique is one of the requisites and critical to achieve high fidelity simulation by accurately describing the vibration of the structure since initial mesh is regenerated at every pseudo time step due to the blade flutter or vibration.

7.1 Advanced Blade Tip Deforming Mesh

The conventional method as illustrated in Fig. 7.1 regenerates mesh inside domain with the fixed outer boundaries. However this may cause significant numerical instability due to the high mesh skewness when the vibrating structure is close to the boundaries like rotor tip clearance. In this study an advanced deforming mesh algorithm is developed to improve mesh quality over rotor tip clearance. The basic idea is to reposition the casing grid points followed by the rotor tip vibration (or displacements) within each pseudo time step such that the mesh near rotor tip region can keep high normality as shown in Fig. 7.2.

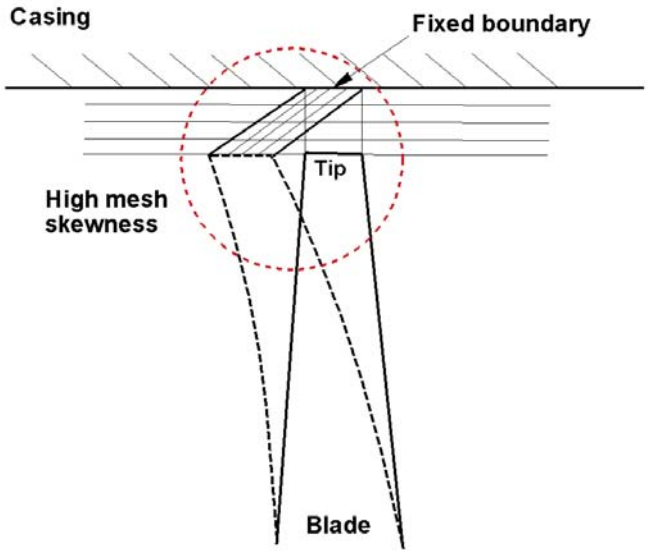

Figure 7.1: Moving mesh with fixed boundary at rotor casing

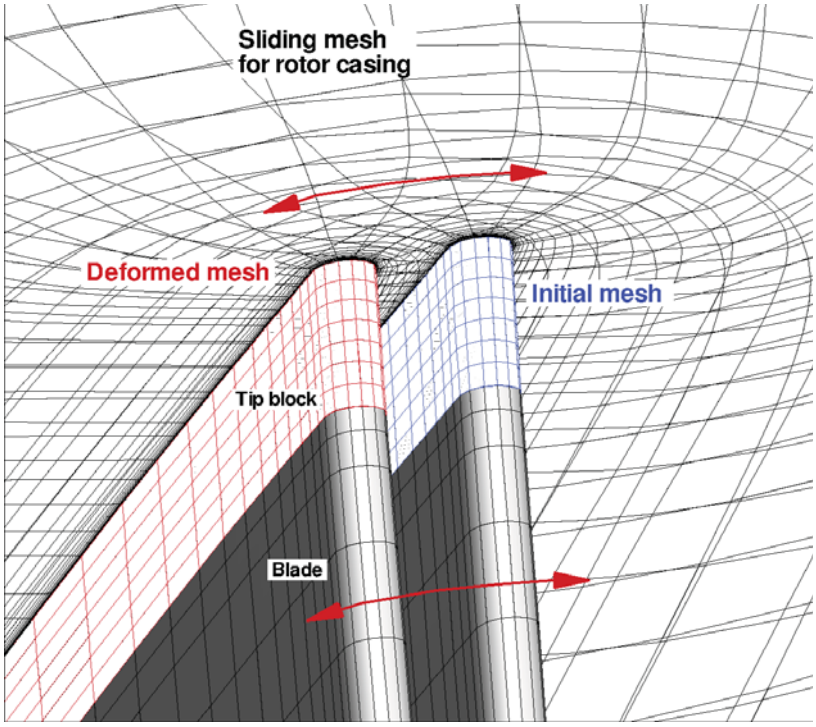

Figure 7.2: Moving mesh with sliding rotor casing

In summary, new coordinate x'_{casing} on the casing surface of the rotor tip block boundary is found using Eq. (7.1).

$$x'_{casing} = x^o_{tip} + u_{x/tip} + \Delta U_x \tag{7.1}$$

where

$$\Delta U_x = \frac{S_{casing} - S_{tip}}{S_{tip} - S_{tip-1}} (u_{x/tip} - u_{x/tip-1})$$

where x^o_{tip} represents the initial x-coordinate of rotor tip boundary. ΔU_x is the amount of displacements to be moved in the x-direction obtained by the extrapolation. The subscript, $_{tip-1}$ denotes the grid one point below of rotor tip surface. S is the distance from the rotor axis to corresponding coordinates.

Next, new radius $R'_{casing} (= \sqrt{{y'_{casing}}^2 + {z'_{casing}}^2})$ corresponding x'_{casing} is found by the interpolation of the given (x_o, R_{casing}). Finally y'_{casing} and z'_{casing} determined by Eq. (7.1) are updated using R'_{casing} as follow:

$$\begin{aligned} y'_{casing} &= R'_{casing} cos(\theta) \\ z'_{casing} &= R'_{casing} sin(\theta) \end{aligned} \tag{7.2}$$

where

$$\theta = tan^{-1}(\frac{z^o_{casing}}{y^o_{casing}})$$

The rest of casing surface mesh is then regenerated using an efficient blade deforming mesh algorithm developed by borrowing an idea suggested by Chen et al. [24]. Again the rest of the casing grid points are projected toward the given (x_o, R_{casing}) to make sure all new points be placed on the design casing surface.

7.2 Blade Passage Deforming Mesh Generation

The deforming mesh generation for the blade passage is briefly described. The initial mesh point on the blade surface is $p1$ and the deformed position is $p2$. Then, the displacement vector $(\delta x_1, \delta y_1, \delta z_1)$ is determined. To elongate the deformed mesh by the same grid stretching ratio as initial mesh, the length of each segment (S_j) along the initial mesh line is determined as

$$S_j = S_{j-1} + \sqrt{(x_j - x_{j-1})^2 + (y_j - y_{j-1})^2 + (z_j - z_{j-1})^2} \tag{7.3}$$

Then, the amount of relative displacement at each node due to the blade motion, $\delta x_j, \delta y_j, \delta z_j$, can be estimated by the linear interpolation using the displacements of the blade surface($j = 1$) and the outer boundary($j = jend$) as shown in Fig. 7.3.

$$x_j = \frac{x_{jend} - x_1}{s_{jend} - s_1} s_j + \frac{x_1 \cdot s_{jend} - x_{jend} \cdot s_1}{s_{jend} - s_1} \tag{7.4}$$

$$y_j = \frac{y_{jend} - y_1}{s_{jend} - s_1} s_j + \frac{y_1 \cdot s_{jend} - y_{jend} \cdot s_1}{s_{jend} - s_1} \tag{7.5}$$

$$z_j = \frac{z_{jend} - z_1}{s_{jend} - s_1} s_j + \frac{z_1 \cdot s_{jend} - z_{jend} \cdot s_1}{s_{jend} - s_1} \tag{7.6}$$

Once the casing surface is obtained, regeneration of inner mesh is straightforward. The deformed mesh of a blade-to-blade surface is first obtained, and radially stacked from the blade hub to the casing. The mesh near blade is simply moved with the blade surface. This

algorithm was tested for a blade-to-blade section as shown in Fig. 7.4. This moving mesh method works robustly for large deformations as well.

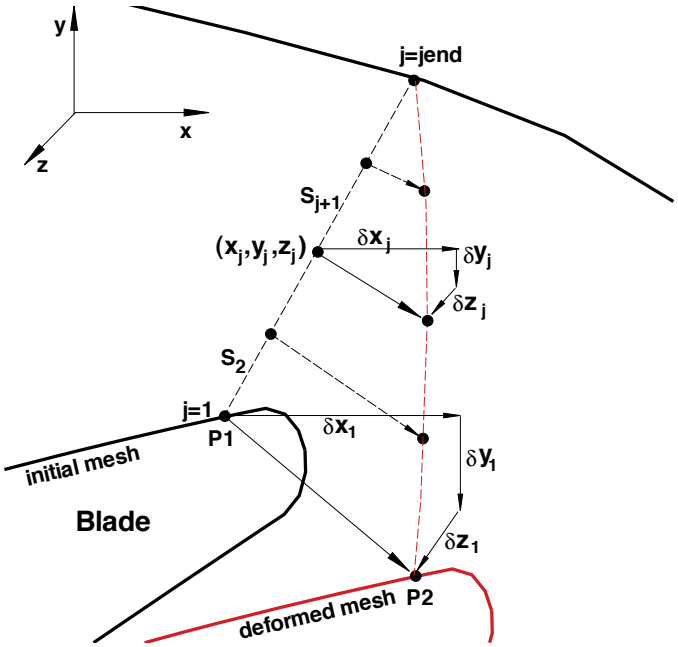

Figure 7.3: Test of the spring mesh system for a blade-to-blade section

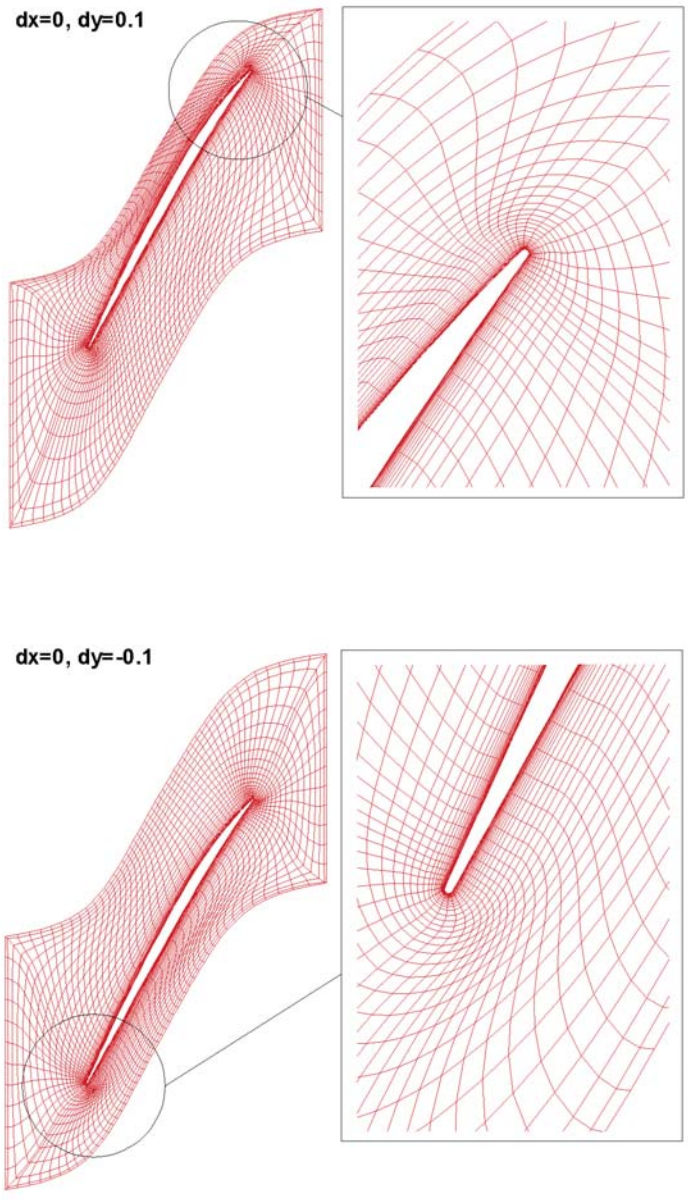

Figure 7.4: Test of the spring mesh system for a blade-to-blade section

Chapter 8

Validation Study

To validate the high fidelity numerical methodologies for turbomachinery aeromechanical simulation developed through this study, the comprehensive application problems are solved. First, the delayed detached eddy simulation of turbulence is validated for an airfoil stalled flow at a large angle of attack. In addition, a 3D wing supersonic flutter boundary is predicted using the fully coupled fluid/structure interaction with the validated high fidelity delayed detached eddy simulation of turbulence.

For turbomachinery validation, NASA Rotor 37, 67, and Stage 35 are chosen for validation models since the experimental data such as rotor speedline data, radial profiles of total pressure, total temperature, adiabatic efficiency and flow angles are available. To validate basic turbomachinery capabilities including turbomachinery inlet/outlet and the wall function boundary conditions, NASA Rotor 37 and 67 computations are first conducted using RANS for the full speedline conditions from choke to near stall. The capability of DES for turbomachinery simulation is proved by solving rotating stall inception for the full annulus NASA Rotor 67. The fully coupled fluid-structure interaction with advanced moving mesh

algorithm, which is developed for turbomachinery blade flutter, is used to simulate NASA Rotor 67 stall flutter behavior.

The mixing plane approach developed for 3D multistage turbomachinery steady simulation is verified for NASA Stage 35 full speedline. GE 1-1/2 stage aircraft engine axial compressor with inlet guide vane is also simulated at a design condition to validate the mixing plane boundary condition and the fully conservative unsteady rotor/stator sliding boundary condition by the comparison of current prediction with design data provided. Finally, two phase lag boundary conditions developed for a sector of annulus turbomachinery flutter and NSV simulation are validated for NASA Rotor 67 flutter at peak condition and the verification is achieved based on the comparison with the full annulus flutter simulation.

8.1 DES of Airfoil Stalled Flows

The experimental data of lift and drag are available for NACA0012, the stall flow simulations for NACA0012 are carried out at 45° angle of attack. Since airfoil stall at a large angle of attack is flow instability typically associated with massive separation, it is a big challenge for most of CFD researchers relying on RANS approaches to predict accurately the stall flow characteristics. The large stall vortex structures are formed around airfoil leading edge and travel along the airfoil suction surface as they grow, and finally get separated from the airfoil surface near the trailing edge. When airfoil stall happens, the aircraft may lose lift and serious consequence may occur. Hence accurate prediction of airfoil stall is very important to determine the flight envelop of aircraft.

This validation study employs the 5th order low diffusion WENO shock capturing scheme and 4th order central differencing scheme recently developed in our group [101–

103, 120]. The purposes of this validation are two-folds: 1) Apply the aforementioned new high order schemes to DDES and demonstrate their performance, 2) Demonstrate the DDES advantages over RANS model for airfoil stalled flow with massive separation.

8.1.1 Boundary Conditions

Steady state freestream conditions are used for the upstream portion of the outer boundary. For downstream boundary, the static pressure was specified as freestream value, and the streamwise gradients of other variables were forced to vanish. The periodic boundary condition is used in spanwise direction. The wall treatment suggested in [102] to achieve flux conservation by shifting half interval of the mesh on the wall is employed. If the wall surface normal direction is in η-direction, the no slip condition is enforced on the surface by computing the wall flux $F_{1/2}$ in the following manner:

$$\mathbf{F_w} = \begin{pmatrix} \rho V \\ \rho uV + p\eta_x \\ \rho vV + p\eta_y \\ \rho wV + p\eta_z \\ (\rho e + p)V \end{pmatrix}_w = \begin{pmatrix} 0 \\ p\eta_x \\ p\eta_y \\ p\eta_z \\ 0 \end{pmatrix}_w \tag{8.1}$$

A third-order accuracy wall boundary formula is used to evaluate $p|_w$,

$$p_w = \frac{1}{6}(11p_1 - 7p_2 + 2p_3) \tag{8.2}$$

8.1.2 3D Flat Plate Boundary Layer

The validation of the DDES in this paper for a thin flat plate boundary layer is conducted in the same manner as done by Spalart et al. [37].

Fig. 8.1 shows the coarse mesh constructed to have 91 grid points in the x-direction(parallel to the wall), 81 grid points in the y-direction(normal to the wall), and 6 grid point in the z-direction(tangential to the wall). The size of the refined mesh is $301 \times 121 \times 6$ as shown in Fig. 8.2.

The Reynolds number of 6.5×10^6 and Mach number (M) of 0.1 are used. The coarse mesh is constructed to have streamwise grid spacing, $\Delta_{\|}$ (or Δx for the present 3D flat plate) of $0.033L$, which is about 2 times larger than the turbulent boundary layer thickness. In this study, using $\delta = 0.37(Re_L)^{-0.2}L$ [136], δ of $0.016L$ is obtained. Δx of the fine mesh for MSD test section is $0.00417L$, which is about 26% of the boundary layer thickness. For the fine mesh, the test section length L has 201 mesh points in the x-direction. Both the coarse grid and the fine grid have the dimensionless distance y^+ given by Eq. (8.3) less than unity. The coarse grid used in this study corresponds to the natural grid, and the fine mesh is a severe grid that can cause the MSD as indicated by Spalart et al. [37].

$$y^+ = Re\frac{u_\tau y}{\nu} = Re\sqrt{\frac{\tau_w}{\rho}}\frac{y}{\nu} \tag{8.3}$$

where

$$\tau_w = \frac{1}{Re}\mu\left(\frac{\partial U}{\partial y}\right)_w \tag{8.4}$$

Fig. 8.3 shows the turbulent boundary layer profiles computed by the S-A model [114],

the DES and the DDES using the coarse mesh. Good agreements with the law of the wall including the logarithmic overlap layer are achieved with the fine mesh. Fig. 8.4 shows the results from the fine mesh. The DES predicts a large velocity deviation from the law of the wall near the boundary layer edge, whereas the DDES and RANS model accurately predict the law of the wall (equation 6.15).

In Fig. 8.5 the predicted velocity profile ratio ($\frac{u}{V_\infty}$) and the turbulent eddy viscosity ($0.002\frac{\nu_t}{\nu}$) inside boundary layer predicted by the URANS and the DES using the fine mesh, are compared with the MSD test results presented in [37]. Current results verify that the predicted eddy viscosity by the DES is lower by about 75% compared to the URANS, which is about the same as the MSD test results obtained by Spalart's. Consequently the wall parallel velocity outside of the logarithmic overlap layer($35 < y^+ < 350$) predicted by the DES is lower than the URANS.

As shown in Fig. 8.6, the eddy viscosity predicted by the DDES is fully preserved inside the turbulent boundary layer. Fig. 8.6 also indicates that f_d is behaved as intended to be 1 in the LES region outside of the boundary layer and 0 elsewhere such that the DDES model can preserve the RANS mode inside boundary layer to prevent the MSD problem. All these results show that the hybrid RANS/LES approach, DDES, is correctly implemented and the DDES achieves the goal to remove the MSD.

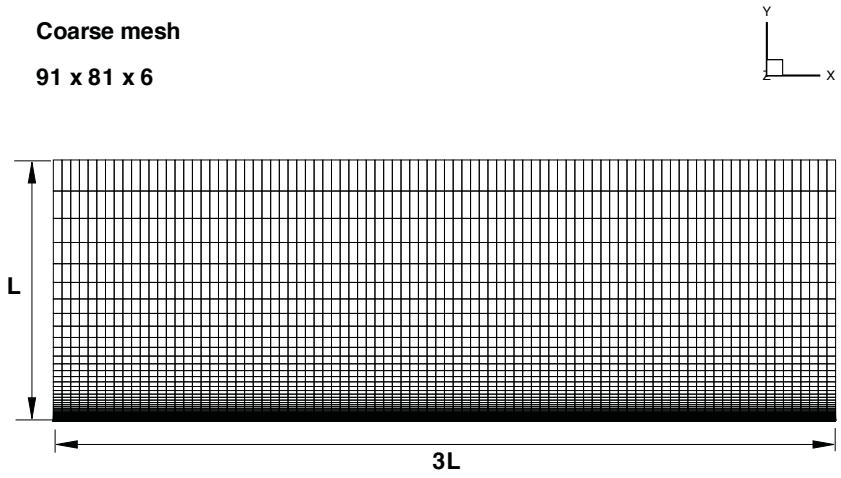

Figure 8.1: Coarse mesh for the flat plate; $\Delta x \approx \Delta z \approx 0.033L$

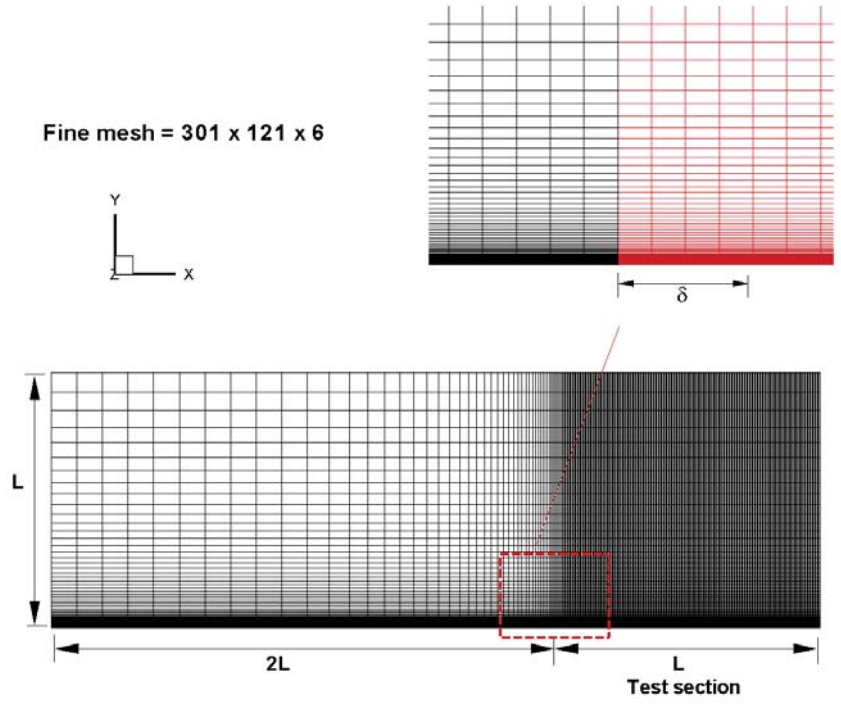

Figure 8.2: Fine mesh for the flat plate; $\Delta x \approx \Delta z \approx 0.00417L$

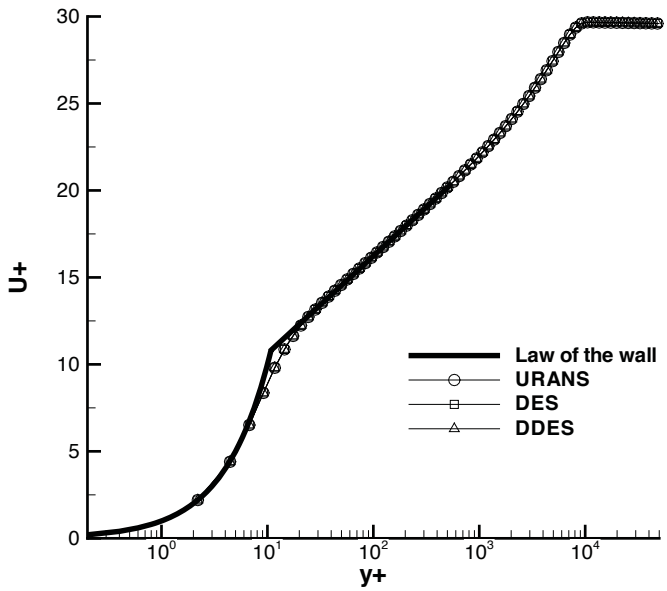

Figure 8.3: Predicted turbulent boundary layer using the coarse gird; $\Delta x = 0.033L$, $Re = 6.5 \times 10^6$, $M = 0.1$

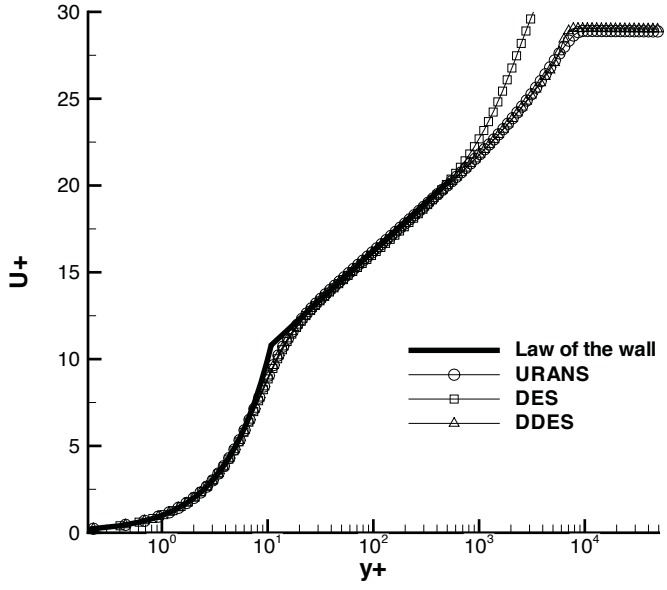

Figure 8.4: Predicted turbulent boundary layer using the fine gird; $\Delta x = 0.00417L$, $Re = 6.5 \times 10^6$, $M = 0.1$

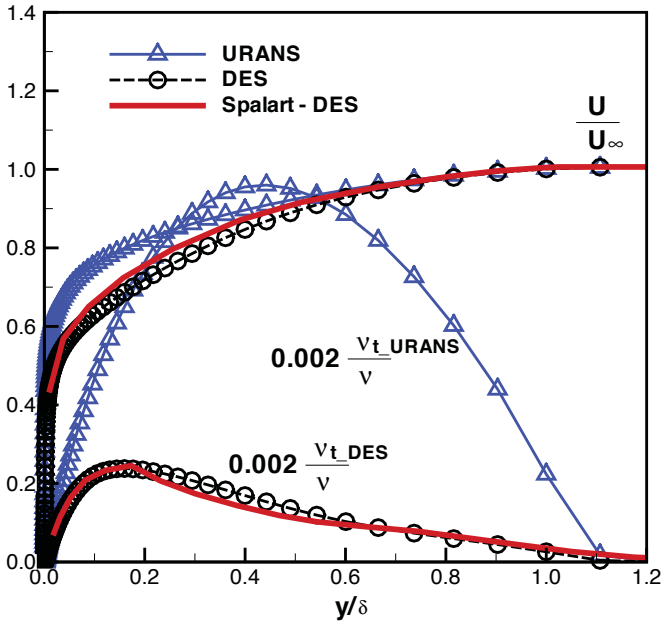

Figure 8.5: Distributions of $u/U_\infty, 0.002\frac{\nu_t}{\nu}$ in the flat plate boundary layer

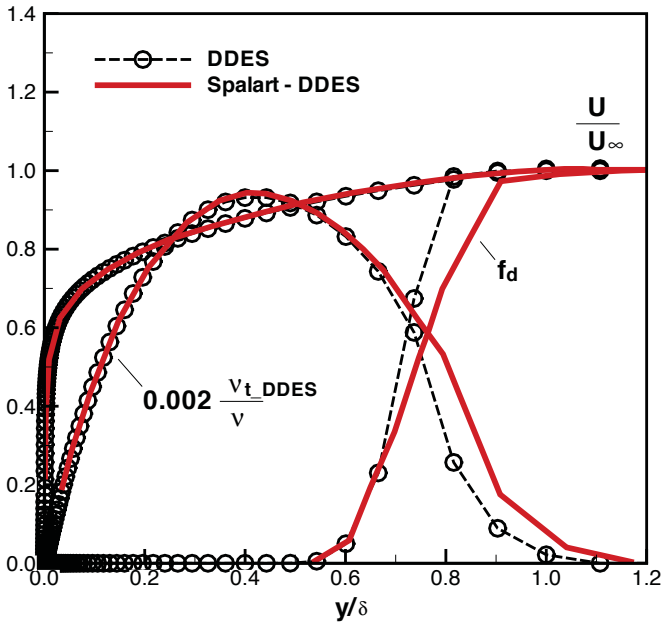

Figure 8.6: Distributions of $u/U_\infty, 0.002\frac{\nu_t}{\nu}$, and f_d in the flat plate boundary layer

8.2 URANS, DES and DDES for NACA0012 Stall Simulation

Simulation of the NACA0012 aerodynamic stall flows at 45° angle of attack is carried out to demonstrate the capability of the DES and DDES for prediction of stall flows with massive flow separation. The Reynolds number of 1.3×10^6 and Mach number of 0.5 are used based on the experiment [137, 138].

Unsteady simulation is performed over dimensionless time ($T = Chord/V_\infty$) 200 with a pseudo time CFL number of 3. The number of pseudo time steps within each physical time step is determined by having the residual reduced by at least three orders of magnitude, which is usually achieved within 60 iterations. The dimensionless physical time step of 0.02 is used.

The computational mesh for the 3D NACA0012 airfoil with the span length of one chord is first constructed using an O-mesh topology since O-grids can minimize mesh skewness near the airfoil surface. The mesh is then partitioned into 48 blocks for the parallel computing. Two different mesh sizes; mesh A and mesh B, are used for mesh refinement study. Fig. 8.7 shows mesh B that consists of 193 nodes around airfoil, 31 nodes in the spanwise direction, and 101 nodes in the direction of normal to the wall. The size of mesh A is $145 \times 81 \times 21$. The first grid spacing on airfoil surface for both mesh A and B yields y^+ less than unity. The far field boundary is located about 54 times of the airfoil chord to avoid wave reflection.

Fig .8.8 shows pseudo time step residuals for 4 physical time steps obtained by the URANS, DES and DDES. The residual levels of physical time steps are similar for the

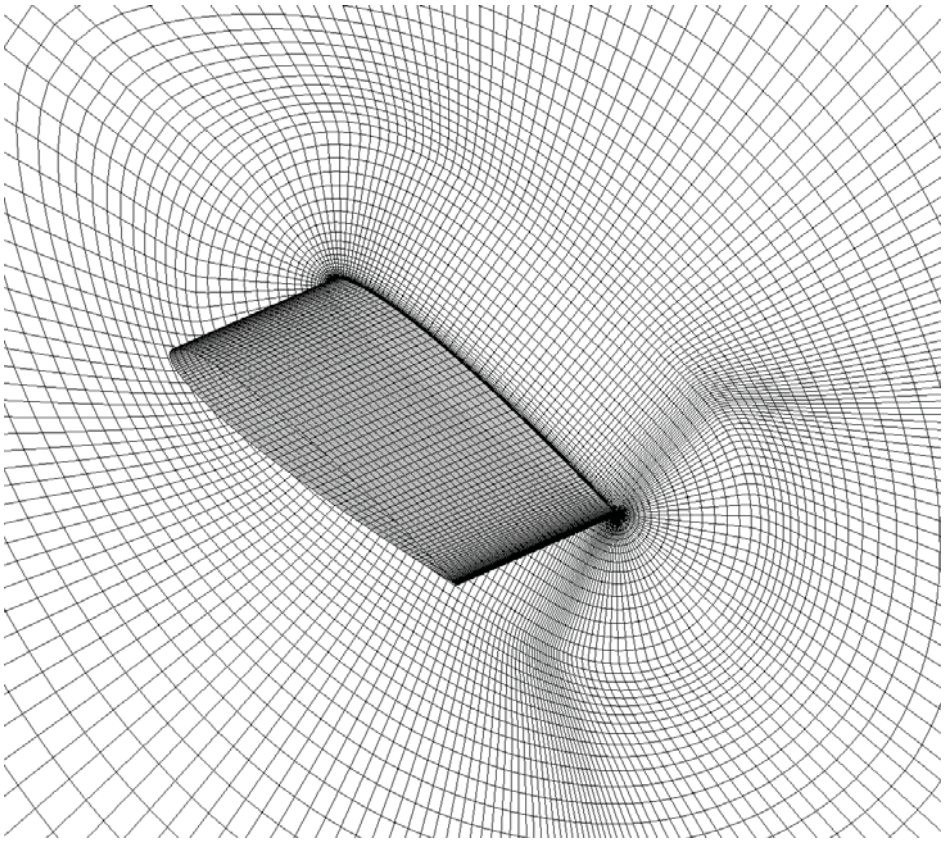

Figure 8.7: 3D mesh for NACA0012 airfoil at 45° AOA; $193 \times 101 \times 31$, $d_n = 1.0 \times 10^{-5} c$, $\Delta z/c = 0.033$

URANS, DES and DDES. However, within physical time step the detached eddy simulations show better convergence behavior than the URANS. At least four order of residual reduction is achieved roughly 15 pseudo iterations for the DES and DDES, whereas for the URANS more than 10 steps are needed compared to the DES and DDES.

Fig. 8.9 shows the fine mesh B near leading edge. The wall parallel grid spacing at the center of leading edge is $0.0028L$, which is about 7.8 times larger than the measured boundary layer thickness($\delta \approx 0.00036L$) predicted by the DES as seen in Fig. 8.10. The mesh is safe from the MSD. This mesh size explains why the DES gives similar results to the DDES for this stalled airfoil flow simulation.

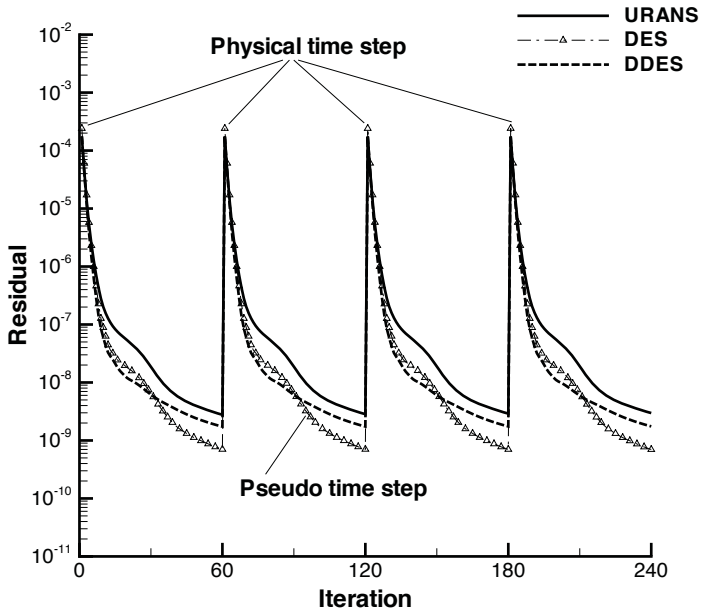

Figure 8.8: Unsteady pseudo step residual at AOA 45° from DDES, DES and URANS

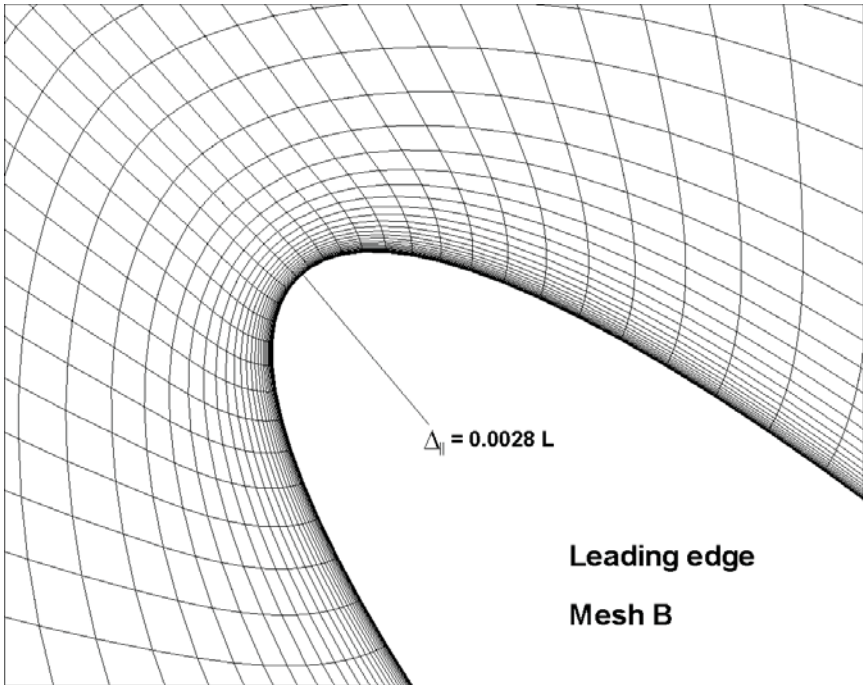

Figure 8.9: Computational Mesh near NACA0012 airfoil leading edge

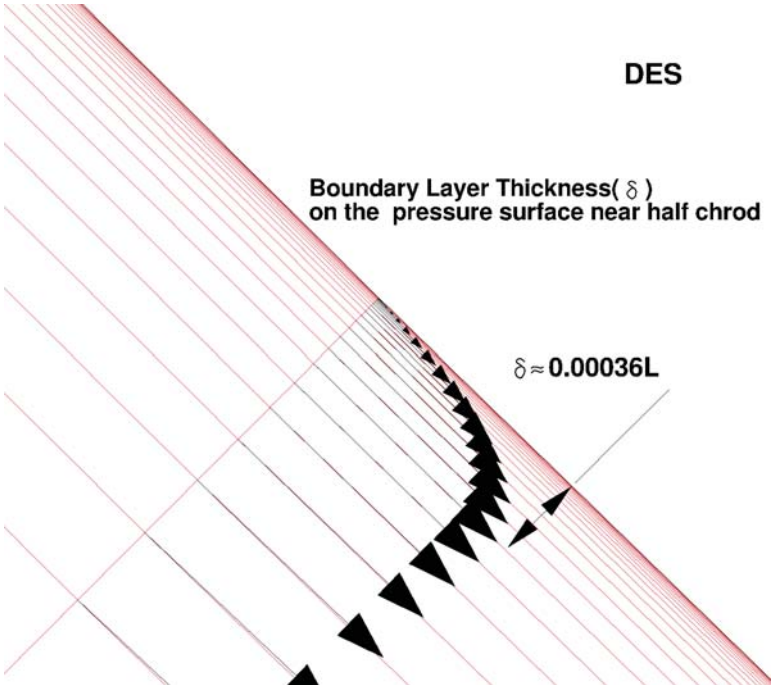

Figure 8.10: Measured boundary layer thickness(δ) on the pressure surface near half chord for the DES

The predicted instantaneous drag coefficients(C_D) by the URANS, DES, DDES and their time average are displayed in Fig. 8.11. The URANS predicts the drag in a manner of phase locked sinusoidal oscillation due to vortex shedding, while the DES and the DDES predict the drag in a more chaotic manner. The URANS, DES and DDES simulations are very well converged based on the mesh size.

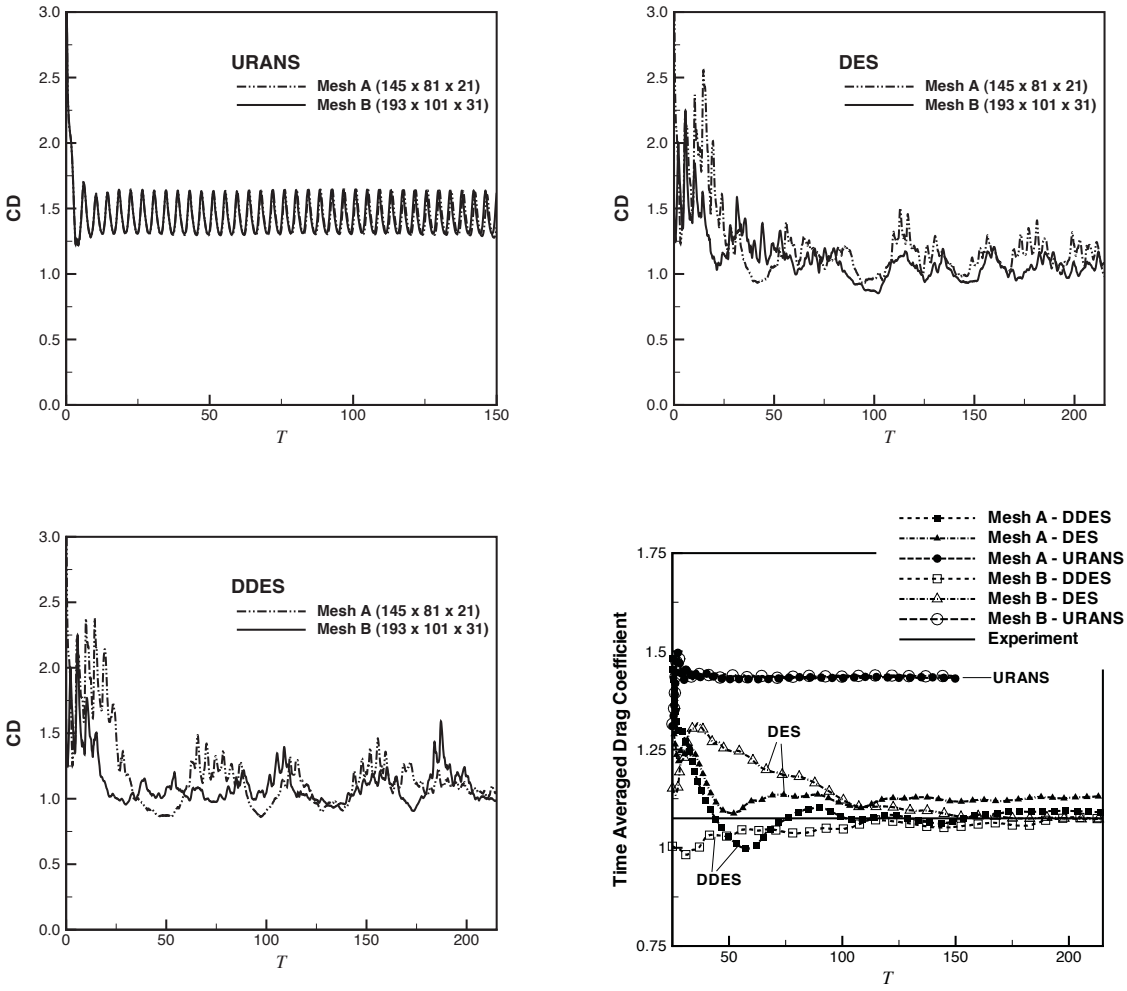

Figure 8.11: Instantaneous drag coefficients predicted by URANS (top left), DES (top right), DDES (bottom left) and time averaged drag coefficients (bottom right)

The time averaged drag and lift coefficients of the stalled NACA 0012 airfoil are compared with the experiment in table 8.1. To remove the effect of initial transitional flow,

average values were obtained from time level of 25 to over 200. The URANS overpredicts the drag by 32.15% and the lift by 31.98% for the fine mesh whereas the DES and the DDES accurately predict the drag and the lift with an error less than 0.2%, an amazingly excellent agreement. For the coarse mesh, the DDES also shows smaller errors for both the drag and the lift compared to the DES.

Table 8.1: Predicted drag(C_D) and lift(C_L) coefficients

C_D	URANS	DES	DDES	Experiment
Mesh A($145 \times 81 \times 21$)	1.387477	1.110929	1.089881	1.075
Mesh B($193 \times 101 \times 31$)	1.420658	1.074691	1.076483	
C_L	URANS	DES	DDES	Experiment
Mesh A($145 \times 81 \times 21$)	1.394412	1.117606	1.097295	1.085
Mesh B($193 \times 101 \times 31$)	1.432015	1.085730	1.086740	

Fig. 8.12 displays the instantaneous vorticity at non-dimensional time of 200 predicted by the URANS, the DES, and the DDES. For all the cases, the flow separation occurs nearly at the same location near leading edge as shown by the vorticity streaks. The URANS captures the phase locked vortex shedding that usually occurs at low Reynolds number flow, while the detached eddy simulations using the DDES and DES show more chaotic and turbulent vortical flow structures in the region of massive separation and capture many small turbulent eddies behind the airfoil.

The predicted frequency for the drag coefficients(C_D) by the URANS, the DES, and the DDES are shown in Fig. 8.13. The chord of NACA0012 studied is 24 inch model [137]. The drag coefficients between the dimensionless time $100T$ and $200T$ are used for the frequency analysis. The peak frequency for the URANS is about 68 Hz, while those of the DDES and DES are about 13 Hz. Although it is not possible to judge whether the DDES/DES or the URANS predicts the dynamic stall frequency more accurately due to

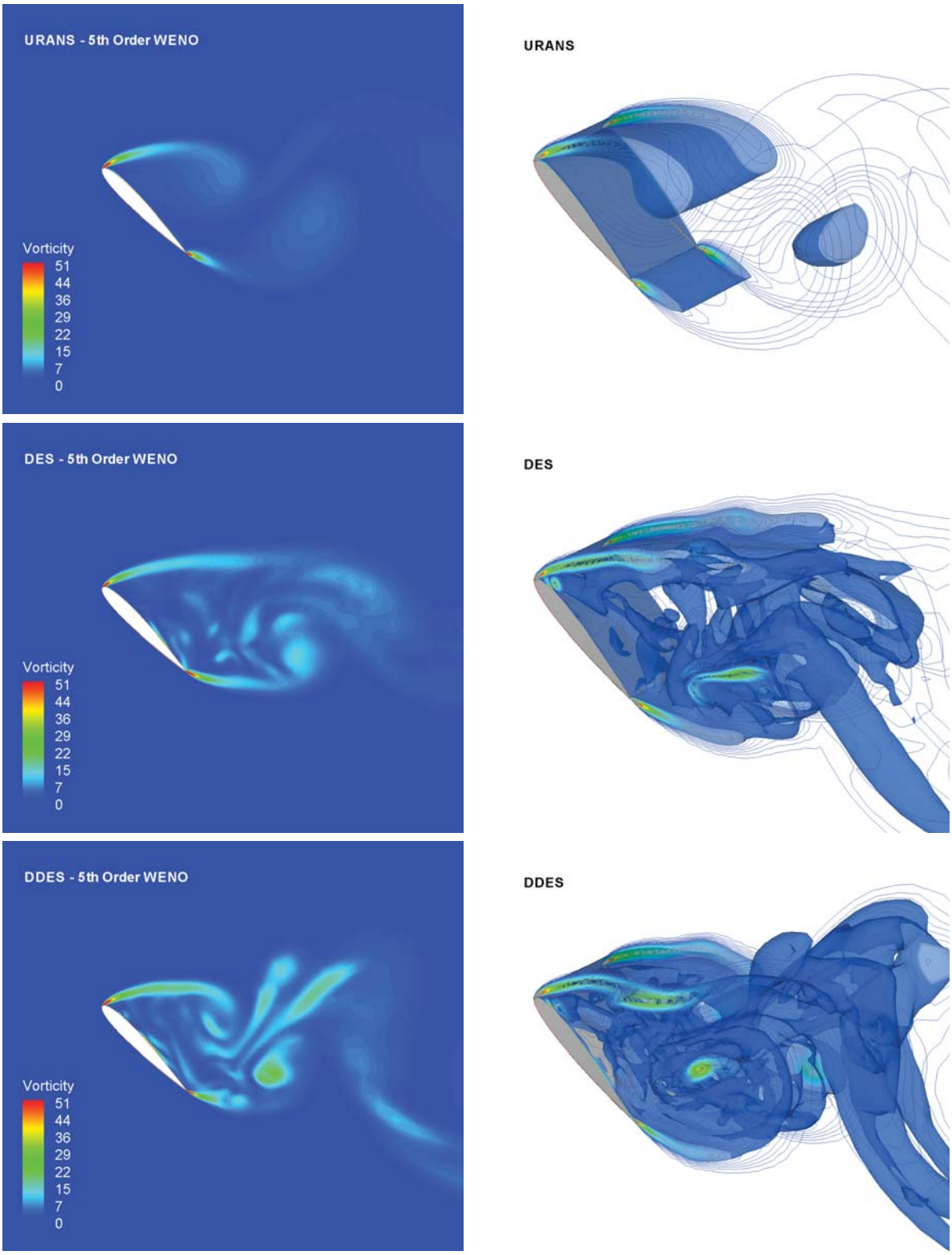

Figure 8.12: Vorticity at $T = 200$ predicted by URANS(top), DES(middle), and DDES(bottom)

lack of the measured frequencies, overall this study indicates that the URANS and DES or DDES predict the airfoil stalled flow with massive separation not just different quantitatively, but also qualitatively. The qualitative difference has a great significance. For example, the flows predicted by URANS and DES/DDES may trigger very different structural response (e.g. wing vibration) if the fluid-structural interaction is considered. The URANS may predict a phase locked sinusoidal vibration. The DES/DDES may predict a vibration with different pattern and frequency. Such difference could be fatal to diagnose and cure aeroelasticity problems of aircraft. This raises a very important question that needs to be further investigated by the research community.

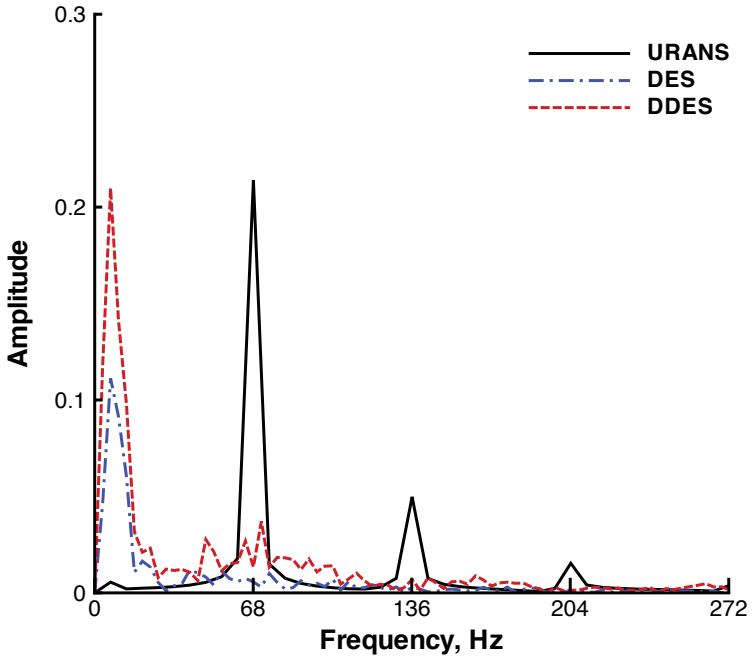

Figure 8.13: Frequency analysis for drag coefficients predicted by URANS, DES and DDES

8.3 Comparison of WENO Schemes for NACA0012 Stall Flows

At 45° AOA, the DDES with the 5th order WENO scheme for the inviscid flux and the 4th order central differencing for the viscous terms shows an excellent performance for the stalled flow prediction. For comparison, the 3rd order WENO scheme with the 2nd order central differencing is used for the stall flow simulations at four different angle of attack. For simplicity, the 3rd order WENO scheme is termed as WENO 3 and and the 5th order WENO scheme as WENO 5.

Fig. 8.14 shows the predicted residuals for a pseudo time step using high order detached eddy simulations. For WENO 5, three order reduction in pseudo residual is achieved roughly within 20 iterations for AOA 60°. WENO 3 and WENO 5 show similar convergence behavior at AOA 17°, but for AOA 60° WENO 3 converges earlier than WENO 5 by about one order.

In Fig. 8.15, the instantaneous Cp distributions on NACA0012 surface. Although the flow is massively separated behind the airfoil, WENO 3 predicts little variations in the Cp distributions on the suction surface. While the Cp on the suction surface predicted by WENO 5 shows a large fluctuation at $T = 160$. Note that no measured data for surface pressure are available, it is hard to judge which result is more accurate.

Fig. 8.16 shows surface isentropic Mach number predicted by WENO 3 and WENO 5. The isentropic Mach number (M_{is}) on the airfoil surface can be calculated by

$$M_{is} = \sqrt{\frac{2}{\gamma - 1}\left\{\left(\frac{P_{t\infty}}{P_{wall}}\right)^{\frac{\gamma-1}{\gamma}} - 1\right\}} \tag{8.5}$$

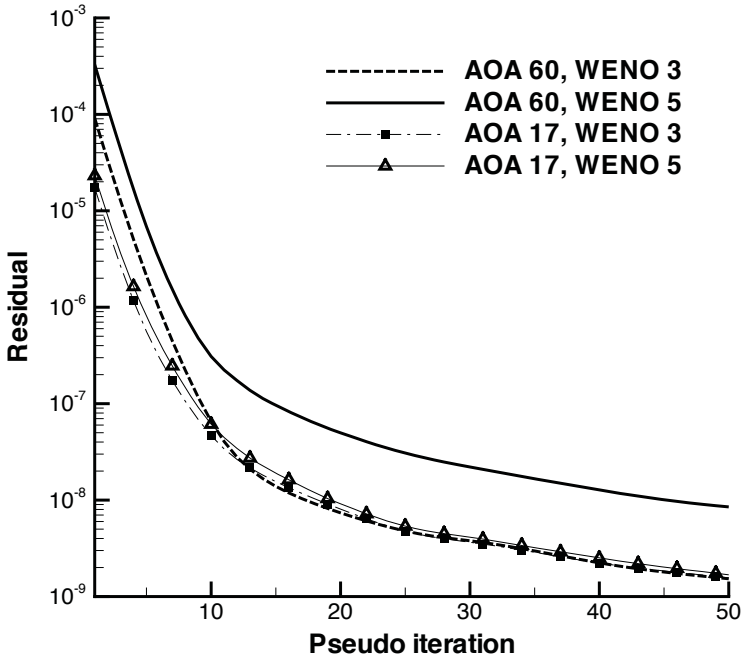

Figure 8.14: Pseudo step convergence behavior at AOA 17° and AOA 60° obtained by WENO scheme with DDES

where $P_{t\infty}$ denotes the normalized freestream total pressure, and P_{wall} is the normalized static pressure on wall. γ is the ratio of specific heat. WENO 3 shows little changes in the isentropic Mach number during the stall, whereas WENO 5 significant variations in the isentropic Mach number on the suction surface around 40% axial chord. WENO 5 simulates the stall flows in more realistic manner than WENO 3. As illustrated in Fig. 8.17, a highly fluctuating recirculating flow that causes such an aerodynamic instability on the suction surface is well captured with WENO 5.

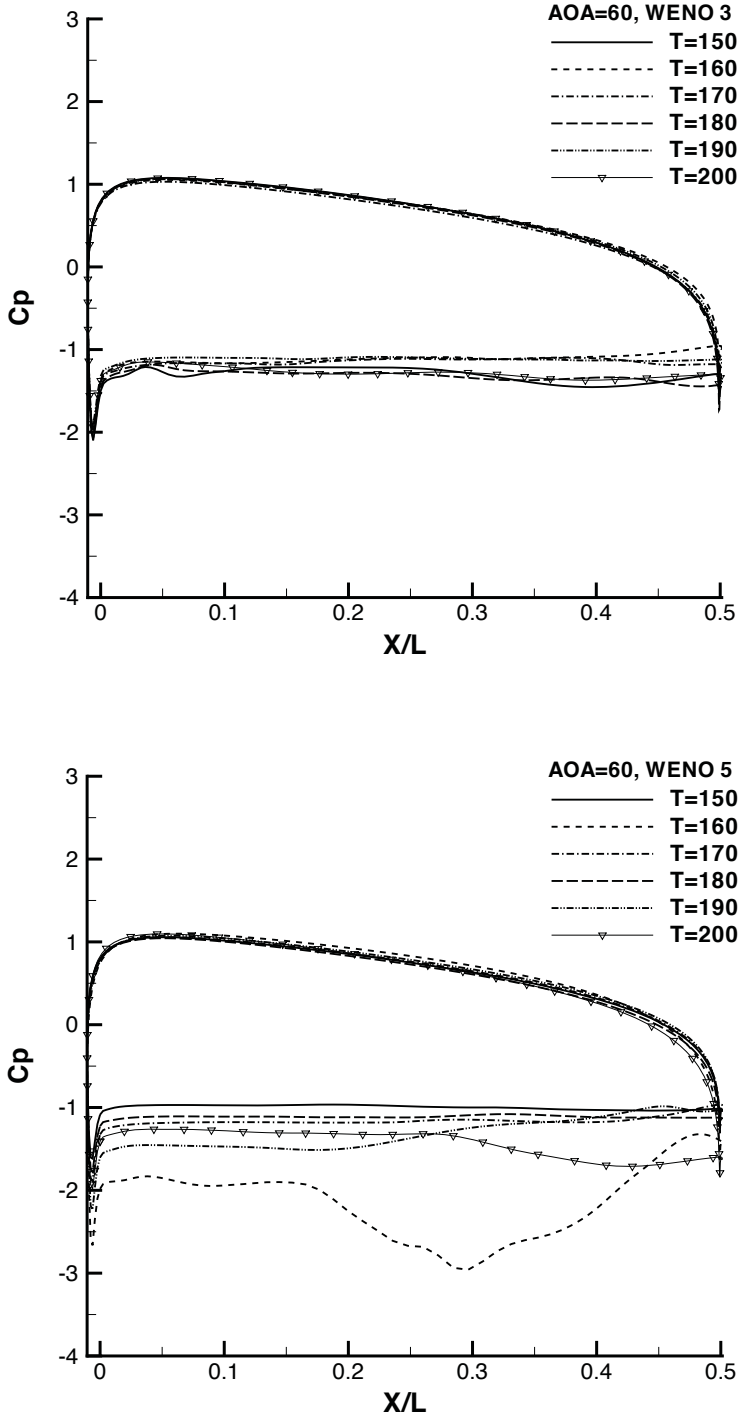

Figure 8.15: Instantaneous Cp at mid span for AOA 60° predicted by WENO scheme with DDES; 3rd order(top), 5th order(bottom)

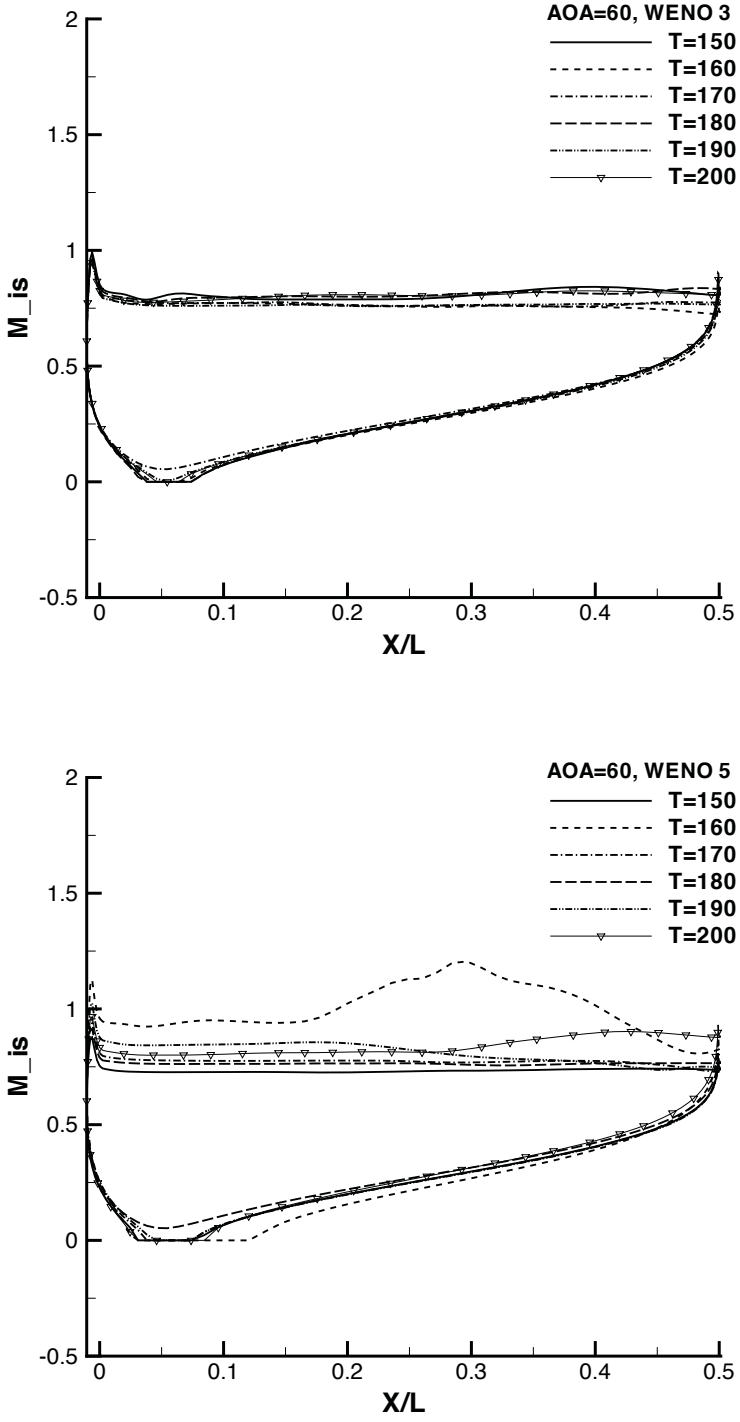

Figure 8.16: Instantaneous surface isentropic Mach number(M_{is}) distributions at mid span for AOA 60° predicted by WENO scheme with DDES; 3rd order(top), 5th order(bottom)

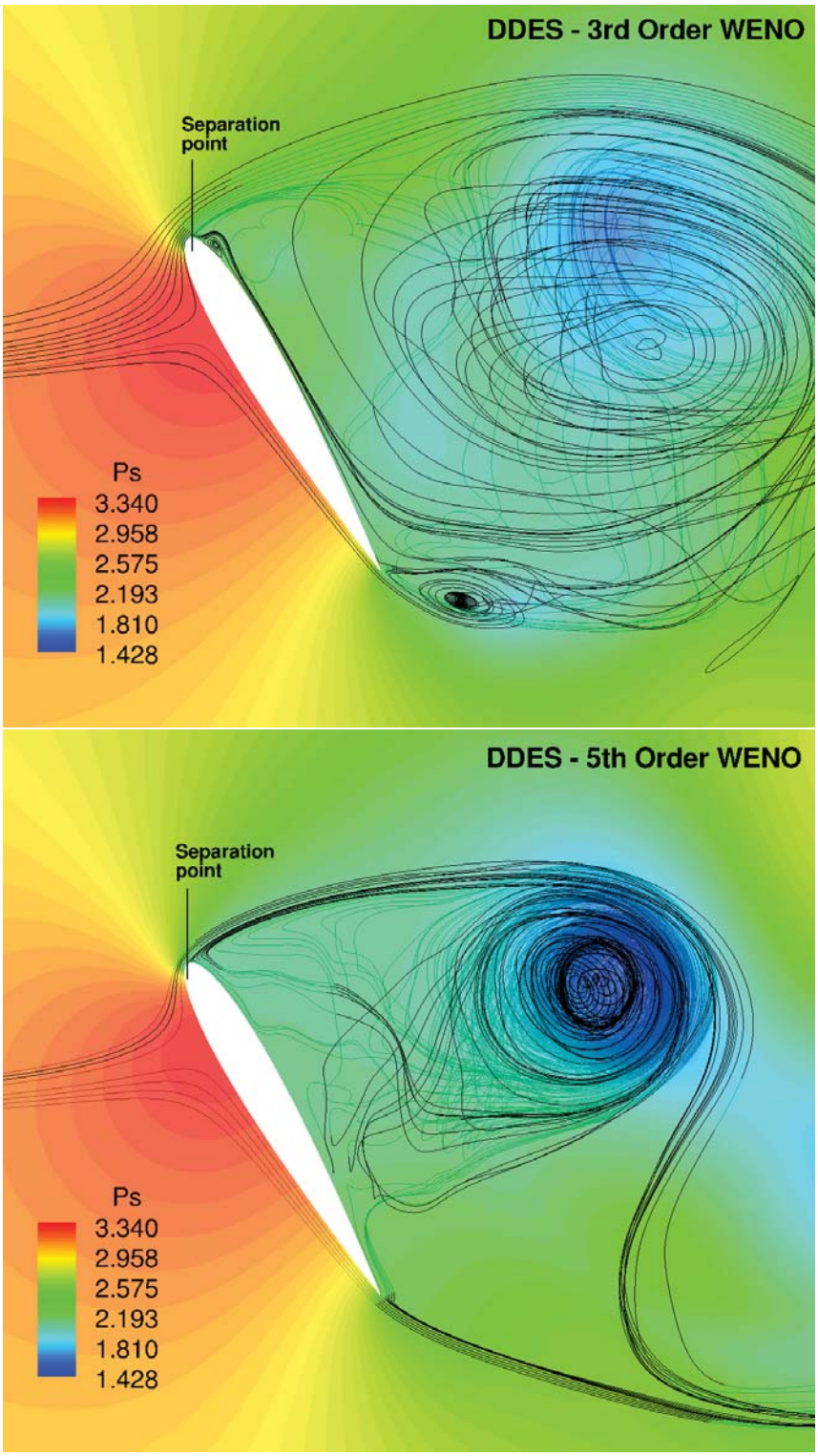

Figure 8.17: Streamlines of AOA 60° at $T = 150$ with the normalized static pressure contour predicted by WENO scheme with DDES; 3rd order(top), 5th order(bottom)

Fig. 8.18 shows the vorticity contours of 50% span at $T = 150$ and $T = 160$. WENO 5 captures a large changes in the stalled flow pattern behind the suction surface between $T = 150$ and $T = 160$, whereas WENO 3 simulates the stalled flow similarly at $T = 150$ and $T = 160$. The dynamic stall with the large eddies behind the airfoil are clearly resolved at 60° AOA by WENO 5.

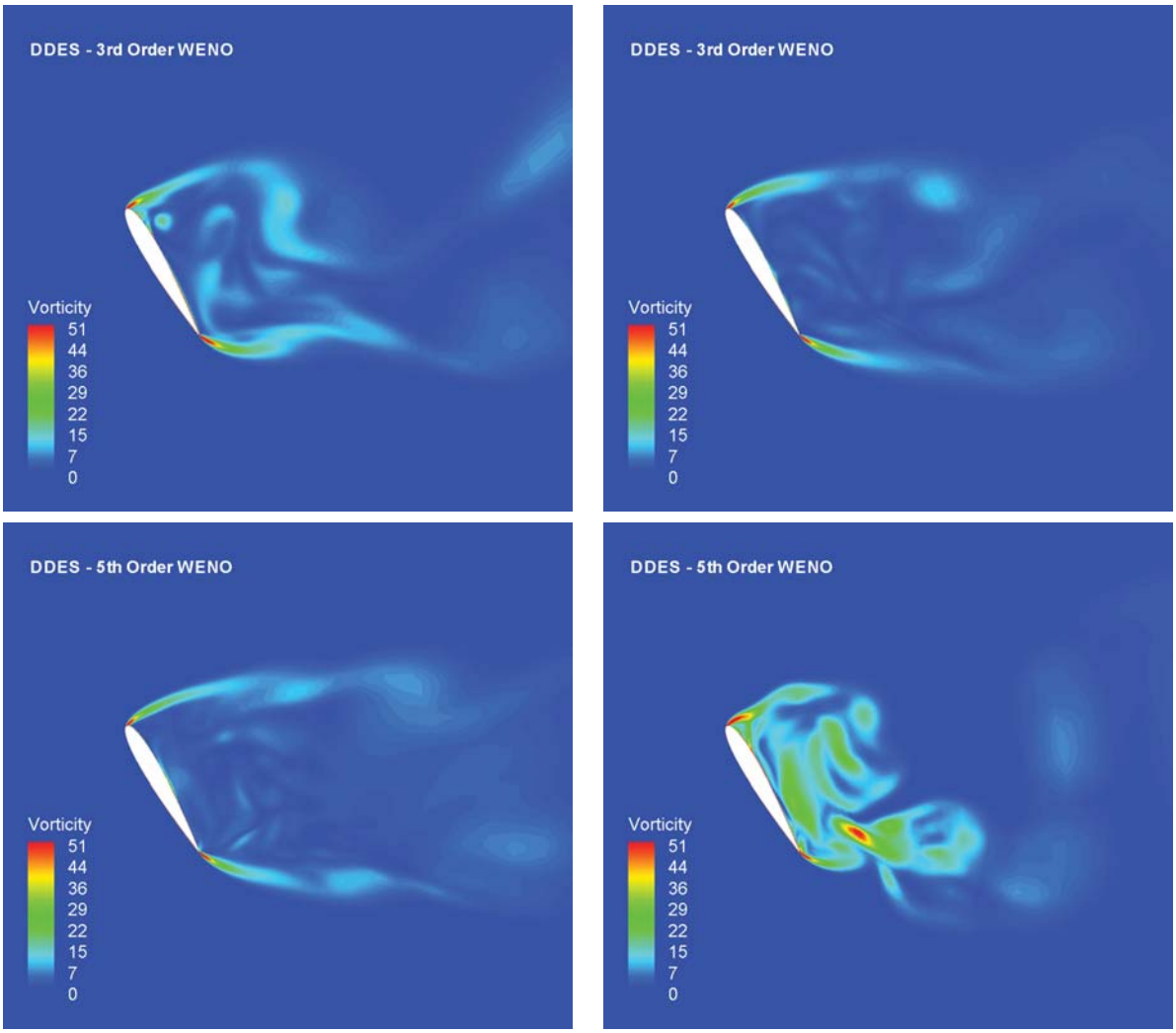

Figure 8.18: Vorticity of AOA 60° predicted by WENO scheme with DDES; 3rd order at $T = 150$(top left), 3rd order at $T = 160$ (top right), 5th order at $T = 150$(bottom left), 5th order at $T = 160$ (bottom right)

Vorticity contours for the stalled flows at AOA of 26° and 17° are shown in Fig. 8.19. Overall, the stalled flows behind the airfoil are very realistic for both WENO 5 and WENO 3. As angle of attack increases, both WENO 3 and WENO 5 demonstrate the larger flow separation and more dynamic vortex shedding.

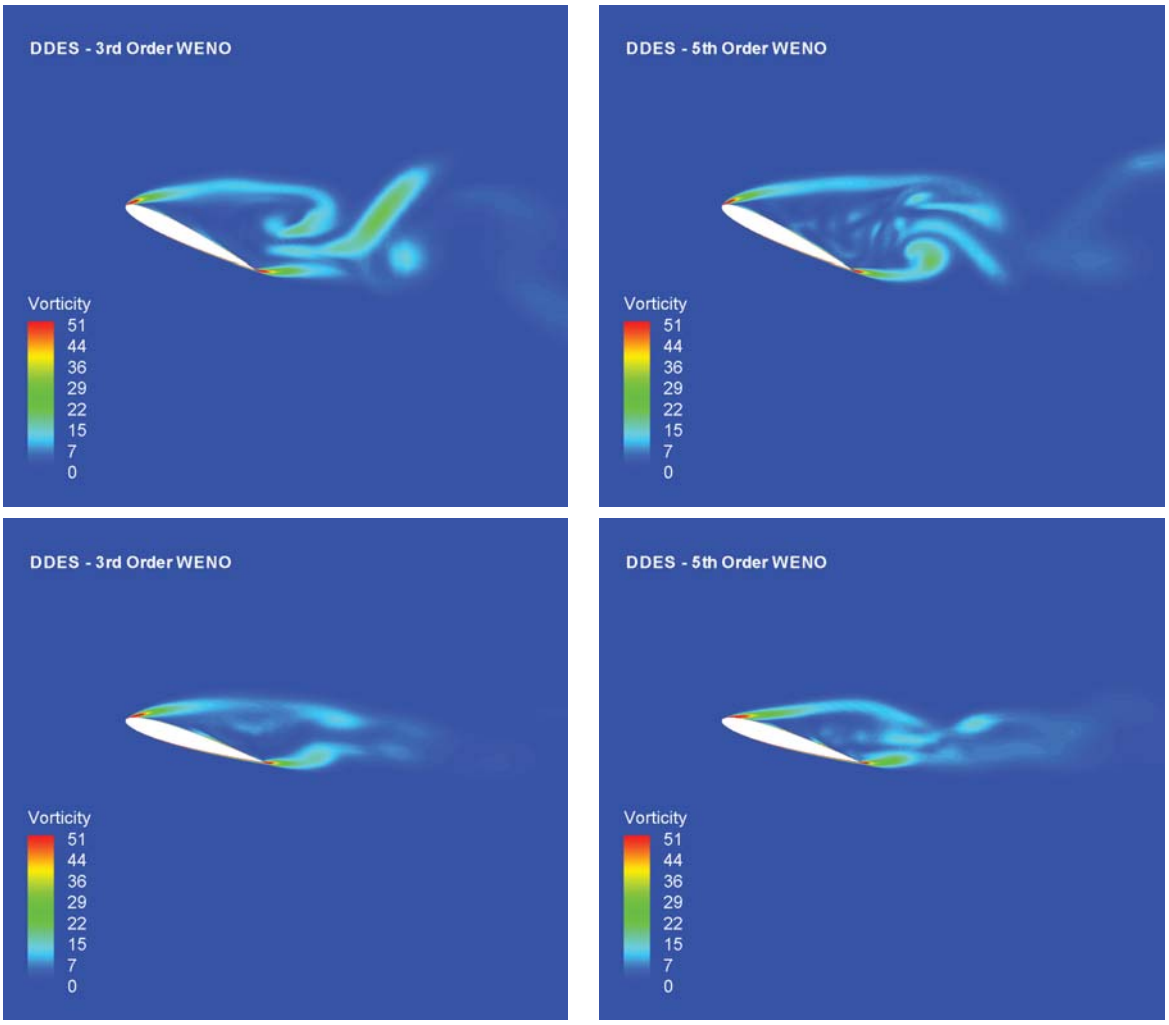

Figure 8.19: Vorticity of AOA 26°(top) and 17°(bottom) at $T = 260$ predicted by WENO scheme with DDES; 3rd order(left), 5th order(right)

Fig. 8.20 represents the coefficients of lift (*CL*) and drag (*CD*) predicted by WENO 3 and WENO 5 at AOA of 17°, 26°, 45°, 60° respectively. It is shown that the higher angle of attack gives rise to the larger fluctuations of the instant drag and lift coefficients. Before

AOA of 45°, the predicted lift coefficients are higher than the drag, while the drag and lift are similar at AOA of 45°. At AOA of 60°, the predicted drag coefficients are higher than the lift due to the massive separation. It is clear that the the lift and drag are significantly increased at AOA of 26°, indicating the stalled flow over the airfoil starts to highly fluctuate at AOA of 26°.

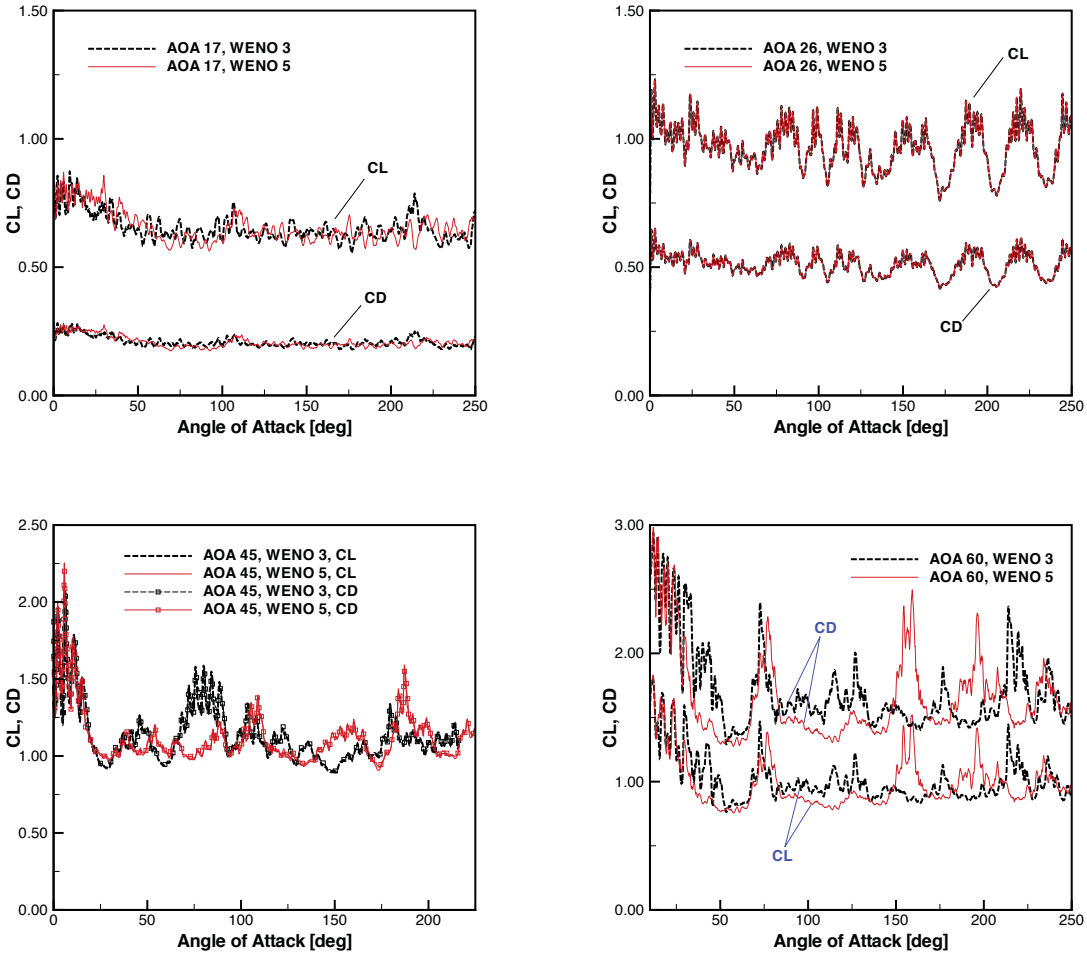

Figure 8.20: Instantaneous lift and drag coefficients for AOA 17°, 26°, 45°, 60° predicted by WENO scheme with DDES

The time averaged *CL* and *CD* at different angle of attack predicted by WENO 3 and WENO 5 are plotted with the experiment in Fig . 8.21. At AOA of 60°, WENO 5 overpredicts the lift by 6.8% and the drag by 6.7% compared to the experiment, while WENO 3 overpredicts the lift by 13.7% and the drag by 11.8%. For the angle of attack less than 45°, both schemes predict the stalled flow similarly with little difference in the predicted lift and drag. For instance, the lift coefficients predicted by WENO 3 and WENO 5 are are higher by roughly 5.2% than the experiment and the drag coefficients are also overpredicted by about 14% at AOA of 26°. Overall, WENO 3 and WENO 5 accurately predict the lift and drag compared to the measurement.

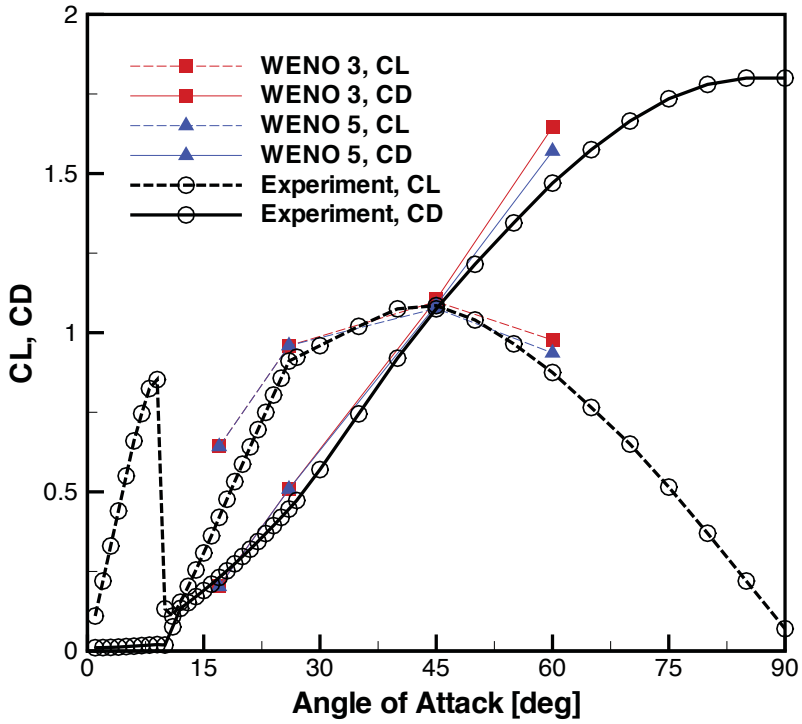

Figure 8.21: Time averaged lift and drag coefficients predicted by WENO scheme with DDES

8.3.1 Summary

This paper has developed a numerical methodology using high order schemes for DDES. The DDES is validated for a 3D flat plate turbulent boundary layer using a severe grid designed to generate Modeled-Stress Depletion of DES97. The DES shows 75% reduction of the eddy viscosity in the wall boundary layer, whereas the DDES preserves the eddy viscosity at the same level as the URANS.

Numerical simulation of a stalled flow over NACA0012 airfoil at 45° angle of attack is conducted using the URANS, the DES and the Delayed DES of turbulence. The DES and DDES predicted the drag and lift in excellent agreement with the experiment, whereas the URANS overpredicts the drag and lift by about 32%.

The comparison of the the 5th and 3rd order order WENO scheme indicates that the 5th order predicts accurately the lift and drag for over 45° AOA than the 3rd order WENO scheme. At AOA of 60°, the 5th order WENO scheme overpredicts the lift by 6.8% and the drag by 6.7% compared to the experiment, whereas the 3rd order WENO scheme overpredicts the lift by 13.7% and the drag by 11.8%. However, both the 3rd order and 5th order WENO schemes predict the stalled flow similarly with little difference in the predicted lift and drag for the angle of attack less than 45°.

8.4 DES of AGARD Wing 445.6 Supersonic Flutter

The purpose of this validation study is to simulate the challenging supersonic AGARD wing flutter boundary using a high fidelity DDES [37] with a fully coupled FSI. Delayed Detached Eddy Simulation of supersonic flutter of a 3D wing is conducted at free stream Mach number of 1.141 using a fully coupled fluid/structure interaction (FSI). Unsteady 3D compressible Navier-Stokes equations are solved with a system of 5 decoupled structure modal equations in a fully coupled manner.

To our knowledge, no DDES has ever been used for fluid-structural interaction. Even though DES concept is much newer than RANS and LES concept, its application for turbulence simulation has achieved encouraging success. Wang and Zha [139] simulate a co-flow jet airfoil using DES at high angle of attack with the results significantly improved compared with that obtained by RANS. Furthermore, Wang and Zha [25] apply the DES to fluid-structural interaction and accurately predict the limited cycle oscillation amplitude and frequency. Im and Zha [140] use DDES and accurately simulate a massive separation flow of NACA0012 airfoil. DDES appears to be a suitable compromise between the physical models of turbulence and CPU efficiency.

The 5th order WENO scheme for the inviscid flux and the 4th order central differencing for the viscous flux are used with the Low Diffusion E-CUSP (LDE) Scheme to resolve nonlinear shock wave/turbulent boundary layer interaction of the vibrating wing. An efficient spring mesh system is implemented for mesh deformation. The high-scalability parallel computing is applied to save wall clock time [141]. The supersonic flutter boundary predicted is in excellent agreement with the experiment. This appears to be the first

time that a numerical simulation matches the experimental supersonic flutter boundary accurately.

8.4.1 Boundary Conditions

For the subsonic flutter calculations, steady state freestream conditions are used at the upstream portion of the outer boundary. At downstream boundary, the static pressure is specified as freestream value, and the streamwise gradients of other variables are forced to vanish. In spanwise direction, the periodic boundary condition is used. For the supersonic flutter case, all the variables are extrapolated at downstream boundary. The supersonic inflow condition with all variables specified is applied at the upstream portion of the outer boundary. The rest of the boundary conditions for the supersonic case are the same as those for the subsonic cases. The wall treatment given by Eq. (8.1) to achieve flux conservation by shifting half interval of the mesh on the wall is employed.

8.4.2 Moving Mesh

A CPU efficient deformation mesh technique is one of the requisites in FSI to accurately describe a moving structure. An algebraic deformation mesh technique for the 3D wing is implemented by using the spring mesh algorithm suggested by Chen et al. [24]. The algorithm is tested for a 2D airfoil with sharp trailing edge as shown in Fig. 8.22. This moving mesh method works robustly for large deformation. Once the moving mesh for a 2D wing section is generated, the 3D mesh is generated straightforwardly by stacking each airfoil section from the root to tip due to the small deformation in the spanwise direction. Note

that an important factor affecting the deformed mesh quality is the initial mesh skewness, in particular near the wing surface. Therefore, the O-mesh topology is used in this study to maintain the mesh orthogonality near the wing surface.

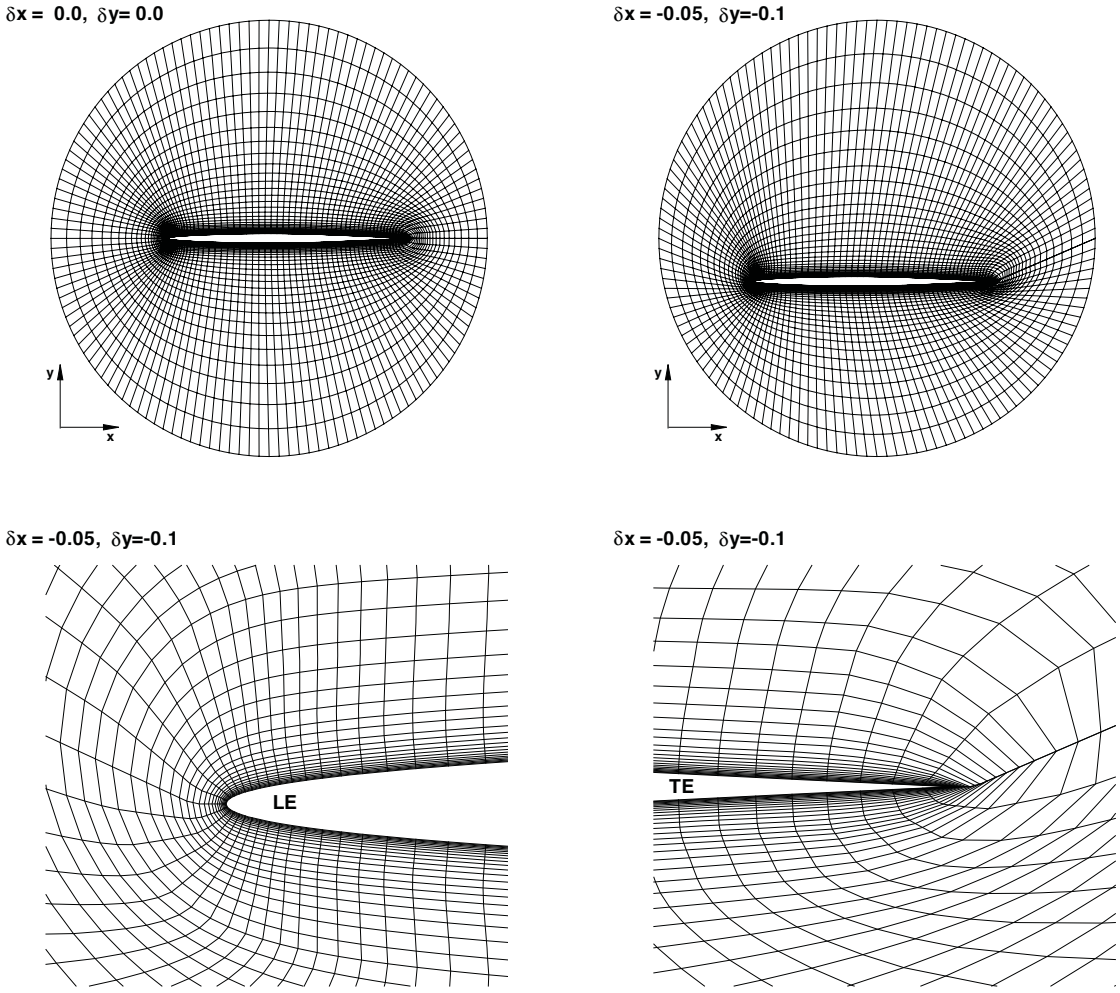

Figure 8.22: Moving mesh test for an airfoil; initial mesh(top left), deformed mesh by $\delta x = -0.05, \delta y = -0.1$(top right), magnified view of deformed mesh near leading edge(bottom left), magnified view of deformed mesh near trailing edge(bottom right)

8.4.3 AGARD Wing 445.6 Model

A limited number of AGARD standard wing configurations were tested [4] in order to promote the evaluation of existing and emerging unsteady aerodynamics codes and methods for flutter from subsonic to supersonic regime. In this study, the AGARD Wing 445.6 Weakend 3 is used for flutter simulation. This wing model has the symmetric NACA65A004 airfoil with a 4% thickness, and the wing structural details are listed in table 8.2.

Table 8.2: AGARD Wing 445.6 Weakend 3 model at test Mach number of 1.141 [4]

Airfoil section	NACA 65A004
Measured panel mass($\bar{m}$) [kg]	1.8627
Panel span(H) [m]	0.762
Sweep angle at half chord [deg]	43.15
Root chord(b_s) [m]	0.559
Tip chord(b_t) [m]	0.3682
Air density(ρ_∞) [kg/m^3]	0.0783
Dynamic pressure(q) [Pa]	5041.791
Flutter frequency(ω_f) [rads/s]	109.9
Mass ratio($\bar{\mu} = \frac{\bar{m}}{\rho_\infty V}$)	182.74
Flutter index($V_f = \frac{U_\infty}{b_s \omega_f \sqrt{(\bar{\mu})}}$)	0.4031

8.4.4 Results and Discussion

First five mass normalized mode shapes in the report [4] are used, which are displayed in Fig. 8.23. Those are identified that 1st, 3rd and 5th mode are bending, and 2nd and 4th mode are torsion. As initial conditions for the structure, 1st mode initial velocity of the structure in the modal coordinates is assumed as 0.0001 whereas others including modal displacements are set to zero. The uniform modal damping ratio(ζ) of 0.005 is applied for

all flutter computations since no structural damping is available [51]. The physical time step 0.05 with the pseudo time CFL number of 1 is used. Before the flutter computation, the unsteady DDES simulation is conducted for about 2000 physical steps to provide initial FSI flow field. The residual in each pseudo time step is required to be reduced by two orders of magnitude, which is achieved usually within 20 iterations.

Computational Mesh Test

Mesh convergence test is done for Mach number of 0.678. Four mesh sizes were tested; mesh A=137 (around airfoil)$\times$61(normal to the surface)$\times$60(span), mesh B=$137\times 76\times 60$, mesh C=$137\times 91\times 60$, mesh D=$137\times 91\times 70$. When the mesh is changed, the mode shapes corresponding to the surface mesh coordinates are found by a spline interpolation. The 1st grid spacing away from the the wing surface is set to yield y^+ less than unity. The far field boundary is located 50 root chords away from the wing. The O-mesh topology is used as shown in Fig. 8.24. The outer span boundary from the wing tip is 1 span length of the wing. Total 16 partitioned blocks are used for parallel computation.

Fig. 8.25 shows the modal displacements of mode 1 and mode 2 for different meshes. The flutter velocity index V_f used for mesh test is 0.415445. The predicted responses for both mode 1 and mode 2 using mesh C are well converged with mesh D. Therefore, mesh C is chosen for flutter simulations in this study.

Fig. 8.26, and Fig. 8.27 shows the predicted modal displacements with $V_f = 0.4196$, $V_f = 0.42187$ respectively. It is shown that $V_f = 0.4196$ results in the decaying responses of wing vibration, whereas $V_f = 0.42187$ leads to the neutral responses. Compared with

the flutter velocity index of 0.4174 at the stability limit by the experiment [4], the present prediction at Mach number of 0.678 only over-predicts by 0.5%.

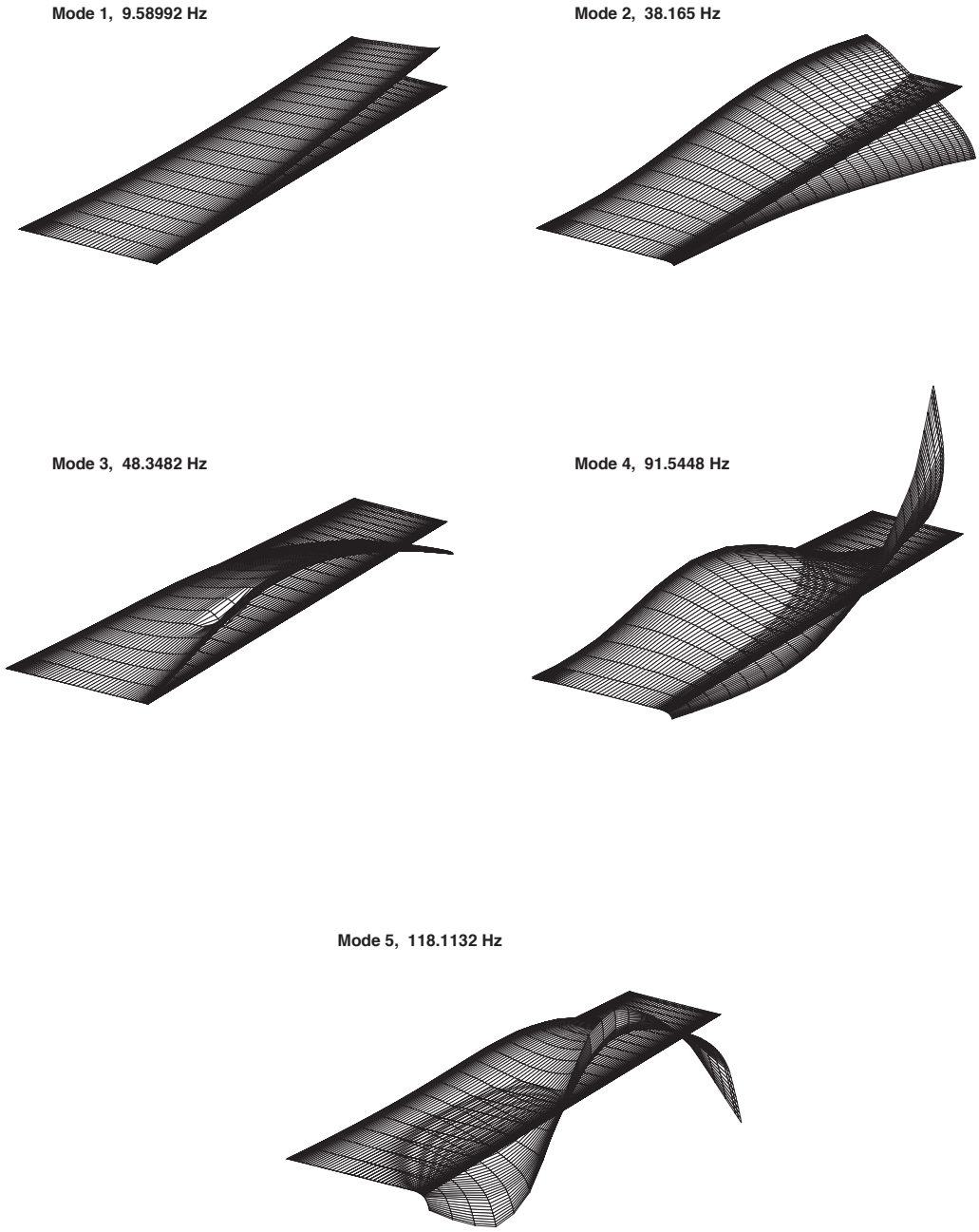

Figure 8.23: Five modal deflections for AGARD Wing 445.6 Weakend 3 [4]; mode 1(top left), mode 2(top right), mode 3(middle left), mode 4(middle right), mode 5(bottom)

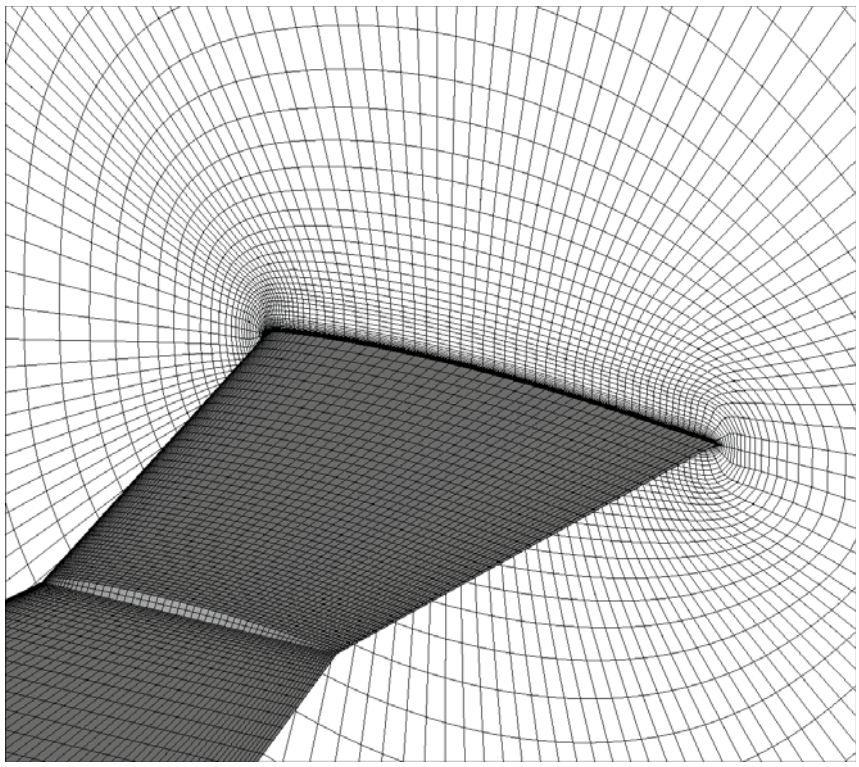

Figure 8.24: Computational mesh of 137×91×70 for AGARD Wing 445.6 Weakend 3

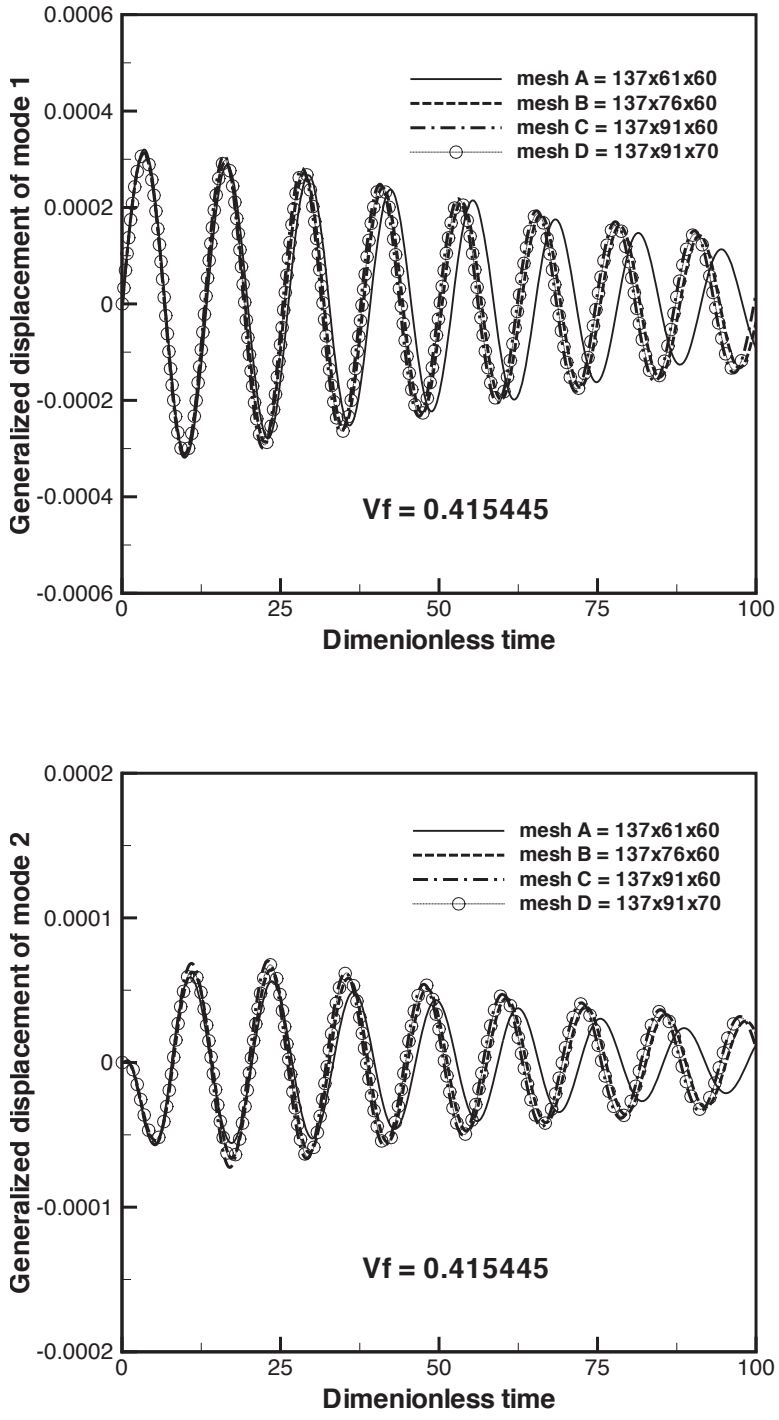

Figure 8.25: Mesh convergence test for the AGARD Wing flutter; $M = 0.678$, $V_f = 0.415445$

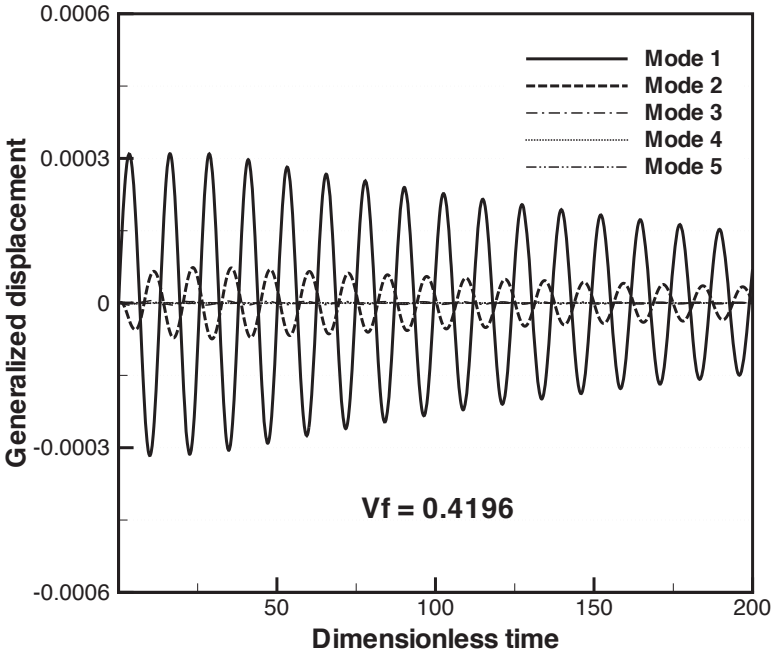

Figure 8.26: Damped response of the AGARD Wing flutter; $M = 0.678$, $V_f = 0.4196$

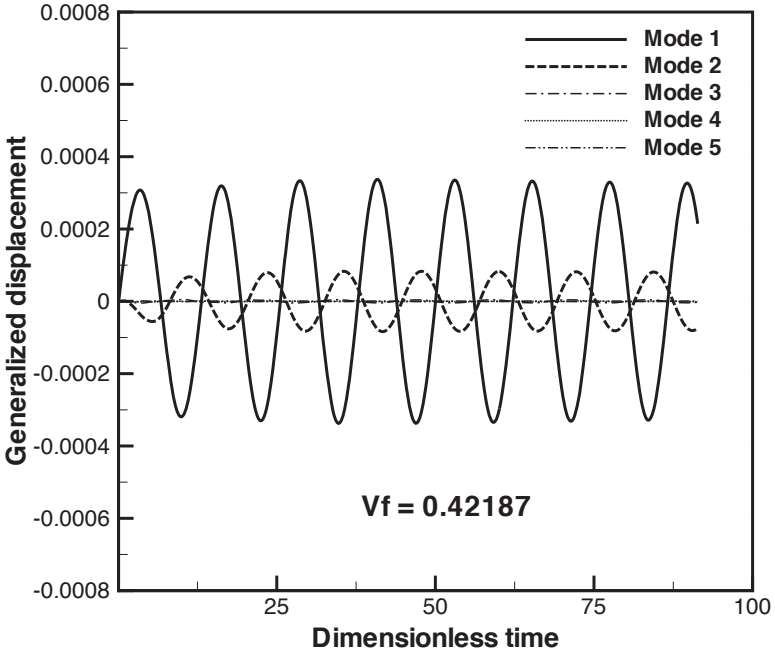

Figure 8.27: Neutral response of the AGARD Wing flutter; $M = 0.678$, $V_f = 0.42187$

Supersonic Flutter Simulation of AGARD Wing 445.6

The predicted modal displacements for Mach number of 1.141 with different flutter velocity index(V_f) setting are displayed in Fig. 8.28. At $V_f = 0.3765$, the response decays in time, while $V_f = 0.4304$ leads to divergent responses. A neutrally stable point, the flutter boundary, is captured at $V_f = 0.3993$, which is a harmonic oscillation. The damped oscillation with $V_f = 0.3963$, 0.75% below the measured flutter boundary, indicates that the present FSI approach has good accuracy and is sensitive to a small change of the flutter speed index.

Fig. 8.29 represents the lift(C_l), the drag(C_d), and the momentum coefficient(C_m) for $V_f = 0.3993$, and $V_f = 0.4304$. At the flutter boundary, all show a type of limited oscillation with same phase angle, period, and amplitude, whereas C_d, C_m with $V_f = 0.4304$ amplifies with time. It is shown that the lift force acting on the wing surface in particular has larger effect due to the flutter than the drag. The momentum coefficient increases too, but its phase is lagged by a half period of oscillation compared to the lift coefficient.

Fig. 8.30 shows the modal force defined as $\frac{\tilde{\phi}_j^{*T}}{m_j^*} \cdot \mathbf{F}^* \cdot {V_f}^2 \cdot \frac{b_s^2 L}{\bar{V}} \cdot \bar{m}$ for $V_f = 0.3993$, and $V_f = 0.4304$. For all 5 modes, the modal force also increases with the flutter speed index, $V_f = 0.4304$. It is expected that the wing vibrates mainly in the plunging motion and slightly in the torsional mode since the first mode is bending and the second mode is torsion.

Fig. 8.31 illustrates how the wing vibrates during the flutter with the flutter velocity of $V_f = 0.4304$. The distance of the trailing edge is larger than that of the leading edge, which indicates that both the pithing and the plunging are associated with the wing flutter.

The wing with the pitching (or torsion) motion experiences the increase in angle of attack (AOA) during the wing flutter.

Fig. 8.32 shows an instantaneous Mach number contours near the tip section during the supersonic flutter. The unsteady shock waves near the trailing edge are well captured. Fig. 8.33 shows an instantaneous Mach number contours of root span, 50% span, tip span at $T = 200$. At root span, the expansion waves are seen near leading and trailing edge, but at 50% span the oblique shocks appear near the trailing edge instead of the expansion waves. The shocks near the trailing edge become stronger toward tip, and the normal shock boundary layer interaction causes a minor flow separation on the pressure surface.

The surface isentropic Mach number at $T = 150$ and $T = 200$ is plotted in Fig. 8.34. Certainly the difference of the isentropic Mach number is larger near the leading edge due to the variation of the AOA.

The predicted flutter boundary at a supersonic condition, $M = 1.141$ is presented in Fig. 8.35. $V_f = 0.3993$ is the flutter velocity index at the flutter boundary resolved in this computation, which is 0.9% lower than the experiment. To our knowledge, the present solution is the first time that a numerical simulation matches the experiment accurately for the supersonic flutter boundary.

8.4.5 Summary

The supersonic flutter boundary of the 3D AGARD wing is simulated using the delayed detached eddy simulation with a fully coupled fluid/strcuture interaction. The low diffusion E-CUSP scheme with a 5th order WENO reconstruction for the inviscid flux and a set of 4th order central differencing for the viscous terms are used to accurately capture the shock wave/turbulent boundary layer interaction of the vibrating wing. The present simulation at Mach number of 1.141 achieves excellent agreement with the measured data. It appears to be the first time that a numerical prediction of supersonic flutter boundary matches with experiment accurately. The results indicate that the developed DDES methodology with high order shock capturing scheme and fully coupled FSI is robust and accurate.

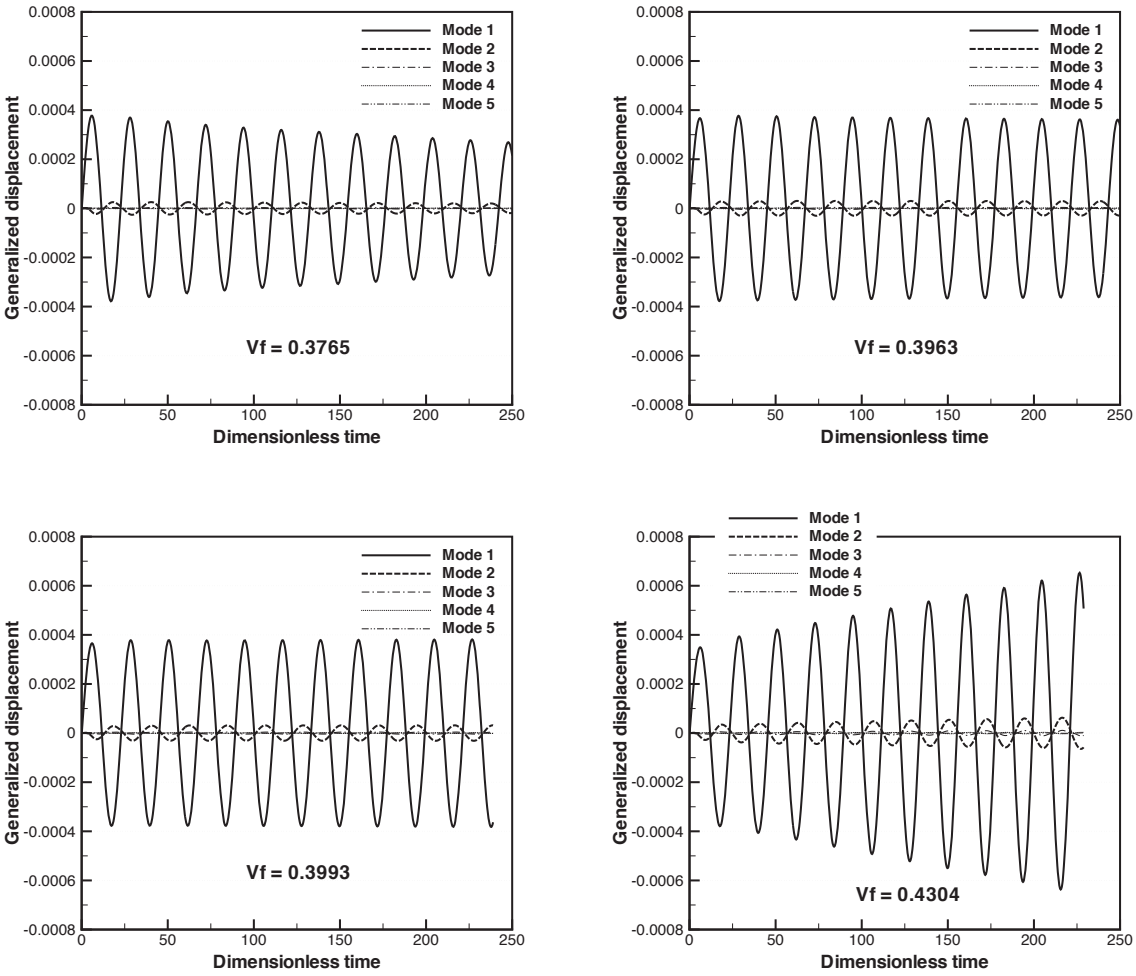

Figure 8.28: Modal displacements of the AGARD Wing flutter for $M = 1.141$; $V_f = 0.3765$(top left), $V_f = 0.3963$(top right), $V_f = 0.3993$(bottom left), $V_f = 0.4304$(bottom right)

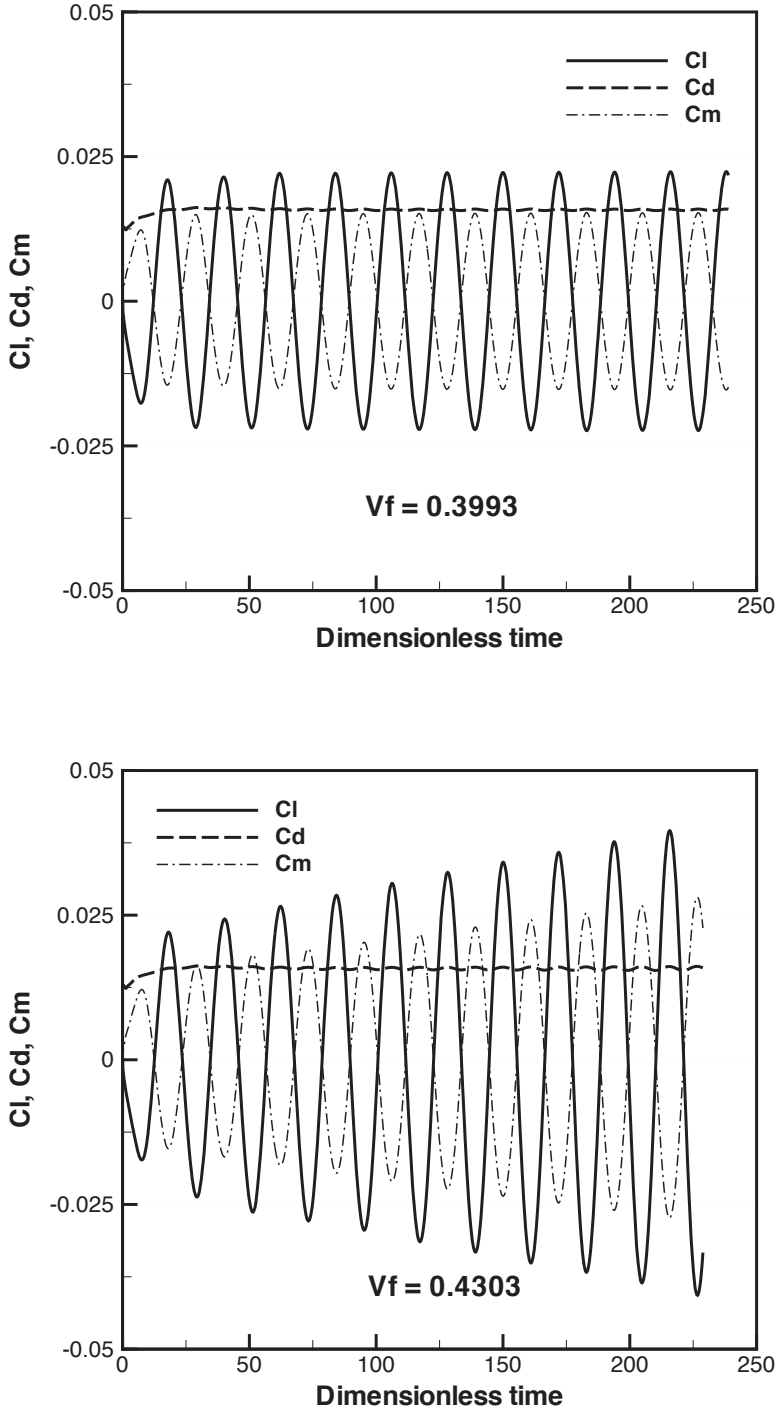

Figure 8.29: Predicted lift(C_l),drag(C_d), and momentum coefficients(C_m) of the AGARD Wing at the supersonic flutter boundary; $V_f = 0.3993$(top), $V_f = 0.4304$(bottom)

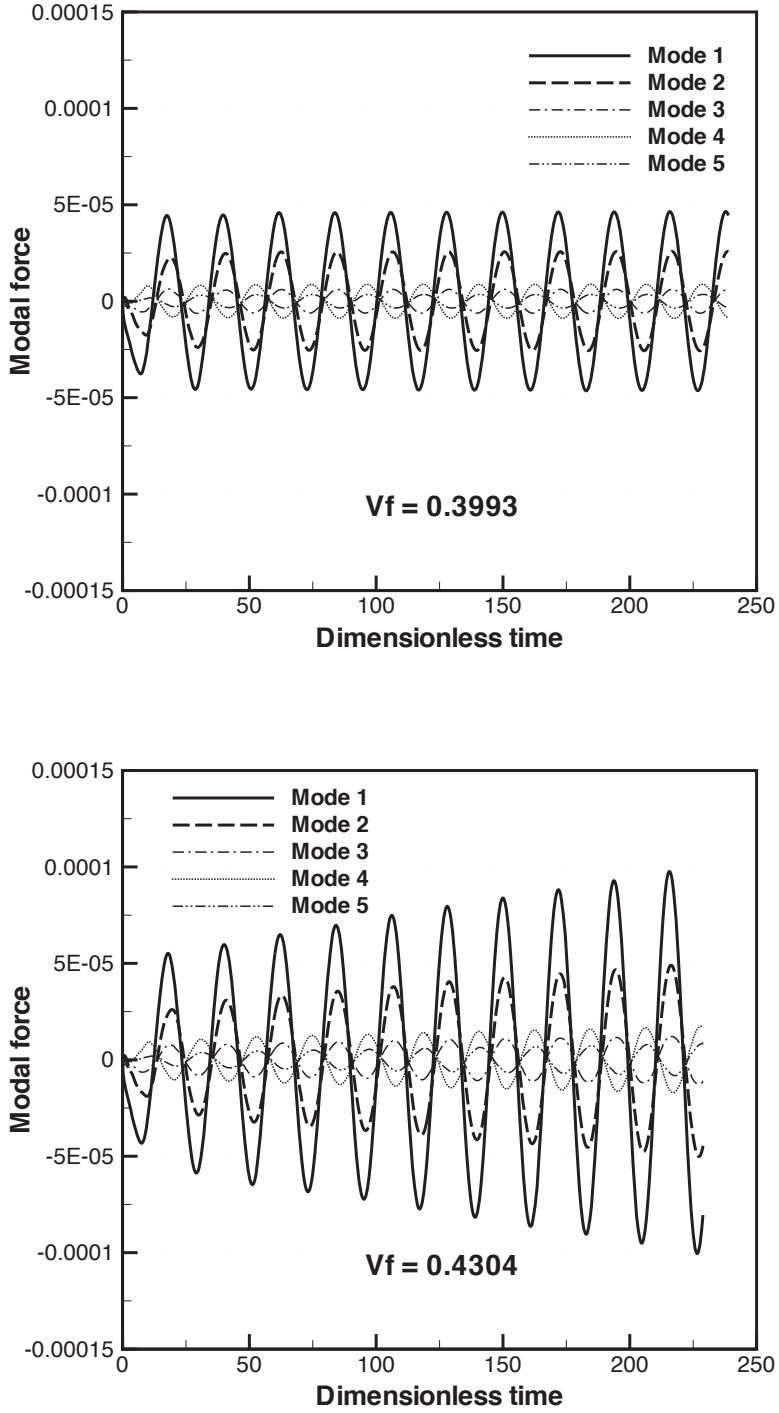

Figure 8.30: Predicted modal force ($\frac{\tilde{\phi}_j^{*T}}{m_j^*} \cdot \mathbf{F}^* \cdot {V_f}^2 \cdot \frac{b_s^2 L}{\bar{V}} \cdot \bar{m}$) of the AGARD Wing at the supersonic flutter boundary; $V_f = 0.3993$(top), $V_f = 0.4304$(bottom)

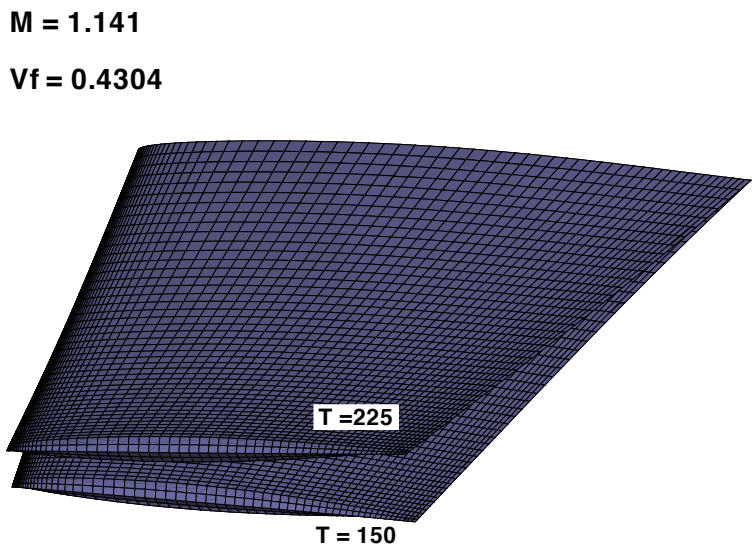

Figure 8.31: Wing fluttering from the fully coupled FSI simulation for $M = 1.141$ and $V_f = 0.4304$

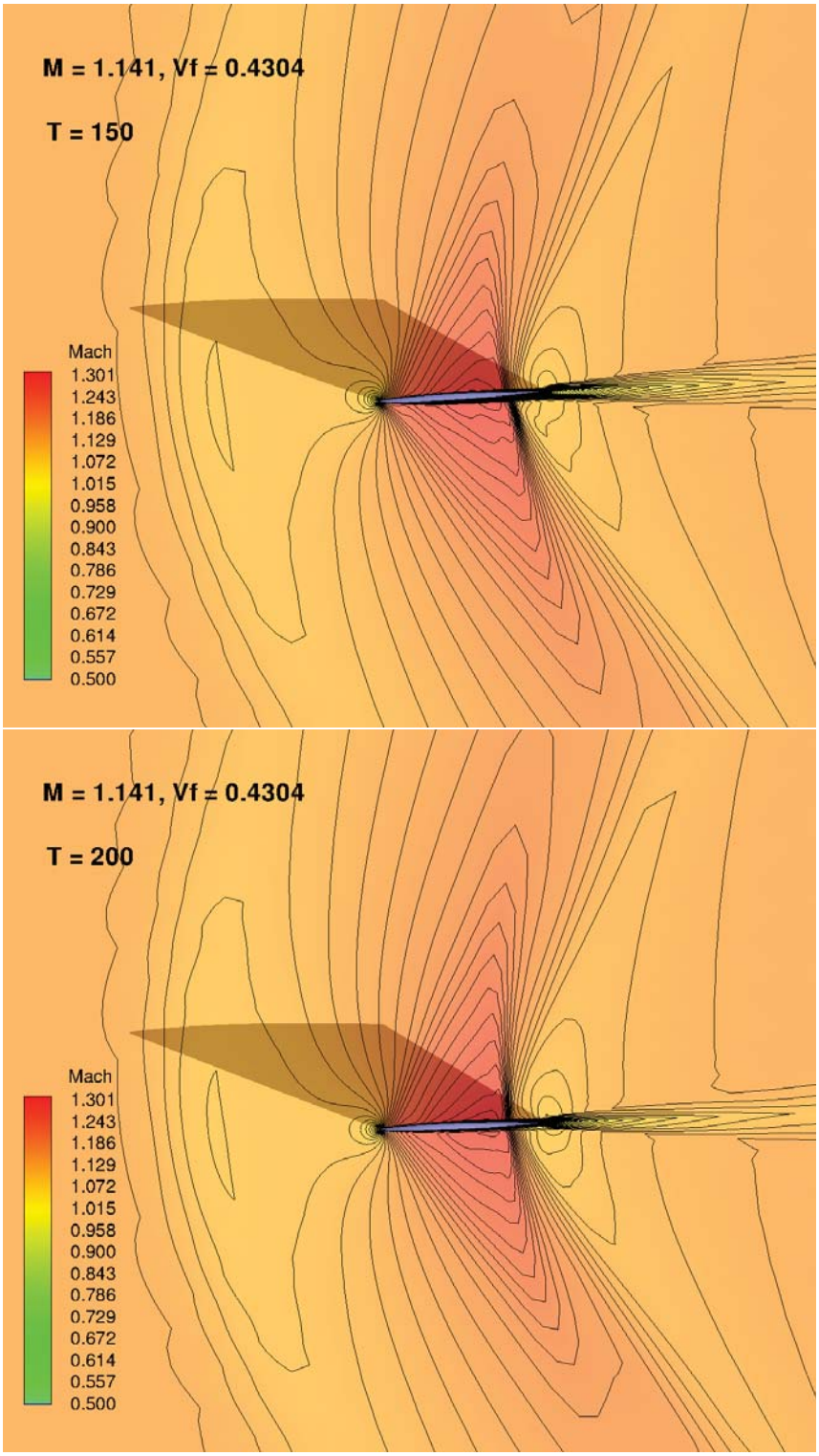

Figure 8.32: Instantaneous Mach number at tip section for $M = 1.141$ and $V_f = 0.4304$; T=150(top), T=200(bottom)

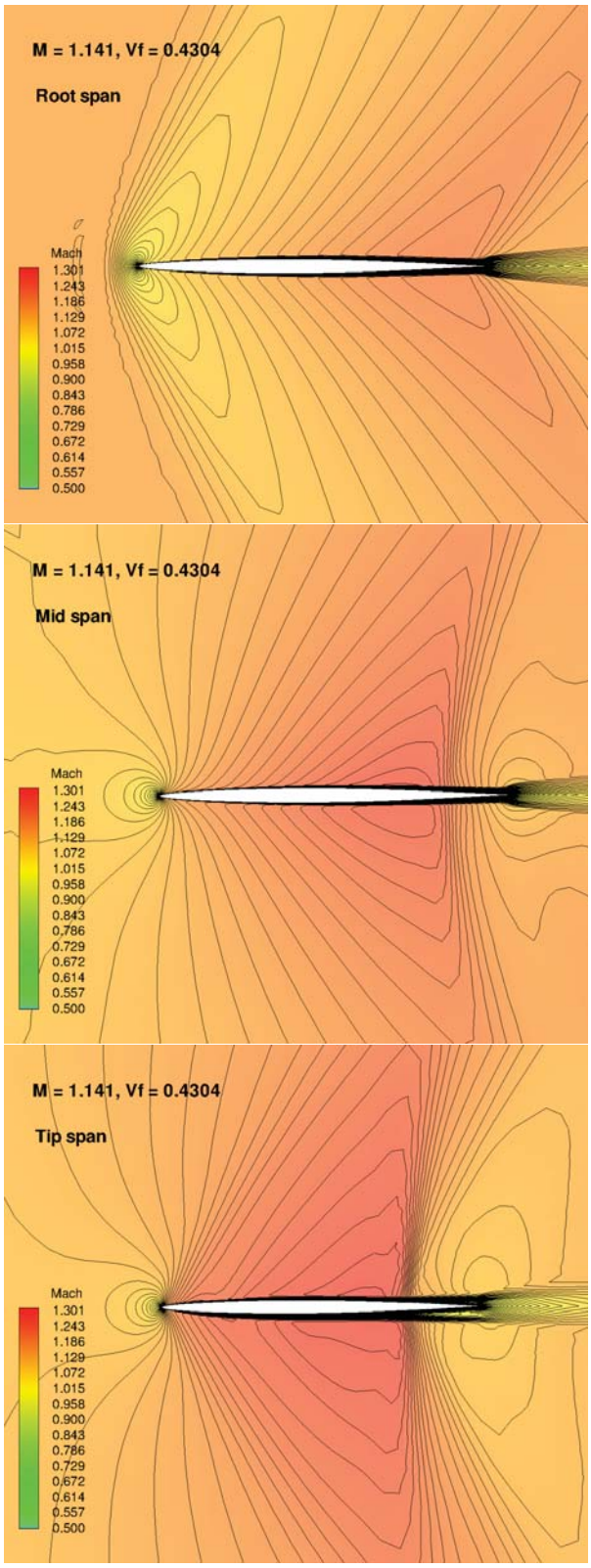

Figure 8.33: Instantaneous Mach number at T=200 for $M = 1.141$ and $V_f = 0.4304$; root span(top), 50% span(middle), tip span(bottom)

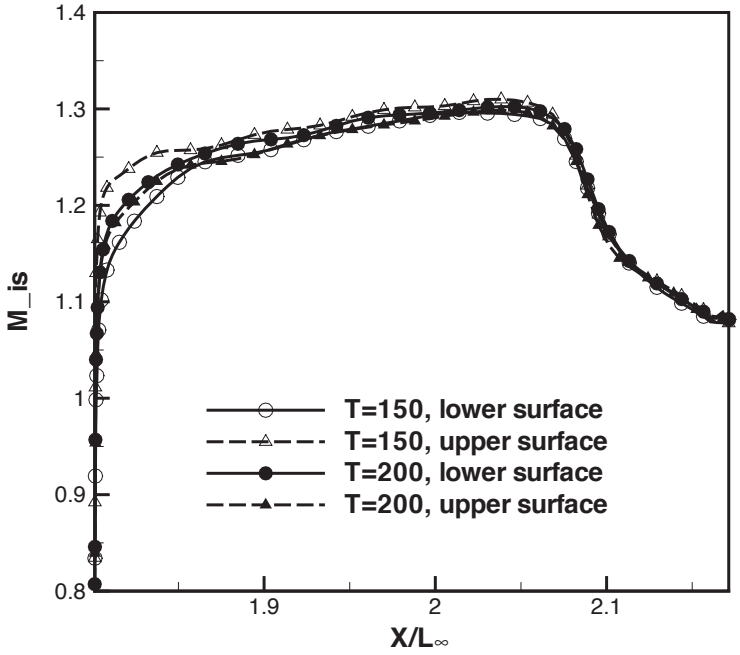

Figure 8.34: Variation of surface isentropic Mach number at tip section during the supersonic flutter for $M = 1.141$ and $V_f = 0.4304$

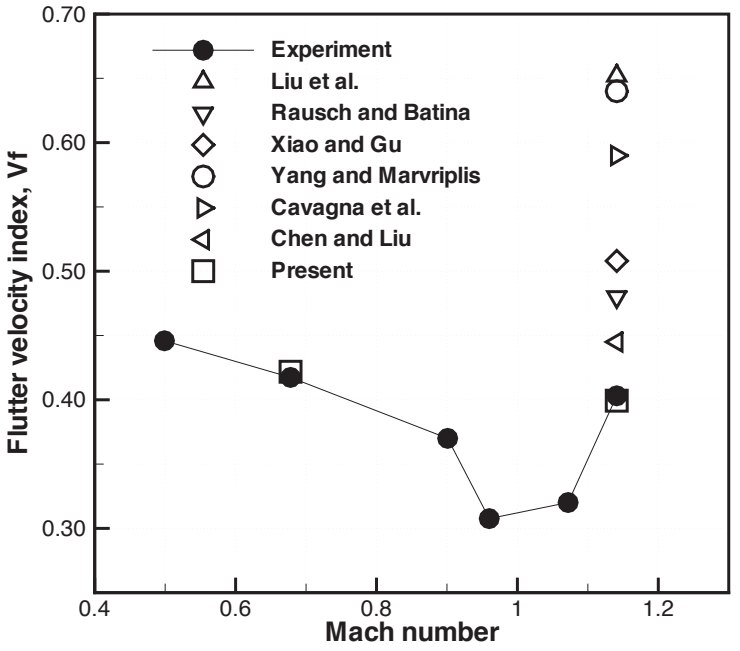

Figure 8.35: Flutter velocity index of AGARD Wing 445.6 Weakend 3

8.5 DES of Stall Inception for a Full Annulus Compressor Rotor

Full annulus detached eddy simulation(DES) is conducted in this study to investigate stall inception for an axial transonic rotor - NASA Rotor 67. A low diffusion E-CUSP scheme with a third order MUSCL reconstruction is used to discretize the inviscid fluxes and second order central differencing is used for the viscous terms. The purpose of this work is to investigate rotating stall phenomena in the full annulus of a high speed transonic axial rotor using the detached eddy simulation (DES) of turbulence. To our knowledge, this is the first time that DES is used to analyze a transonic rotor stall inception. The computations using URANS were also performed for comparison.

The NASA Rotor 67 used in this study was designed to have axial inlet flow and was tested in isolation. This rotor is a high-speed machine designed to have 22 blades, a total pressure ratio of 1.63, supersonic tip speed of Mach number 1.38, and shaft speed of 16,043 RPM. The original experiments [130] were measured at only near peak and near stall conditions. Unfortunately no experimental measurement with regard to stall inception of NASA Rotor 67 is available. However, the experiment of Hah et al. [75] could be used as the qualitative comparison reference for the present study since the rotors are at high-speed regime with similar design specifications.

It is observed that the rotating stall is initiated by the local spike flow disturbance, which quickly induces the rotor to stall roughly over 2 rotor revolutions. The stall cell covering more than 6 blade tip passages propagates at 48% of rotor speed in the counter rotor rotation direction. The process of rotating stall is captured by the full annulus DES, which indicates

that the blockage created by the low energy vortical flow structure pushes the tip leakage flow to the adjacent blade behind the detached sonic boundary. The unsteady Reynolds averaged Navier-Stokes (URANS) simulation is also performed for comparison. The DES predicts the stall inception roughly one rotor revolution earlier than the URANS model. Overall, the DES predicts the stall inception more realistically.

8.5.1 Boundary Conditions

As aforementioned in chapter 6, turbomachinery boundary conditions developed in the present work are used for rotating stall simulation including 1% inlet total pressure perturbation. In particular, the inlet and outlet flow conditions from the experiment [130] are imposed for the single passage validation.

8.5.2 Computational Grid

Two types of 3D mesh were used in this study: (1) the single passage mesh for the code validation shown in Fig. 8.36; (2) the full annulus grid for rotating stall simulations shown in Fig. 8.37.

For the single passage, O-mesh topology is employed since O-grids are orthogonal along the blade surface, thereby minimizing the undesirable grid skewness. The inlet and exit boundaries were located at the same positions of the measurement [130] as sketched in Fig. 8.36.

The tip gap is shown to have a significant effect on overall performance of axial compressors [131]. The fully gridded tip mesh generation technique adopted in this study

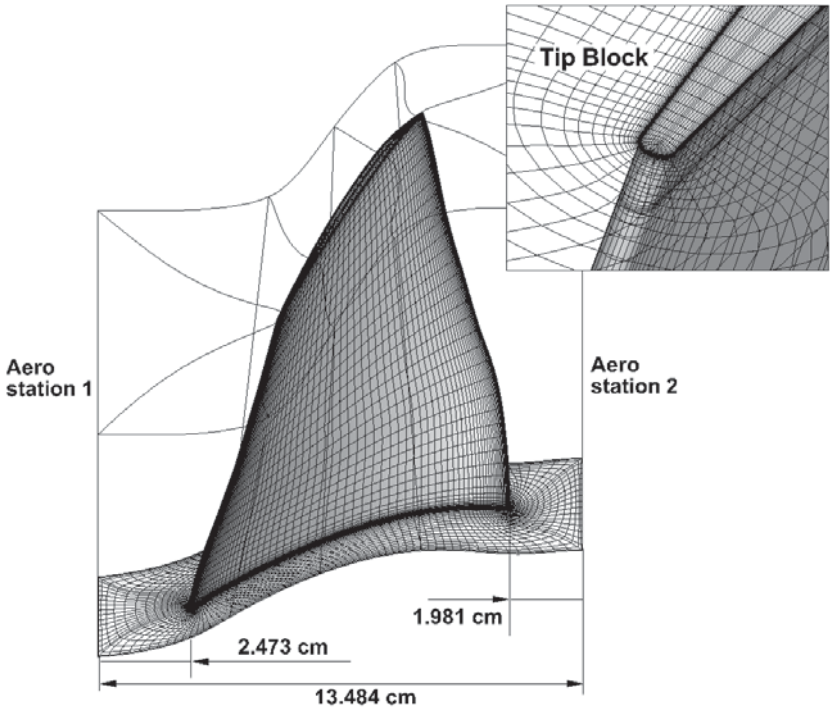

Figure 8.36: Single passage grid of NASA Rotor 67 with a fully gridded tip block used for the code validation

is shown to better predict the tip clearance flow than the pinched tip or simplified tip model [132]. In the model of the fully gridded tip, about 4 to 10 points in the tip clearance are generally considered as adequate to predict the primary effects of the leakage flow in axial compressor [84, 131, 132, 142]. However, it is not possible to determine the precise impact of the tip clearance modeling on the flow solutions due to the lack of detailed flow measurements in the tip clearance of NASA Rotor 67.

To precisely describe the rotor tip, a fully gridded tip block with nominal clearance of 0.66% of tip chord, an O-grid with mesh size of $161 \times 12 \times 9$, was used. The mesh uses 9 points in the radial direction to describe the tip clearance. Excluding the tip region, the main grid dimension is $161 \times 80 \times 52$ respectively in the direction of around the blade, blade to blade and span.

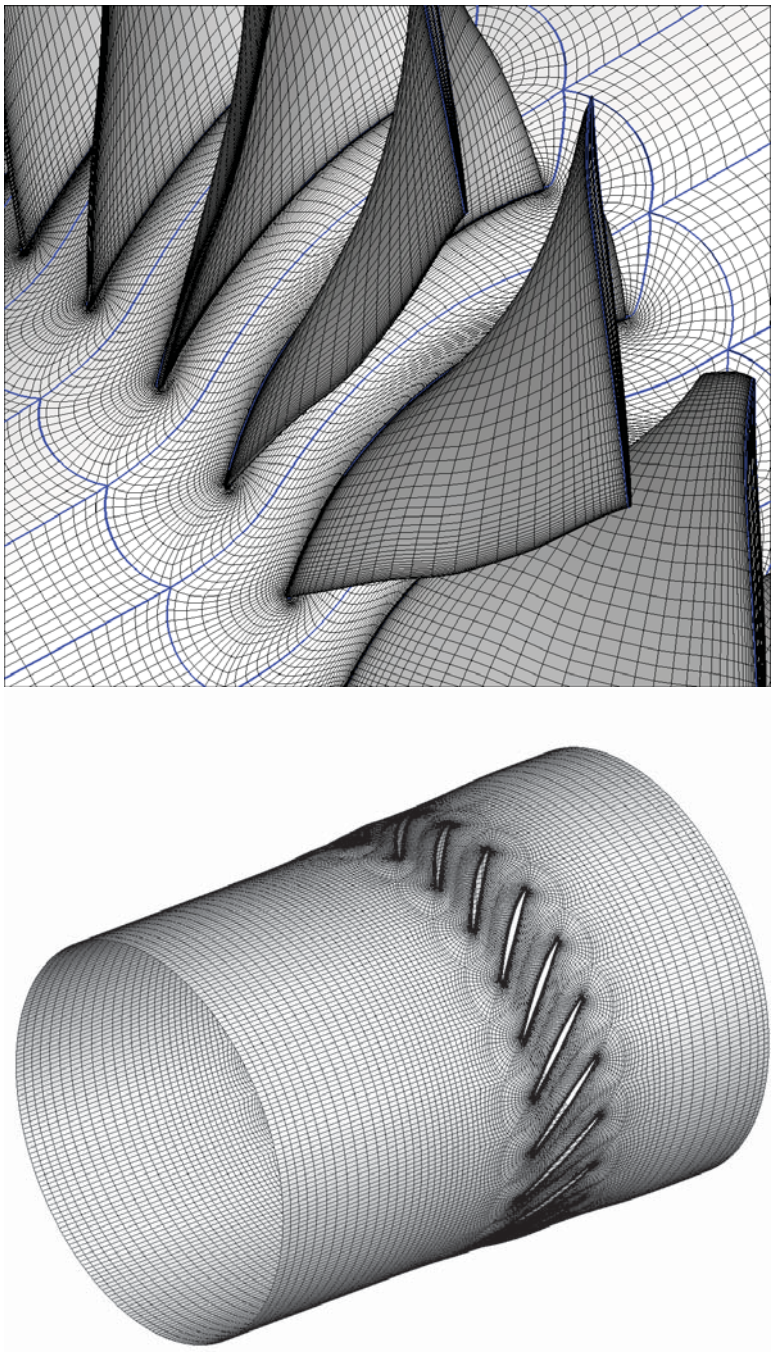

Figure 8.37: Full annulus grid of NASA Rotor 67 using H-O-H mesh topology used for the rotating stall simulation

For the full annulus, H-O-H mesh topology presented in Fig. 8.37 is used to improve mesh quality and density around the blades. The effect of grid size on solution accuracy for Rotor 37 using H-O-H grids with O-grid tip clearance region by McNulty [132] shows remarkably similar predictions using three grids approximately with 2000,000, 350,000 and 400,000. Similar results are obtained for the mesh refinement study using the single passage in this study. Their mesh size is similar or coarser than what we used. Khaleghi et al. [81] uses a NASA Rotor 67 full annulus mesh with about 6 million grid points to capture the stall cell rotating at about 30% of rotational speed. The mesh size of a single blade used by Khaleghi et al. [81] is also very similar to what we used. The steady state mesh refinement study conducted in this paper indicates that the solution is converged based on mesh size. The excellent agreement between the predicted radial profiles of Rotor 67 compared with the experiment also evidences that the mesh is fine enough to resolve the wakes. The low diffusion E-CUSP scheme employed in the paper also contributes to minimize the numerical diffusion and hence mesh size

Considering a disturbance with its wavelength on the order of the circumference, it is desirable to locate the boundary of the computational domain far away from the rotor blade. In this study the inlet and outlet plane are located 7 and 6 axial tip chord length respectively away from the rotor. The 1*st* grid spacing on the blade surface was set to 5×10^{-5} times the blade hub chord length which gives $y^+ < 3$, while on the hub and casing surface it was set to 2×10^{-3} times blade hub chord which can give y^+ around 50. Therefore, the wall function BCs are used on the hub and casing.

8.5.3 Code Validation

To validate numerical methods used in this study, single passage simulations using the SA turbulence model were performed before the full annulus simulations. Periodic boundary conditions were employed at lower and upper boundary. Grid refinement test was first carried out using three different grids. The experimental data used for validating the numerical results are those reported by Strazisar et al. [130]. In their report, aerodynamic performance measurements were made at 2.473cm upstream of the leading edge(Aero station 1), 27.38% of blade root chord, and at 1.981cm downstream of the trailing edge(Aero station 2), 21.94% of blade root chord. To make an accurate comparison between numerical and experimental results, the locations of boundary, tip clearance, and inlet and outlet flow conditions given by the experiment are used. The mesh refinement tests are conducted using three different mesh sizes. Mesh A is 121(around blade) $\times$ 60 $\times$ 39(span), mesh B is 161 $\times$ 80 $\times$ 52 shown in Fig. 8.36, and mesh C is 201 $\times$ 100 $\times$ 65.

The predicted rotor speed line at 100% speed is presented in Fig. 8.38. The computed and experimental mass flows are normalized using the corresponding choked mass flow rate. The calculated mass flow at choke condition was 34.50 kg/sec, 1.3% lower than the experimental value of 34.94 kg/sec. The total pressure ratio predicted by mesh A is slightly lower than fine mesh results. The predicted adiabatic efficiency at 100% speed is presented in Fig. 8.39. The predicted near peak efficiency was 91.37% using mesh C, 1.63% lower than experiment, while 90.86% with mesh B and 90.98% with mesh A were predicted. Such prediction error is within the acceptable range [143, 144].

The spanwise distribution of experimental and computed total pressure, total temper-

ature, absolute flow angle(α), and adiabatic efficiency obtained by mesh B are shown in Fig. 8.40 and Fig. 8.41. All quantities used for comparison are circumferentially mass averaged in the same way as in the experiment. The predicted results agree very well with the experiment, especially the flow angle near the rotor tip region for both peak and near stall condition. The present numerical schemes capture the total pressure deficit around 40% span very well.

The predicted shock structures near peak and near stall are presented in figure 8.42 and 8.43. These also agree well with measured contour plots presented in the report [145]. Two distinct shocks exist; a detached or nearly attached bow shock and a passage shock. Near peak condition shows both shocks but weak, however near stall there is one strong bow shock. This is believed that the passage shock shown near peak is shifted upstream of blade blade leading edge due to increase in back pressure and eventually two shocks are combined as a strong detached shock. This can explain the reason why the efficiency near stall is lower than peak efficiency.The fact that compression process with split shocks can reduce total pressure loss or shock loss when it goes under one strong normal shock.

For comparison, the DES simulation at near stall was carried out using the mesh C. The predicted rotor pressure ratio of DES is 0.04% lower than that of the RANS, while the predicted rotor adiabatic efficiency is 88.2% by the RANS and 89.1% by the DES. Such a difference is within the result uncertainty. Hence the URANS and the DES are considered as producing the similar near stall simulation due to no serious flow separation occurring in the flow field. This can be further seen in Fig. 8.44, which is the Mach number contours of blade tip span calculated by the RANS(top) and DES(bottom). Both the DES and RANS capture well the strong bow shocks near leading edge and the interaction with tip leakage.

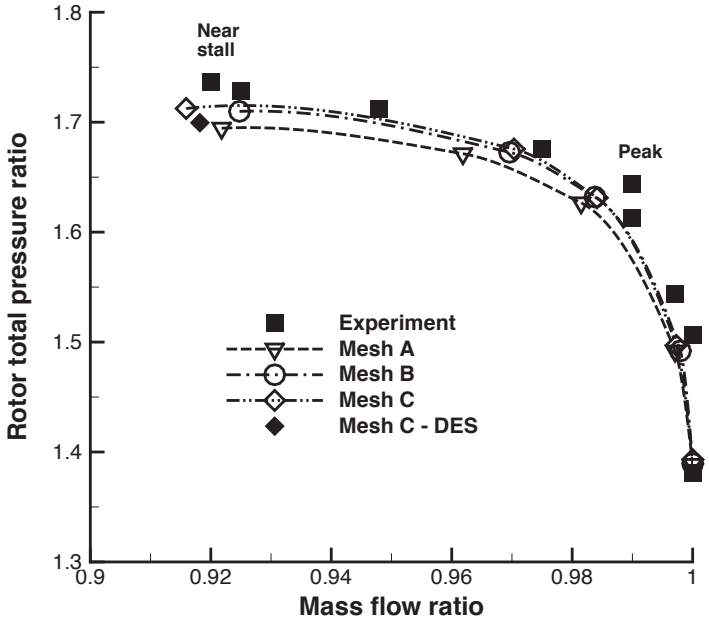

Figure 8.38: Predicted rotor speed line

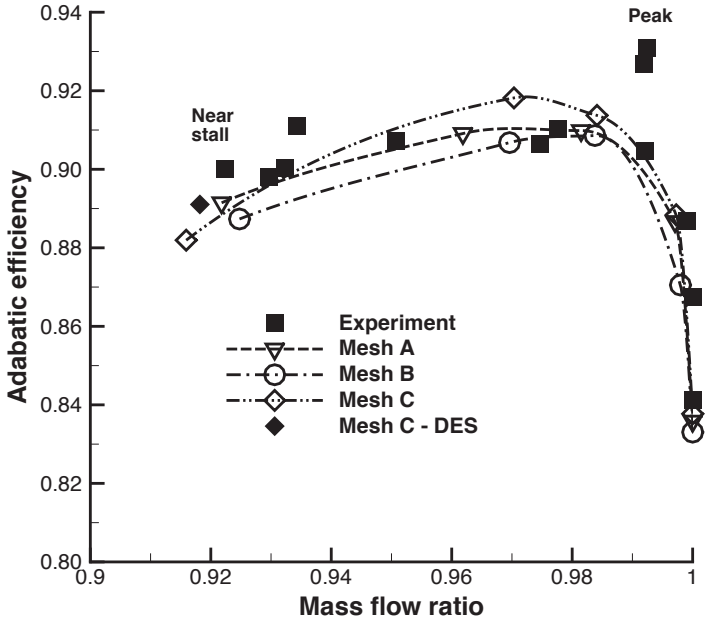

Figure 8.39: Predicted adiabatic efficiency

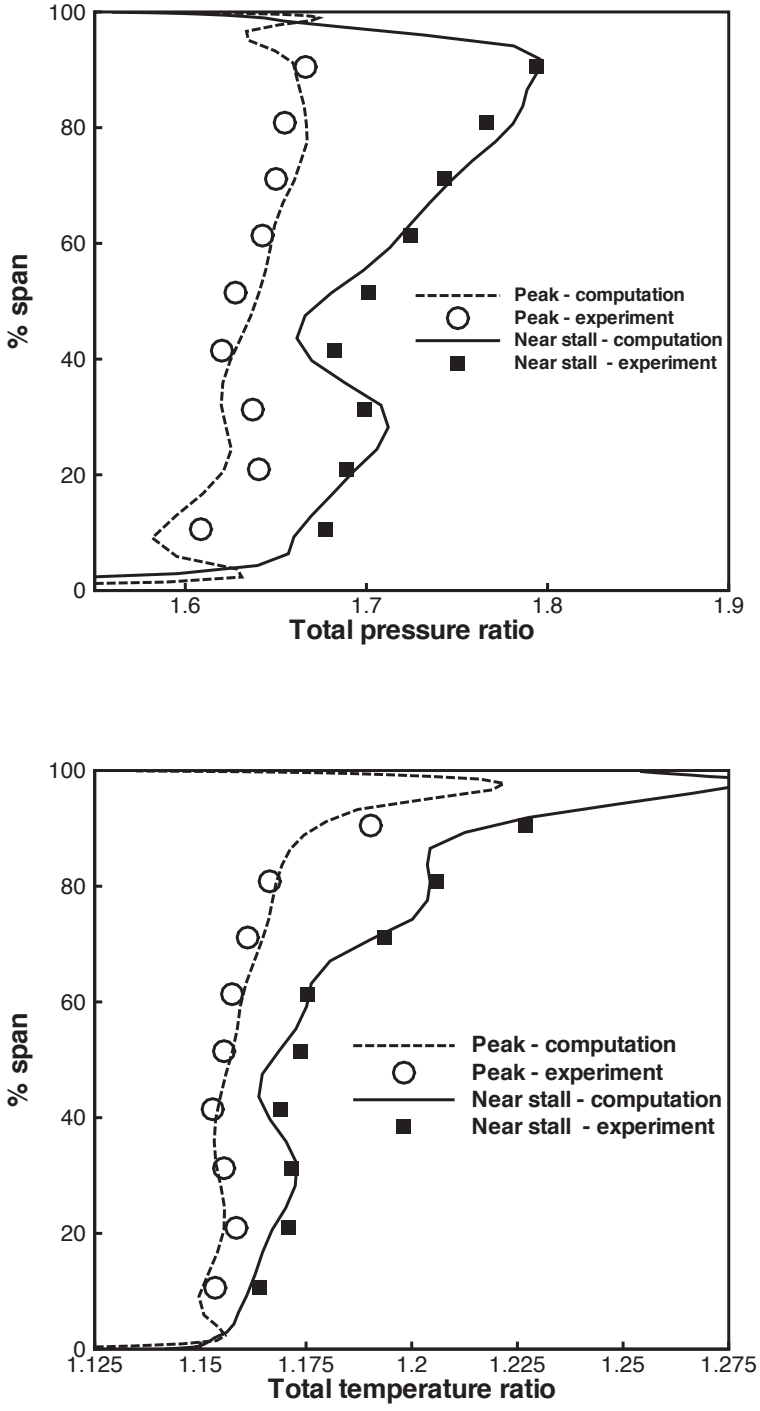

Figure 8.40: Spanwise distributions of pitchwise mass-averaged quantities at peak efficiency and near stall; total pressure(top), total temperature(bottom)

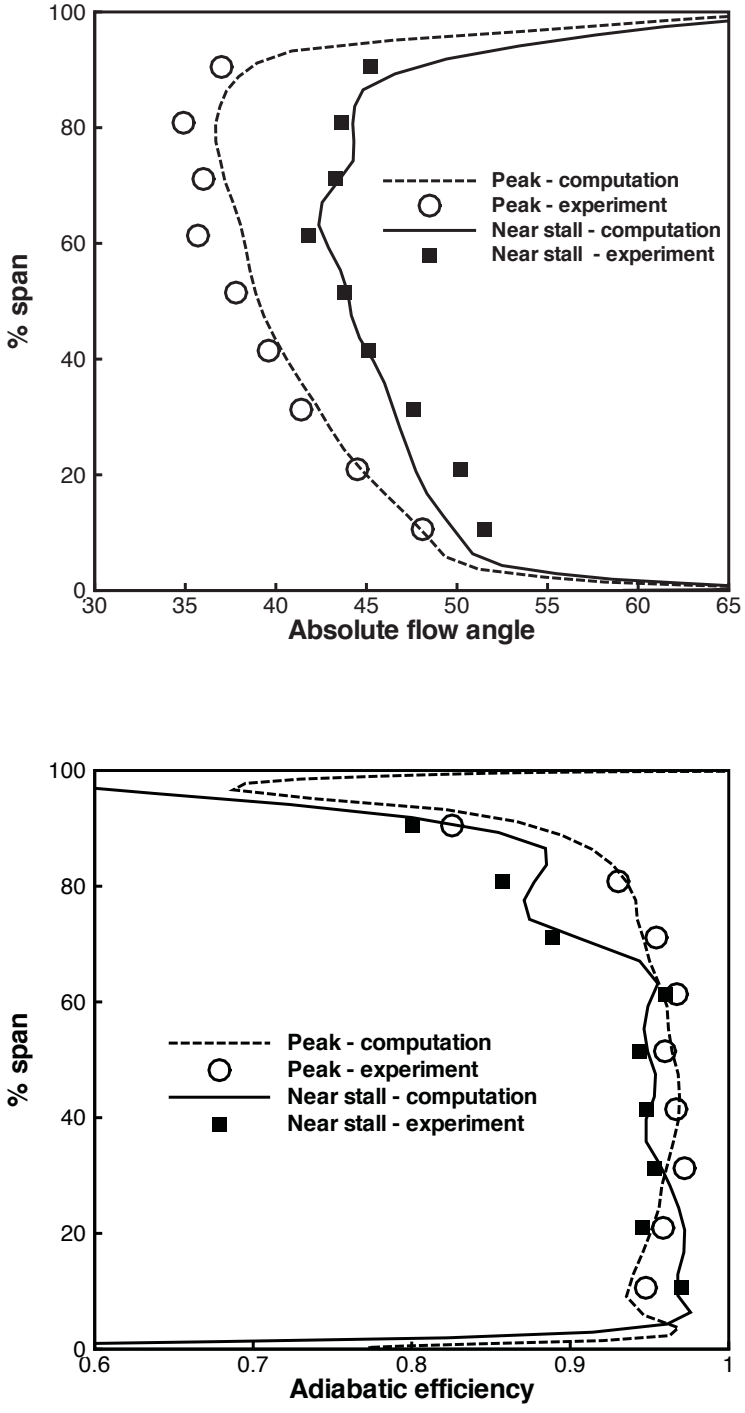

Figure 8.41: Spanwise distributions of pitchwise mass-averaged quantities at peak efficiency and near stall; absolute flow angle(top), adiabatic efficiency(bottom)

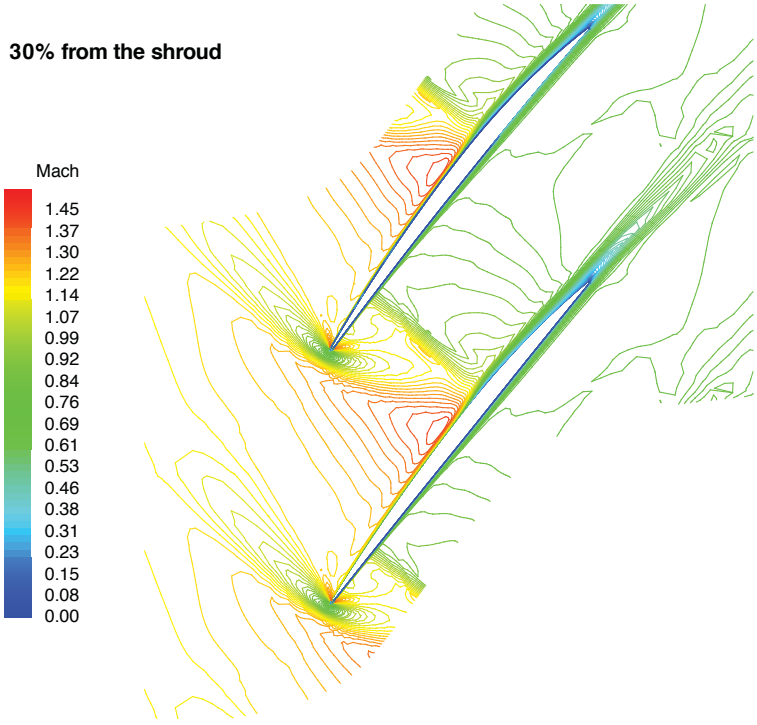

Figure 8.42: Predicted shock structure at 30% span from the shroud at near peak

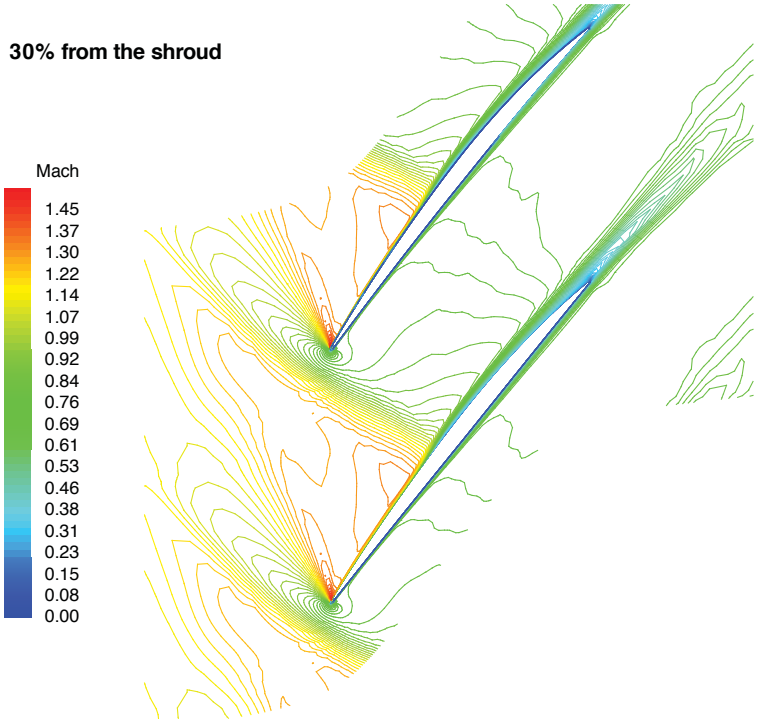

Figure 8.43: Predicted shock structure at 30% span from the shroud at near stall

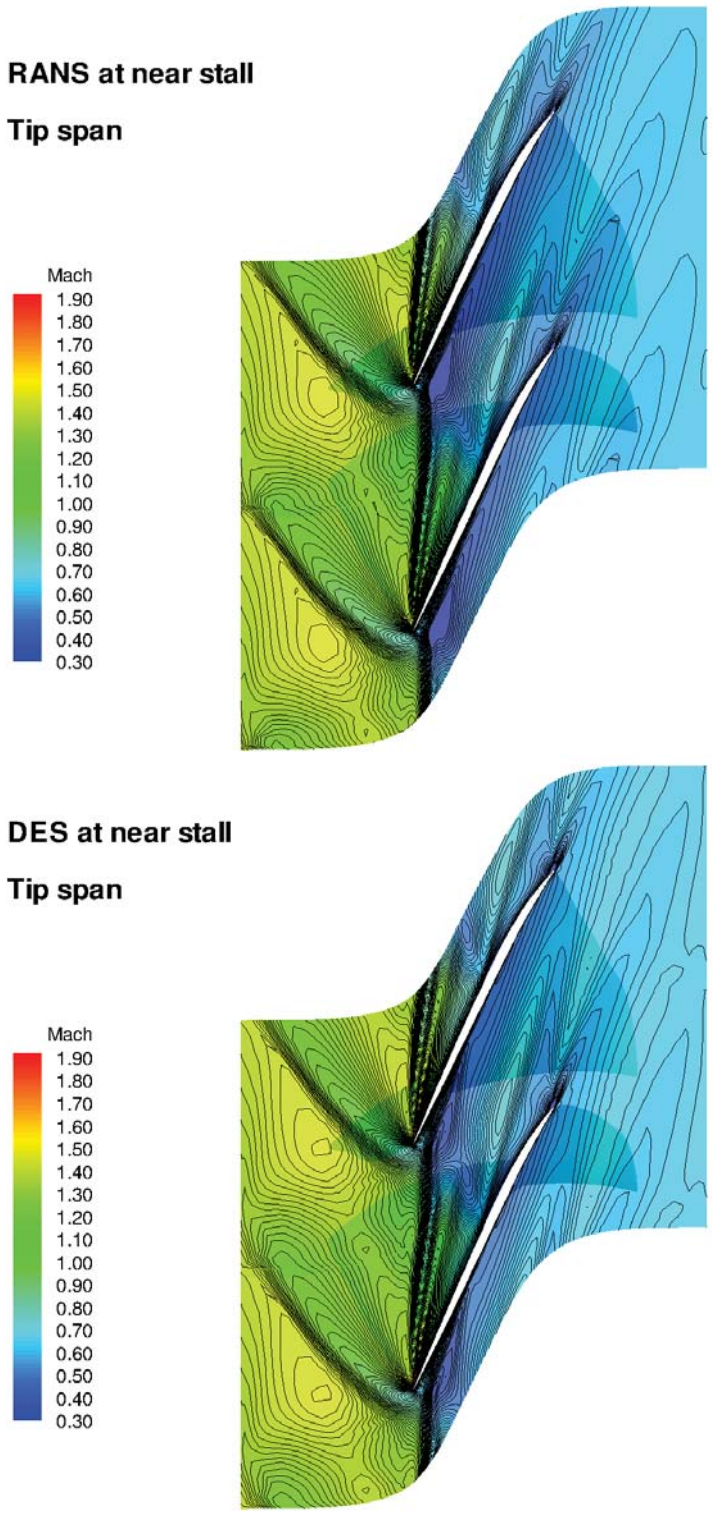

Figure 8.44: Predicted Mach number contours at near stall; RANS(top), DES(bottom)

8.5.4 Detached Eddy Simulation of Rotor 67 Rotating Stall

The full annulus unsteady simulation begins with near stall(or near peak of the rotor characteristics) solutions obtained by the RANS simulation [146]. This approach is employed by other researchers [79–81] for the rotating stall simulations in order to reduce computing efforts.

Fig. 8.45 shows the L2 norm residual convergency history obtained by the RANS simulation at choke, which uses 3000 iterations to achieve the residual of 10^{-9} and the mass flow is converged around 1200 iterations.

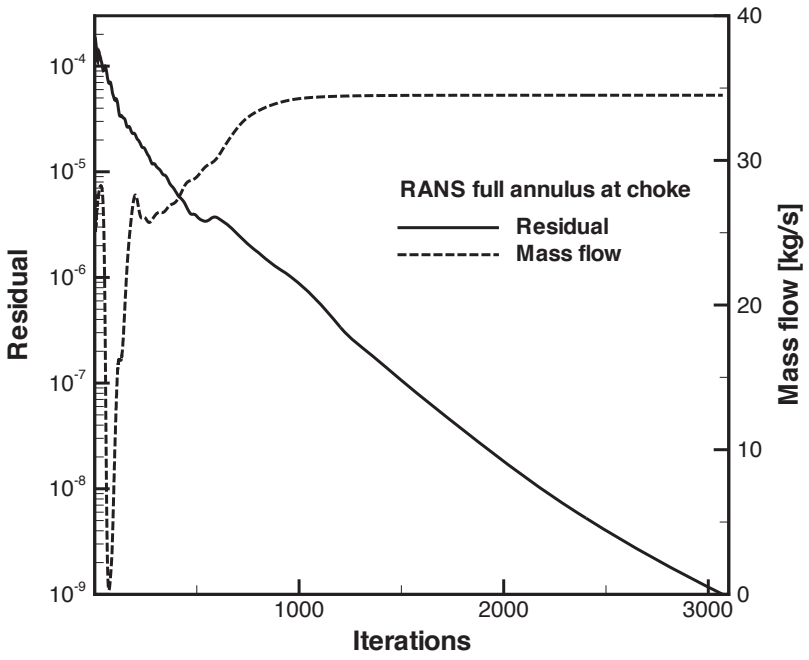

Figure 8.45: Mass flow and residual convergence at choke

It takes a few rotor revolutions for the unsteady simulations using the full annulus to have the spike type rotating stall fully developed. The residual as defined by the right hand side of Eq. (5.94) is reduced three orders of magnitude in each physical time step.

A time step of around 0.000009 sec. is used. The study by Copenhaver et al. [147] shows a time step of 0.00025 sec. is necessary to capture shock instability in a transonic rotor. Hah et al. [148] used a time step of 0.0000125 sec. for predicting the stall inception of a similar high speed rotor originated by the interaction of the passage shocks and tip leakage vortices. As aforementioned, the rotating speed of the spike type stall cell in a high-speed compressor is roughly half of the rotor rotational frequency [74, 75], the time step size adopted in this study is significantly smaller than those used by all other researchers and is sufficient to resolve the primary flow features during the stall inception.

8.5.5 Stall Pressure Rise Characteristics

The predicted rotor total-to-static pressure rise characteristics are illustrated in Fig. 8.46. The dashed line labeled with arabic number is predicted by the DES and the solid line labeled with alphabet is predicted by the URANS.

For the DES, the rotor stalls at a positive slope of the total-to-static pressure rise characteristic. The onset of rotating stall is observed at 0.75 revs, which is point 4 in the characteristics. There is abrupt pressure drop between point 9(2.0 revs) and point 11(2.5 revs). The primary stalling event at point 9 is that rotating stall quickly grows toward inner span with the occurrence of the second stall cell, which will be further discussed in the following sections.

For the URANS the stall onset occurs at point d(1.5 revs), which is near zero slope of the characteristic. The inception predicted by the DES is spike type. The stall onset predicted by the URANS is 1.25 revs later compared to the DES. The URANS shows a

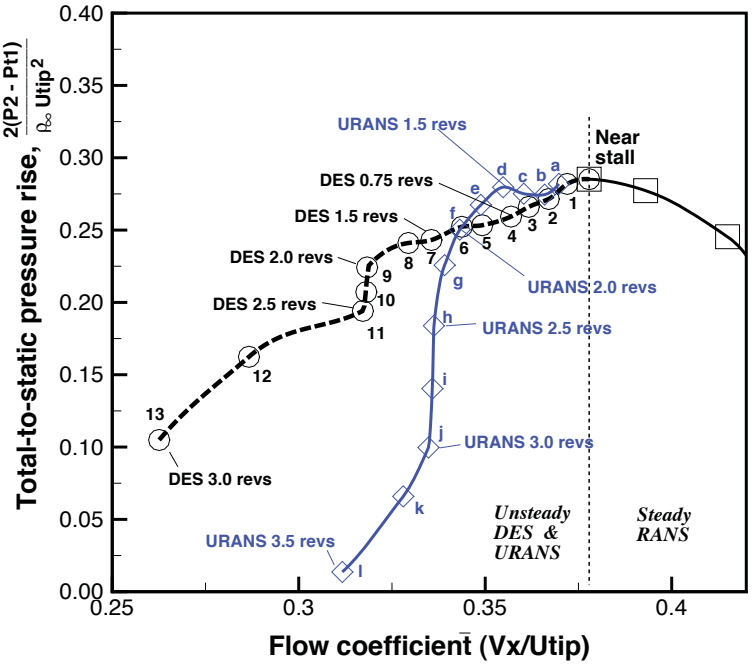

Figure 8.46: Rotor total-to-static pressure rise characteristics; DES(the dashed line), URANS(the solid line with diamond), RANS(the solid line with square)

sharper pressure drop than the DES during the stall process.

Rotating Stall Onset and Propagation

Rotating stall is usually initiated around rotor tip. The numerical probes are hence located at the rotor tip 50% tip chord length upstream and downstream as sketched in Fig. 8.47.

Fig. 8.48 represents the circumferential distributions of the upstream static pressure at the rotor tip span predicted by the DES and the URANS during the stall inception. An evidence of spike type inception, a local pressure increase, is well captured by the DES. Obviously the phase locked oscillation is broken in the spike region. The annulus region containing the spike is about $180^\circ \sim 340^\circ$ at 1.375 revs. Fig. 8.48 also indicates that

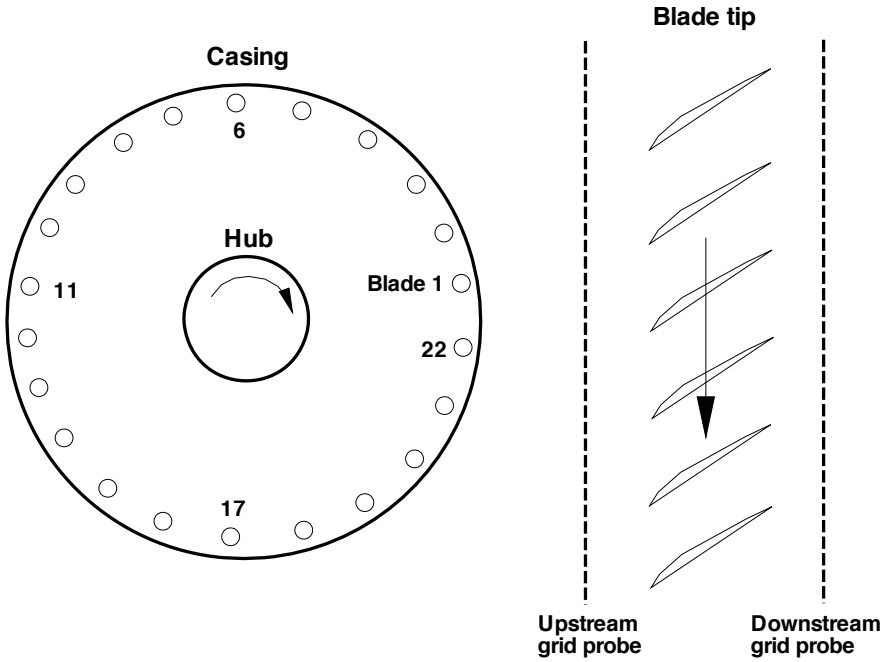

Figure 8.47: Location of the numerical measurement probe

the stall inception predicted by URANS is spread over the whole rotor annulus, whereas the spikes by the DES are distributed only for a limited area. The type of stall inception predicted by the URANS is more like a modal type instead of spike type.

The circumferential distributions of the upstream axial velocity at the rotor tip span are presented in Fig. 8.49. The velocity decrease spike is clearly captured by the DES. The peak amplitude predicted by the URANS is smaller than the DES, whereas the frequency of the oscillation is about same as the DES.

The term "stall cell" used in the current study is to describe a continuous structure of disturbances. Fig. 8.50 shows the variations of instantaneous axial velocity at the rotor tip upstream by the DES and the URANS. The stall cell speed can be determined by the angle

of pressure/velocity field rotation and the duration. Both the DES and the URANS show that the stall cells propagate at 48% of the rotor speed in the opposite direction of the rotor rotation. The rotating stall is fully developed within 2 rotor revolutions for both the DES and the URANS. Hah et al. [75] recently reported the experiment on a high speed axial rotor with supersonic tip similar to NASA Rotor 67. In their observations, the spike type rotating stall is fully developed at about 2 rotor revolutions and the stall cell rotates roughly at half of the rotor speed.

Fig. 8.51 illustrates the variations of instantaneous static pressure at the upstream of the rotor tip. The second stall cell propagates slower by 11% for the DES and by 5% for the URANS.

The stalled flow at the rotor downstream can be more turbulent than the upstream due to the flow separation in the stalled passage and its convection to downstream. Fig. 8.52 shows the time traces of axial velocity at the downstream of the rotor tip. Compared to upstream, the flow field is more fluctuating for the DES. The speed of the stall cell propagation is about the same between the RANS and DES.

Fig. 8.53 illustrates entropy contours at the axial cross section of near rotor leading edge. Entropy stands for the degree of energy loss, hence high entropy reflects the stalled portion of the annulus. Both the DES and the URANS demonstrate the rotating stall starts from the rotor tip area, and grow along the circumference as well as inward. Both stall cells are developed to the whole annulus roughly for two rotor revolutions. In the case of DES, the second stall cell is visible at 2.0 revs. Particularly the abrupt and large disturbance originated from the rotor tip is captured at 2.0 revs by the DES. A large structure of vortical flow that plays a role in the stalled area will be shown in the section of tip clearance vortex.

Fig. 8.53 also indicates that the top 50% of blade span is stalled within 2 rotor revolutions for both the DES and the URANS simulations. The rotating stall predicted by the DES is a part-span stall since more than one local stall cells are merged into one big stall cell as the rotating stall develops.

Fig. 8.54 shows instantaneous negative axial velocity contour at the rotor tip span. The negative axial velocity represents the stalled area. The DES shows that the primary stall cell is identified by about 6 to 7 stalled passages at 0.75 revs(onset), and grows over half annulus at 2 revs. For the URANS, the primary stall cell is seen at 1.5 revs(onset) with its length scale about same as the DES, and extends over half annulus at 2.5 revs. The second stall cell is observed at 2 revs for the DES, whereas the occurrence of the second stall is not clear for the URANS. Overall the rotating stall predicted by the DES is more chaotic and realistic.

Fig. 8.55 shows the radial distributions of total pressure ratio and absolute flow angle at downstream during rotating stall. At near stall, the RANS using the full annulus shows good agreement with the experiment. Total pressure ratio predicted by the URANS is significantly decreased compared to the DES. In particular, the DES shows the total pressure suddenly drops between 1.75 revs and 2.25 revs. It was found in the present study that the stalled area quickly extends to the whole annulus with the appearance of the second stall cell observed around 2 rotor revolutions. Both the DES and the URANS show that the flow field is disturbed up to 40% span with increasing absolute flow angle within 2 revs from the onset. Increase in absolute flow angle implies decrease in the mass flow.

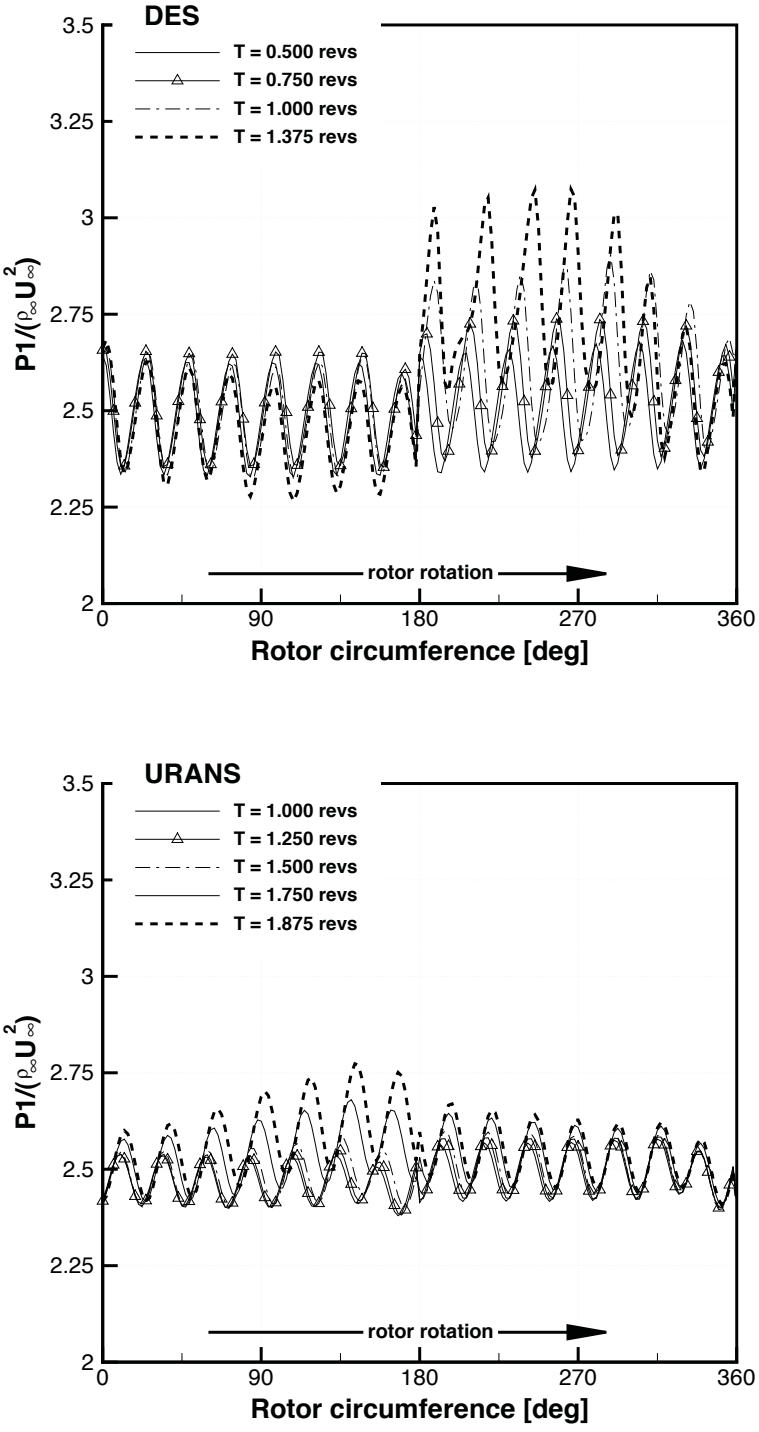

Figure 8.48: Circumferential static pressure distributions during the stall inception at the upstream of the rotor tip span; DES(top), URANS(bottom)

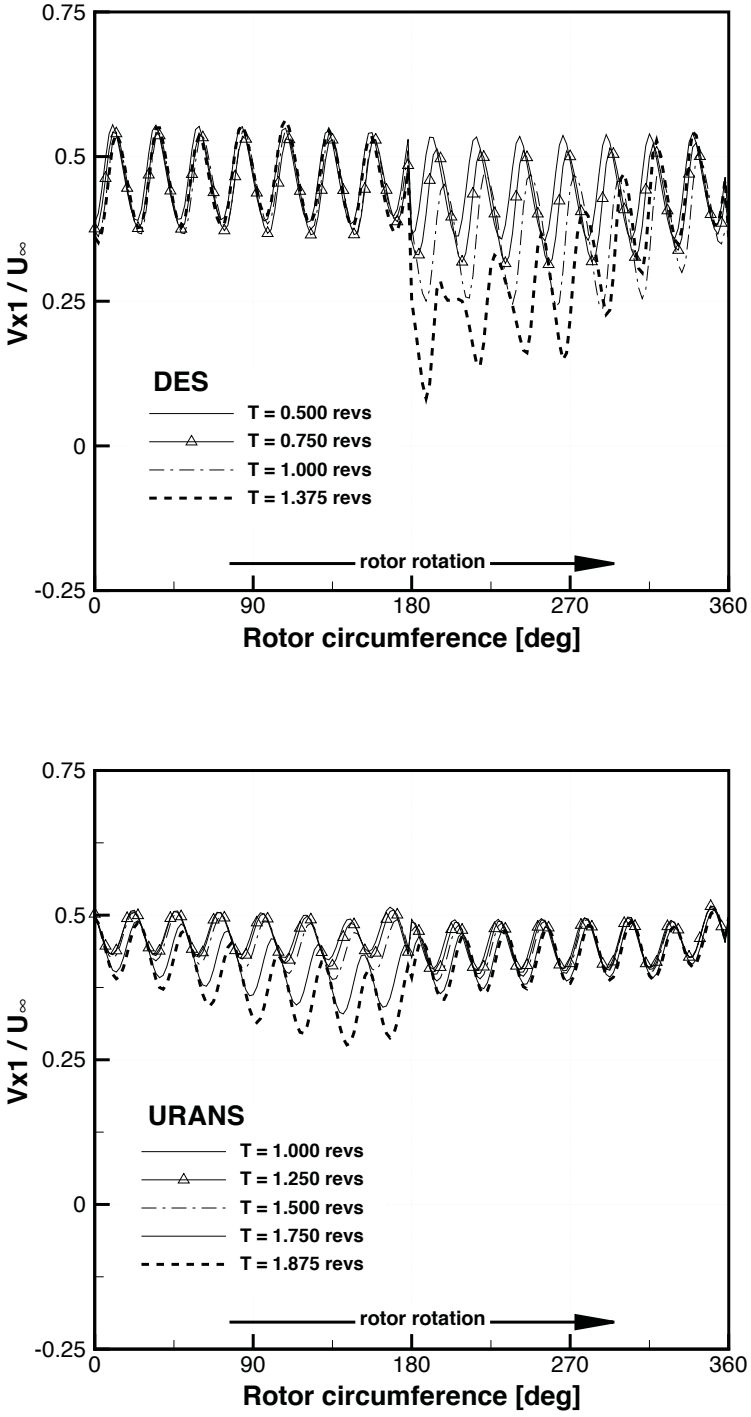

Figure 8.49: Circumferential axial velocity distributions during the stall inception at the upstream of the rotor tip span; DES(top), URANS(bottom)

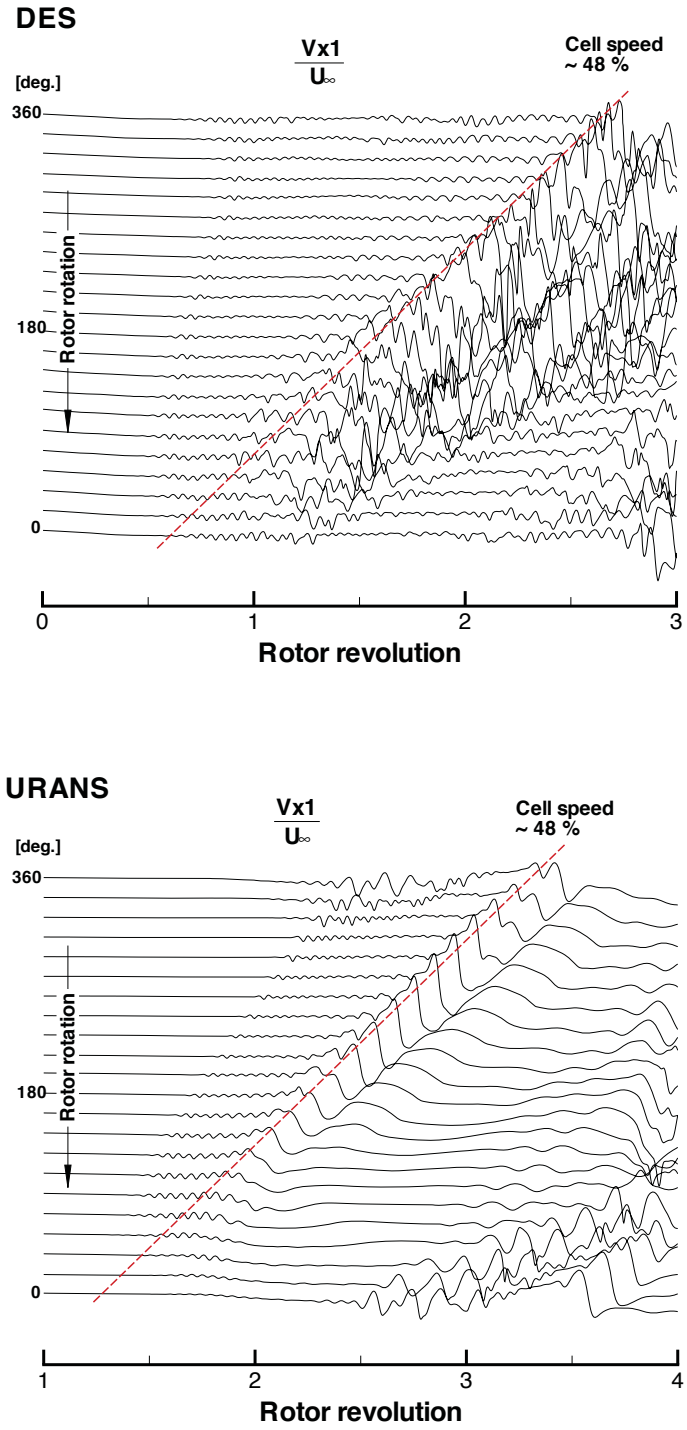

Figure 8.50: Time traces of axial velocity at the upstream of the rotor tip span; DES(top), URANS(bottom)

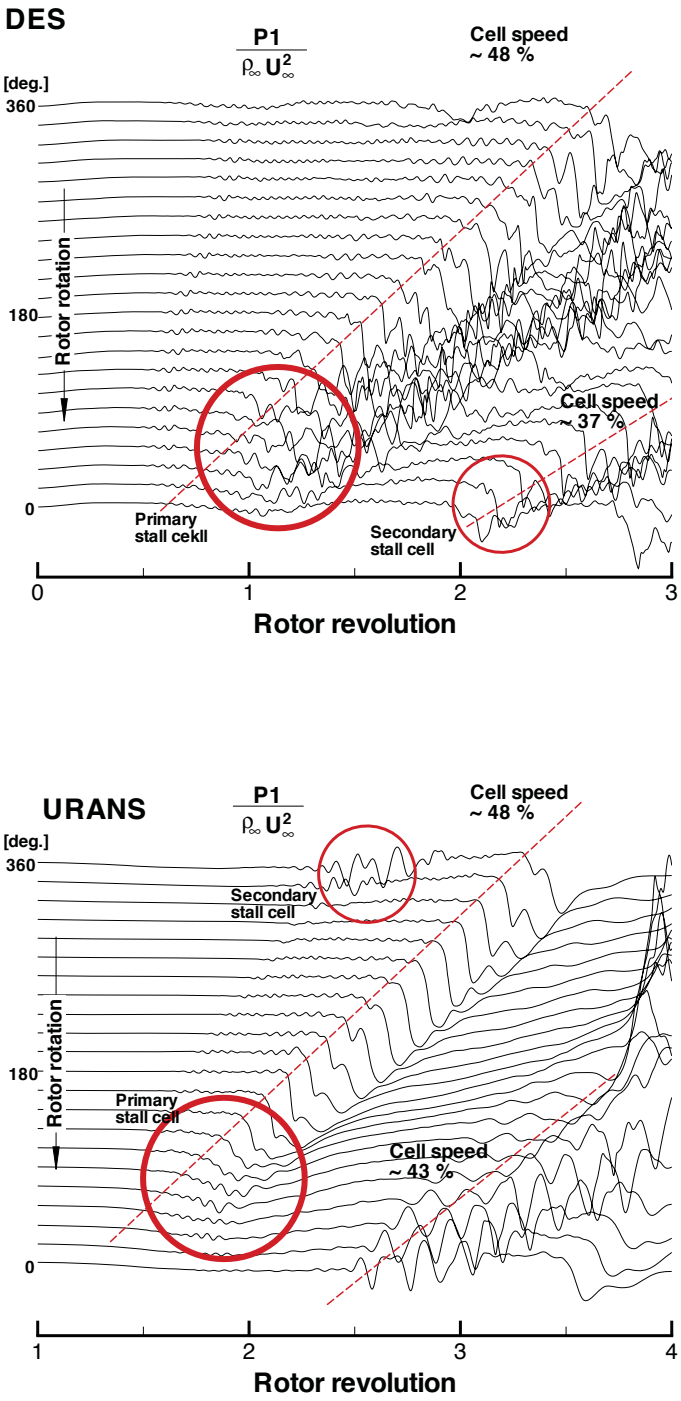

Figure 8.51: Time traces of static pressure at the upstream of the rotor tip span; DES(top), URANS(bottom)

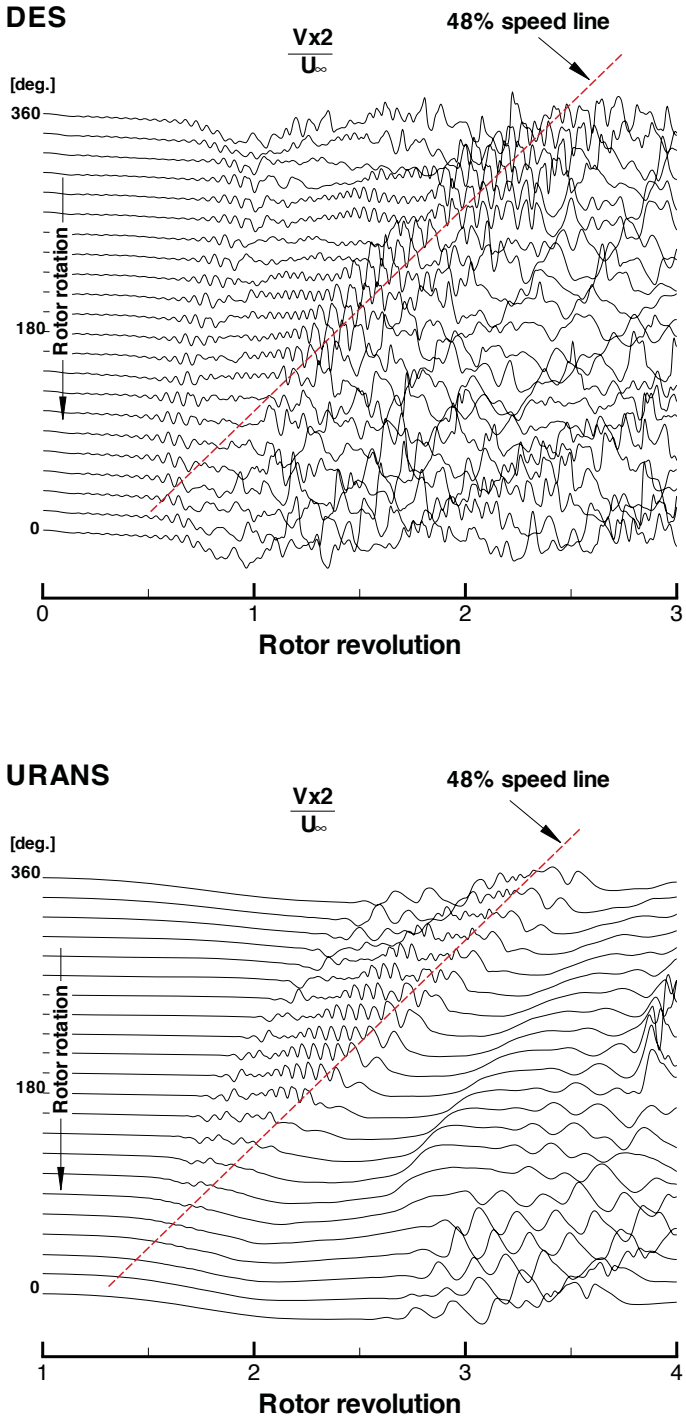

Figure 8.52: Time traces of axial velocity at the downstream of the rotor tip span; DES(top), URANS(bottom)

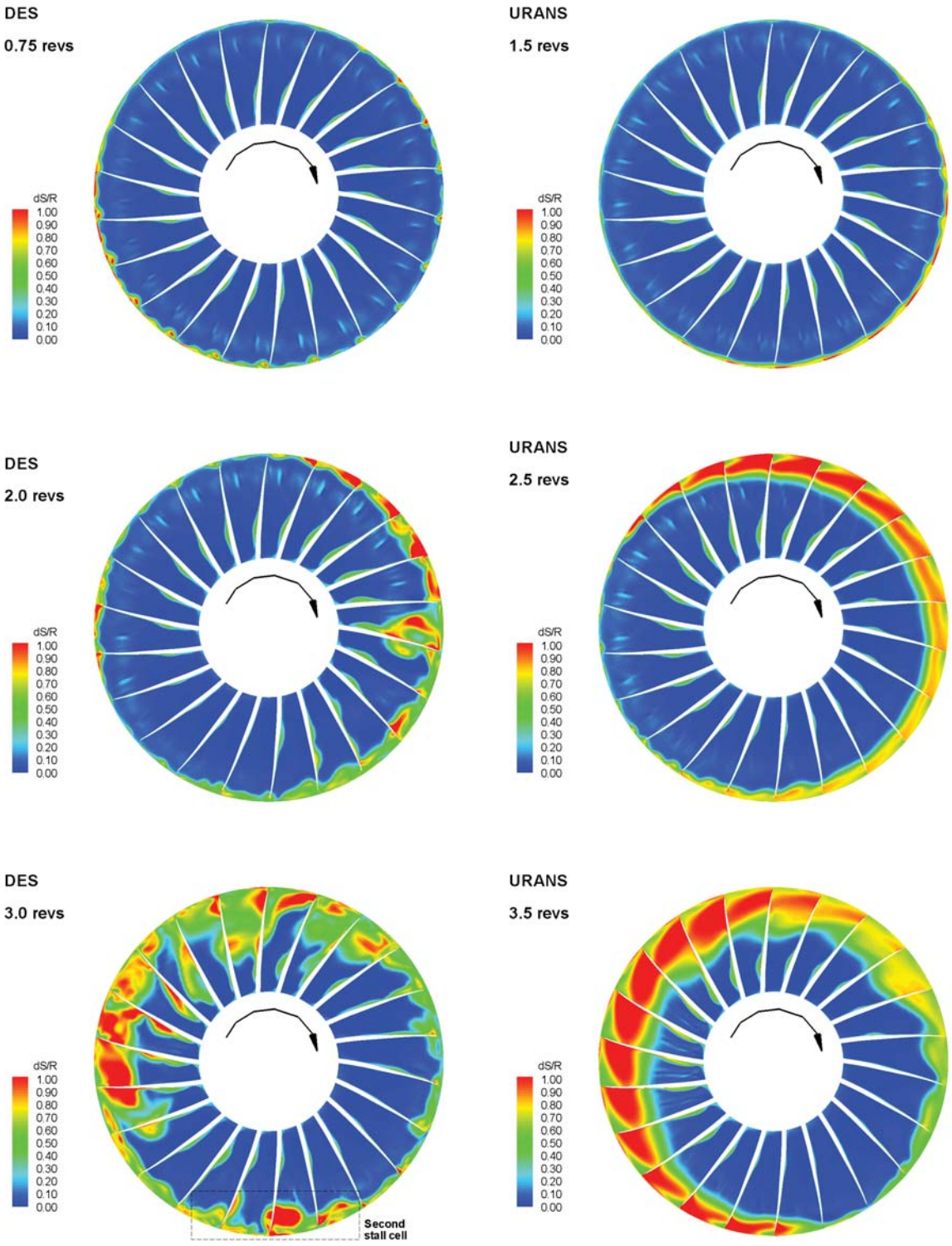

Figure 8.53: Entropy change of axial plane near rotor leading edge during the rotating stall; DES(left), URANS(right)

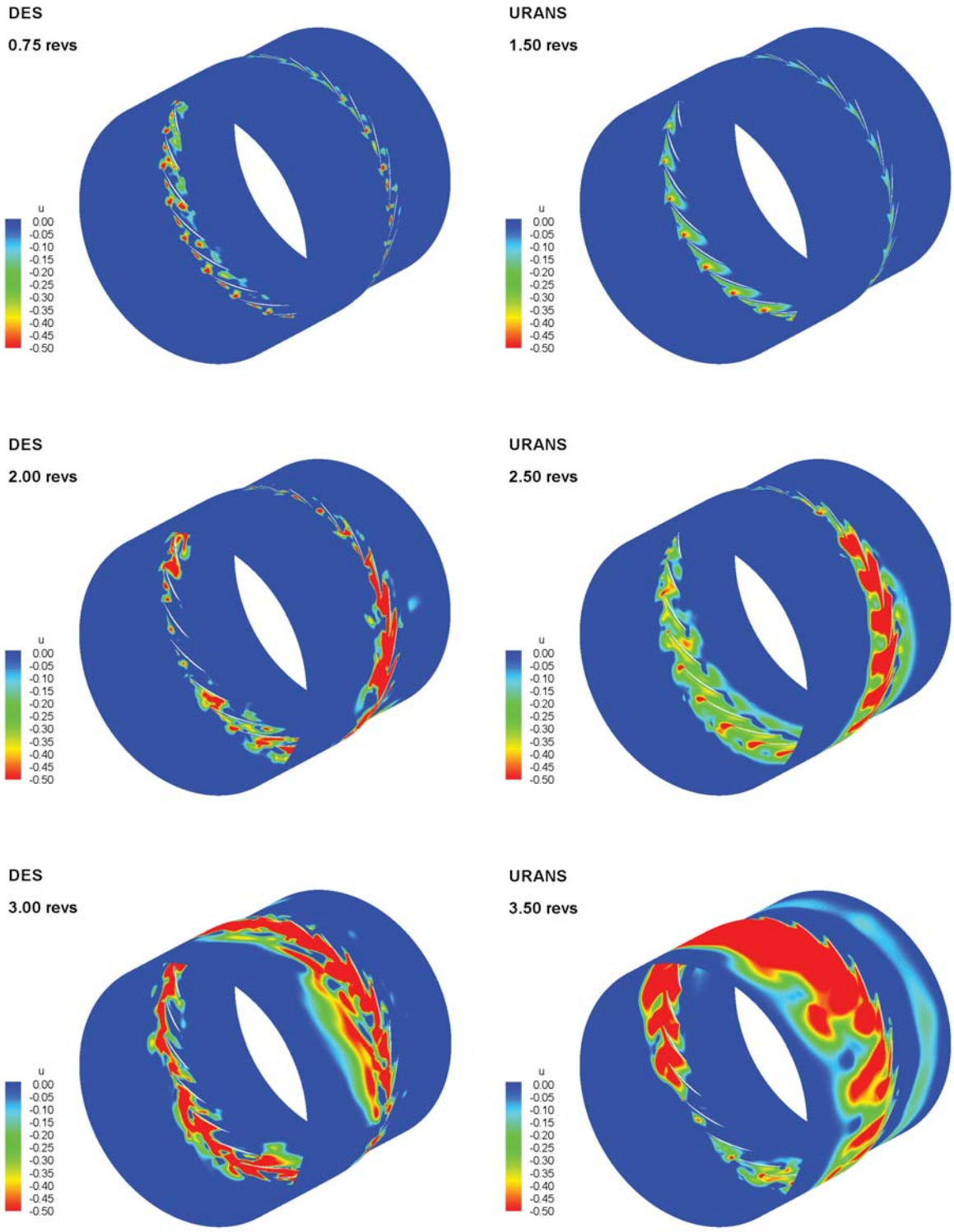

Figure 8.54: Contour of negative axial velocity at the rotor tip span during the rotating stall; DES(left), URANS(right)

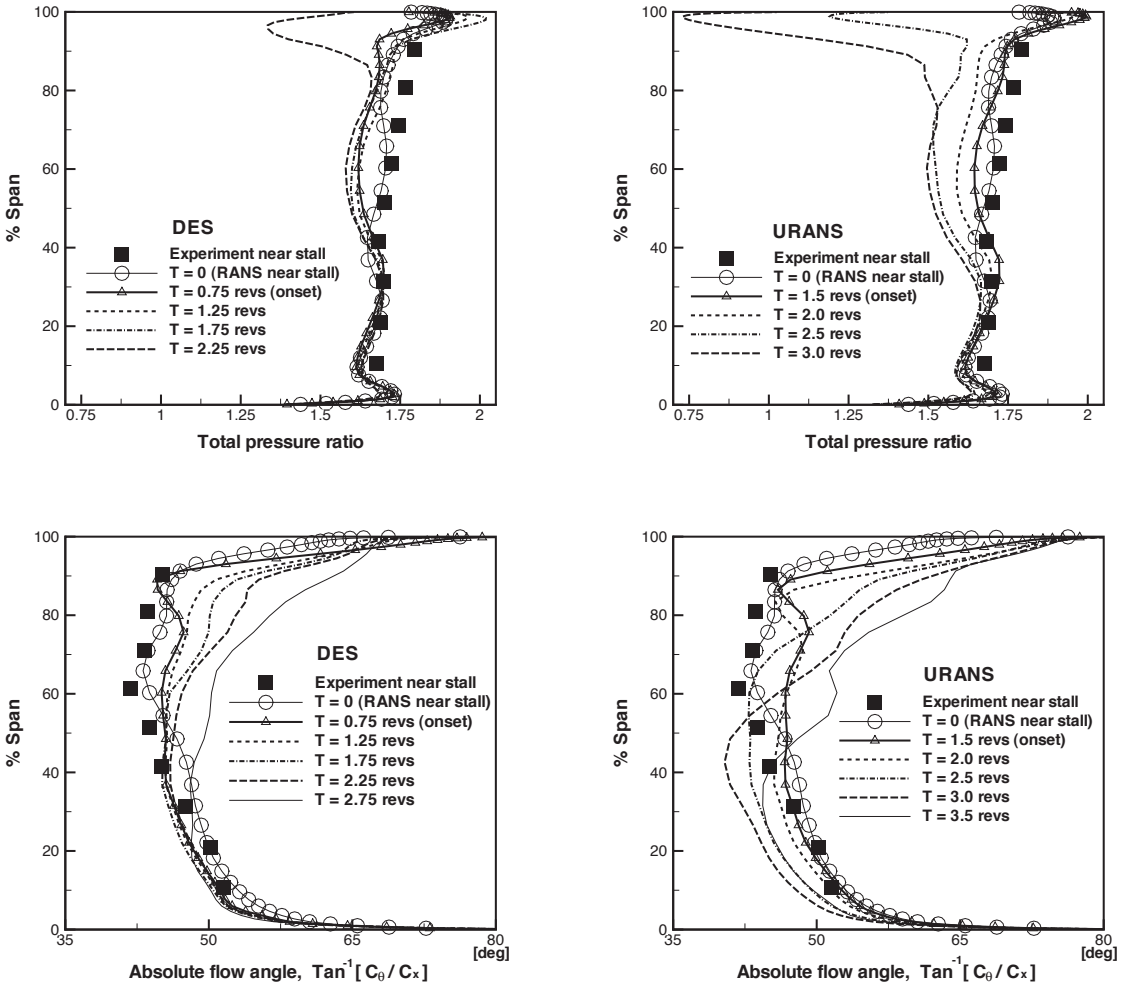

Figure 8.55: Spanwise distributions of pitchwise mass-averaged quantities during the rotating stall; total pressure ratio by DES(top left) and by URANS(top right), absolute flow angles by DES(bottom left) and by URANS(bottom right)

Role of Tip Clearance Vortex

The rotating stall observed in this study is initiated from the rotor tip region. Investigation on the tip leakage flow structure and its effect on the stall inception are discussed in this section at four time instances, before half rotor revolution prior to stall onset, at the onset(0.75 revs by the DES, 1.5 revs by the URANS), half rotor revolution after the onset, and one and half rotor revolution after the onset. The tip leakage flow structure half rotor

revolution prior to the onset is shown in Fig. 8.56. Near the tip leading edge the incoming flow is rolled up by the tip leakage jet, and a vortex structure is formed. The Mach number contours indicate that the sonic boundary is attached to the blade passage.

Fig. 8.57 illustrates the tip leakage flow structure at the onset of rotating stall. The spilled flow from the rotor tip clearance to the next blade is captured by both the DES and the URANS. However, the back flow is not observed at the onset of rotating stall. In this study, the reverse flow near the rotor tip trailing edge is observed within half rotor revolution after the onset. The tip leakage vortex near the rotor tip leading edge is obviously captured by the DES. The leading edge spillage flow from the previous blade tip clearance is seen behind the detached sonic boundary where the flow is subsonic.

Fig. 8.58 shows the tip leakage flow structure colored with total pressure half rotor revolution after the onset. The flow near rotor tip trailing edge goes back to the blade passage for both the DES and the URANS. The flows through the tip clearance are spilled to the next blade due to the severe blockage generated by the vortex structure with very low total pressure. The DES predicts the tip flow field in highly three dimensional, chaotic, and complex manner, whereas the tip flow structure by the URANS model is well organized and repetitive over the stalled blade passages.

Fig. 8.59 illustrates the formation of tip clearance vortex about one and half rotor revolution after the onset of rotating stall. Compared to the stall onset, the disturbance length scale is dramatically grown, and the path area of the spillage flow is much extended toward rotor upstream. In particular, the DES demonstrates that the vortical flow structure originated at the rotor tip travels counter to the rotor rotation at the rotor upstream. Consequently the flow field surrounding the vortex is highly disturbed with significant entropy

increase. It explains how the rotating stall quickly develops to the whole annulus through the spike inception.

8.5.6 Summary

The unsteady detached eddy simulation (DES) was conducted to investigate rotating stall in a full annulus transonic rotor - NASA Rotor 67. Before rotating stall simulations, the single passage calculations using the RANS and the DES were performed from the choke to the near stall condition in order to validate the numerical methods employed in this study. The predicted radial profiles including total pressure, total temperature, absolute flow angle, and adiabatic efficiency showed good agreement with the experiment. The flows predicted by the DES and the RANS with periodic boundary are similar before the near stall point due to no serious flow separation.

The DES shows that the rotor stalls though the spike inception. The spikes observed for 6 to 7 blade passages at the rotor tip span propagates at 48% of the rotor speed in the opposite direction of rotor rotation. The stall cell that contains the spikes extends to the full annulus roughly within 2 rotor revolutions. The second stall cell followed by the primary stall cell rotates at a 11% lower speed, and is eventually merged with the primary stall cell.

Rotating stall predicted by the URANS is a deep stall with large pressure drop, but the stall cell rotates at the same speed and in the same direction as predicted by DES. However, the occurrence of the second stall cell is not clearly captured by the URANS. In addition, the type of stall inception predicted by URANS is not as clear as the spike pattern predicted by DES and is more like a modal inception.

The route to rotating stall is demonstrated by both the DES and the URANS. The flows through tip clearance are spilled to the next blade behind the sonic plane due to the severe blockage created by the vortex structures in passages. The reverse flow near the rotor trailing edge is observed after the onset of the rotating stall. The DES shows that the vortical flow structures originated from the rotor tip have a large effect on the disturbance development during the spike type rotating stall.

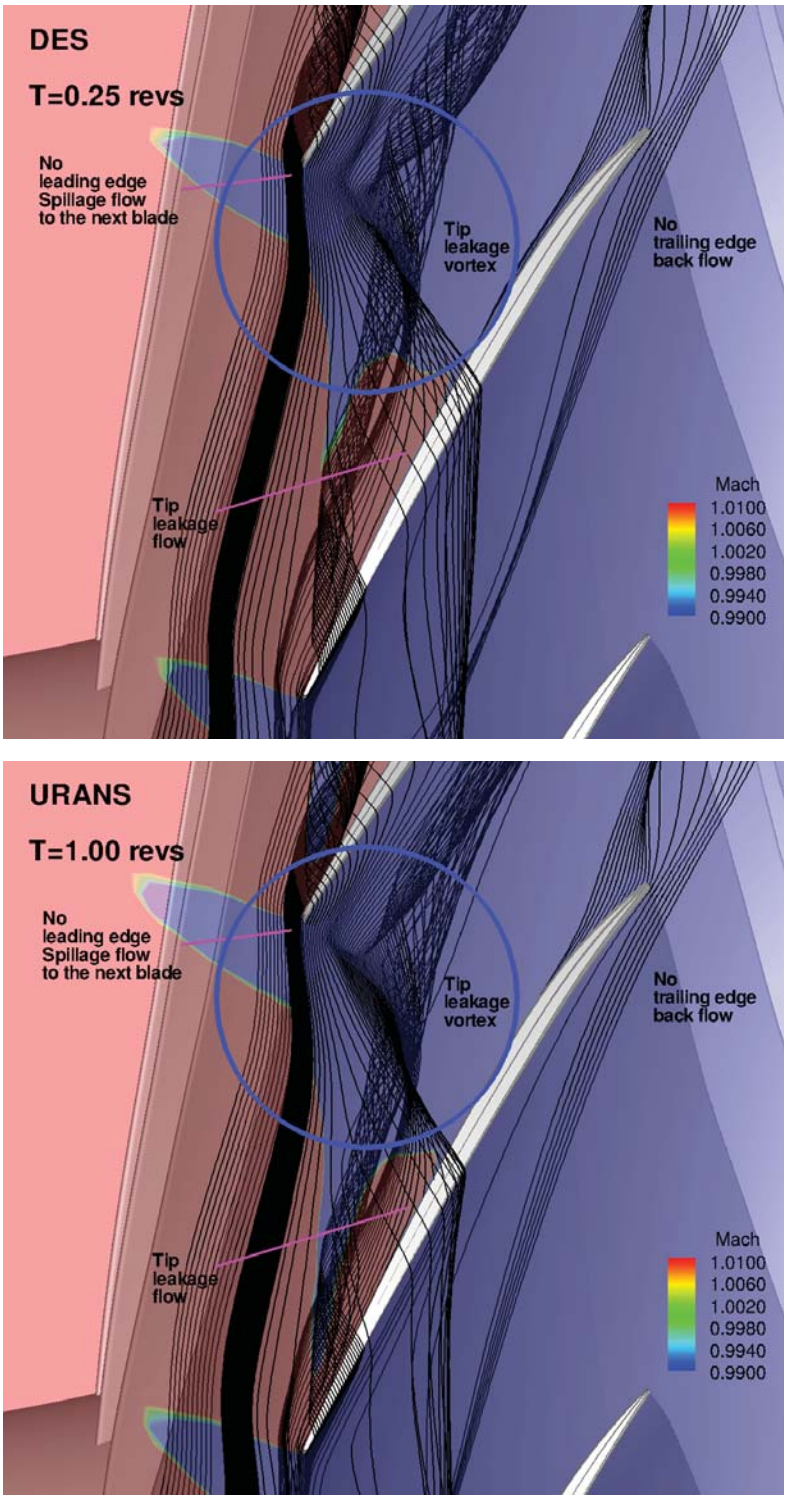

Figure 8.56: Tip leakage flow structure before half revolution from the stall onset with Mach number contour indicating sonic boundary; DES(top) at 0.25 revs, URANS(bottom) at 1.0 revs

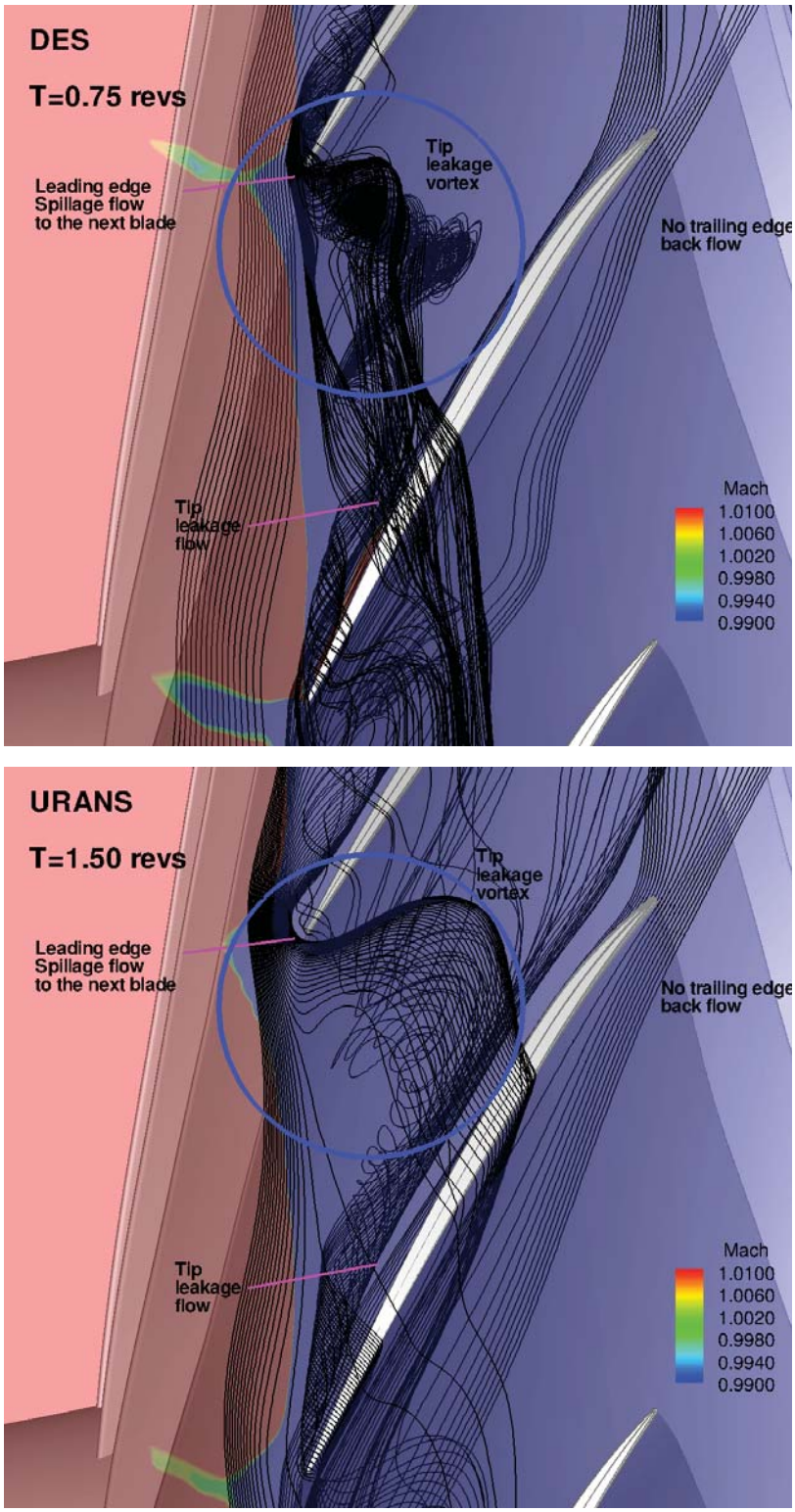

Figure 8.57: Tip leakage flow structure at the stall onset with Mach number contour indicating sonic boundary; DES(top) at 0.75 revs, URANS(bottom) at 1.5 revs

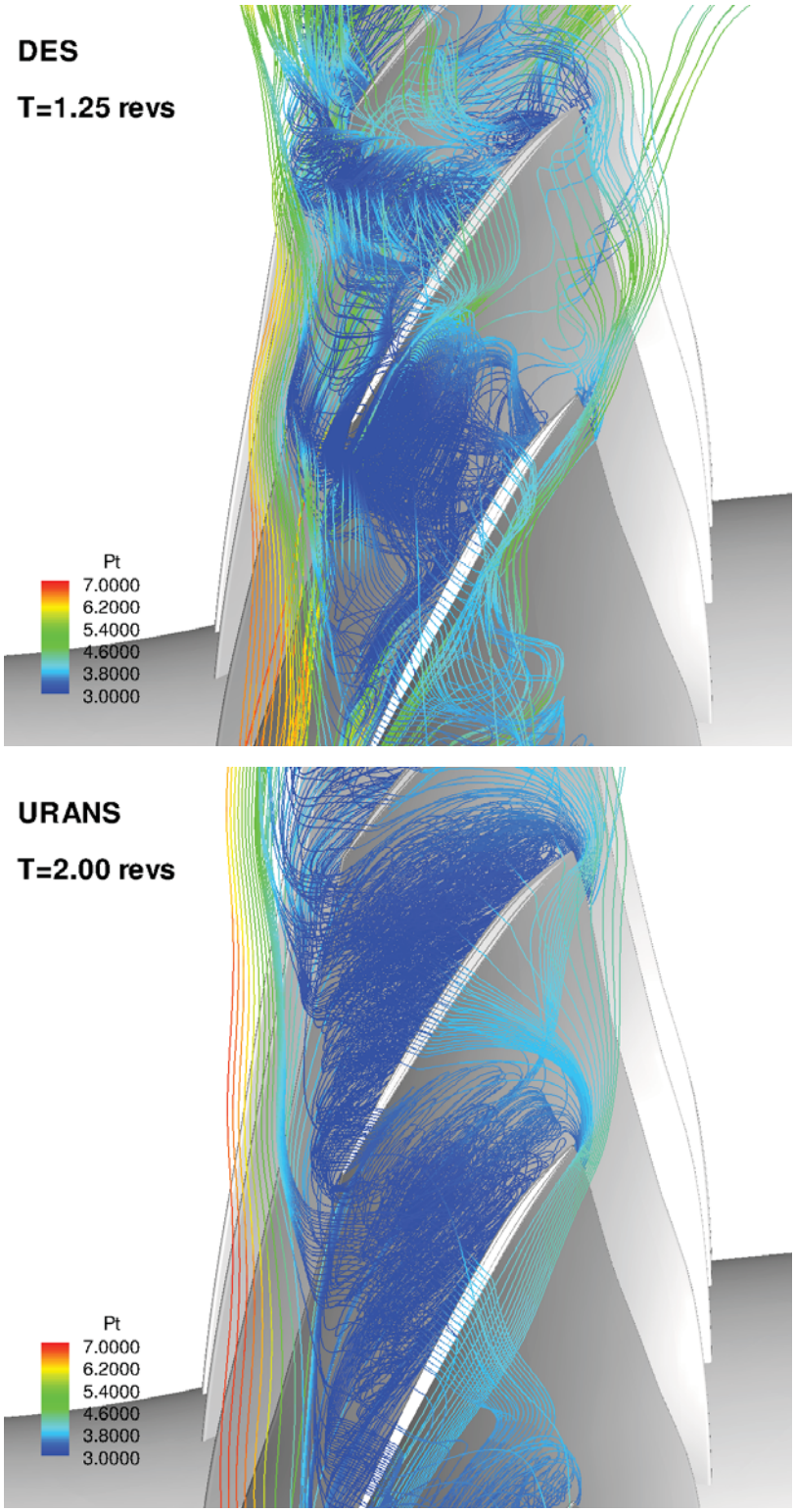

Figure 8.58: Tip leakage flow structure colored with normalized relative total pressure after half revolution from the stall onset; DES(top) at 1.25 revs, URANS(bottom) at 2.0 revs

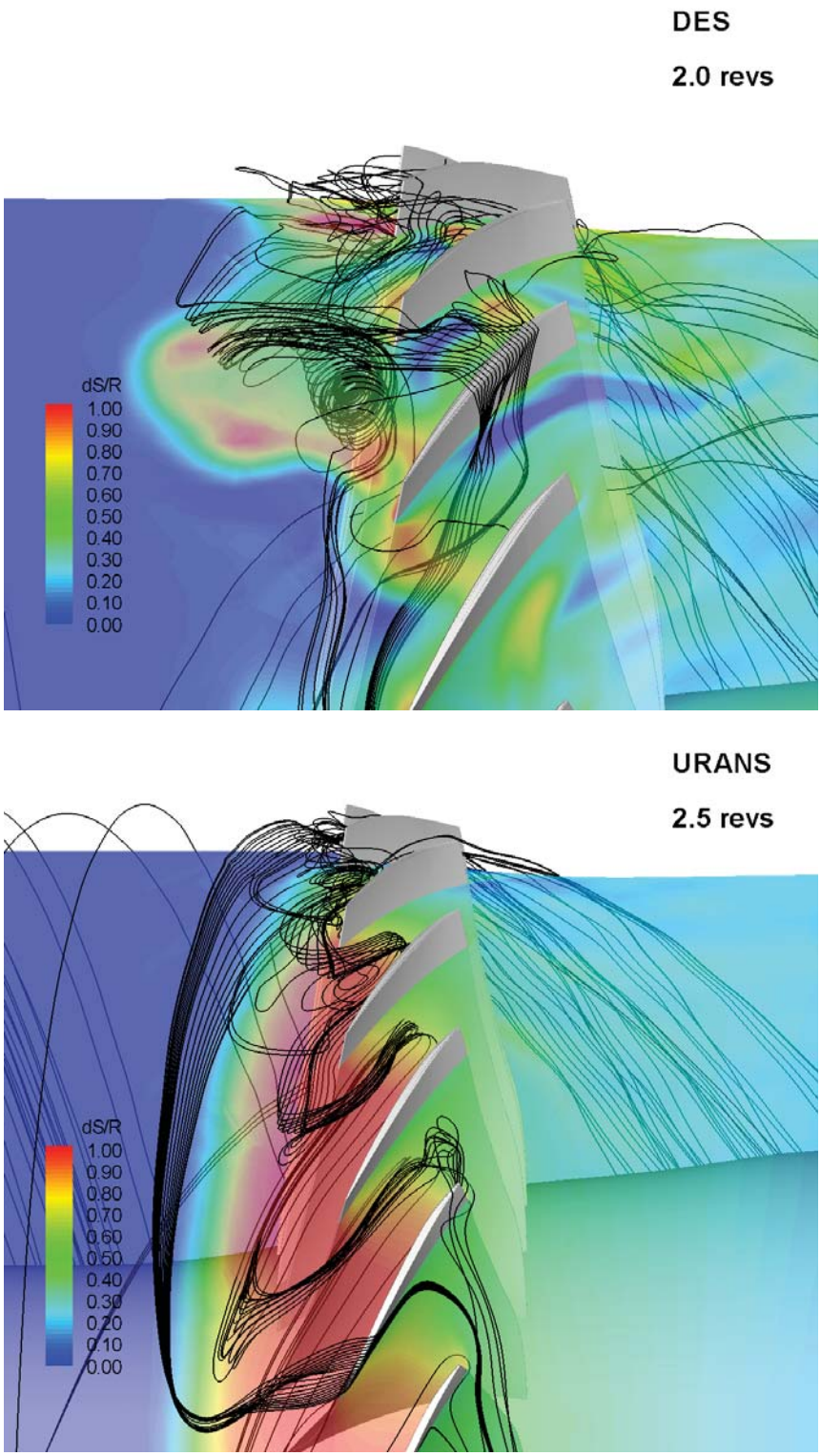

Figure 8.59: Tip leakage flow structure colored with entropy change after about one and half rotor revolution from the stall onset; DES(top) at 2.0 revs, URANS(bottom) at 2.5 revs

8.6 DES of Compressor Flutter with FSI

The purpose of this study is to develop the simulation capability of 3D flutter for a transonic rotor using high order DES and the fully coupled fluid/structure interaction. The 5th order WENO scheme for the inviscid flux and the 4th order central differencing for the viscous flux are used to accurately capture interactions between the flow and the vibrating blades. Detached-eddy simulation (DES) approach suggested by Spalart [36] is employed to better capture flutter in stall. Recently its high fidelity toward the stalled flow simulation was demonstrated by the present author in [35]. To facilitate the FSI for the transonic rotor blades with the tip speed of supersonic, an advanced moving mesh generation technique that can significantly improve mesh skewness at the rotor tip clearance are developed.

Flutter simulations are first conducted from choke to stall using 4 blade passages. Stall flutter initiated at rotating stall onset, grows dramatically with resonance. The frequency analysis shows that resonance occurs at the first mode of the rotor blade. Before stall, the predicted responses of rotor blades decayed with time, resulting in no flutter. Full annulus simulation at peak point verifies that one can use the multi-passage approach with periodic boundary for the flutter prediction.

8.6.1 NASA Rotor 67

NASA Rotor 67 used in this study is an isolated transonic high speed fan rotor with a supersonic rotor tip. Experimental measurements of the flow field were made at operating conditions of near peak efficiency and near stall aimed to be used for CFD validation. Unfortunately no test data in stall and for flutter are available. The design specifications of

Rotor 67 are summarized in table 8.3. A detailed description of the blade and flow-path geometry as well as performance data is provided in reference [130].

Figure 8.60: NASA Rotor 67 image from NASA Glenn Research Center

Table 8.3: NASA Rotor 67 design specifications

Quantity	Value
Number of rotor blades	22
Rotational speed [RPM]	16043
Design mass flow rate [kg/s]	33.25
Measured choke mass flow [kg/s]	34.96
Design pressure ratio	1.63
Tip speed [m/s]	429
Tip relative mach number	1.38
Tip diameter at inlet/exit [mm]	514/485
Hub-tip ratio at inlet/outlet	0.375/0.478
Tip clearance [mm]	1.1
Rotor aspect ratio	1.56

8.7 Mode Shape for NASA Rotor 67

For the present flutter simulation of NASA Rotor 67, we use the first five mode shapes normalized by the generalized mass as displayed in Fig. 8.61 was obtained by using ABAQUS. The rotor blades are assumed as titanium alloy properties with Young's modulus=1.172×10^{11} Pa, Poisson's ratio=0.3, and density 4539 kg/m^3 since the material properties used in original design has not been reported. The effect of centrifugal force is taken into account. The blades are modeled as fixed at the rigid body rotor. The grid data on the blade surface used in CFD mesh is imported for ABAQUS FE modeling. The first five natural frequencies of Rotor 67 is 584.04 Hz, 1474.9 Hz, 2017.5 hz, 3181.7 Hz, and 3789.9 Hz. For the normal operating condition with 16043 RPM, the blade passing frequency(BPF) is 5882.4 Hz.

8.7.1 Computational Mesh for NASA Rotor 67

Fig. 8.62 shows the full annulus mesh for NASA Rotor 67 constructed by applying the H-O-H mesh topology. For the 4 blade flutter FSI computations, the part of 4 blade(blade1 $\sim$ blade 4) in the full annulus mesh was taken. The mesh convergence test are done for three different mesh sizes via the previous rotating stall simulation by the present author. The current mesh size shows a good agreement with the experiment [130] for the rotor speed-line prediction. The single passage mesh has 121(around blade)$\times$77(blade-to-blade)$\times$47(span). A fully gridded tip model with nominal tip clearance, an O-grid with mesh size of 121$\times$12$\times$9, was used. The mesh uses 8 points in the spanwise direction to resolve tip clearance flow. The 1st grid spacing on the the blade surface was set to 5×10^5

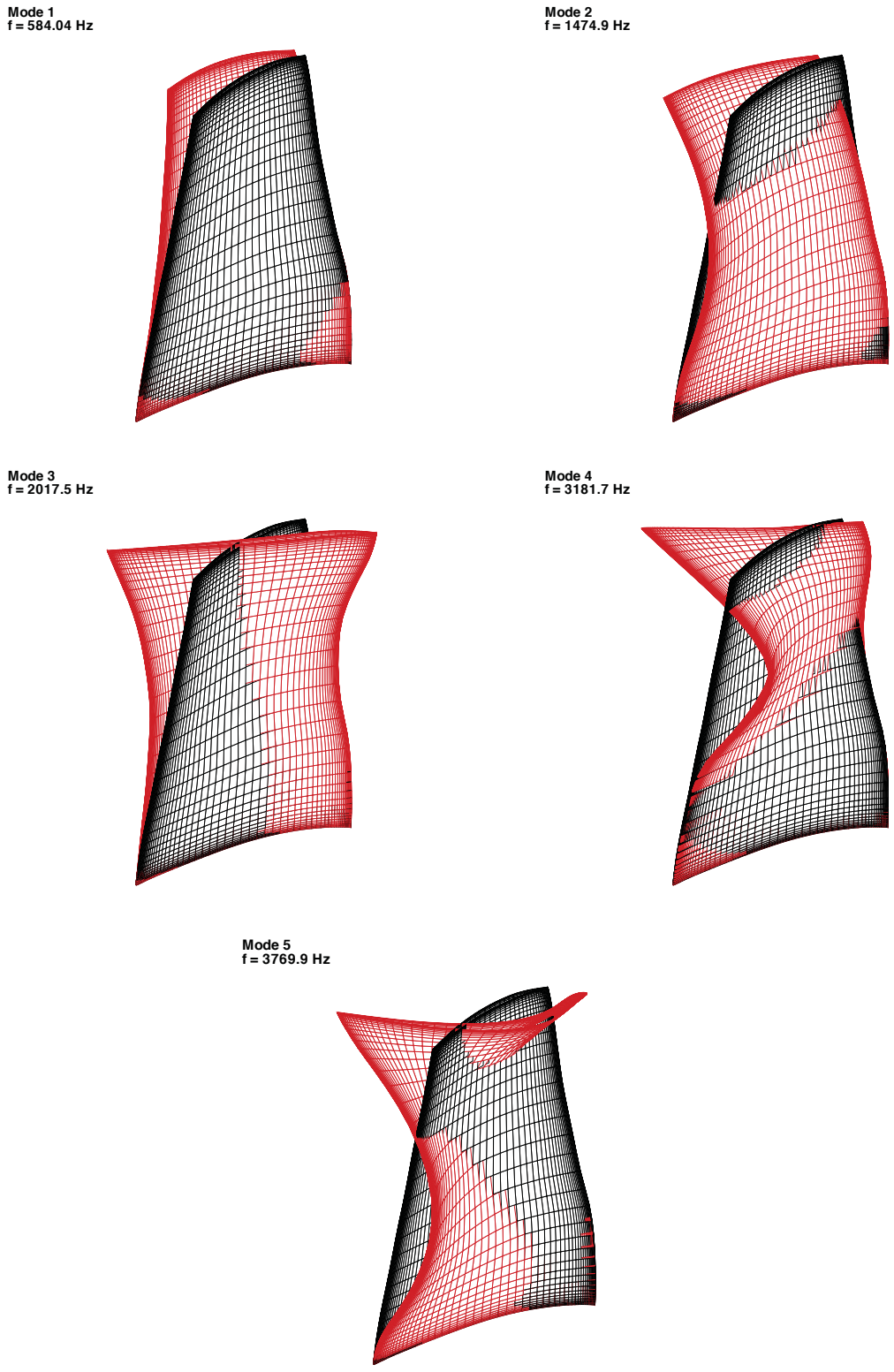

Figure 8.61: Five modal deflections of NASA Rotor 67

times the blade hub chord length which gives $y^+ < 5$, while on the hub and casing surface it was set to 2×10^3 times blade hub chord which can give y+ around 50. Therefore, the wall function BCs [29, 149] are used on the hub and casing. Total 56 blocks were used for the parallel computation.

8.7.2 Boundary Conditions

The rotor inlet condition described in chapter 6 is used. As aforementioned, the pressure at the peak of the rotor speed line is applied for the back pressure condition since axial compressors operating near the peak of their pressure rise characteristic have the potential to induce rotating stall [79, 150, 151]. The spanwsie distributions of the back pressure are determined by the radial equilibrium equation (6.12). The advanced deforming mesh introduced in chapter 7 is used to describe the blade motion during the blade flutter.

8.7.3 Results and Discussion

Flutter simulations are conducted at total 8 different operating conditions including choke, peak, and near stall. Several rotor revolutions are needed to see whether the responses are divergent or damped with time. Full annulus flutter simulation at peak condition are performed in order to validate the 4 blade passage simulation with periodic boundary condition. The value of modal damping typically determined by experiment is very small, on the order of $1 \sim 3$ percent of critical damping. In the current study, a uniform damping ratio of 0.005 is used for rotor flutter simulation. The effects of dynamic pressure changes in NASA Rotor 67 flutter is investigated by varying reduced velocity(V^*).

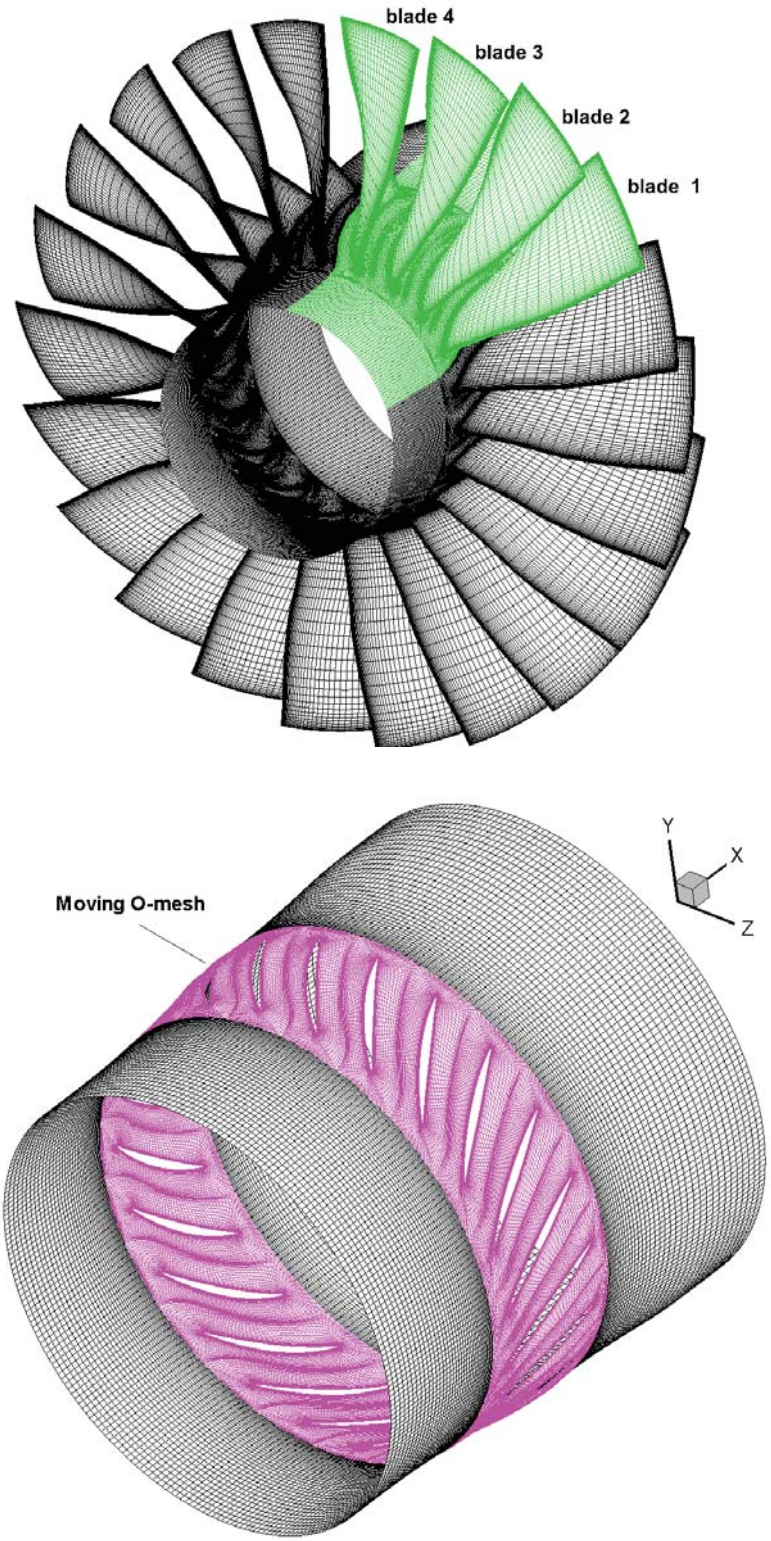

Figure 8.62: Full annulus mesh of NASA Rotor 67 constructed by using H-O-H mesh topology

4 Blade Passage Simulation

Using the 4 Blade Passages, computations for investigating flutter in NASA Rotor 67 was first performed. 8 points including choke, peak, and near stall and stall were considered. The unsteady simulations are started with the initial solution obtained by each steady state calculation. The residual is reduced three orders of magnitude in each physical time step. The physical time step, 0.0025revs(rotor revolutions) with a CFL number of 2 is used. Periodic boundary conditions are used at lower and upper boundary of the blade passage.

The focus of NASA Rotor 67 flutter simulation is to investigate flutter behavior, in particular flutter boundary at the design speed of 16043 RPM. Using the design conditions in table 8.3, the estimated mass ratio($\bar{\mu}$) is 4299.5, and the reduced velocity(V^*) is about 0.4357.

Fig. 8.63 shows the modal displacements of the second blade at choke, peak and near stall. It is clearly shown that the blade oscillations decay with time, resulting in no flutter at choke, peak and near stall. The amplitude level at near stall is larger than those at choke and peak even though the mass flow through the compressor decreases toward stall.

Fig. 8.64 displays the normalized surface static pressure distributions of a rotor blade(the second blade) at 50% span. It is obvious that the static pressure and its difference between the rotor pressure surface and suction suction surface increases toward stall, as a result increased blade loading and displacements. The modal displacements at near stall are compared in Fig. 8.65. Blade 1, 2, 3 and 4 vibrate with almost same level of phase angles and amplitudes without flutter.

Flutter boundary of the compressor rotor was captured in stall operation. Fig. 8.66

shows the first 5 modal displacements in the stall flutter. Fig. 8.67 demonstrates how the rotor blade flutter initiates in higher modes. Occurrence of flutter can be identified with changes in response type from the damped to the divergent, which is captured in higher modes about 2.3 revs. Flutter starts simultaneously for all modes, however the 1st mode has a significantly larger displacement than the following modes as it develops. Therefore, the effects of higher modes on the stall flutter may not be influential.

After the flutter onset 4 blades experience the transient state with the damped oscillations for about 3 revs. It may be explained by rotating stall inception. In general stall inception develops without flow breakdown for about 2 or 3 rotor revolutions after the onset, and eventually goes into the fully developed rotating stall. The axial symmetry of rotating flow changes to a non-symmetric disturbance at the very beginning of rotating stall. It can lead each blade to vibrate with different amplitudes and phase angles as presented in Fig. 8.68. After the stall flutter onset, the phase angle difference is clearly captured with diverging oscillations. The phase difference is related to nodal diameter and usually identified from experiments [6, 8].

Fig. 8.69 shows the speedline, and flutter boundary is found at point D. Except for the stall operation, the rotor blades die out in terms of time including choke, peak and near stall. When the compressor throttles with the reduction of the mass flow, the pressure ratio of the rotor blades increases from the point A to point C. On the contrary, the rotor pressure ratio decreases slightly and then increases from the point D (stall flutter onset). This type of rotating stall can be categorized into the progressive type stall.

Fig. 8.70 represents Mach number contour of the rotor tip span at 2.5 revs, just after flutter onset. The disturbed flow region due to the flow separation indicates very low Mach

number close to zero. The rotor tip passage is usually disturbed partly around the onset of the stall flutter. Rotating stall usually takes place around rotor tip and propagates in the opposite direction of the rotor rotation behind the detached sonic boundary from the rotor blades where the flow is subsonic.

Fig. 8.71 shows the velocity vector with sonic boundary at the rotor tip span. When the rotor flutter is triggered, the sonic boundary is attached to the rotor leading edge. The flow near the leading edge points out toward the rotor circumferential pitch line with the local flow separation.

Flow instability near the rotor tip may be understood by the fluctuations in the static pressure of the rotor upstream [31, 69, 79] as plotted in Fig. 8.72. It is obvious that the instability of the upstream flow occurs at 2.3 revs, which corresponds to flutter onset point as captured in Fig. 8.66, -8.67. At 5.7 revs, the fluctuation in the static pressure grows dramatically.

Fig. 8.73 is velocity vector field at the tip span. As the rotating stall fully develops, the sonic boundary is fully detached from the rotor. The incoming flow toward rotor leading edge is largely disturbed and the rotating instability propagates toward both upstream of the rotor and the rotor circumferential direction. Needless to day, the highly disordered flows largely contribute to the blade flutter.

Fig. 8.74 shows static pressure of the suction surface variations during the stall flutter. The strong shocks on the oblique surface at T = 0 revs are distributed in the same manner for all 4 blades, however these disappear at T=8.7 revs. This phenomena can be understood by the detachment of the sonic plane from the blade passages as the stall develops. Static pressure on the pressure/suction surface is non-uniformly distributed for each blade. Hence

the blade loading acting on each blade can enforce the blades to flutter in the different phase angles and in the opposite directions.

Fig. 8.75 represents the blade vibration at T=8.7 revs. The blade oscillations are non-periodic and likely non-synchronized since the blade 3 and 4 vibrate in the opposite direction with the different amplitudes.

The frequency of the vibrating blades during the stall flutter was obtained using FFT (fast Fourier transform) analysis. The time traces of modal displacements are used for the FFT input variables. Fig.8.76 shows frequency ratio ($\frac{\omega}{\omega_n}$) which is defined by the vibration frequency of the blade divided by the blade natural frequency. Resonance occurs at the 1st mode natural frequency of 584.04 Hz. Once the stalled flutter initiated it cannot be stopped in general and gradually diverges. In the current study, the response of the rotor blades amplifies dramatically after a sudden change in the response at about 7 revs as displayed in Fig.8.66, -8.67, -8.68.

Full Annuls Simulation

The full annulus flutter simulation of NASA Rotor 67 is conducted at peak point to validate the 4 blade flutter simulation with periodic boundary conditions. The full annulus mesh is constructed using the same mesh used for the 4 blade flutter simulation as presented in Fig. 8.62. Total 308 blocks are used for the parallel computations.

Fig. 8.77 presents the 1st mode displacements of the full annulus NASA Rotor 67. All of 22 blades vibrate showing the damped responses with very similar phase angle and amplitude level.

Fig. 8.78 shows Mach number contour of the 30% span from the shroud at 5 revs. The λ-shape passage shocks are clearly captured around the leading edge, which is a major feature of the transonic compressor rotor reported by the experiment [130] and other researchers [143, 144]. The flow field of each blade passage predicted by using the fully coupled FSI approach shows very similar pattern along the rotor circumference. The surface pressure distributions at 50% span and the tip span are presented in Fig. 8.79 and Fig. 8.80. Obviously 22 blades show identical distributions, and hence each vibrating blade can show periodic behavior.

Comparison of first two modal displacements for the second blade was illustrated in Fig. 8.81. The predicted displacements from the full annulus FSI and the 4 blade passage FSI decay in the same manner for the amplitude and phase angle. By taking into account the main objective of the FSI is to find out the flutter boundary at a given or target design condition, the full annulus FSI calculation is not necessary since the 4 blade passage calculation with periodic boundary gives the same results before the stalled flutter.

From the design point of view, it is critical to find flutter boundary using proper parameters. One way to simulate unstalled flutter is to use the parameter, reduced velocity(V^*). The increase of V^* can stand for the increase in freestream dynamic pressure at a certain design point or a given back pressure.

Flutter computations with alternating V^* were performed at near stall condition. Fig. 8.82 shows 1st mode displacements with $V^* = 0.4357, 0.6357$ and 0.8357. The damped responses are obtained with $V^* = 0.4357$ and 0.6357. However, for $V^* = 0.8357$, the oscillation of the modal displacement diverges with time. It is obvious that flutter boundary locates somewhere between $V^* = 0.6357$ and $V^* = 0.8357$. Unlike the stall flutter where

the flow fields largely disturbed due to the massive flow separation, the oscillation of the vibrating blades gradually amplifies like wing flutter.

8.7.4 Summary

A fully coupled fluid/structure interaction method for axial compressor flutter was developed. An advanced moving mesh technique that can significantly improve the mesh quality over the blade tip was implemented. Using the 4 blade passages of NASA Rotor 67, flutter simulations were conducted from the choke to stall by applying the DES of turbulence with the higher order spatial schemes. Flutter occurs in Rotor 67 as rotating stall develops. Before stall the responses of the rotor blades decay with time, resulting in no flutter.

The full annulus simulation at peak efficiency condition was performed to verify the multi-passage approach with periodic boundary. It is shown that the multi-passage approach with periodic BC can be applied to predict flutter boundary of transonic rotor compressors when the flow is unstalled. The frequency analysis indicates that the compressor rotor flutters with the 1st mode resonance in stall operation. The unstalled flutter of the multi-passage was simulated by increasing the reduced velocity. This approach can facilitate the prediction of the engine flutter under various operating conditions.

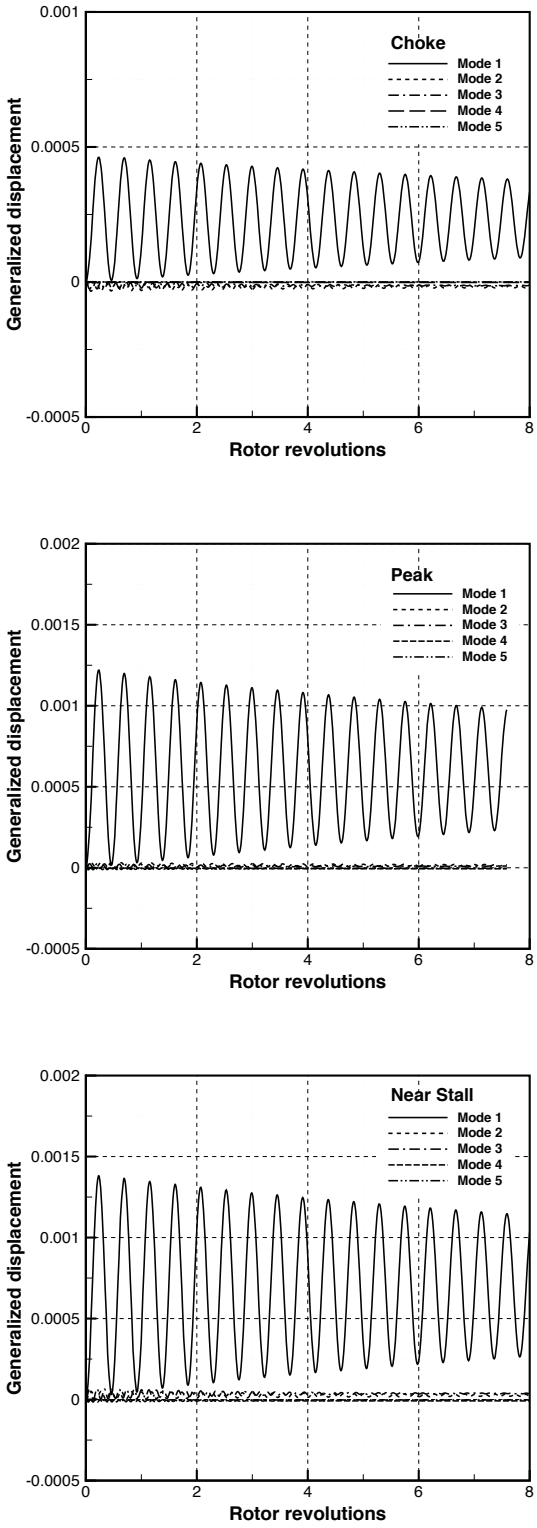

Figure 8.63: The damped responses of blade 2 at choke, peak and near stall

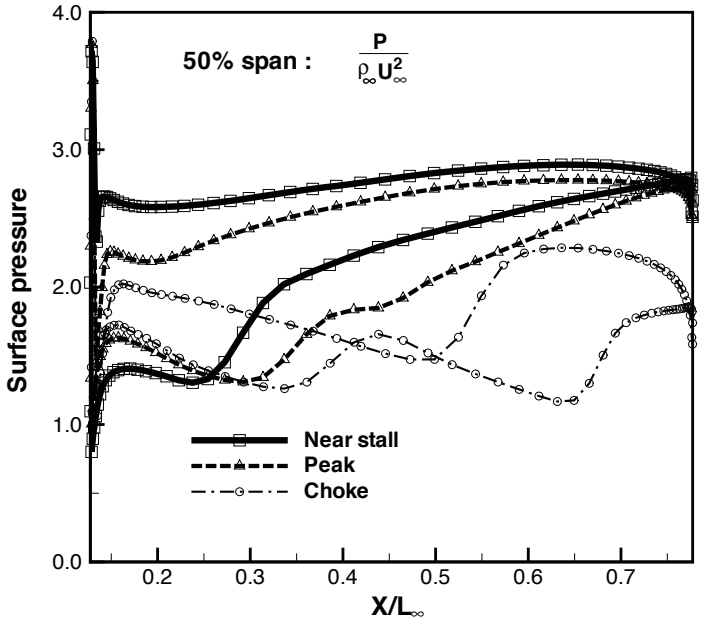

Figure 8.64: Comparison of surface static pressure distributions of NASA Rotor 67

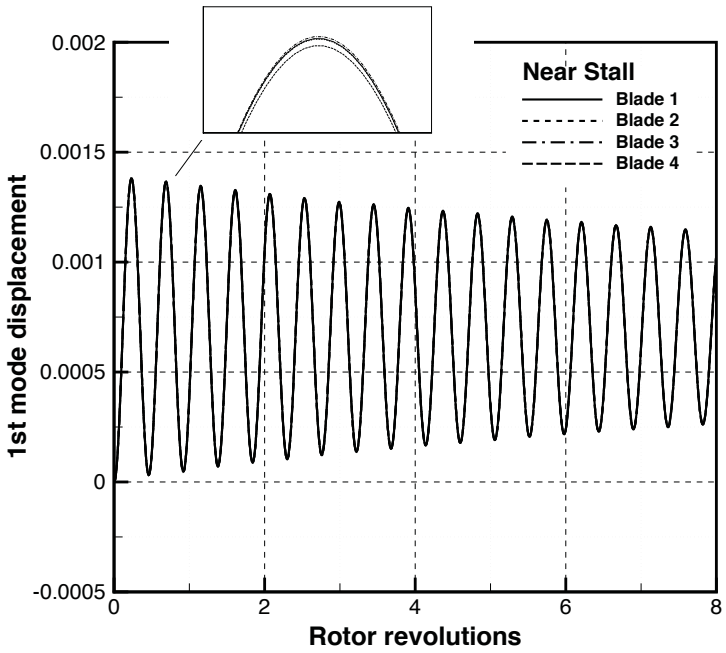

Figure 8.65: Time traces of the 1st mode displacements of NASA Rotor 67 near stall

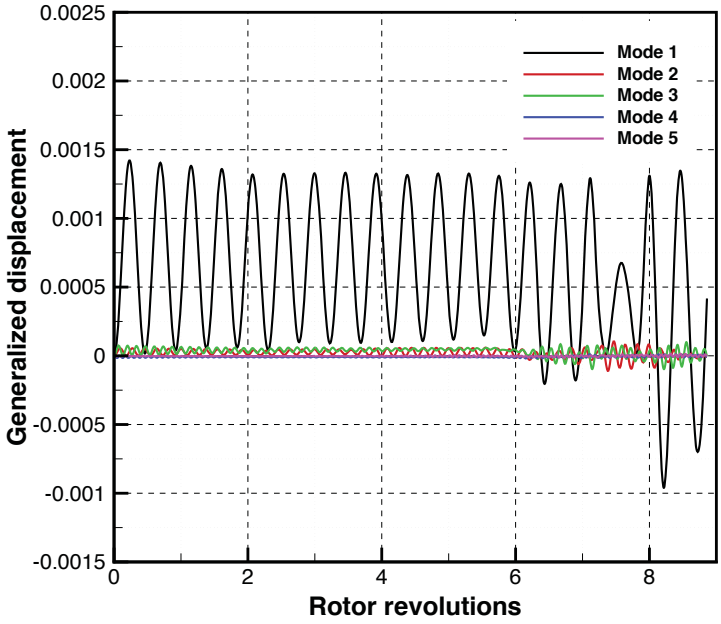

Figure 8.66: Time traces of the generalized displacements of blade 2 in stall flutter

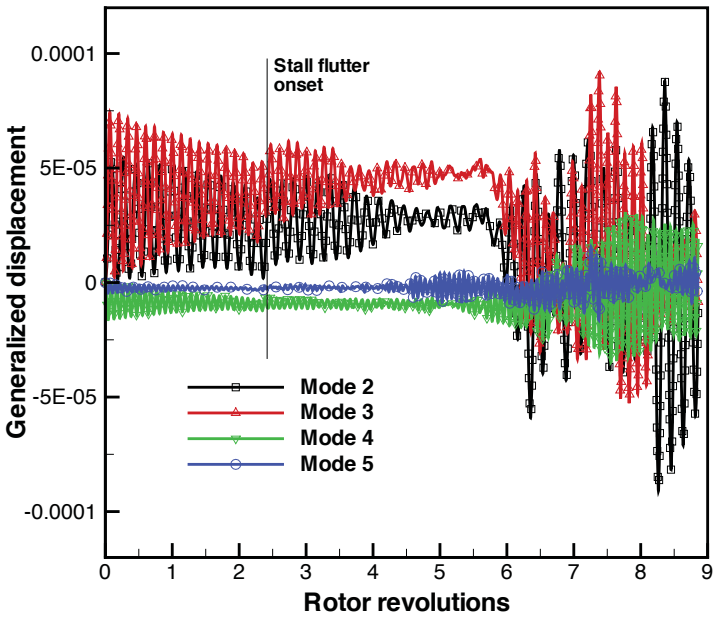

Figure 8.67: Time traces of the 2nd, 3rd, 4th and 5th mode displacements of blade 2 in stall flutter

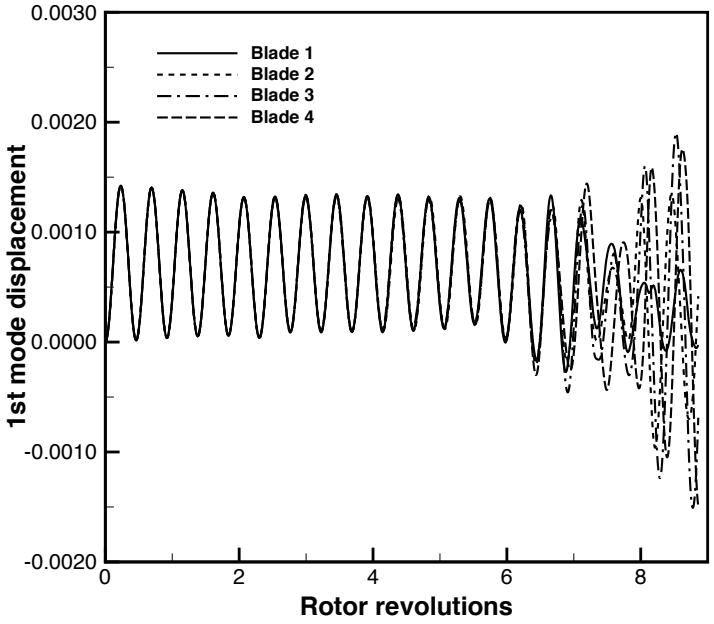

Figure 8.68: Variations of the blade 1st mode displacements in stall flutter

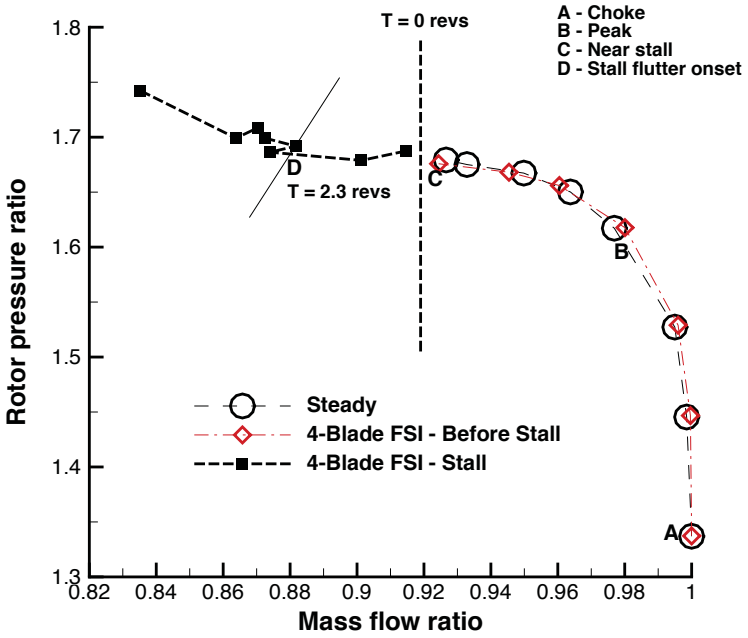

Figure 8.69: The predicted speedline of Rotor 67 by fluid/structure coupled simulation

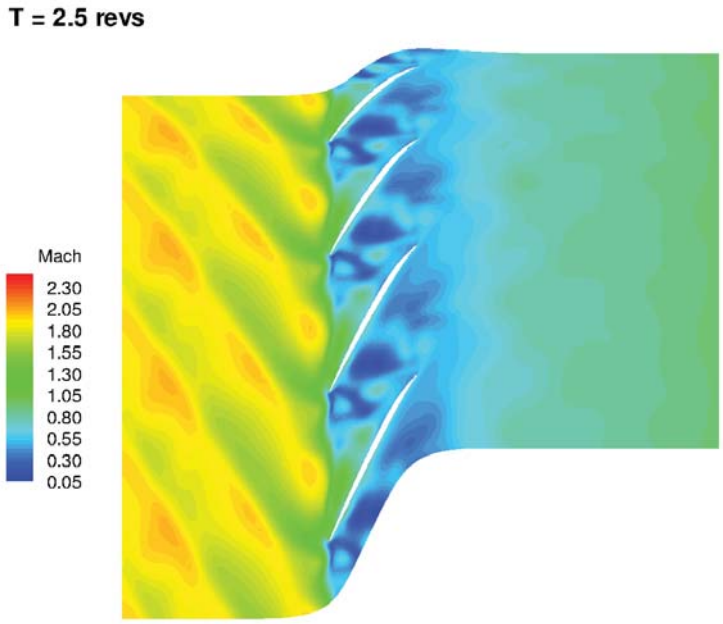

Figure 8.70: Mach number contour of the rotor tip span around flutter onset

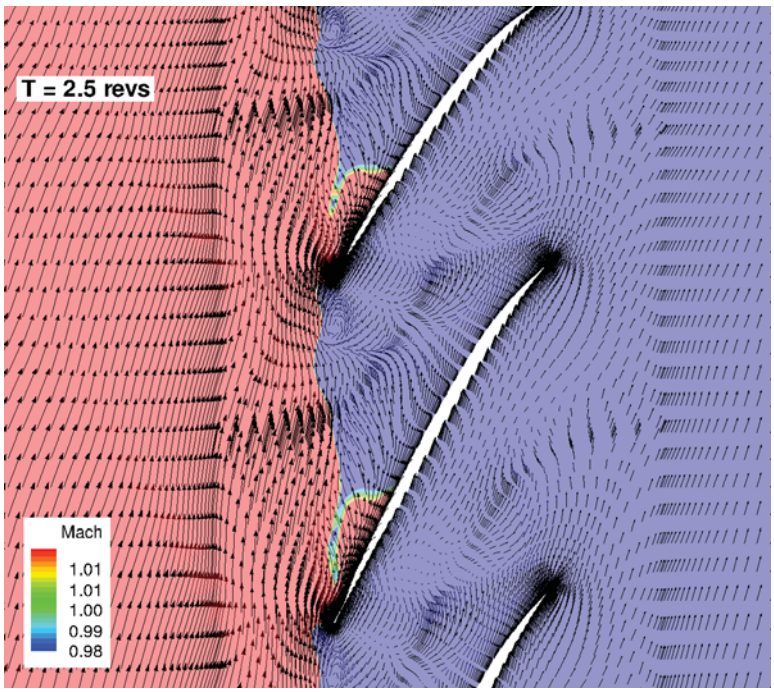

Figure 8.71: Velocity vector of rotor tip section at 2.5 revs with Mach number contour indicating sonic boundary

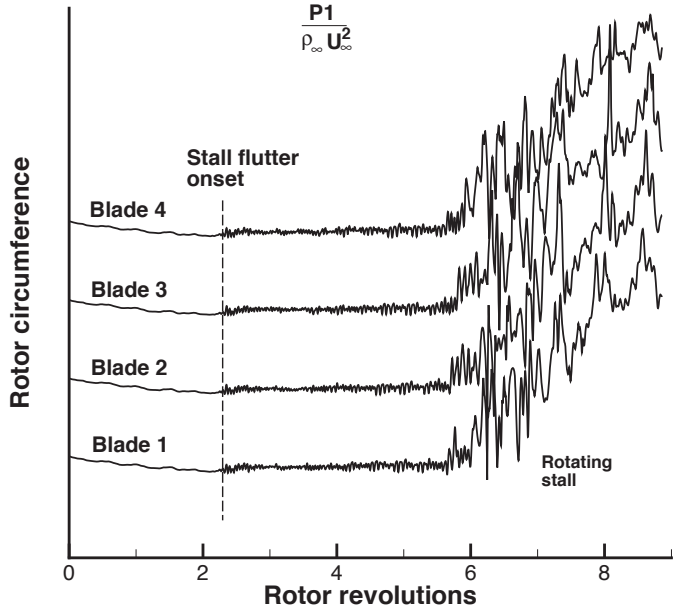

Figure 8.72: Time traces of rotor upstream static pressure at rotor tip span

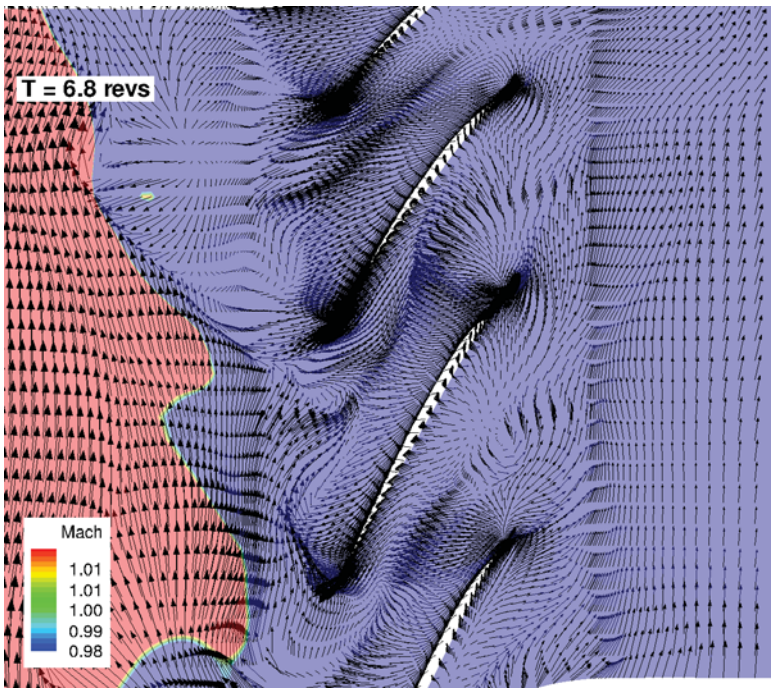

Figure 8.73: Velocity vector of rotor tip section at 6.8 revs with Mach number contour indicating sonic boundary

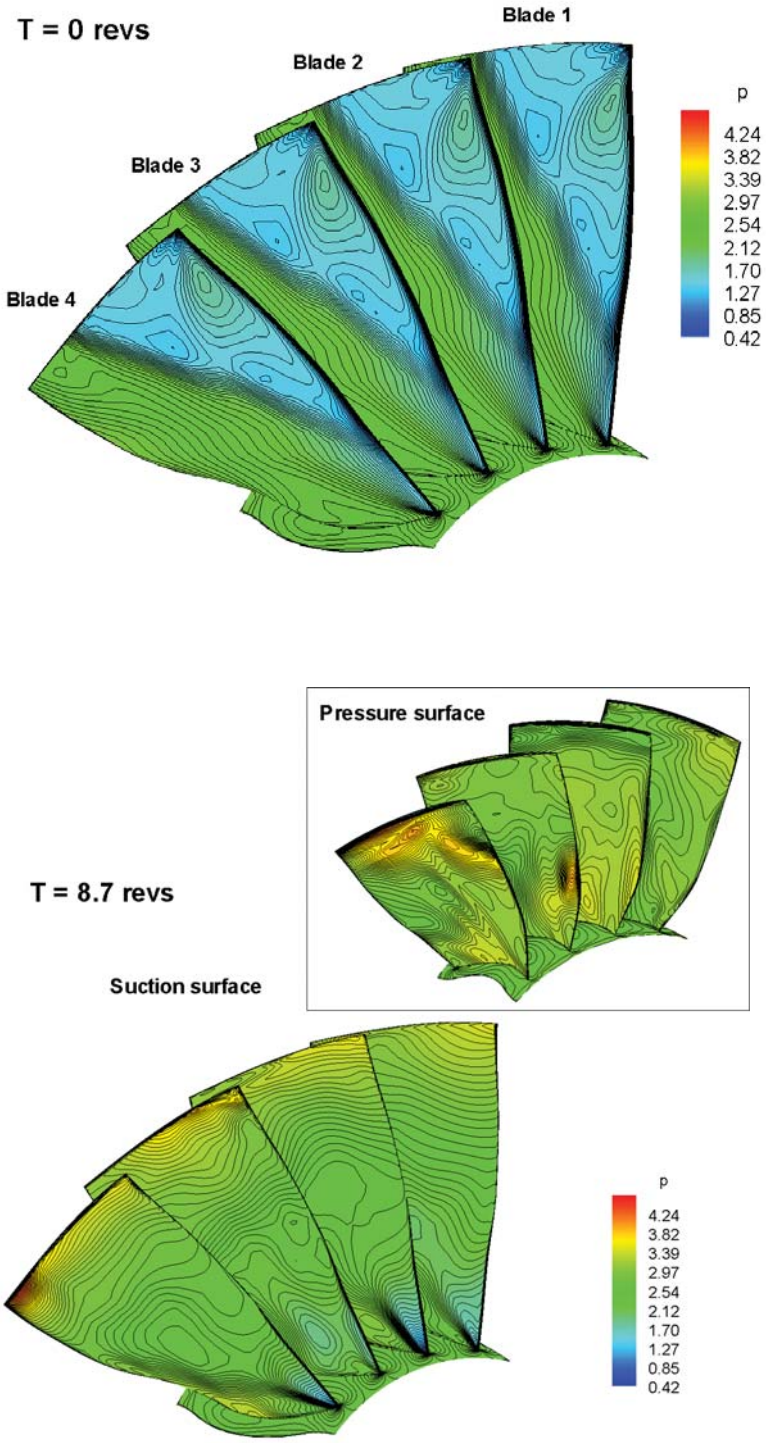

Figure 8.74: Variations in surface static pressure during the stall flutter

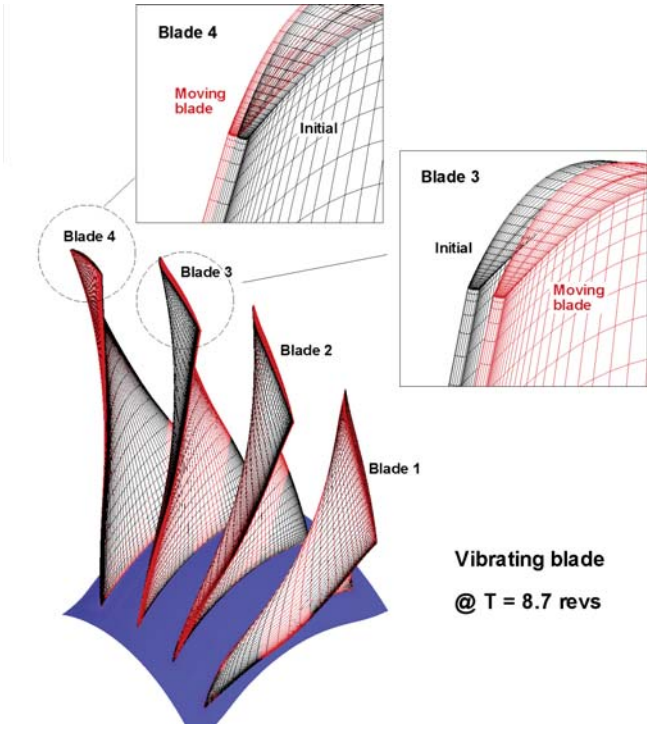

Figure 8.75: Blade vibration at T=8.7 revs

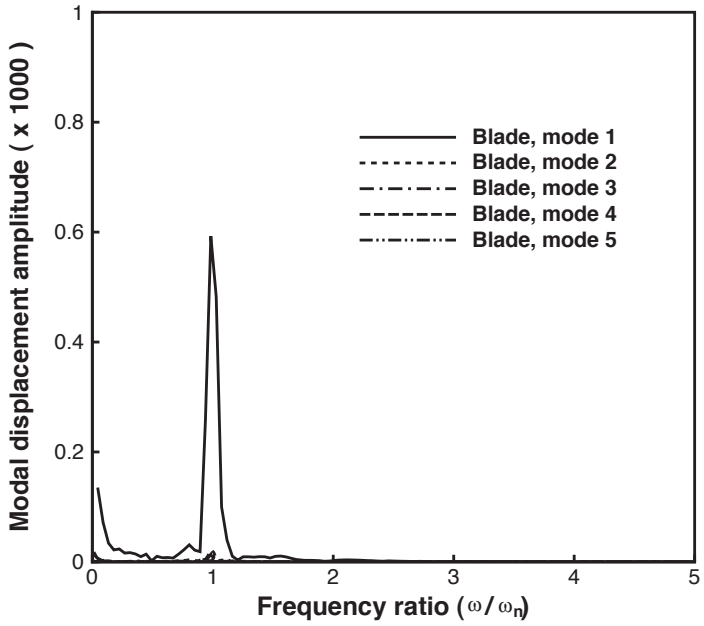

Figure 8.76: Frequency ratio of Rotor 67 stall flutter predicted by FFT

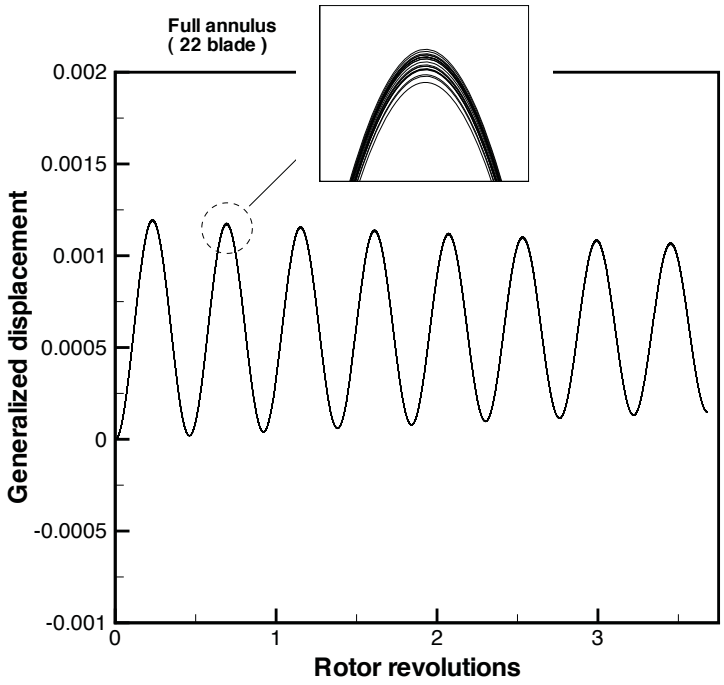

Figure 8.77: The damped responses of full annulus Rotor 67

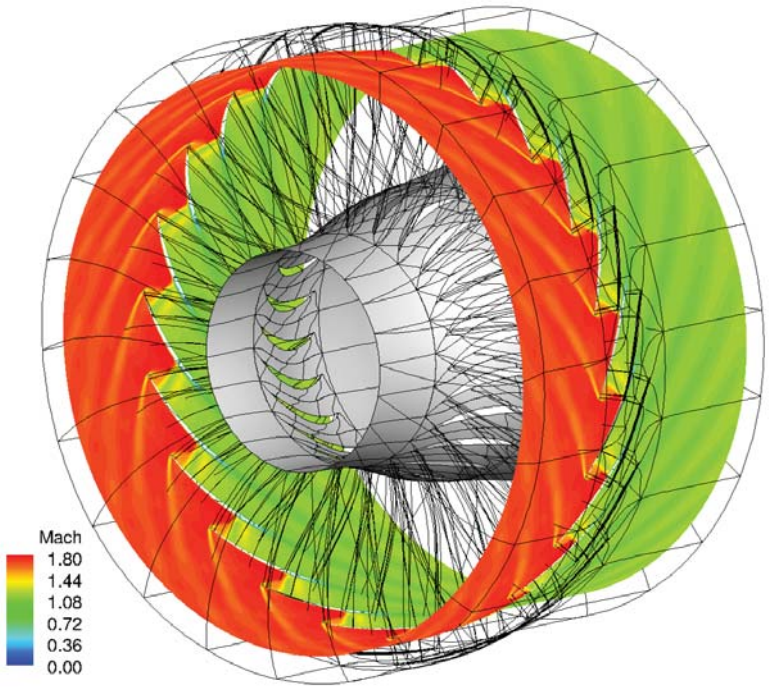

Figure 8.78: Mach number contour of 30% span from the shroud at peak predicted by the full annulus FSI

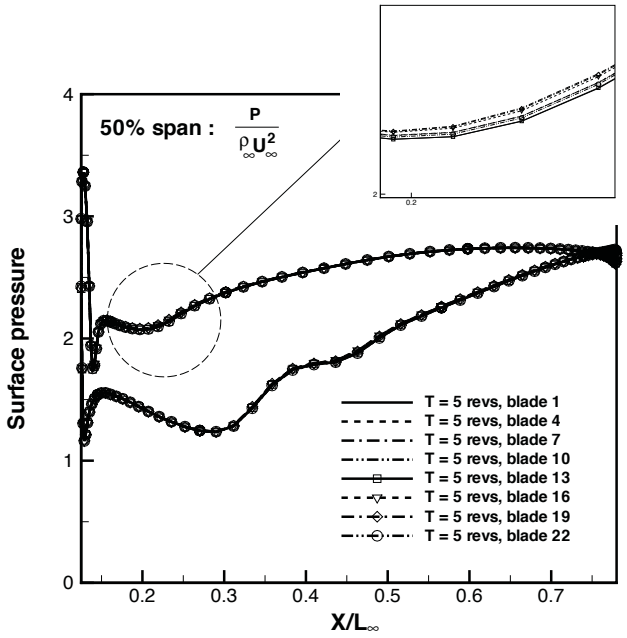

Figure 8.79: Surface pressure distributions of 50% span at peak predicted by the full annulus FSI

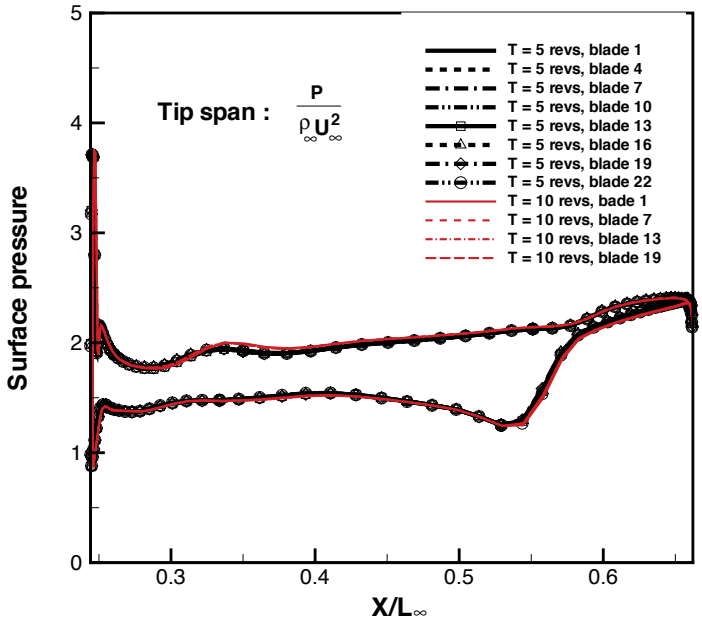

Figure 8.80: Surface pressure distributions of the tip span at peak predicted by the full annulus FSI

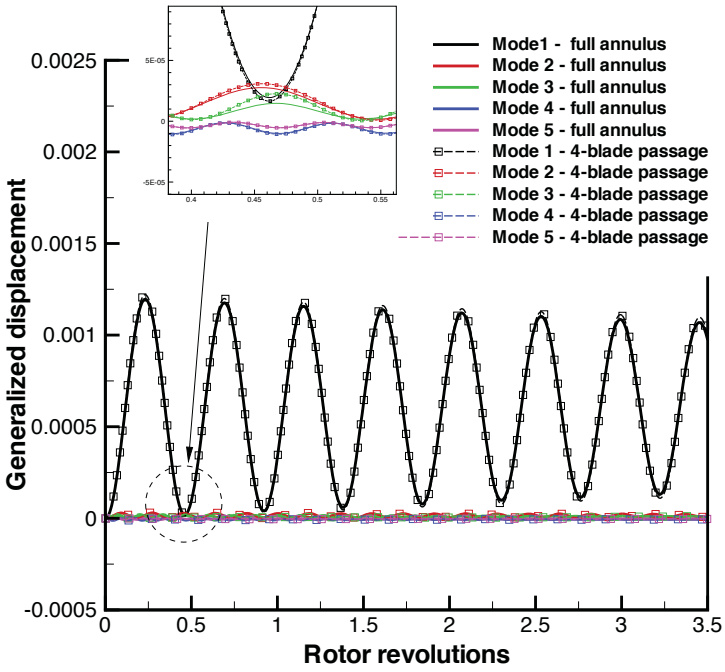

Figure 8.81: Comparison of the modal displacements between the full annulus and the 4-blade passage

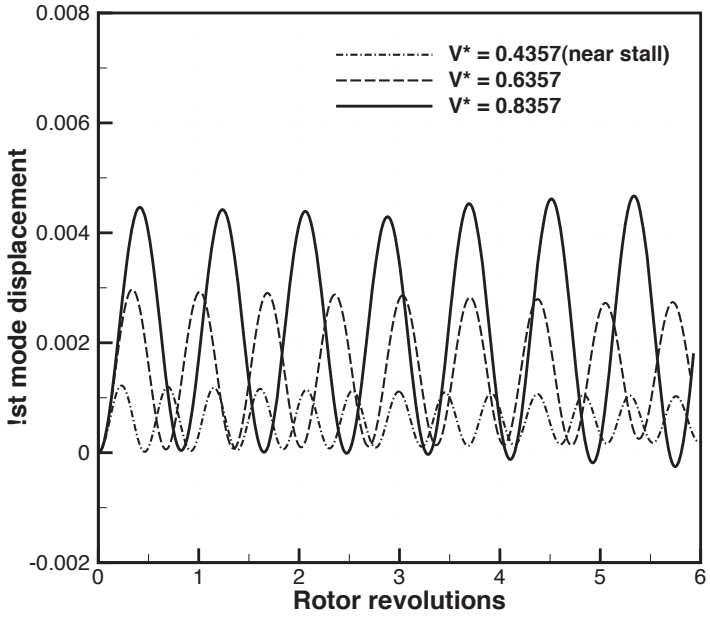

Figure 8.82: Effects of reduced velocity(V^*) on NASA Rotor 67 flutter at near stall

8.8 Compressor Flutter Prediction Using Phase Lag BC

The purpose of this study is to develop phase lag boundary conditions to facilitate use of a sector of annulus for turbomachinery flutter simulation, which can tremendously reduce computing efforts. A time shifted phase lag (TSPL) and the Fourier series phase lag (FSPL) approaches are implemented for the lower/upper circumferential periodic boundaries where a time shifted periodicity exits. The full annulus flutter for NASA Rotor 67 is conducted to validate the present single passage simulations with phase-lagged boundary conditions. The fully coupled FSI (fluid/structure interaction) approach introduced in chapter 5 is used to accurately predict the interactions between the fluid and the vibrating blades, in which the flow field and structure always respond simultaneously by exchanging the unsteady aerodynamic force and structural deformation within each physical time step via a successive iteration on the pseudo-time step. An advanced moving mesh generation introduced in chapter 7 is used to improve mesh quality over the rotor tip clearance. Since there is shock/boundaery layer interaction in the transonic NASA Rotor 67 that has 22 blades and pressure ratio of 1.63 at design speed of 16043 RPM, the Low Diffusion E-CUSP (LDE) Scheme introduced in chapter 5 is used with the 3rd order MUSCL scheme for the inviscid flux and a 2nd order central differencing for the viscous flux. For turbulence closure, the Spalart-Allmaras (SA) model [114] is applied.

8.8.1 Boundary Conditions

At the rotor inlet, the radial distributions of total pressure, total temperature, swirl angle and pitch angle obtained at near peak operating condition from the experiment [130] are

specified. The components of velocity are extrapolated from the inner domain to determine the rest of variables. At the rotor outlet, the back pressure at near peak is specified at the hub, and the blade spanwise distribution is then determined by solving the radial equilibrium equation (6.12). The components of velocity are extrapolated from the computational domain. On the solid wall, the non-slip boundary condition is applied to enforce mass flux going through the wall to be zero. To avoid the fine mesh near the hub/casing wall, the law of the wall introduced in chapter 6 is applied. The wall static pressure on the hub/casing is also determined by using the radial equilibrium equation, while on the blade wall zero gradient condition is imposed.In addition, the adiabatic condition is used to impose zero heat flux through the wall. For the lower/upper periodic boundaries, two phase lag approaches;1) TSPL (time shifted phase lag), 2)FSPL (Fourier series phase lag) introduced in chapter 6 are used.

Traveling Wave BC

For turbomachinery, flutter often involves traveling wave [152] in which the blades vibrate at the same frequency but with a constant phase difference termed as inter blade phase angle, IBPA(φ). The phase difference is defined as function of blade frequency(ω_j), nodal diameter(N_D) and number of blade (N_B), where the subscript j denotes the blade vibration mode. Since the mass ratio($\bar{\mu}$) of turbomachinery blade is in general very large value, it is necessary to impose a time lag for each mode as follows. As a result, each blade mode starts to vibrate by a time lag.

$$\delta t_j = \frac{\varphi}{\omega_j} \tag{8.6}$$

where

$$\varphi = \frac{2\pi N_D}{N_B} \tag{8.7}$$

Note if the phase difference propagates in the same direction to the rotor rotation, it is called forward traveling wave(FTW). If the phase difference propagates in the opposite direction to the rotor rotation, it is called backward traveling wave(BTW). FTW or BTW is associated with N_D and usually observed during engine test [6]. In this full annulus flutter simulation of NASA Rotor 67, a phase difference for $N_D = 1$ is imposed for numerical experiment and no information available from the experiment. Since the blade 1st mode is usually dominant, the IBPA of $N_D = 1$ is imposed for the 1st mode only.

8.8.2 Computational Mesh and Mode Shape for NASA Rotor 67

The mesh as displayed in Fig. 8.83 generated for the full annulus stall flutter simulation of NASA Rotor 67 in the previous section is also used. For the single passage flutter simulations with phase lag boundary conditions, one blade passage from the full annulus is taken. The first five mode shapes of NASA Rotor 67 used for this validation study are shown in Fig. 8.61.

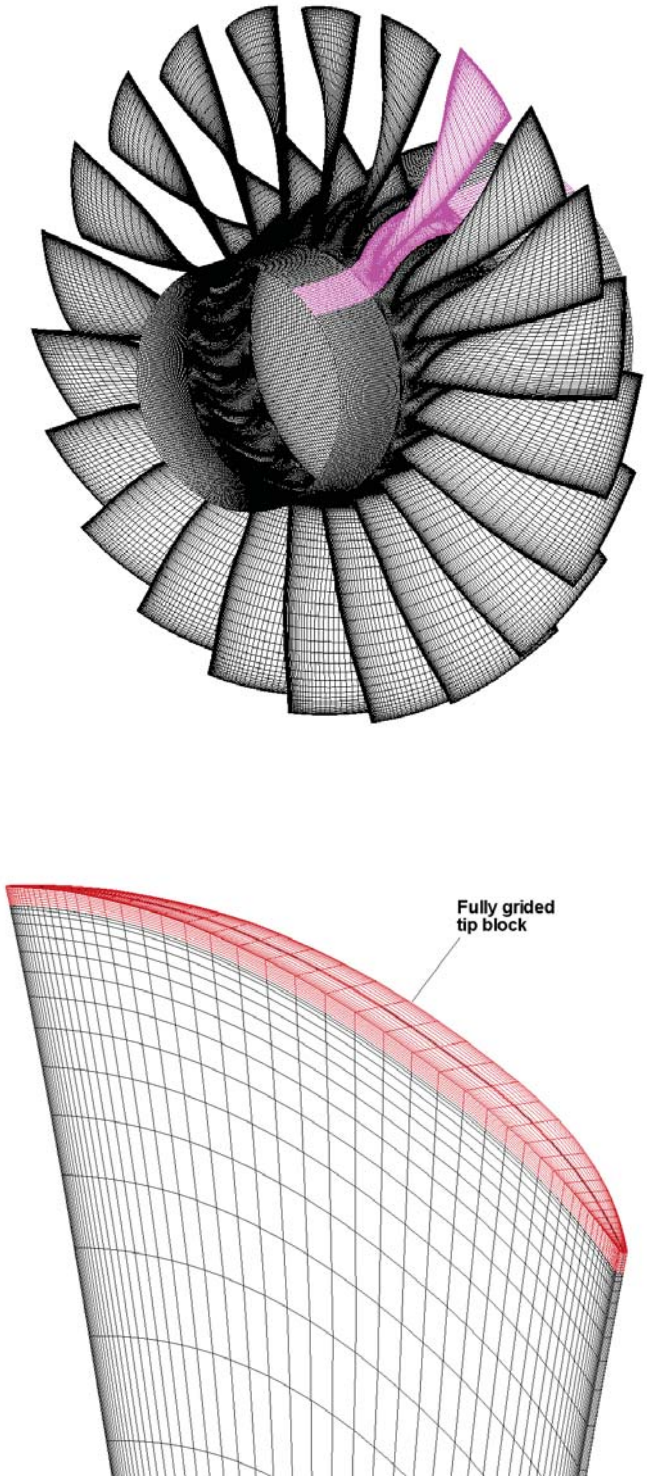

Figure 8.83: Computational mesh for full annulus NASA Rotor 67

8.8.3 Results and Discussion

To validate two phase lag approaches; the time shifted phase lag (TSPL), the Fourier series phase lag (FSPL), the single passage flutter calculations are compared with the full annulus results since the full annulus is the only way to prove any sector of annulus approach with a phase lag BC. Flutter simulations are conducted at near peak condition, where the total-to-total pressure ratio is about 1.62 at design speed of 16043 RPM. In the current study, a uniform structural damping ratio of 0.005 is used. To reduce computational efforts, unsteady computations are started using the steady state full annulus simulation. A nondimensional time step of 0.0171 is used. The residual in each pseudo time step is reduced by three orders, which is achieved usually within 20 iterations.

At near peak condition, the reduced velocity $V^* = 0.43568$, and the mass ratio of the blade $\bar{\mu} = 4299.51$ are obtained. Fig. 8.84 represents the 1st and 2nd modal displacements for the full annulus flutter simulation. The blade responses at near peak are damped out with a constant phase difference. NASA Rotor 67 is shown to have stall flutter by the present authors [7], whereas no flutter event is observed at near peak condition.

Fig. 8.85 shows the backward traveling wave for the 1st mode simulated by the traveling wave BC given as Eq. (8.6). A constant phase difference with $N_D = 1$ is exactly observed. One sinusoidal wave exists in the full annulus, which is $N_D = 1$.

The 1st and 2nd modal force ($\frac{\tilde{\phi}_1^{*T}}{m_1^*} \cdot \mathbf{F}^* \cdot {V_f}^2 \cdot \frac{b_s^2 L}{\bar{V}} \cdot \bar{m}$) for the full annulus are shown in Fig. 8.86. The phase angle difference is clear in the modal forces. The instant modal force shows the transitional period for about 0.02 *sec* (8 rotor revolutions). After 0.02*sec*, the oscillation of aerodynamic excitation force acting on the blade is damped out.

Fig. 8.87 shows static pressure contour at inlet duct of NASA Rotor 67 full annulus. The pressure is about constant at most of the lower span. However, the static pressure shows notable harmonic waves from the mid span annulus. Fig. 8.88 shows instantaneous Mach number at 70% span. The λ-shock in the blade passage is well captured, which is a common shock structure in a transonic rotor [144, 153]. Even though nodal diameter of 1 is imposed for blade fluttering, overall the flow field and shock structure are very much identical.

To find out which harmonic order of Fourier series can predict the flutter close to the full annulus, the single passage simulations using 1st, 2nd, 3rd, and 5th order harmonic are conducted. In addition, to investigate the effects of input frequency ω on flutter, the 1st bending blade eigenfrequency, 1st torsional frequency(2nd mode natural frequency), and blade passing frequency (BPF) are tested. If a frequency is given, then the number of steps($NP = T/\Delta t$) for one cycle of the Fourier phase lag BC is determined.

Fig. 8.89 compares the 1st mode displacements predicted by the full annulus with the Fourier phase lag BC. It is obvious that the FSPL depends on the harmonic order. As the harmonic order increases, difference in the displacements becomes larger. It has been pointed out by He et al. [34] that first few orders(1 or 2) of Fourier coefficients are better to use for turbomachinery blade flutter rather than a higher order harmonic.

Fig. 8.90 shows sum of the Fourier coefficients for the mass flux(ρU) at a lower/upper ghost cell(the middle cell in the upper and lower ghost layer). There is obviously the phase difference between two cells. The Fourier sums for different orders at a lower ghost cell are compared in Fig. 8.91. The overshooting at every period is observed for the high orders.

To investigate the effect of input frequency(ω) on the Fourier phase lag, in addition to

2nd mode blade frequency, two more frequencies including 1st mode blade frequency of 584.04 Hz and BPF of 5882.4 Hz are tested in this study.

Fig. 8.92 compares the 1st and 2nd mode displacements of the full annulus with the 3rd order Fourier phase lag with three different frequencies. It is clear that flutter responses depend on input frequency. The high input frequency shows the larger difference in the blade flutter response to the full annulus. The frequency dependency appears to be a major drawback of the Fourier series phase-lagged BC.

In Fig. 8.93, rotor tip leading edge (LE) vibration in the tangential plane predicted by the full annulus and the FSPL BC are plotted. Regardless of harmonic orders, blade responses are damped out. Again, the FSPL with fewer order harmonic shows better prediction to the full annulus simulation.

The TSPL BC is tested for the single passage with the circumferential angle of the sector geometry $\phi = 16.3636^\circ$ and $N_d = 1$. In Fig. 8.94, the comparison of 1st and 2nd mode displacements predicted by the TSPL, the FSPL with 1st order harmonic and the full annulus are illustrated. The TSPL shows an excellent agreement in the modal displacements with the full annulus simulation. The time-averaged speedline and adiabatic efficiency at near peak are shown in Fig. 8.95 and Fig. 8.96 respectively. The TSPL and the full annulus show better agreement with the experiment [130] than the Fourier series phase-lag.

8.8.4 Summary

Two phase-lagged boundary conditions using the time shift (TSPL) and the Fourier series (FSPL) are developed in this study. The single passage flutter simulations by adopting the TSPL and FSPL at the circumferential boundaries are conducted for NASA Rotor 67 at near peak condition. For validation, the full annulus flutter simulation is also carried out for $N_D = 1$ using a fully coupled fluid/strcuture interaction.

The single blade passage simulation with the TSPL predicts better the blade flutter level at near peak to the full annulus than the FSPL. Even though dependence on input frequency is observed for the FSPL, the FSPL with fewer order harmonic is sufficient to use for turbomachinery flutter.

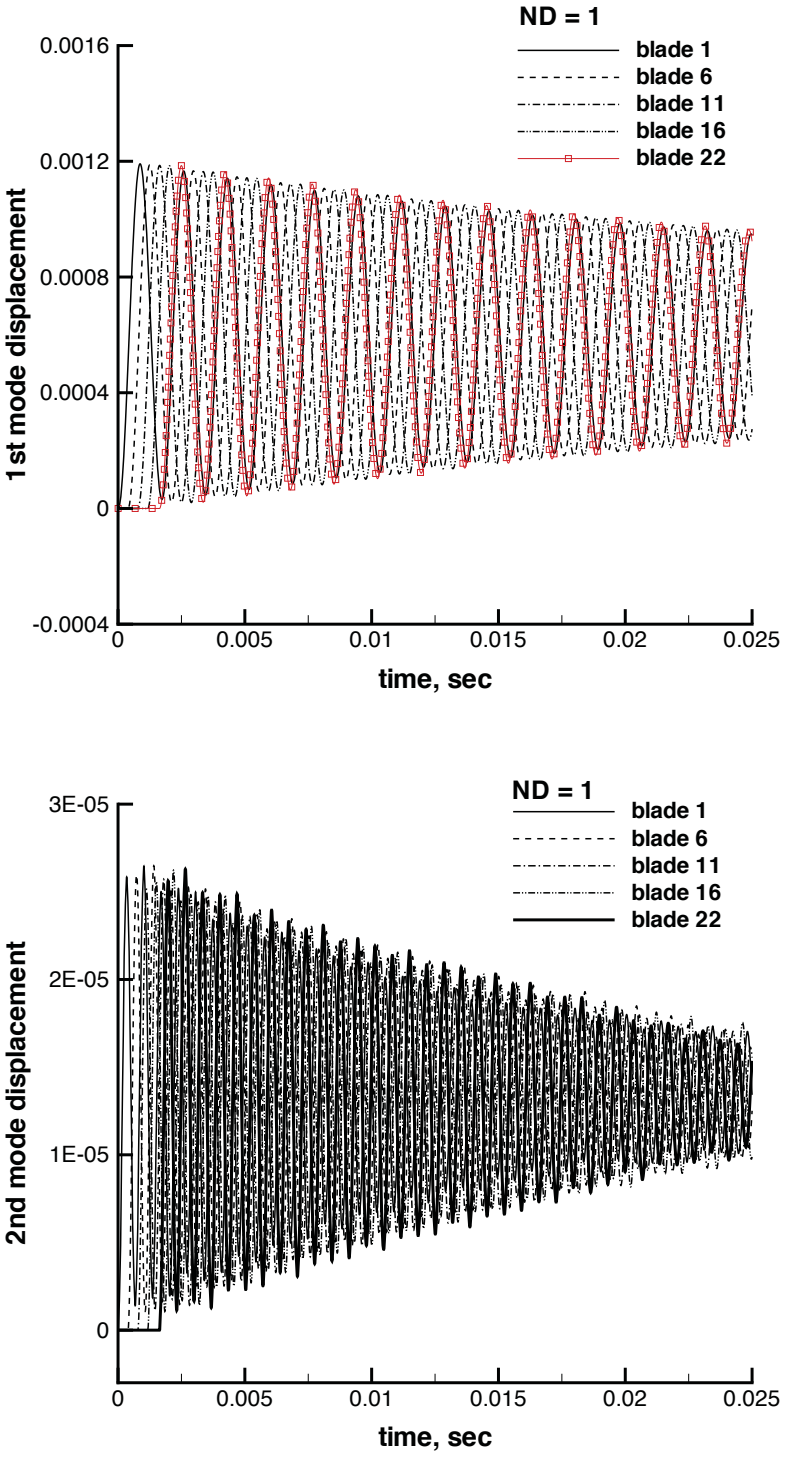

Figure 8.84: Modal displacements from the full annulus NASA Rotor 67 FSI simulation at near peak condition; 1st mode (top), 2nd mode(middle)

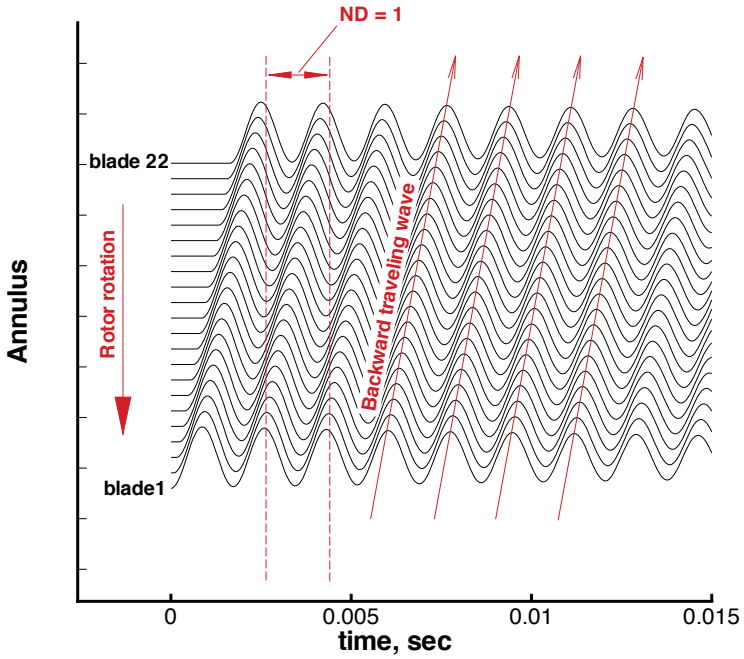

Figure 8.85: Predicted the backward traveling wave (BTW) of the 1st mode with a constant phase angle difference

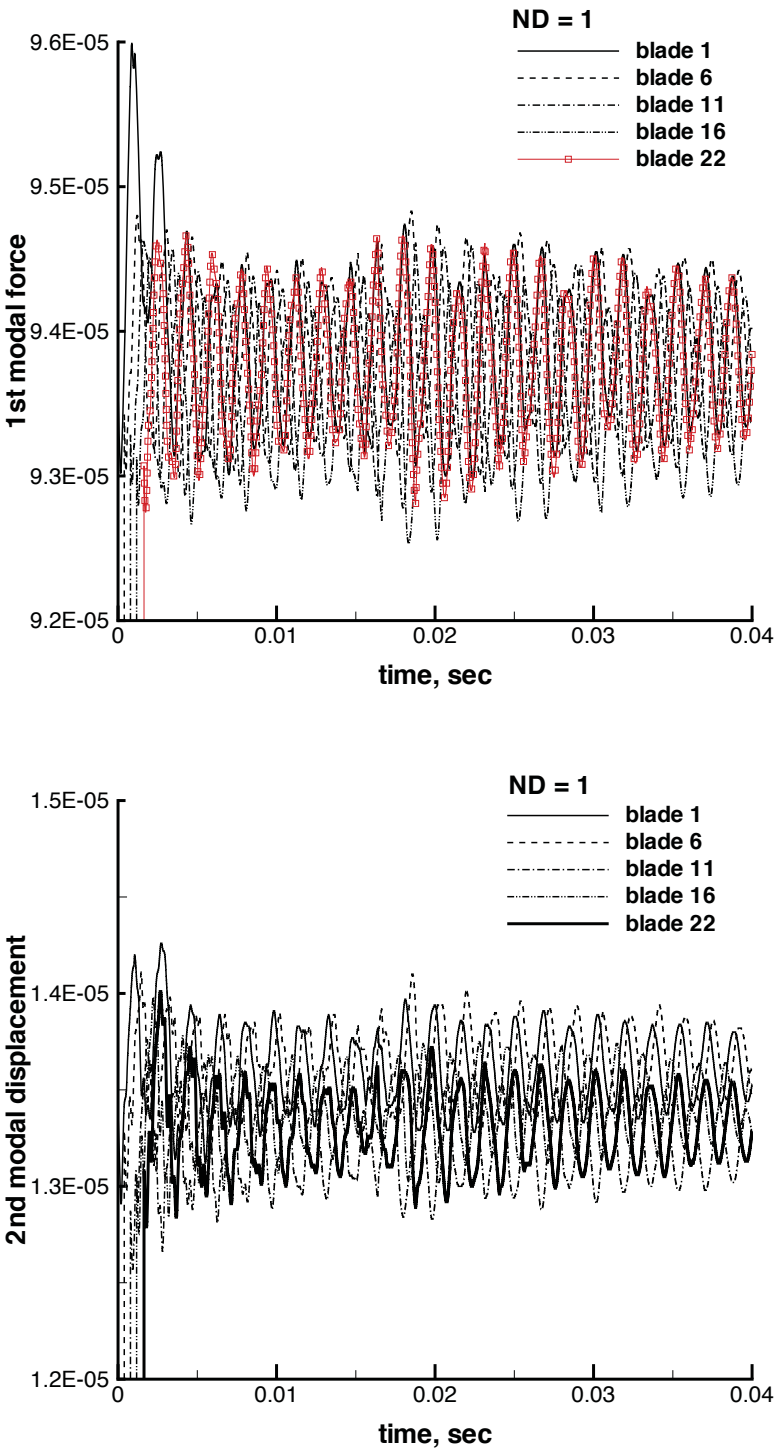

Figure 8.86: Predicted modal force ($\frac{\tilde{\phi}_j^{*T}}{m_j^*} \cdot \mathbf{F}^* \cdot {V_f}^2 \cdot \frac{b_s^2 L}{\bar{V}} \cdot \bar{m}$) from the full annulus FSI at near peak condition; 1st mode(top), 2nd mode(bottom)

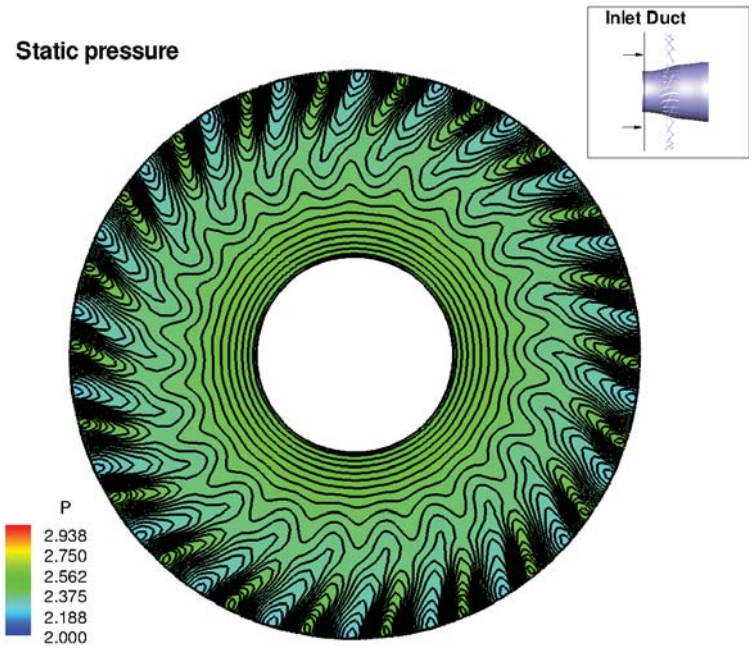

Figure 8.87: Instant static pressure contour of the inlet axial plane from the full annulus FSI at near peak

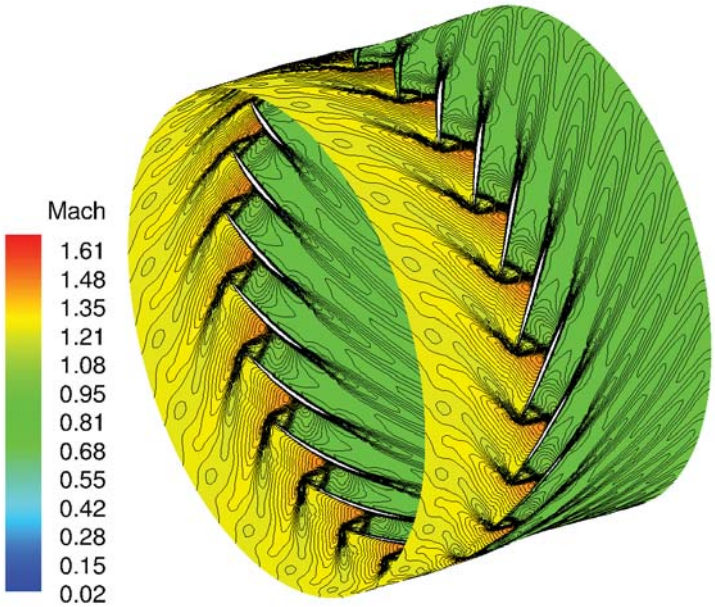

Figure 8.88: Instant full annulus Mach number contour at 70% span at near peak indicating lambda(λ)-shock in the passage

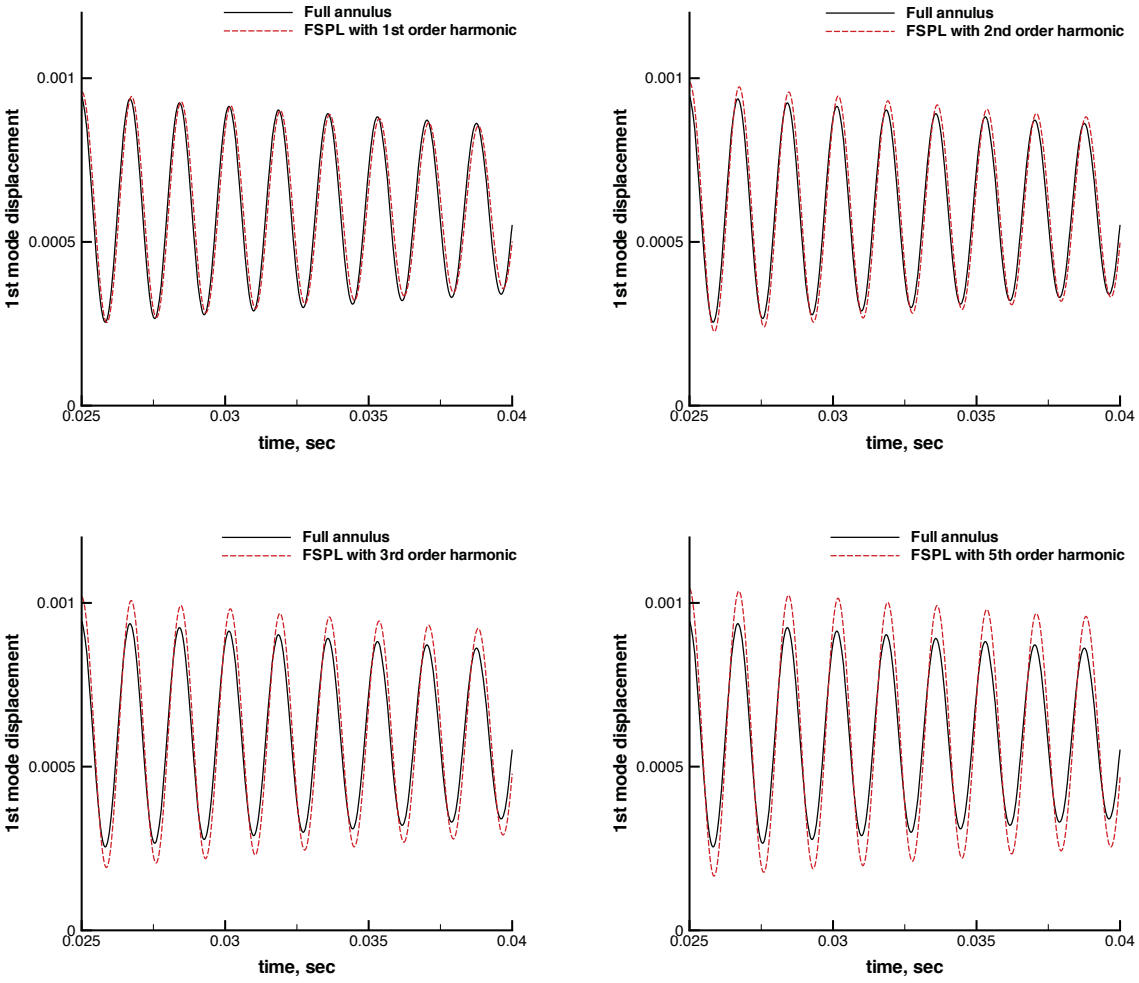

Figure 8.89: The 1st mode displacements predicted by the full annulus and by the single passage FSI with the FSPL BC; 1st order harmonic (top left), 2nd order harmonic(top left), 3rd order harmonic(bottom left), and 5th order harmonic(bottom right)

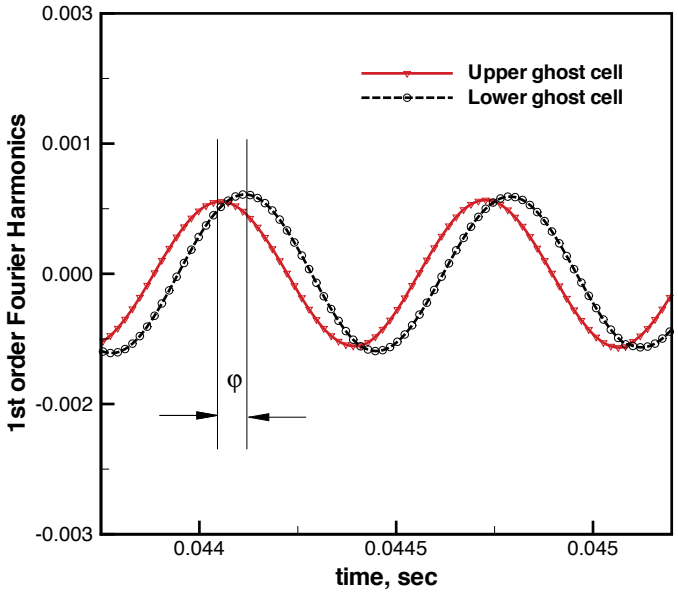

Figure 8.90: The 1st order Fourier coefficients for the normalized mass flux (ρU) at a lower/upper ghost cell with the phase angle, φ

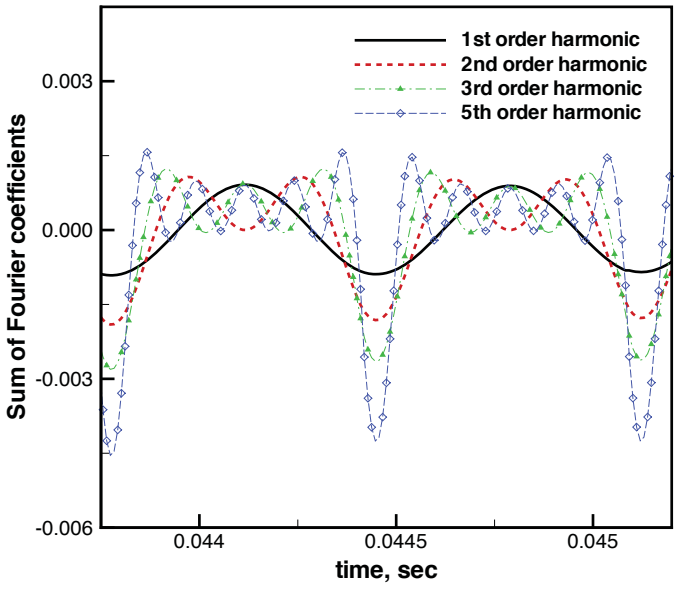

Figure 8.91: Comparison of the Fourier coefficients for the normalized mass flux (ρU) at a upper ghost cell

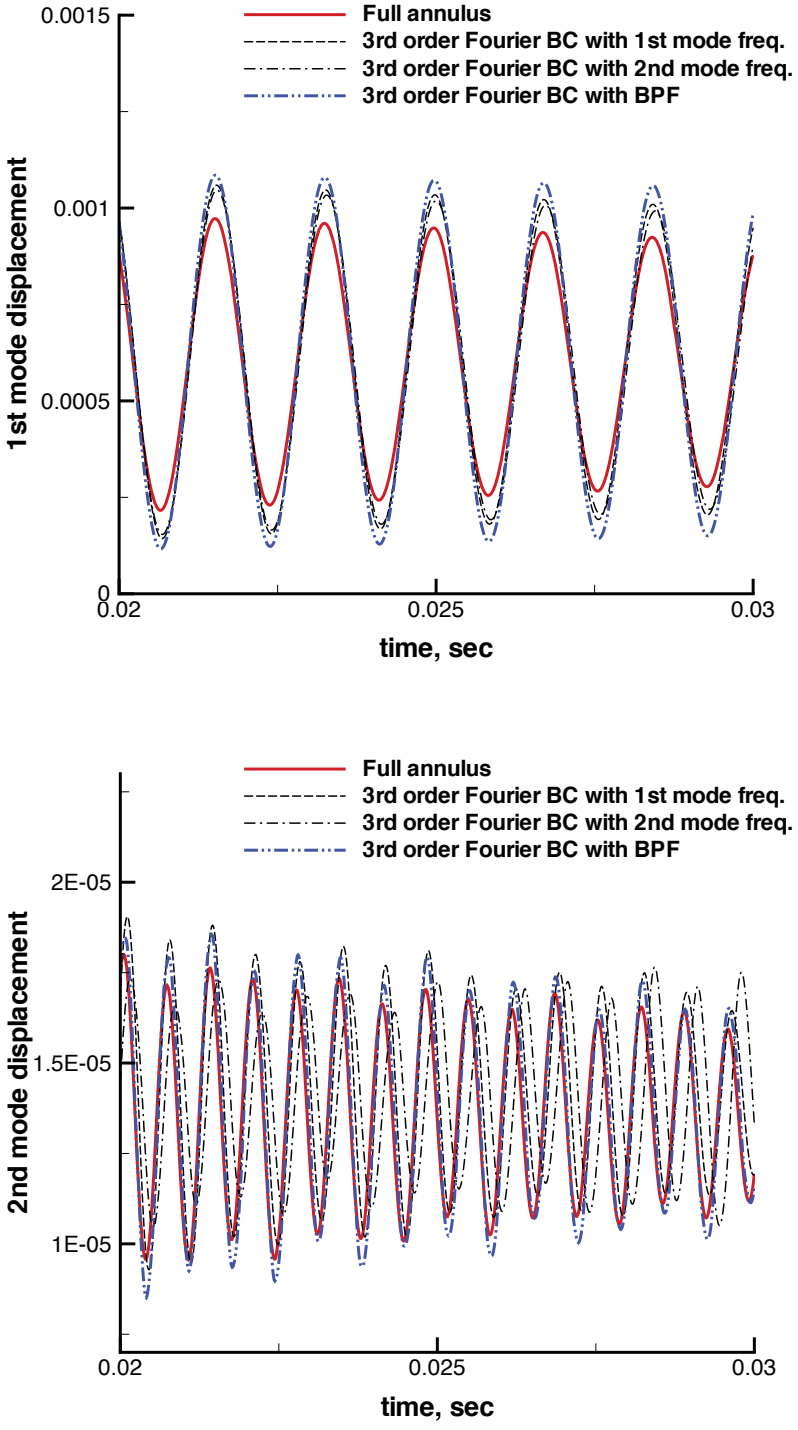

Figure 8.92: The 1st (top) and 2nd (bottom) mode displacements predicted by the FSPL with different frequency input

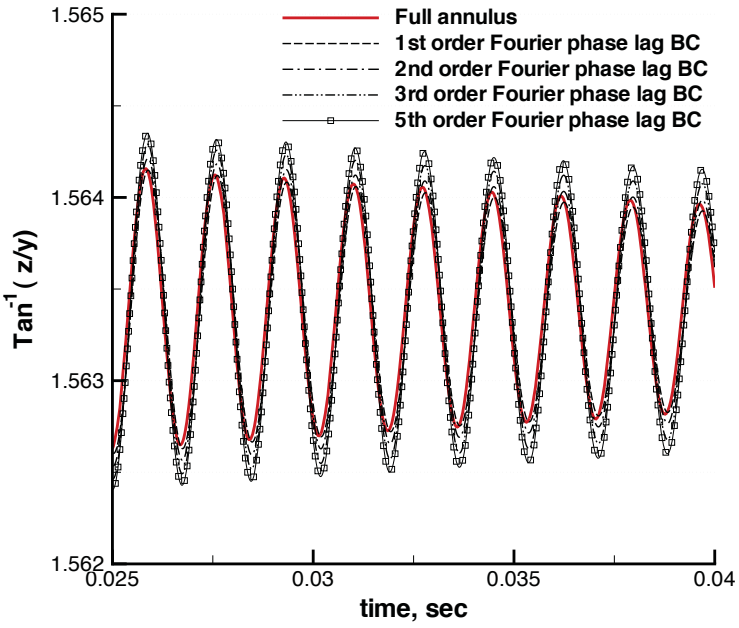

Figure 8.93: Tip LE vibration in tangential plane predicted by the FSPL BC

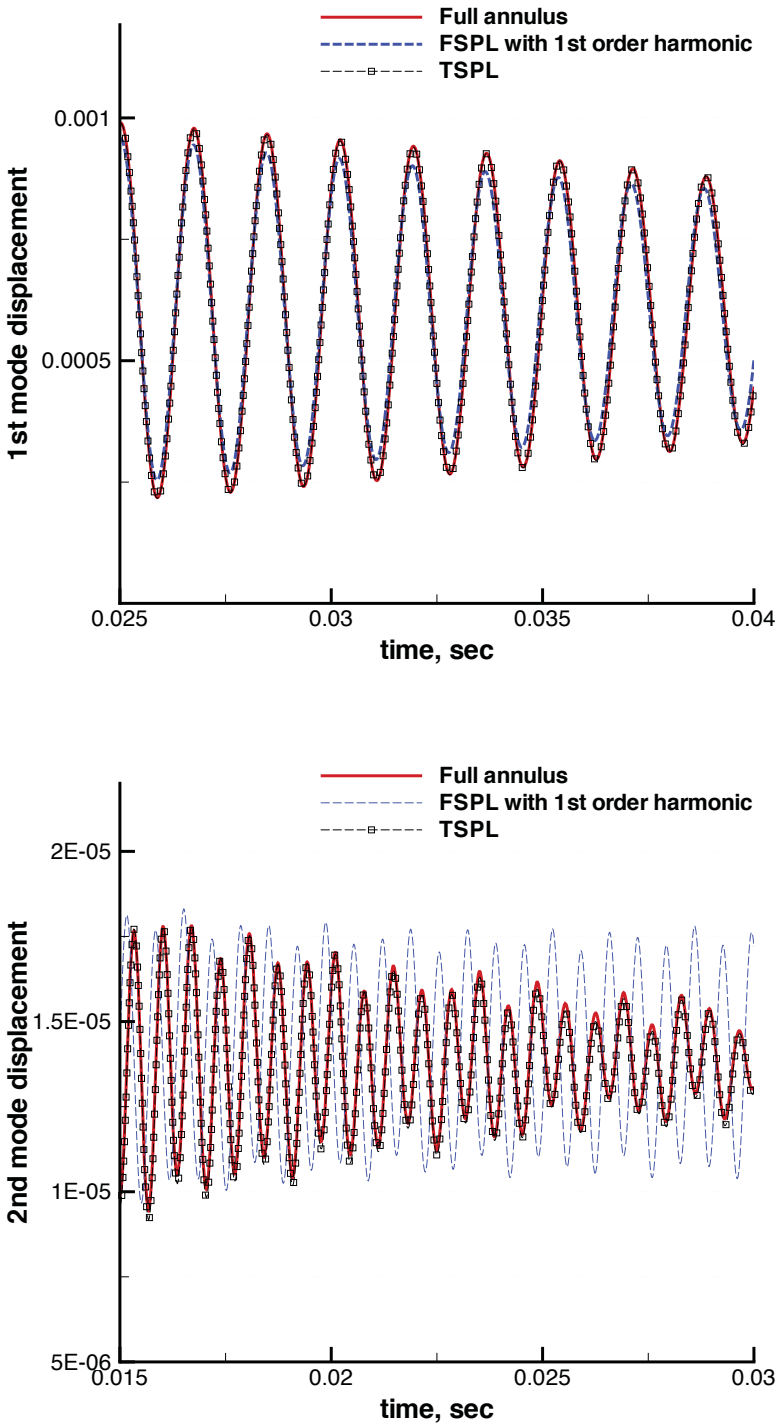

Figure 8.94: Comparison of 1st(top) and 2nd(bottom) mode displacements predicted by the TSPL BC with the full annulus and the FSPL

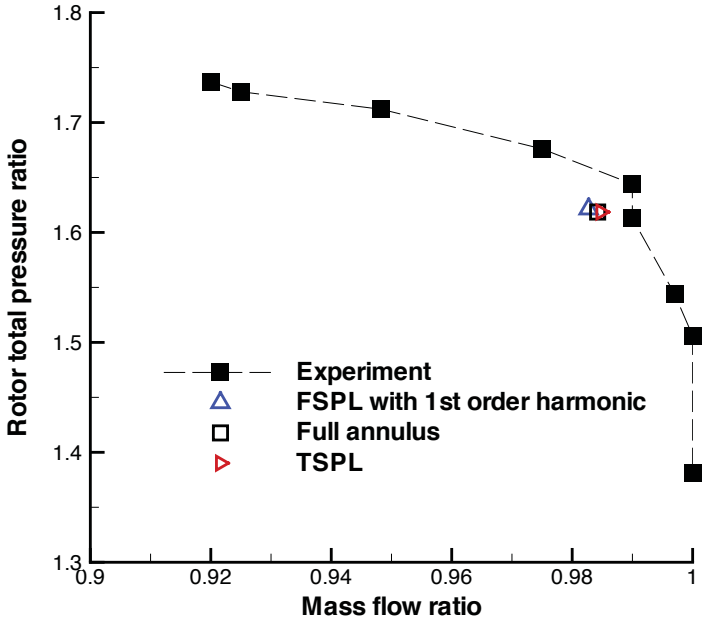

Figure 8.95: Predicted speed line at near peak

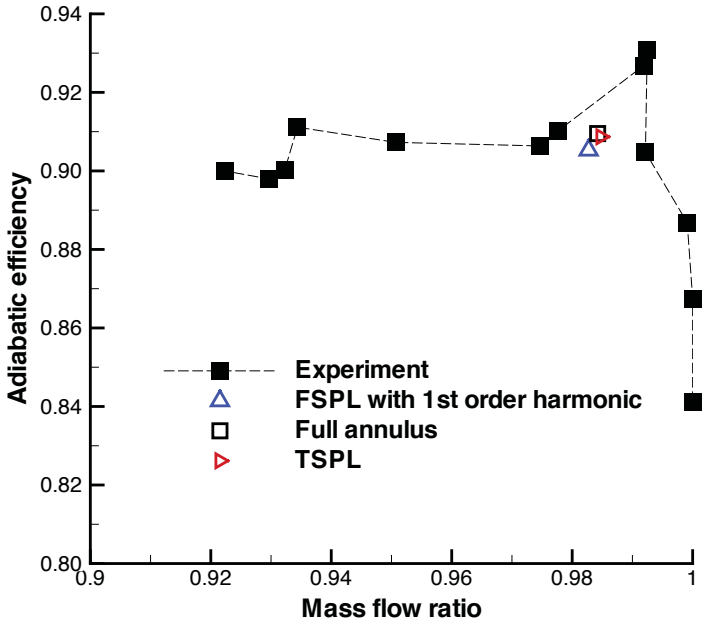

Figure 8.96: Predicted adiabatic efficiency at near peak

8.9 Multistage Compressor Simulation with Conservative Sliding BC

In this study 3D multistage simulations for GE 1-1/2 stage high speed axial compressor with IGV are conducted to validate the unsteady fully conservative sliding boundary condition and the steady mixing plane method for the rotor/stator interface treatment. A 1/7th sector of annulus is used for the unsteady simulation with the Fourier phase lag BC. For comparison, a steady simulation of the same multistage compressor with single blade passage is performed using the mixing plane approach. In addition, NASA Stage 35 is chosen as another validation model for the mixing plane since the measured data including radial profiles of total pressure, total temperature, flow angle and efficiency are available [5].

In the present study, the Low Diffusion E-CUSP (LDE) Scheme [109] as an accurate shock capturing Riemann solver is used with the 3rd order WENO reconstruction for the inviscid flux and 2nd order central differencing for the viscous terms [117]. It is shown that the sliding BC captures wake propagation very well in the interaction between blade rows. The unsteady multistage simulation using sliding BC and phase lag BC predicts almost identical loading distribution to the steady state simulation at the mid-span, but have significant loading distribution difference at tip section.

8.9.1 Boundary Conditions

At the IGV inlet, the radial distributions of total pressure, total temperature, swirl angle and pitch angle are specified for GE 1-1/2stage compressor. For NASA Stage 35, averaged total pressure and total temperature are given from the experiment [5]. The swirl angle

and pitch angle are set to zero. The velocity is taken from the computational domain by the extrapolation in order to determine the rest of variables. At the stator outlet, the static pressure distribution in the spanwise direction is specified for GE 1-1/2stage compressor. For NASA Stage 35, the radial equilibrium equation (6.12) is used to determine the radial distribution of the back pressure from the experiment [5]. The other boundary conditions introduced in chapter 6 are used for the rest of the part. At the lower/upper circumferential periodic boundaries, in-phase condition is used for the steady mixing plane simulation and the Fourier phase lag BC is used for the unsteady simulation.

8.9.2 Steady Simulation of GE 1-1/2 Stage Axial Compressor

Using the mixing plane, the single passage steady computations are performed with CFL number of 1. In-phase condition was applied at periodic boundary. The computational mesh is presented in Fig. 8.97. The rotor tip clearance of about 2.4% tip chord was given. The rotor tip is precisely modeled with 21 grid points using a O-mesh block. The mesh of IGV/rotor/stator is partitioned to total 30 blocks for parallel computation. The mesh around blade was constructed by using the O-mesh. The H-mesh is used for the matched disk at interface of IGV/rotor/stator since the 1/7th annulus mesh used for the unsteady simulation is built by copying the single passage mesh.

Fig. 8.98 shows the predicted speedline by the different mesh size. The baseline mesh for the blade passages is constructed by 197(around blade) $\times$ 81(blade-to-blade) $\times$ 71(span) and the coarse mesh is 121(around blade) $\times$ 81(blade-to-blade) $\times$ 57(span). Two mesh are well converged to GE CFD predictions. However, the difference between GE and

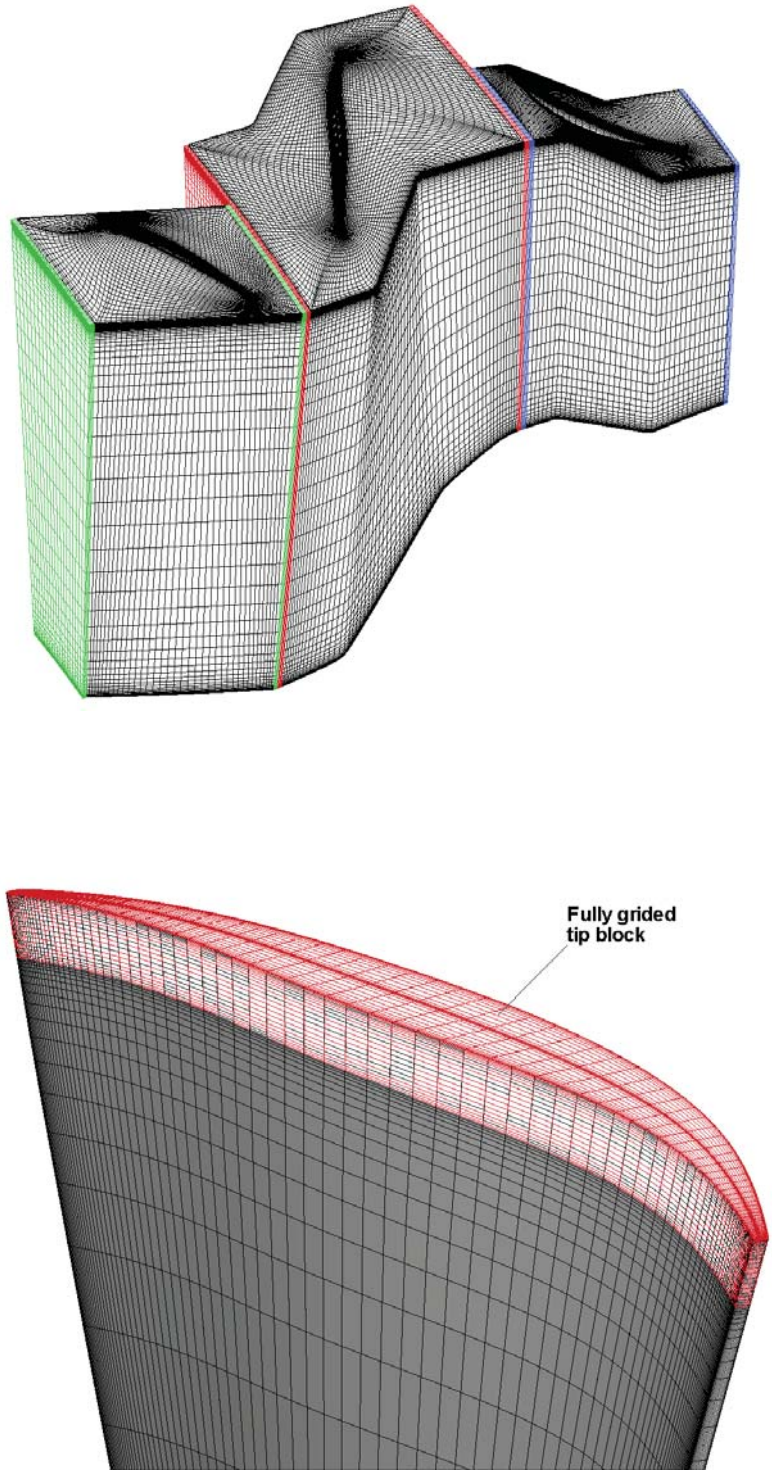

Figure 8.97: Single passage mesh for steady mixing plane simulation; IGV=121(around blade) $\times$ 51(normal to the blade) $\times$ 71(spanwise), Rotor=201$\times$ 51$\times$ 71, Stator=121$\times$ 51$\times$71, tip block = 201$\times$14$\times$21

the baseline simulation become larger as the compressor approaches stall with decrease in the mass flow. It is believed that different numerical schemes or turbulence model between two solvers causes such a difference because the flow is separated and very complex due to tip leakage vortex interaction at near stall.

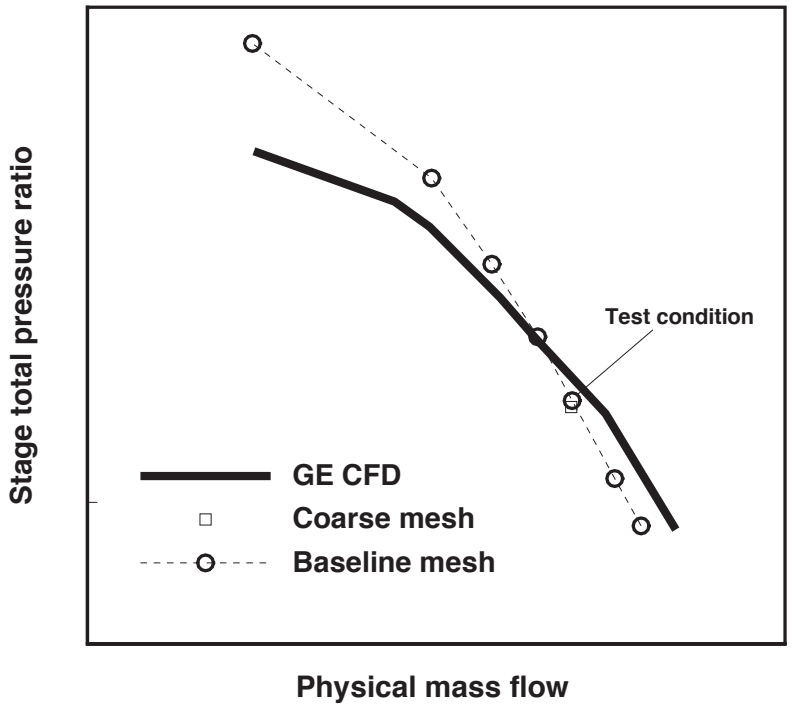

Figure 8.98: Comparison of predicted speedline

Fig. 8.99 shows the predicted radial profiles of total pressure ratio and total temperature at rotor exit. Fig. 8.100 shows the predicted radial profiles of absolute flow angle and adiabatic efficiency at rotor exit. Compared to GE's steady state CFD prediction, all profiles show good agreement. The current results show slightly higher efficiency than GE's steady state CFD results over the 70% span.

In Fig. 8.101, the absolute Mach number and static pressure at 50% span are shown.

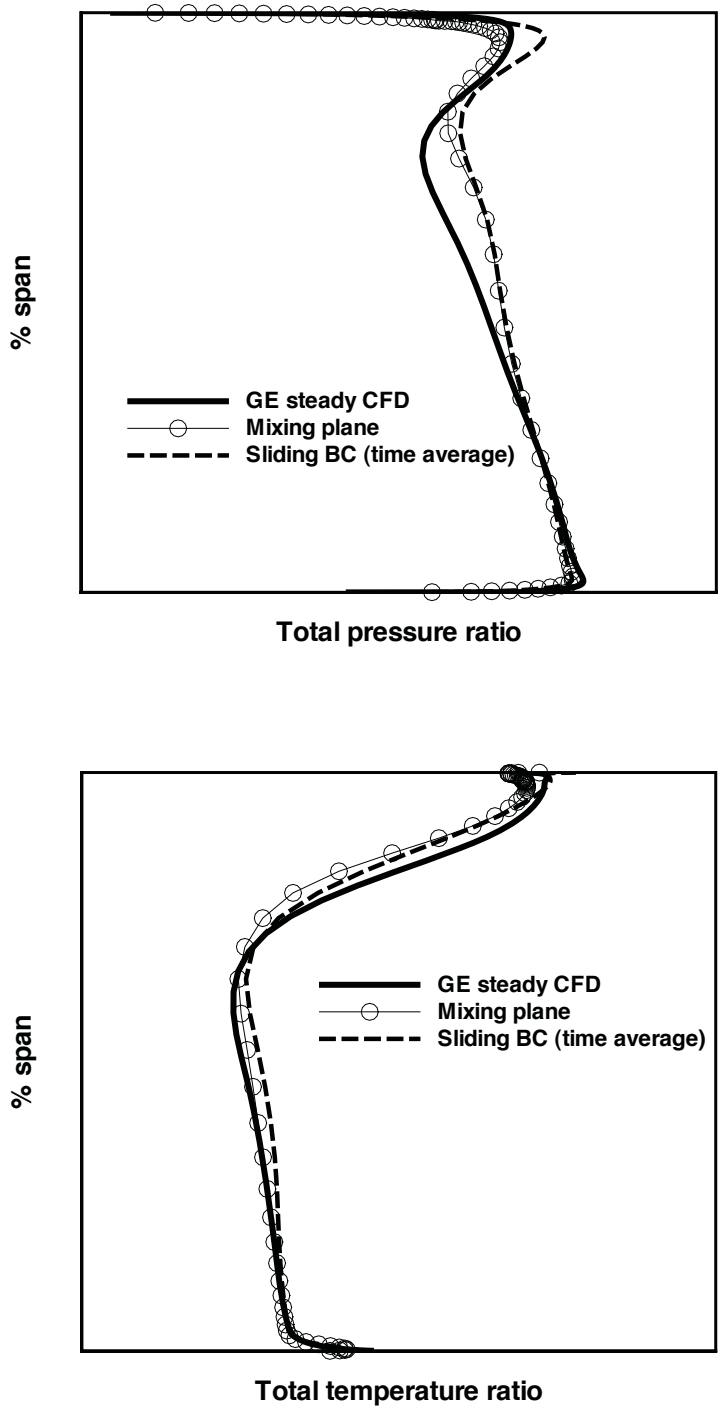

Figure 8.99: Predicted pitch-averaged spanwise profiles at rotor exit plane; total pressure ratio(top), total temperature ratio(bottom)

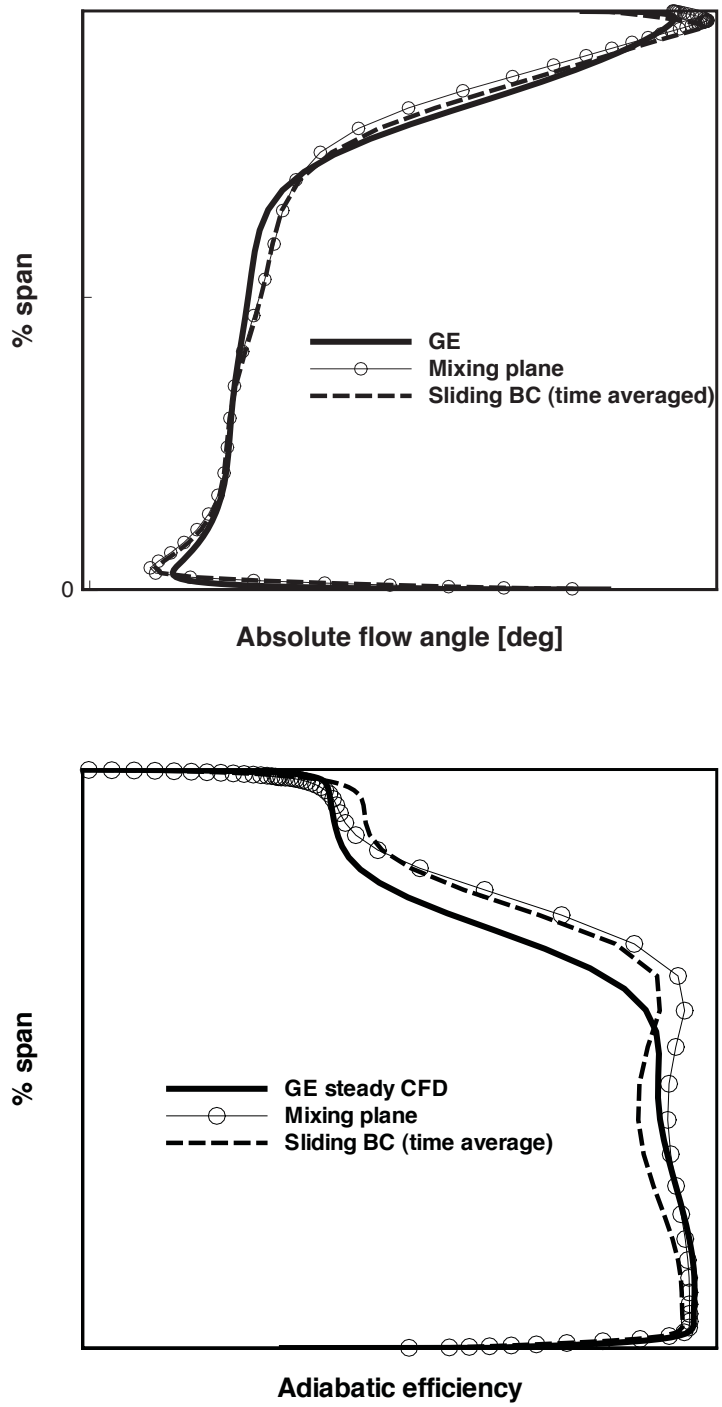

Figure 8.100: Predicted pitch-averaged spanwise profiles at rotor exit plane; absolute flow angle(top), adiabatic efficiency(bottom)

At the interface of IGV and rotor, and rotor and stator, the flow of the upstream outlet boundary is mixed out to the downstream boundary. The discontinuity from the upstream to the downstream at the mixing plane is obvious.

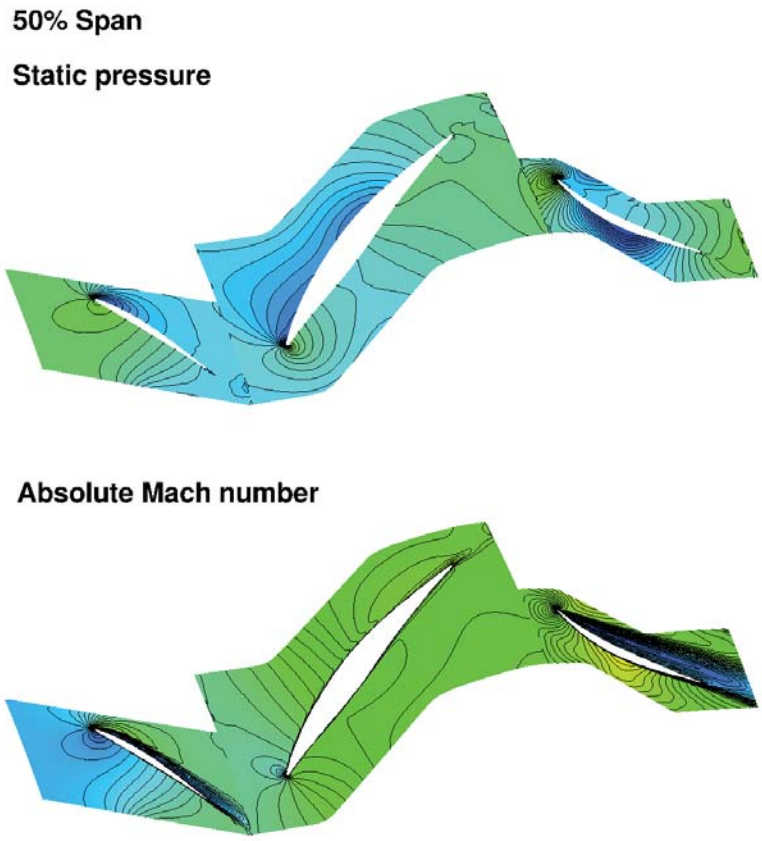

Figure 8.101: Mach number and static pressure contour of 50% span predicted by the mixing plane simulation

8.9.3 Unsteady Simulation of GE 1-1/2 Stage Axial Compressor

Unsteady simulation for 1/7th annulus of the multistage compressor are performed over 2 rotor revolutions using the Fourier phase lag BC. The rotor blade passing frequency is used in the phase lag BC for all the blade rows. The number of pseudo time steps within each physical time step is determined by having the residual reduced by at least two orders of

magnitude, which usually is achieved within 40 iterations. To reduce CPU time, the flow field for the unsteady simulation is initialized using the mixing plane. A time step of about 0.0000016 *sec* and CFL of 1 are used.

Fig. 8.102 shows the interface mesh system that enables information exchange in the the fully conservative manner. 1/7th annulus mesh was split into total 174 blocks for the parallel computation. In particular the grid points of 101 in the blade-to-blade was determined to be able to resolve the blade wall boundary layers and wakes.

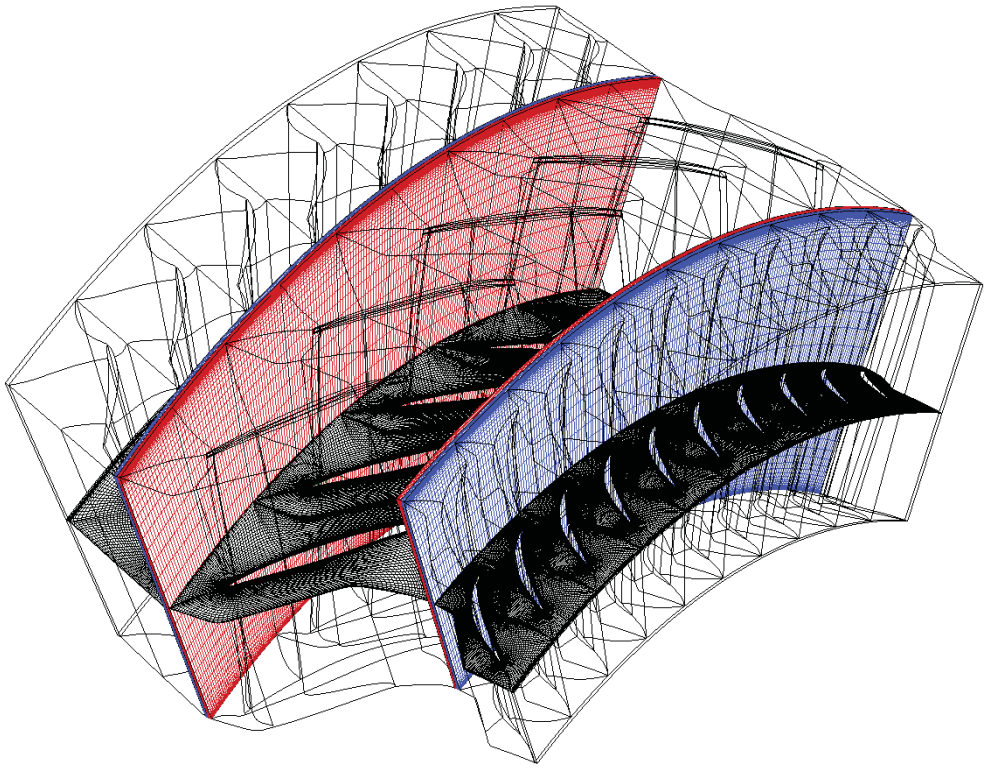

Figure 8.102: 1/7th annulus mesh with H-disk blocks at IGV/rotor/stator interface for the unsteady simulation

Fig. 8.103 illustrates an instant entropy contours, which shows the wake propagation in the blade passage and cross blade rows. The disturbance wakes generated art upstream near trailing edge are traveling downstream blade row without cut-off. Fig. 8.104 shows the instantaneous static pressure at 50% span. There are no shocks in the mid-span passage. The continuous pressure field at blade row interface indicates flux conservativeness of current sliding boundary condition.

The instantaneous pressure at 50% span of the rotor upstream interface is measured during the unsteady simulation as shown in Fig. 8.105. The unsteadiness is clearly captured at the interface due to interaction between IGV and rotor. The static pressure oscillates in a periodical manner, which is called passing frequency. Fig. 8.106 shows the predicted frequency from FFT frequency analysis using the static pressure spectrum in Fig. 8.105. IGV passing frequency (BPF) is sharply captured. There is a low frequency peak, which is a frequency caused by tip flow instability as a source of non-synchronous blade vibration.

Fig. 8.107 and Fig. 8.108 show surface pressure distributions of the rotor blade at 50%, 98% span respectively. The unsteady results are time averaged for 700 time steps. A significant difference between the steady and the unsteady simulation is shown even though the overall loading is similar, whereas the predicted pressures are almost identical at 50% span. The unsteadiness generated by rotor/stator interaction becomes significant toward rotor tip. The reason may be that the mixing plane method cut off the shock propagation upstream and tip vortex propagation downstream. These two factors ultimately affect the predicted tip loading distribution of the blade.

8.9.4 Summary

This paper simulates the GE 1-1/2 stage compressor using steady state calculation with mixing plane boundary condition and unsteady calculation with sliding boundary conditions. The unsteady sliding boundary conditions are fully conservative without interpolation by always having the grid point one-to-one connected.

The steady state multistage simulation using mixing plane BC agrees well with the results of GE's steady state CFD prediction. The unsteady multistage simulation using sliding BC and phase lag BC predicts almost identical loading distribution to the steady state simulation at the mid-span, but have significant loading distribution difference at tip section. The reason may be that the mixing plane method cut off the shock propagation upstream and tip vortex propagation downstream. These two factors ultimately affect the predicted tip loading distribution of the blade.

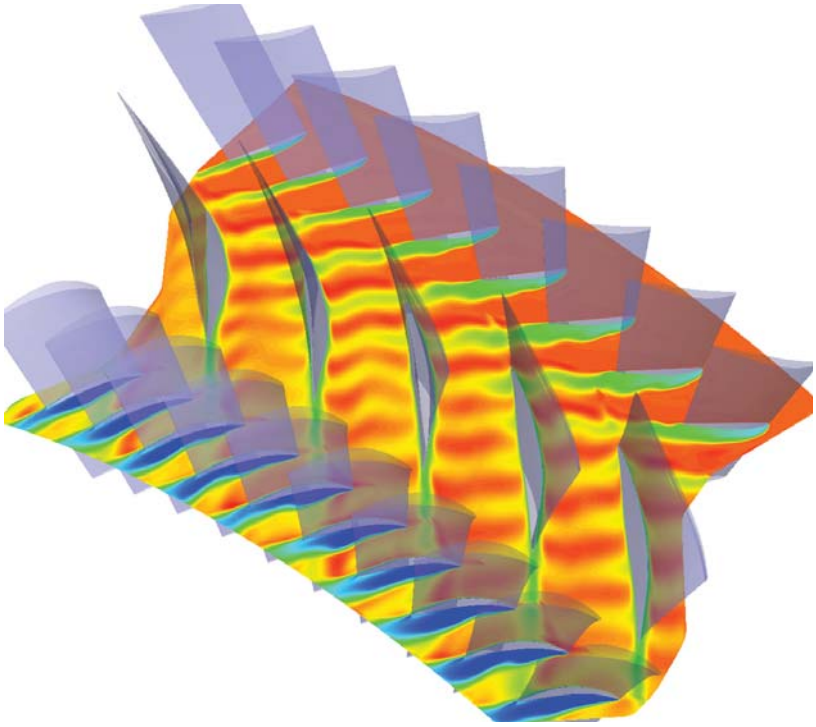

Figure 8.103: Entropy propagation at 50% span

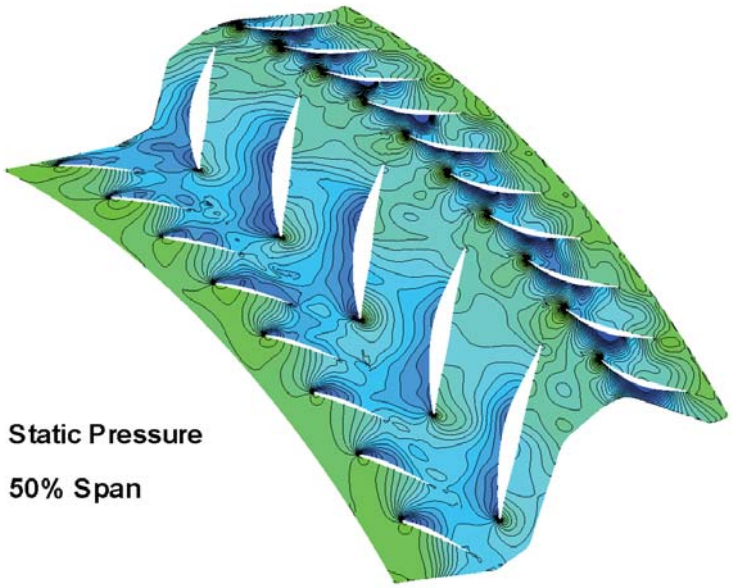

Figure 8.104: Static pressure at 50% span

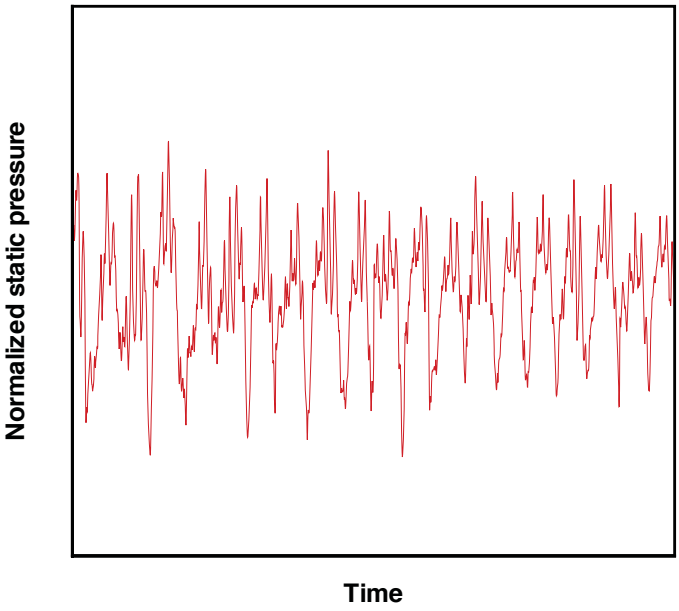

Figure 8.105: Static pressure oscillation at the interface of the rotor tip upstream

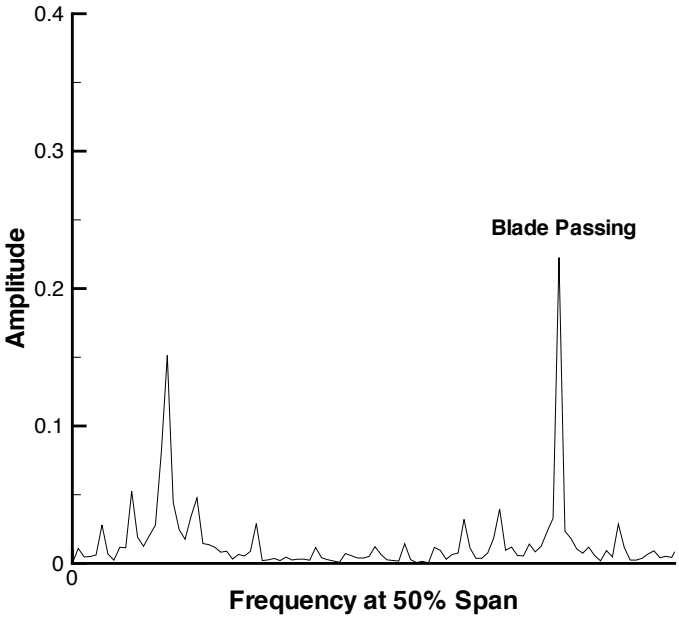

Figure 8.106: Predicted IGV blade passing frequency at 50% span of rotor upstream interface

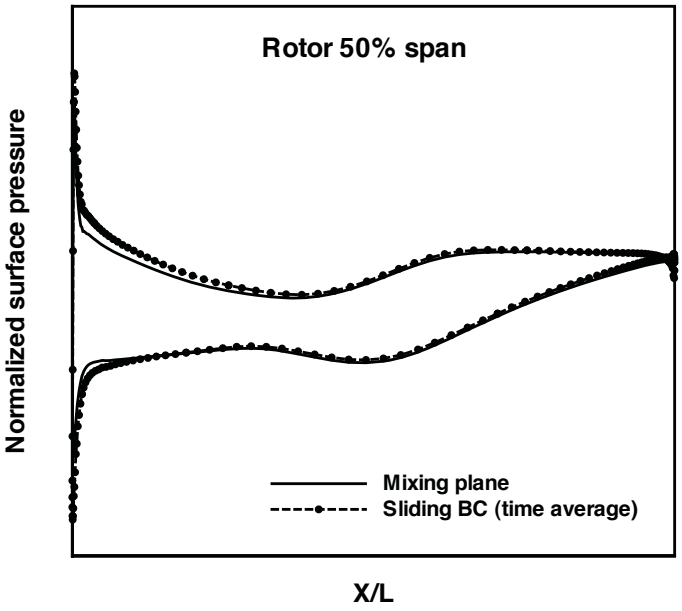

Figure 8.107: Distributions of rotor blade surface static pressure at 50% span

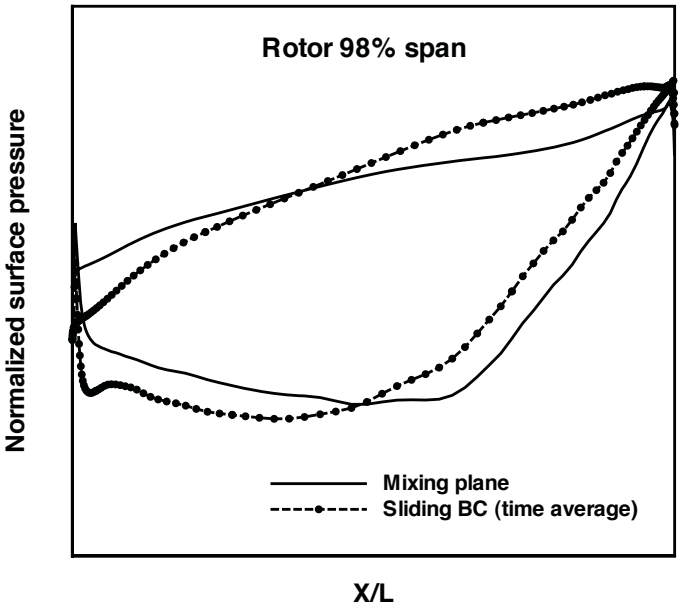

Figure 8.108: Distributions of rotor blade surface static pressure at 98% span

8.10 NASA Stage 35 Simulation Using Mixing Plane

The present steady multistage capability using the mixing plane method is further validated for NASA Stage 35. NASA Stage 35 is designed with 36 rotor blades and 46 stator blades. The designed 100% speed is 17188.7 RPM.

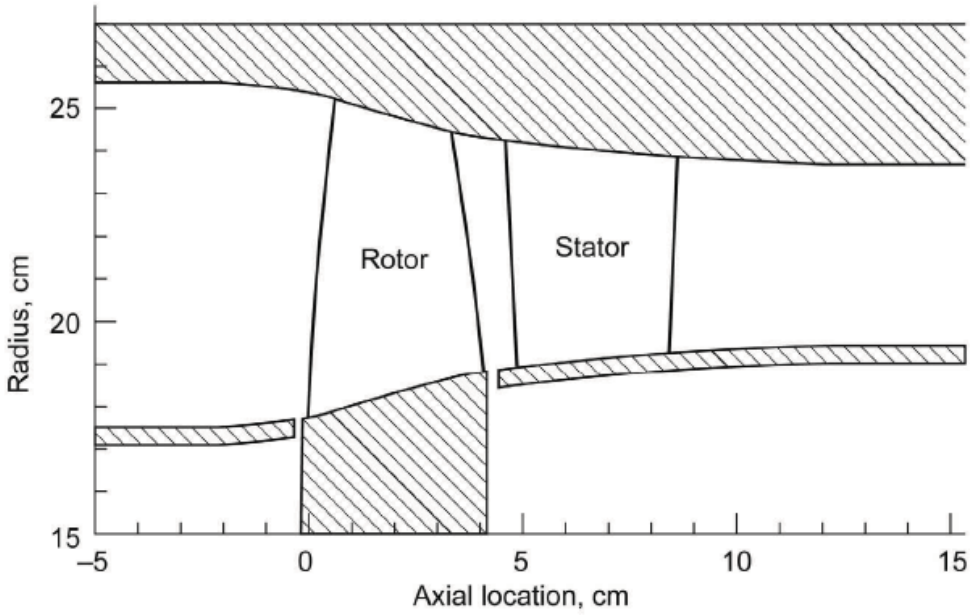

Figure 8.109: Flow path of NASA Stage 35 [5]

The computational mesh as presented in Fig. 8.110. H-O-H mesh topology is used and total mesh size is 832,284. As pointed out by McNulty [132], approximately 2000,000 grid points per single blade passage is enough to predict the transonic rotor flow field. Hence, the present mesh size is believed to be fine. The rotor tip is fully gridded using a O-mesh with 14 cells.The rotor blade O-block is 185(around blade) $\times$ 87(blade-to-blade) $\times$ 60(span) and that of stator is 145(around blade) $\times$ 87(blade-to-blade) $\times$ 60(span).

In-phase condition is applied at lower/upper circumferential boundaries. To achieve complete speedline, the back pressure is increased from choke to near stall. The RANS

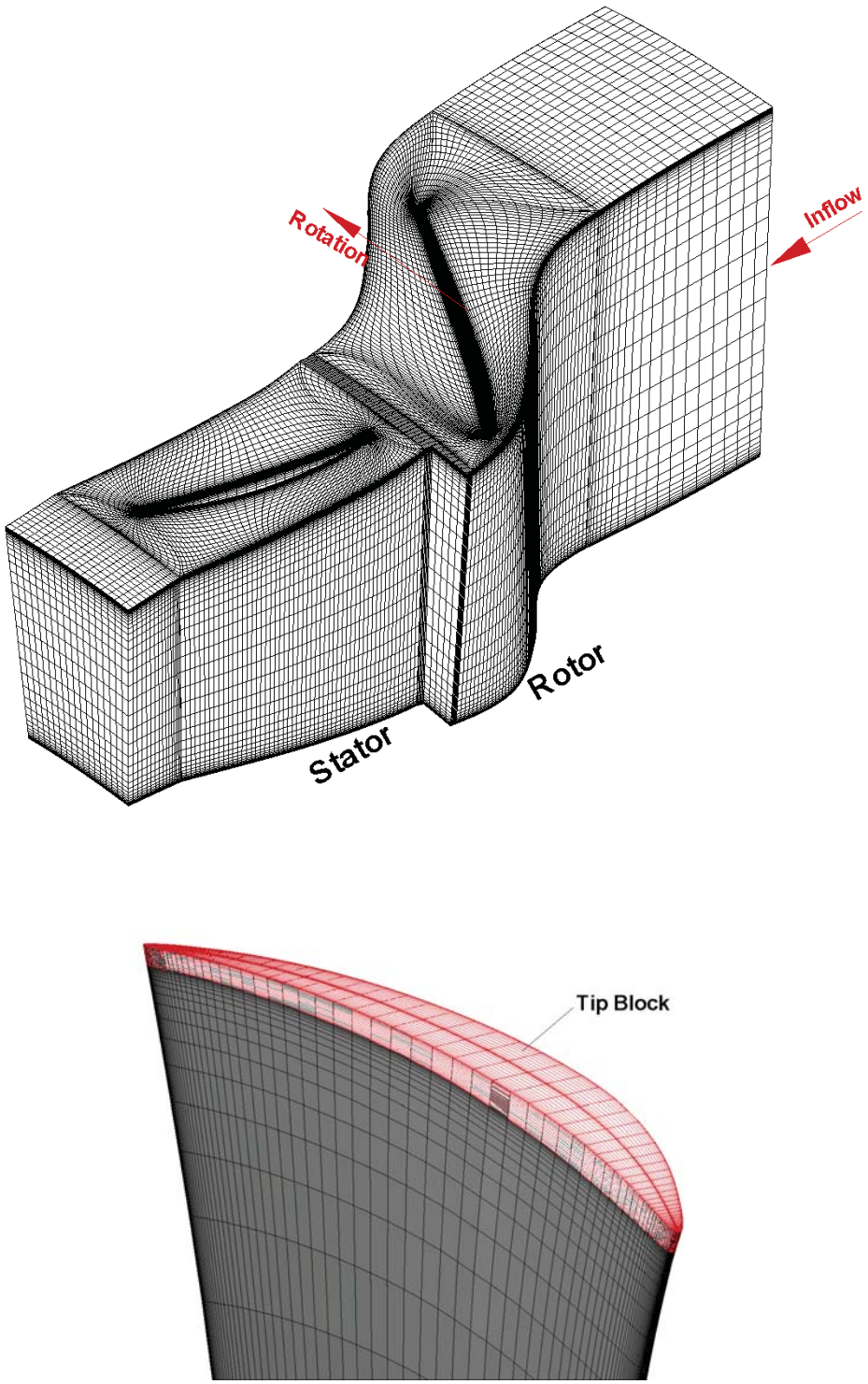

Figure 8.110: Computational mesh for NASA Stage 35

simulation with the SA turbulence model is conducted. The low diffusion E-CUSP scheme with the 3rd order MUSCL reconstruction for the inviscid flux is employed to accurately capture the passage shock/boundary layer interaction in a transonic compressor stage. The 2nd order central differencing for the viscous terms is used.

The predicted speedline of NASA Stage 35 is shown in Fig. 8.111. The present mixing plane using a single blade passage predicts very accurately the measured total pressure ratio versus the mass flow. The full annulus unsteady simulation using a rotor/stator sliding interface BC [154] shows a large discrepancy with the experiment. The multi-passage steady RANS simulation using a mixing plane approach [155] shows also a little difference in the total pressure in particular near stall, while the speedline predicted by the present mixing plane shows an excellent agreement with the measurement over entire mass flow conditions.

Fig. 8.112 shows the predicted adiabatic efficiency(η_c). The peak efficiency is found near choke point and is decreased approaching near stall. Overall current prediction matches well the measured efficiency.

$$\eta_c = \frac{\frac{P_{o3}}{P_{o1}}^{\frac{\gamma-1}{\gamma}} - 1}{\frac{T_{o3}}{T_{o1}} - 1} \tag{8.8}$$

where the subscript $o1$ denotes the rotor inlet and $o3$ denotes the stator outlet.

The predicted radial profiles of total pressure, total temperature, adiabatic efficiency and flow angles are plotted in Fig. 8.113, Fig. 8.114, Fig. 8.115, Fig. 8.116 respectively. There is little difference between the predicted total pressure and total temperature and the experiment. The efficiency predicted by the present mixing plane is however very accurate compared to the experiment. About 2° difference in the predicted absolute flow angle at

the stator outlet is found. Such a discrepancy is very acceptable by taking into account the unsteadiness due to stator/rotor interaction that can not be resolved by steady approaches but unsteady simulations.

Fig. 8.117 shows the static pressure contour at 50% span predicted in this study. A strong passage shock appears at 50% span. Fig. 8.118 shows the predicted entropy contour at the same span. A shock/boundary layer interaction is clearly captured about 50% axial chord on the suction surface where entropy significantly increases. The entropy propagation from the rotor trailing to the stator is cut-off obviously at the interface.

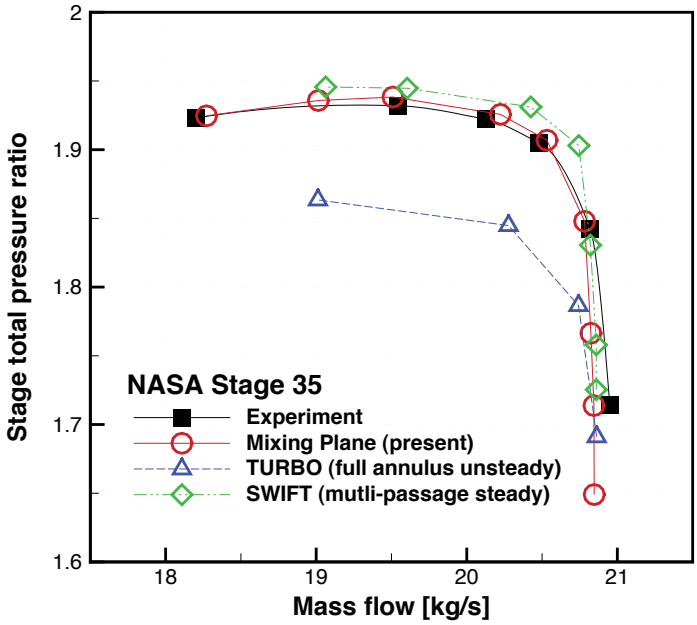

Figure 8.111: Predicted speedline of NASA Stage 35

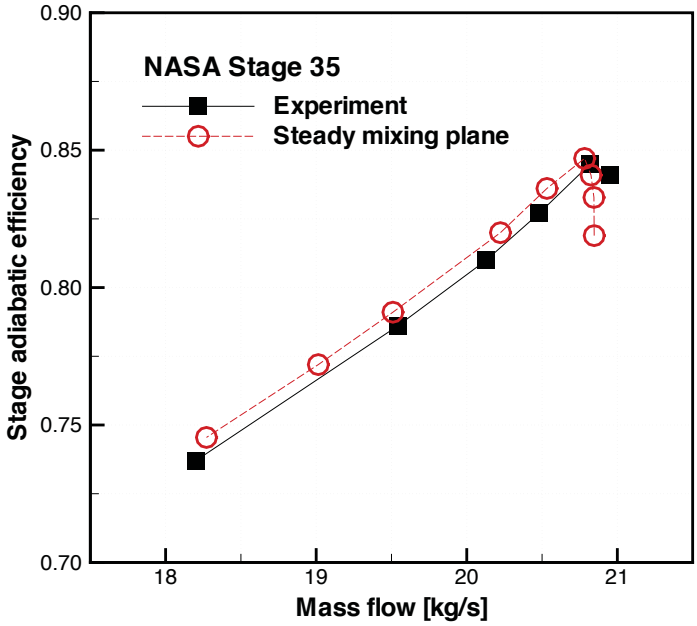

Figure 8.112: Predicted adiabatic efficiency of NASA Stage 35

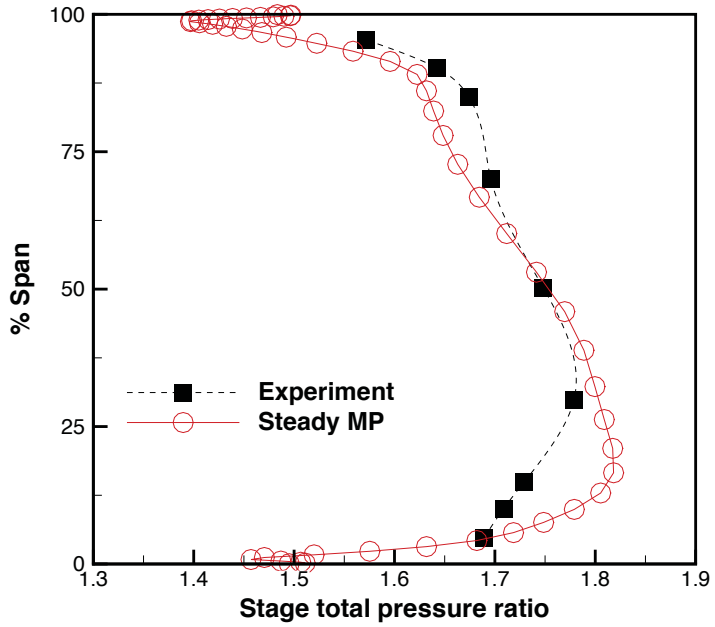

Figure 8.113: Spanwise distributions of the circumferentially mass averaged total pressure for NASA Stage 35

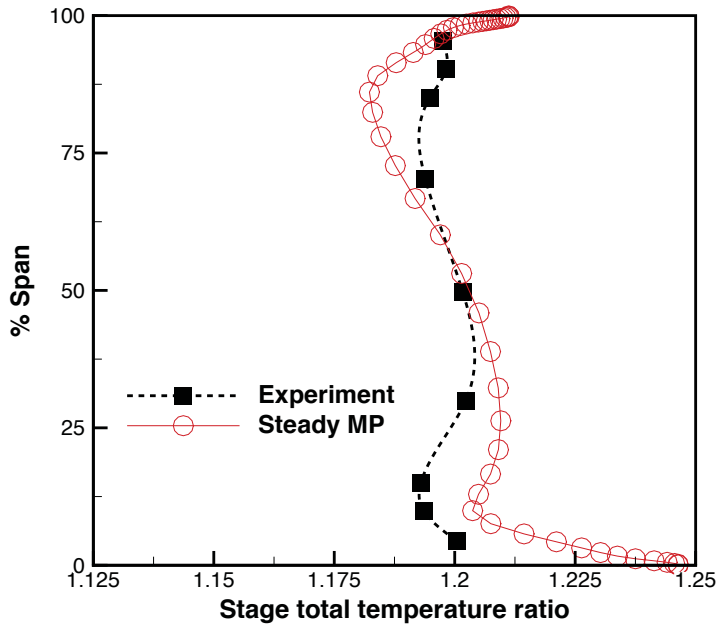

Figure 8.114: Spanwise distributions of the circumferentially mass averaged total temperature for NASA Stage 35

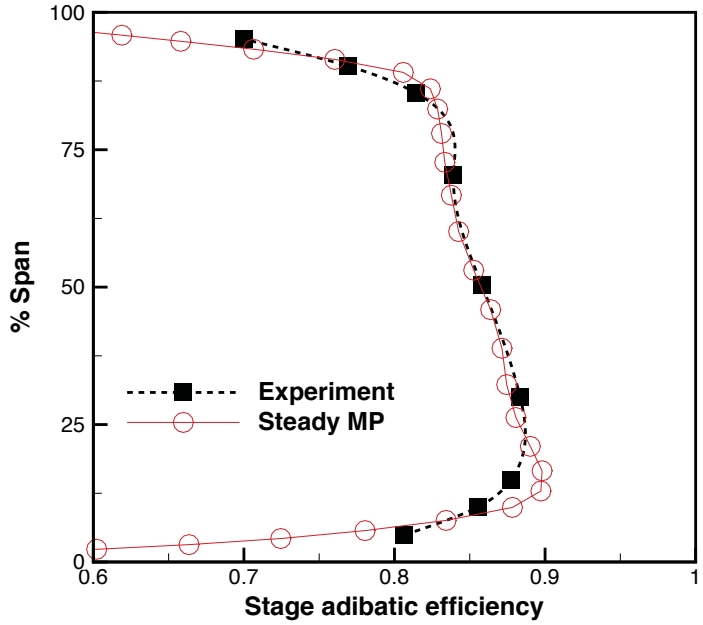

Figure 8.115: Spanwise distributions of the circumferentially mass averaged efficiency for NASA Stage 35

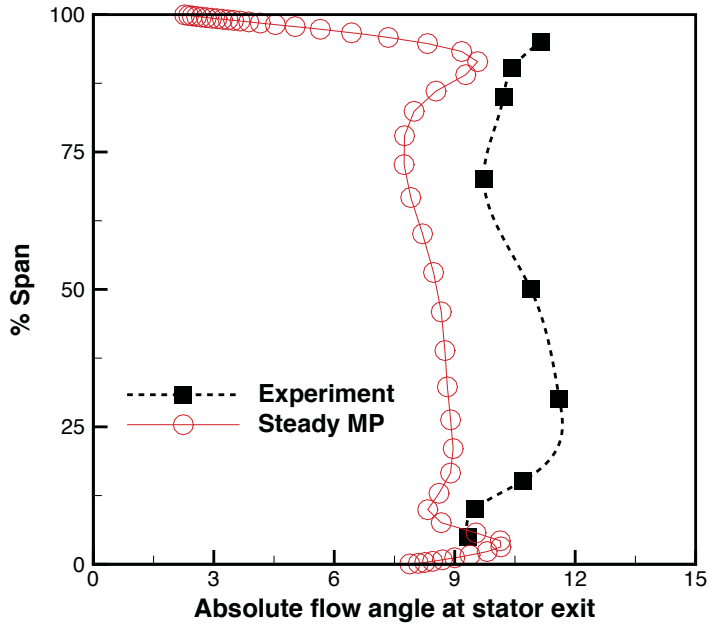

Figure 8.116: Spanwise distributions of the circumferentially mass averaged flow angle at stator outlet for NASA Stage 35

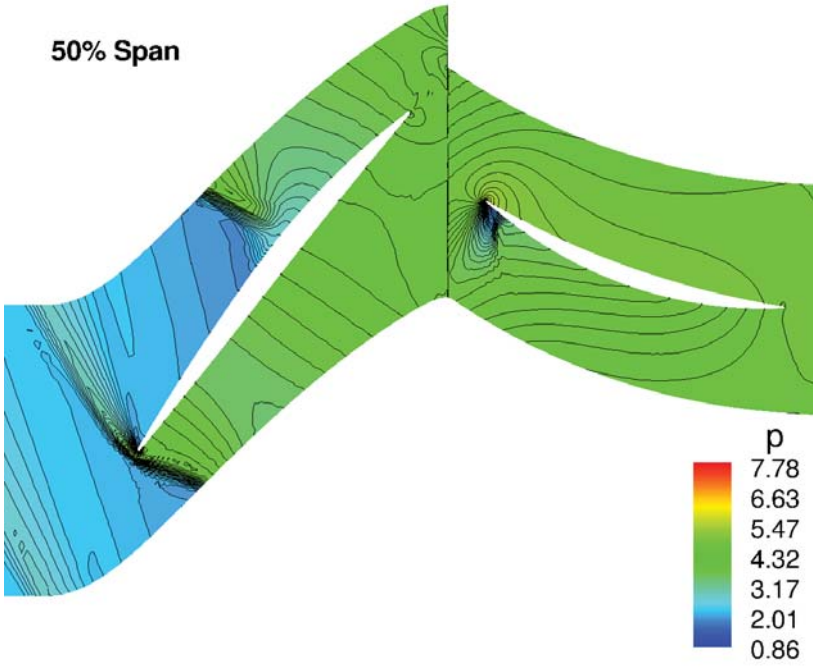

Figure 8.117: Static pressure contour at 50% span of NASA Stage 35

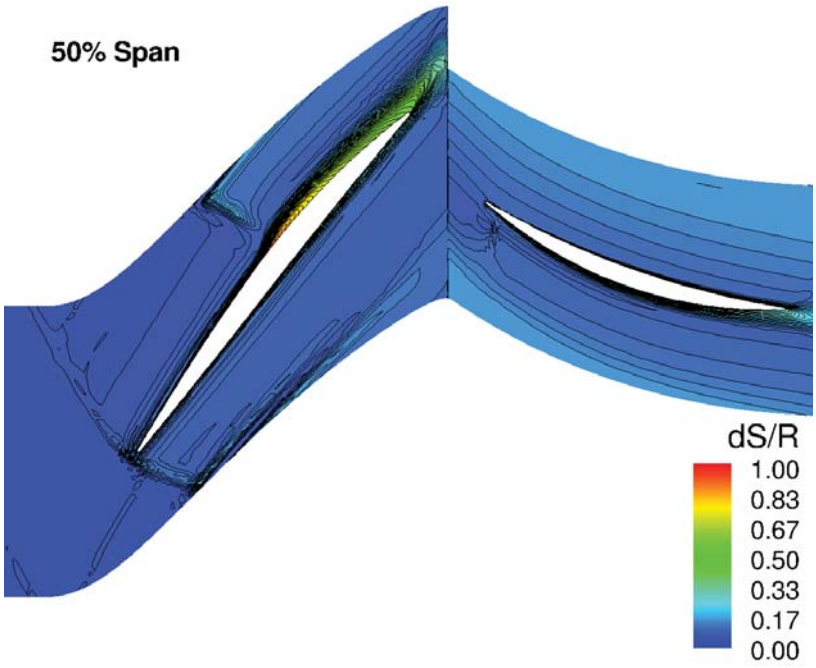

Figure 8.118: Entropy contour at 50% span of NASA Stage 35

Chapter 9

Investigation and Simulation of NSV Mechanism

The non-synchronous vibration (NSV) mechanism of a GE high-speed axial compressor with three different rotor tip shapes is investigated since the NSV occurs mostly in the tip region due to the instability associated with tip clearance flows [1, 2, 14, 15]. Numerical simulations for $1/7$th annulus periodic sector are performed using an unsteady Reynolds-averaged Navier-Stokes (URANS) solver with a fully conservative sliding boundary condition to capture wake unsteadiness between the rotor and stator blades.

The present numerical simulations demonstrate that the tip flow instability as the main cause of the NSV observed in this study is generated by the tornado-like tip vortices travelling circumferentially. The frequency of the vortex passing each blade is roughly equal to the NSV frequency. The NSV frequency is strongly influenced by the tip clearance size and shape. The predicted NSV frequency is in good agreement with the experiment.

9.1 The NSV Compressor

A GE aircraft engine axial compressor exhibits NSV at the first stage rotor blades from the GE-C1 full compressor rig test [14, 18]. The first 1-1/2 stage with the inlet guide vane (IGV) of 56 blades, the rotor of 35 blades and the stator of 70 blades is used for current simulations. The rotor tip clearance of the compressor rig is 1.1% of tip chord. The measured blade NSV is a phase-locked response and close to 1st torsional blade natural frequency. The strain gage on the blade surface shows the NSV frequency of 2600 Hz at around 12880 RPM and 2661 Hz as the rotor speed slightly decreases to 12700 RPM as shown in Fig. 9.1.

9.2 Tip Clearance Model

Three different tip clearance shapes are used in this tip sensitivity study as shown in Fig. 9.2. Tip clearance 1 is designed with a plain rotor tip of 2.4% C_t(tip chord), tip 2 with a plain tip of 1.1% C_t, and tip 3 with a convex type pinched tip of 1.1% C_t around tip center and 2.4%C_t near the rotor tip LE/TE. These three tip clearance shapes correspond to different usage in a realistic compressor and are recommended by GE Aviation to study.

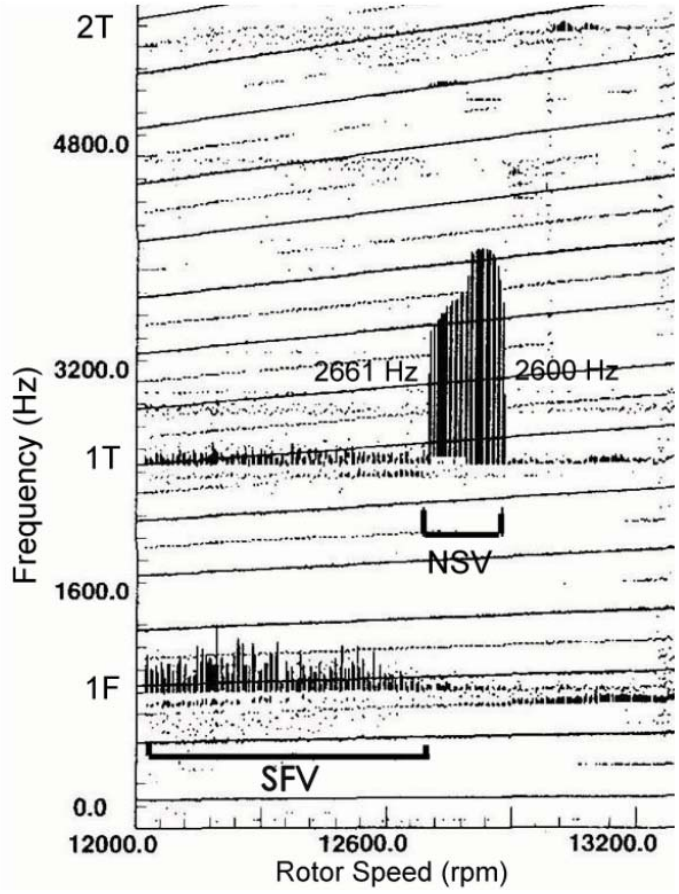

Figure 9.1: Strain gage response of the first-stage rotor blades of the high-speed compressor showing SFV(separated flow vibration) and NSV(non-synchronous vibration)

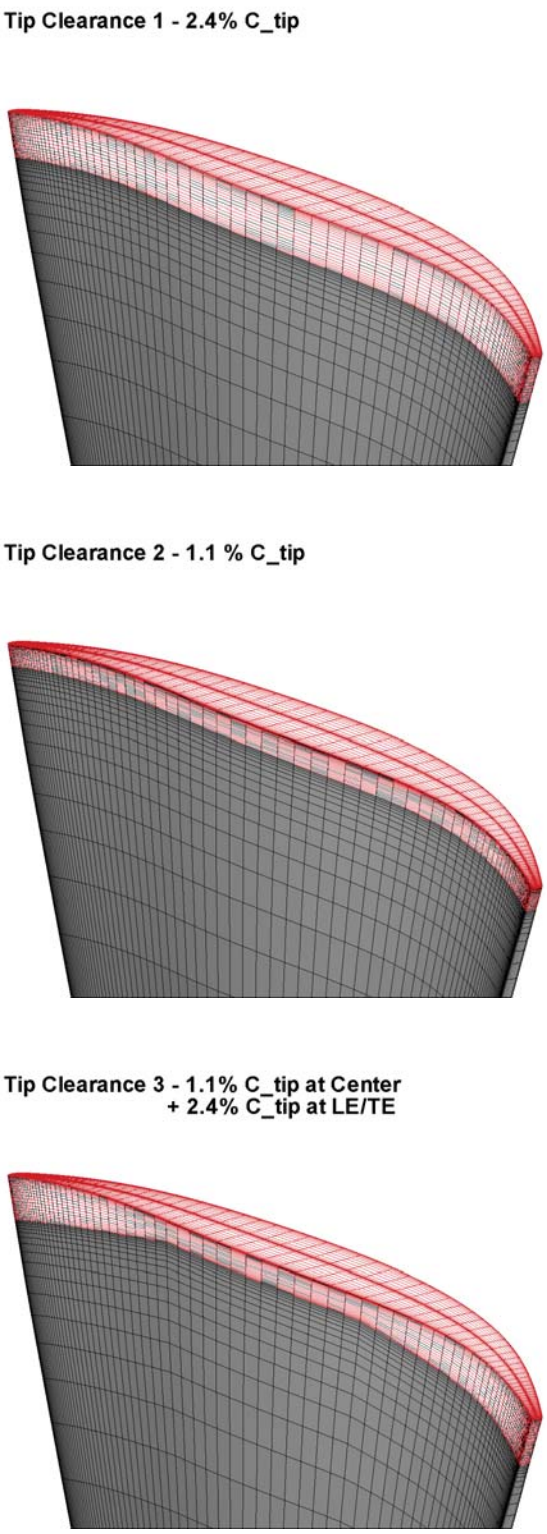

Figure 9.2: Three tip clearance shapes for sensitivity study; plain tip of 2.4% tip chord(top), plain tip of 1.1% tip chord(middle), leading/trailing edge pinched tip of 1.1% tip chord

9.3 Boundary Conditions

The boundary conditions described in chapter 6 are used in this study. In particular, the radial distributions of total pressure, total temperature, swirl angle and pitch angle are given at IGV inlet. The spanwise static pressure is also specified at the stator outlet.

An accurate time-shifted BC is used at lower/upper circumferential periodic boundaries to facilitate 1/7th annulus simulations. A fully conservative sliding boundary condition (BC) at the blade row interface is developed in order to rigorously resolve wake propagation, shocks interaction and rotating instabilities.

9.4 Computational Mesh

The 1/7th sector mesh for 1-1/2 stage of the GE-C1 compressor is presented in Fig. 9.3. The rotor tip clearance is modeled with 21 grid points using an O-mesh block. The mesh of IGV/rotor/stator is partitioned to total 174 blocks for parallel computation. The mesh around blade was constructed by using the O-mesh. For the IGV and stator, 121(around blade)$\times$101(blade-to-blade)$\times$71(blade span) is the mesh size, and for the rotor, 201(around blade)$\times$101(blade-to-blade)$\times$71(blade span). H-mesh layer is used for the matched one-to-one grid point connection at the sliding BC interface of IGV/rotor/stator that enables variable exchange in a fully conservative manner. Each H-mesh layer has a mesh size of 201(tangential)$\times$6(aixal)$\times$71(blade span). The total mesh size for this 1/7 sector of 1-1/2 compressor is 12,127,638. Mesh convergence test was performed using the single passage mixing plane computation and it shows an excellent agreement with GE CFD [28].

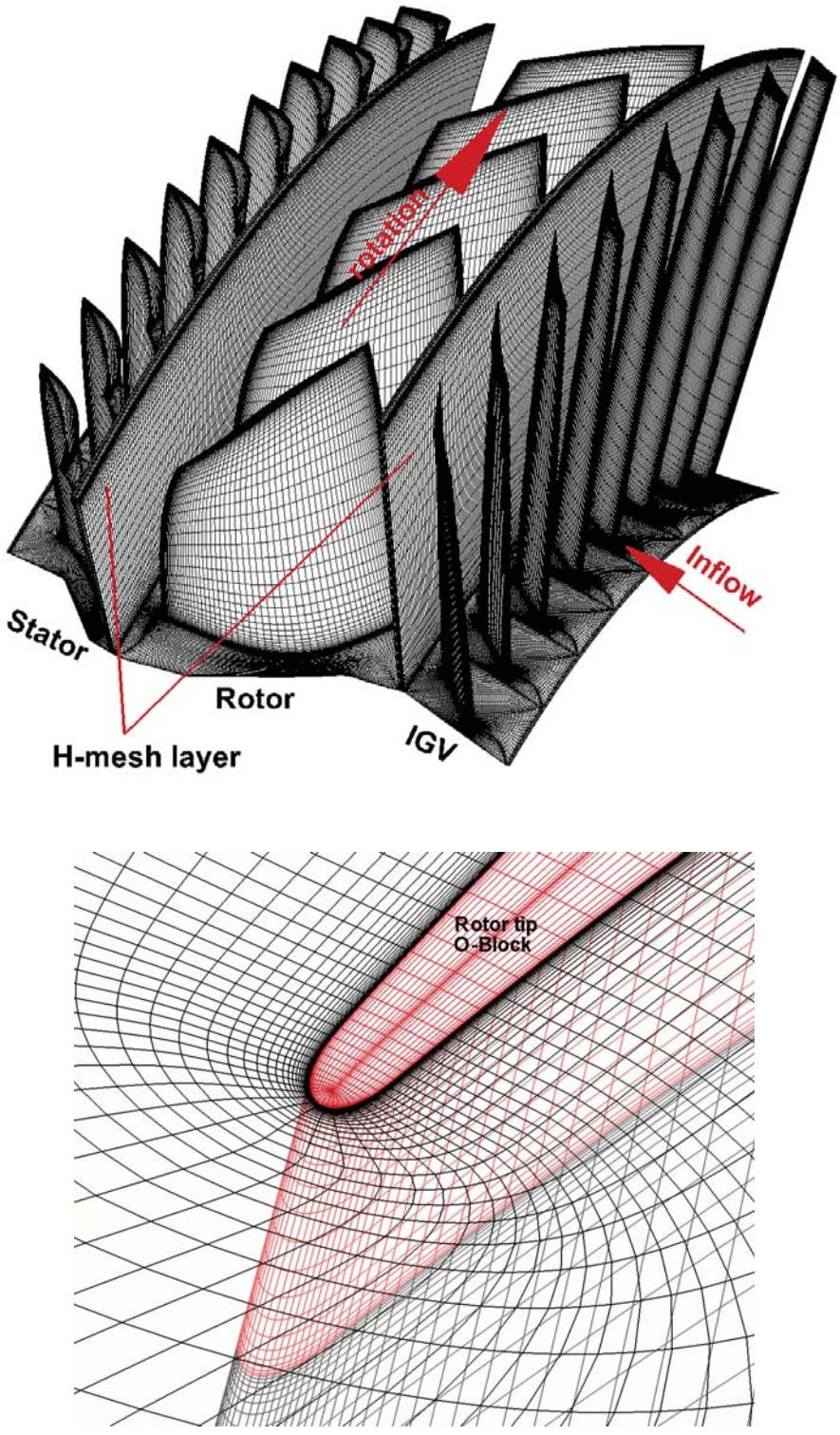

Figure 9.3: 1/7th Annulus mesh for NSV simulation

9.5 Numerical Probes

The numerical probes to acquire static pressure responses at the tip clearance are shown in Fig. 9.4. Total 60 points on a blade surface, 5 points in the middle of tip clearance and 5 points at the casing surface are mounted. The first numeral of the probe number means location around blade surface and the second numeral indicates location of blade span. For example, the probe 64 means the 6th probe from the trailing edge and the 4th probe from the hub, which is on the suction surface of 93% blade span near leading edge.

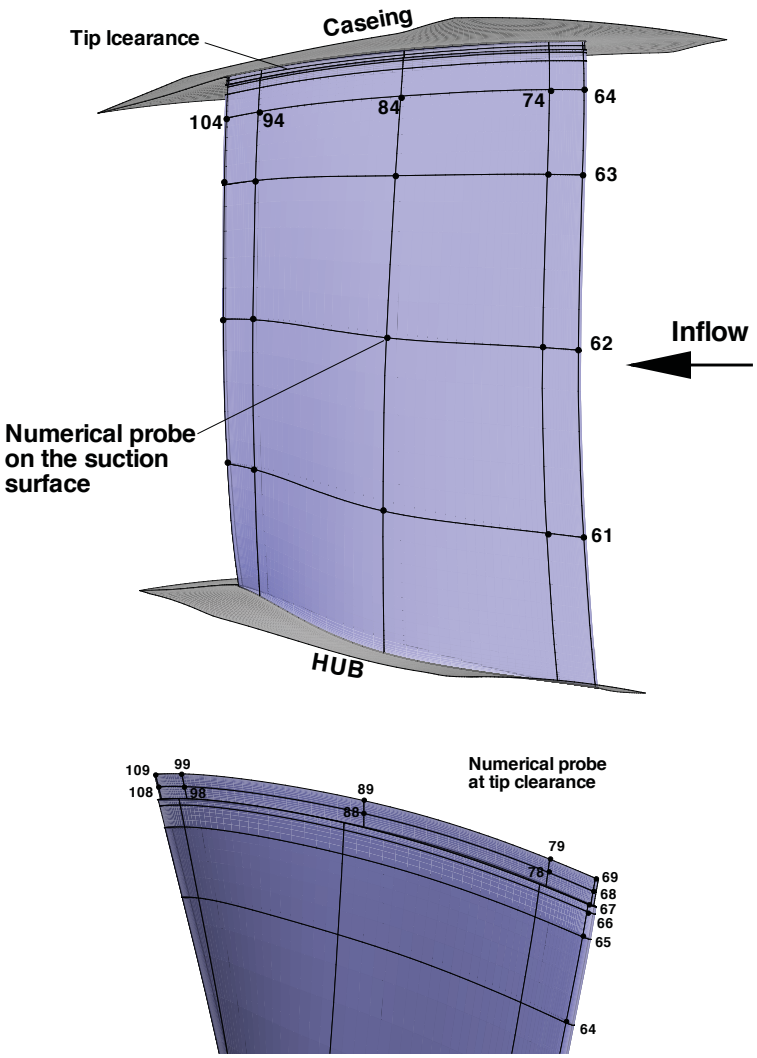

Figure 9.4: Numerical probes of the rotor blade

9.6 Results and Discussion

The rig testing of the axial compressor with 1.1% tip clearance [14] is shown to have the NSV frequency range of 2600 Hz to 2661 Hz, which is located between 12EOL (engine order line) to 13EOL and is near the 2nd mode blade natural frequency as shown in the Campbell diagram in Fig. 9.5. The compressor operating point used for the present NSV simulations is 2600 Hz at 12880 RPM. Note that EOL in Campbell diagram is obtained by integer multiples of rotor shaft frequency with respect to RPM. The Campbell diagram can be used to evaluate whether a blade frequency including natural frequency is synchronous or not with engine shaft.

In this study we conduct the unsteady simulations for the three different tip clearances; 1.1% C_t(tip chord), 2.4% C_t, 1.1% C_t around tip center and 2.4% C_t near LE/TE. The residual is reduced by three orders of magnitude within each physical time step, which is usually achieved within 30 to 40 pseudo time step iterations. A non-dimensional time step of about 0.005 is used.

The Speedline and NSV Location

Since NSV of axial compressors is typically observed in stable operation [1, 2, 14, 15], unsteady flow simulations are first conducted using tip clearance 1 at different back pressure conditions to find NSV dominant region in the speedline. Fig. 9.6 shows the predicted speedline of the 1-1/2 stage axial compressor. Note that the speedline data in Fig. 9.6 are obtained by averaging final 2 rotor revolutions. The point A, B, C and D represent rotor-to-IGV total pressure characteristics for tip clearance 1. The back pressure is gradually

increased from point S to find the near stall point D. After point D the compressor stalls. The point S is about maximum mass flow condition. No NSV events are found at point S. The mass flow rate obtained at point C is higher by roughly 6% than the near stall point D. GE CFD shows the same frequency for tip clearance 1. The mass flow difference between GE and the present study is about 2.6%, which may be caused by the fact that GE CFD considers the rotor only without IGV and stator. Note the mass flows predicted by the present CFD and GE CFD are in the close range of the GE-C1 full compressor NSV experiment [14].

The effect of different tip clearances on the NSV is investigated at point C since the NSV of 2365 Hz with maximum amplitude, which is defined as "peak NSV" in this study, is captured for tip clearance 1. The NSV for tip clearance 2 and tip clearance 3 are obtained by adjusting the back pressure to have about the same mass flow as tip clearance 1.

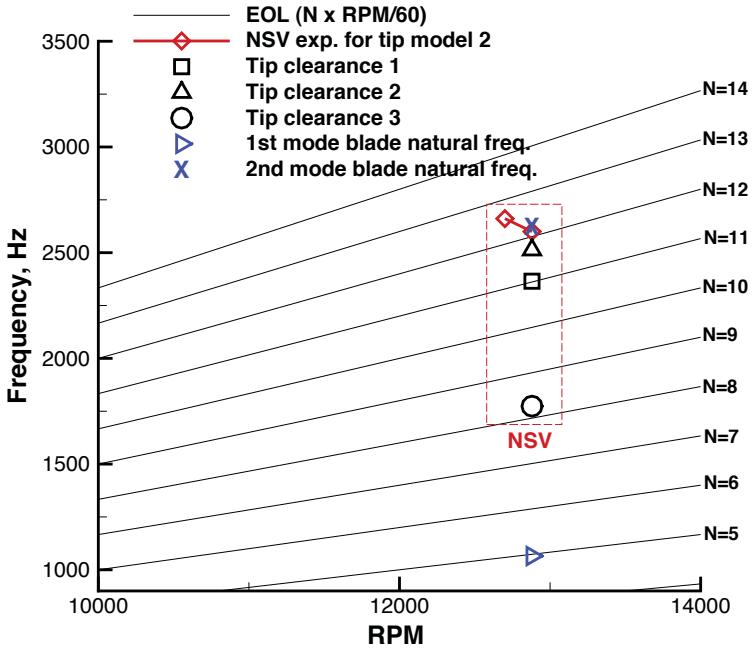

Figure 9.5: Campbell diagram

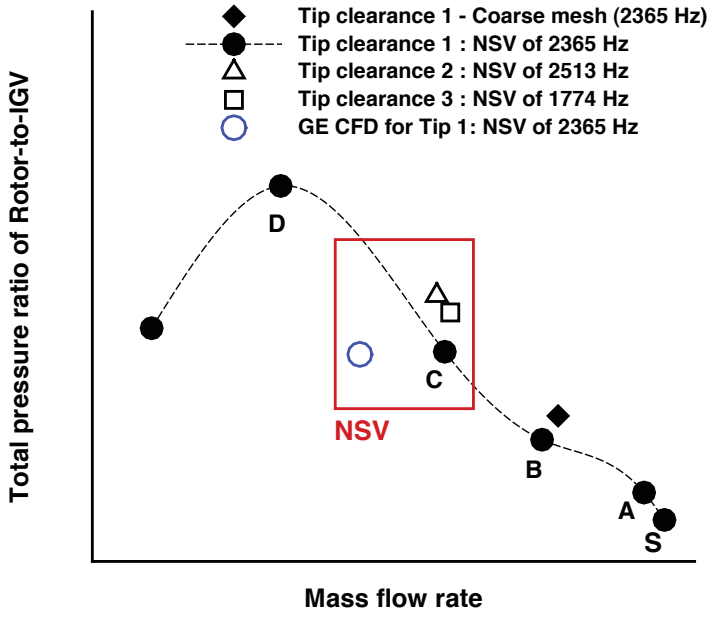

Figure 9.6: Total pressure ratio of IGV-to-Stator versus mass flow rate at the rotor exit

Fig. 9.7 shows time history of the rotor outlet mass flow rate at point C and D for tip clearance 1. In this study the unsteady solutions between 1 and 3 rotor revolutions are used for frequency analysis since the predicted mass flows show periodic oscillations roughly after one rotor revolution. The compressor runs stably without flow breakdown during the NSV. However, the flow field at the near stall point D is highly unstable with large mass flow oscillation. The NSV frequency of 2365 Hz observed at point C disappears at point D. Most of NSV events in axial compressors are observed at a stable operating condition without the mass flow breakdown [1, 2, 14, 15]. Note that tip clearance 2 and 3 also show a periodic mass flow behavior like tip clearance 1.

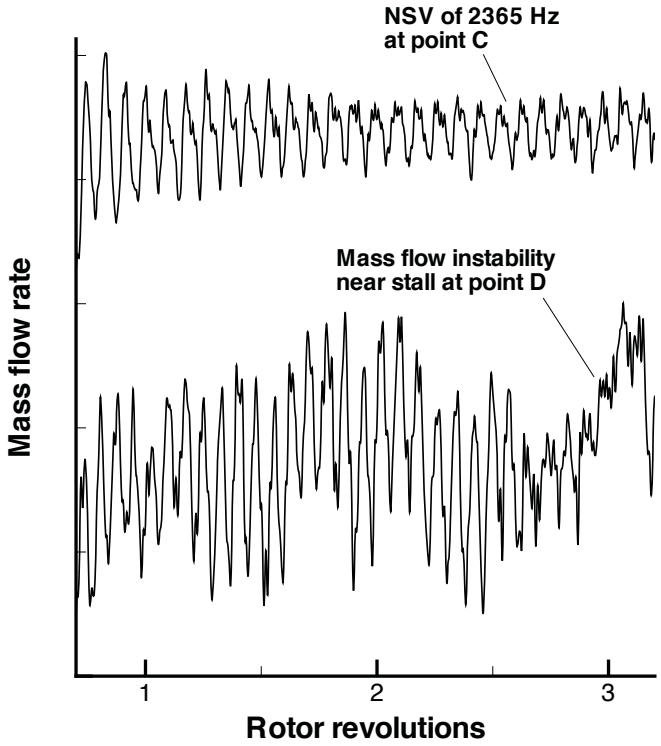

Figure 9.7: Instant rotor outlet mass flow rate for tip clearance 1 at point C and point D

Mesh Refinement Study

The mesh refinement study is conducted at point B using a coarser mesh of 201(around blade)×77(blade-to-blade)×46(blade span) for the IGV, stator and rotor. The total mesh size of the coarse mesh is 6,142,467. As shown in Fig. 9.6, the total pressure ratio of Rotor-to-IGV and mass flow predicted by the coarser mesh is well converged to the baseline mesh with about 0.5% difference. The IGV passing frequency predicted by the coarser mesh at about 50% span of rotor leading edge shows an excellent agreement with the baseline mesh as presented in Fig. 9.8.

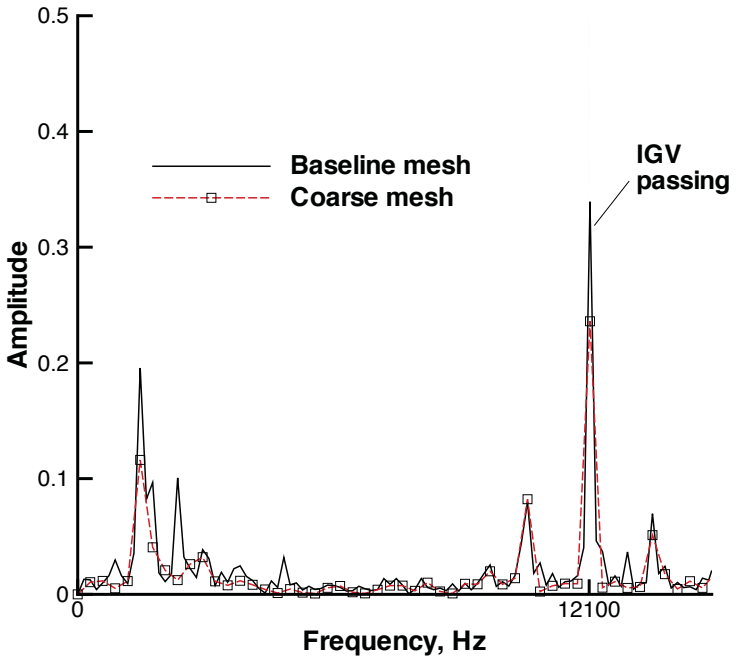

Figure 9.8: IGV passing frequency of tip clearance 1 at point B

NSV for 2.4% Tip Clearance

As aforementioned, for tip clearance 1, a peak NSV frequency of 2365 Hz is observed at point C. All of the static pressure presented and used for frequency analysis in this study are normalized by the IGV inlet dynamic pressure($\rho_\infty U_\infty^2$). Fig. 9.9 shows instantaneous fluctuations of the static pressure on the rotor blade 3. Note that the blade is numbered in the opposite direction of the rotor rotation. It is observed in this study that the peak pressure fluctuations occur near rotor leading edge (LE). It is obvious that the largest amplitude of the pressure oscillation is captured at 78% span near the rotor leading edge(probe 63), while the pressure measurements in the tip clearance shows a weak fluctuation. It should be emphasized by the NSV experiment of Baumgartner et al. [1] that the hot-film measurements show the radial dependency of the rotating instability as the main driver of the NSV observed for the 10 stage high pressure axial compressor. The NSV with high blade vibration amplitude is observed between 65% to 91% of the blade span, while the measurements close to the casing wall are very noisy without high fluctuations.

The pressure fluctuations acquired at 78% span leading edge suction surface of blade 3 at different mass flow is presented in Fig. 9.10. It is clear that fluctuation level of the pressure is significantly amplified at point C. It is shown by the NSV experiments [2, 15] that the blade sensor signal under NSV has a strong periodic content due to the rotating instability. The present numerical simulations also demonstrate a strong periodic signal of the blade surface pressure. However, the phase-locked oscillation of the peak NSV pressure signal at point C is changed as a non-cyclic pattern at near stall point D.

In Fig. 9.11, the changes in the NSV frequencies at 78% span at different mass flow

conditions are clearly captured with frequency analysis using the pressure signals in Fig. 9.10. A NSV of 2365 Hz for tip clearance 1 is captured at point C, while at point D a NSV of 2808 Hz, which is between 13EOL and 14EOL, is captured with about 20% lower amplitude than the NSV at point C. At point B, the frequency of 2365 HZ which is the same as point C is obtained with about 50% lower amplitude than the point C. While at point D, the NSV frequency of 2365 HZ is decaying with its amplitude level about 83% lower than the point C. Like the NSV experiments [14, 16], the compressor with 2.4% tip clearance also shows frequency shift according to operating conditions. Another peak frequency with its amplitude of about 0.3 at point C is also a NSV of 1771 Hz, which is between 7EOL and 8EOL.

Fig. 9.12 shows the instantaneous pressure signals of 5 rotor blades between 2 and 2.5 Rev acquired at 78% span near leading edge at point C (peak NSV of 2365 Hz with maximum amplitude). The pressure fluctuations of each blade is very similar with about the same frequency. If an instability is propagated to the next blade in a form of travelling wave like a spike stall cell, the phase difference in the acquired blade surface pressure must be in order [29]. In addition, the flow instability near the compressor rotor tip region appears to be not a rotating stall since similar periodic contents of the pressure signals are found without the mass flow breakdown as an indication of rotating instability by the experiments as a main cause of NSV in axial compressors [2, 15]. The predicted frequencies for the blade surface pressure signals shown in Fig. 9.12 are plotted in Fig. 9.13. The predicted NSV frequencies are the same for each blade, indicating a similar flow instability at each blade passage during the NSV.

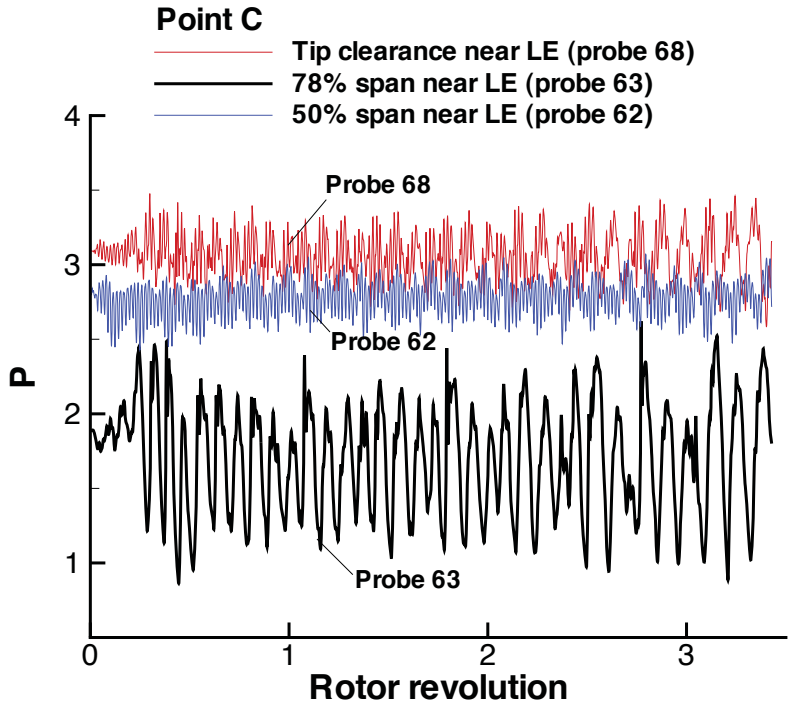

Figure 9.9: Pressure signals at blade 3 leading edge suction surface for tip clearance 1

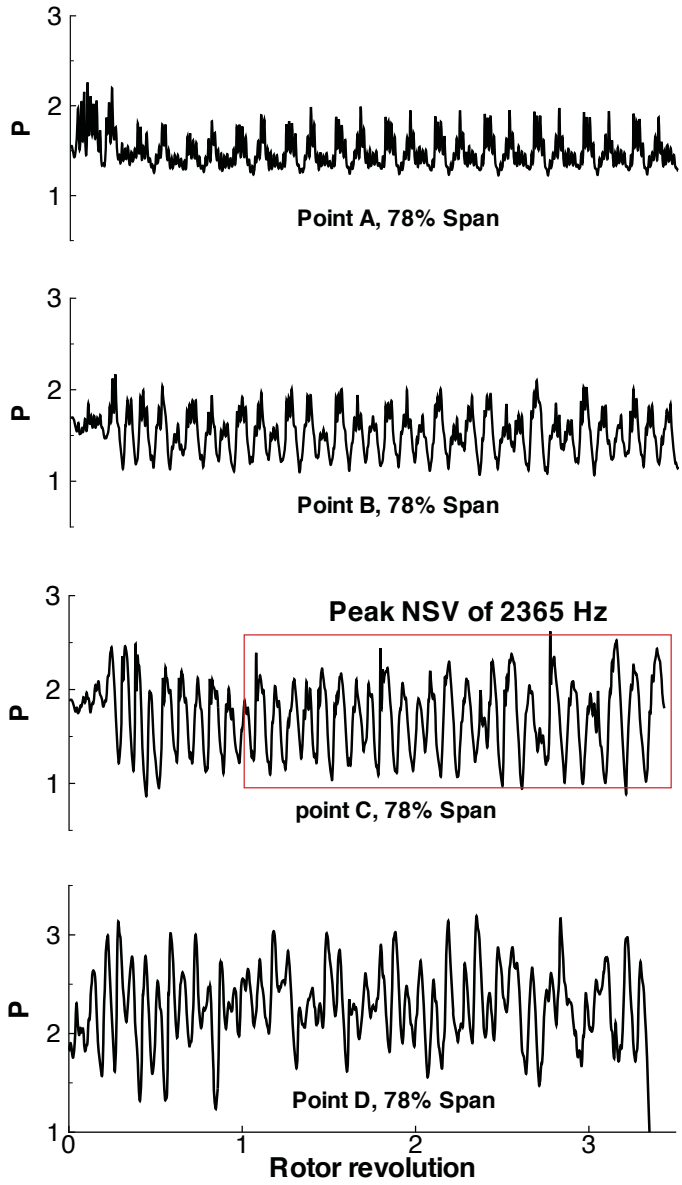

Figure 9.10: Changes in the surface pressures at blade 3 78% span near LE at different mass flows for tip clearance 1

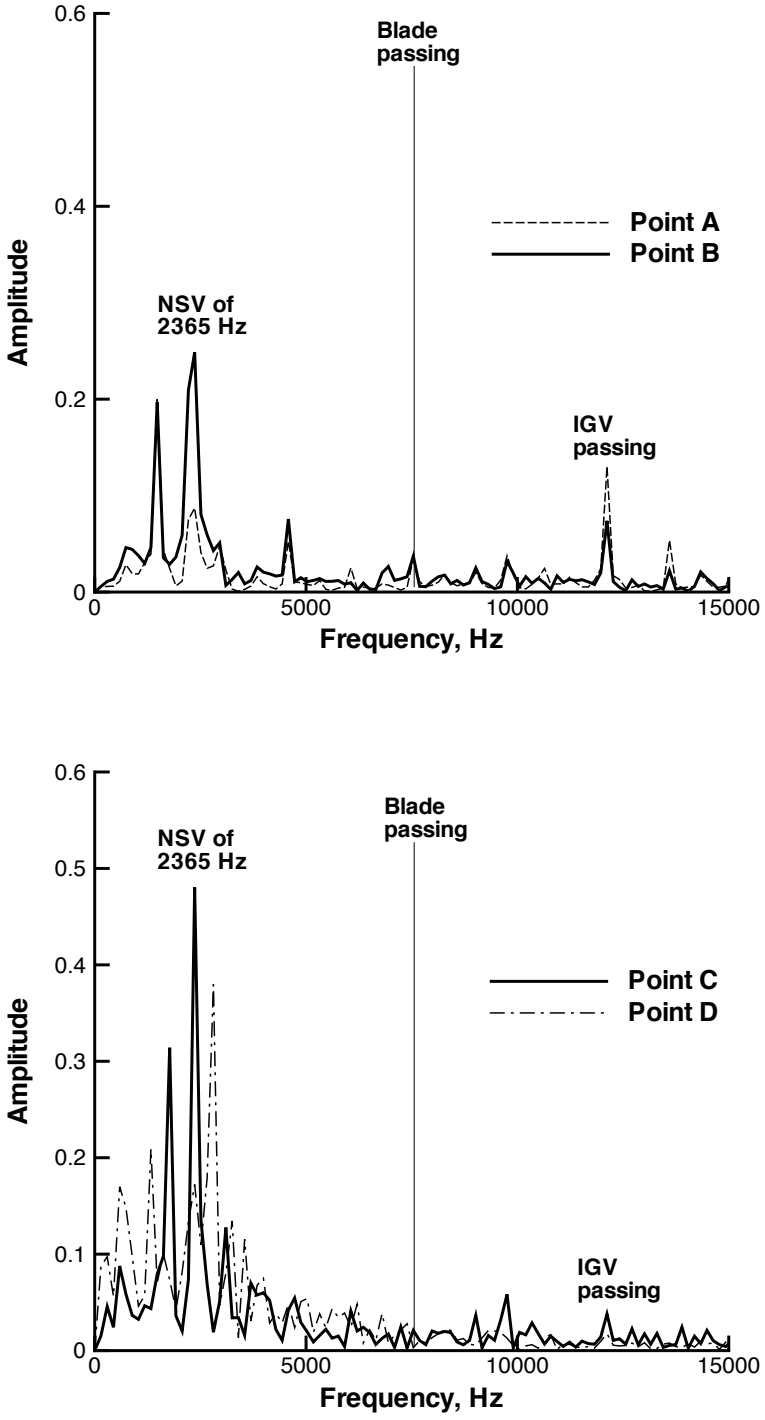

Figure 9.11: Predicted NSV frequencies using blade 3 pressure signal at 78% span near LE suction surface of tip clearance 1

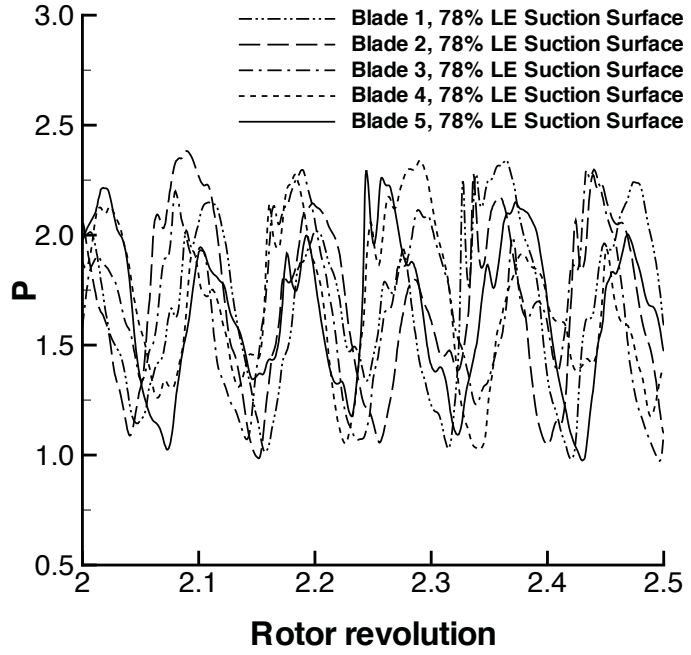

Figure 9.12: Surface blade pressure fluctuations between 2 Rev and 2.5 Rev acquired at 78% span near LE suction surface for tip clearance 1

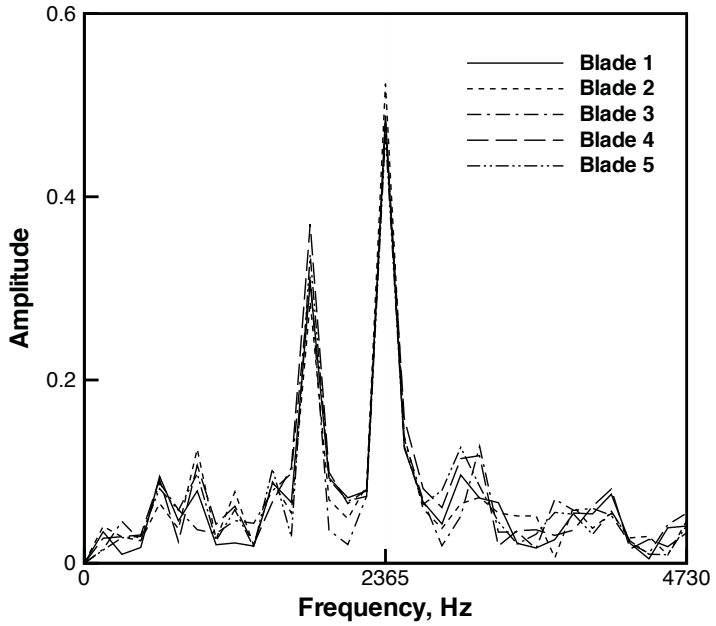

Figure 9.13: Predicted NSV frequencies at 78% span near LE suction surface of tip clearance 1

9.6.1 NSV Mechanism

Fig. 9.14 illustrates an instantaneous tip vortex structure in the vicinity of the rotor tip. A large tornado like vortex is formed with its axis normal to the blade suction surface around the rotor leading edge. This is different from the regular streamwise tip clearance vortex. However, the tornado vortex should be evolved from the streamwise tip vortex when the flow creates the incidence in nearly tangential direction. These tornado vortices create a large blockage of each blade passage and induces reverse flow that interact with incoming flow from the IGV. A similar vortical flow structure is detected by the experimental work of Inoue et al. [73], which is a separation vortex from the blade suction surface and ends up at the casing wall during the short length scale rotating stall of the multistage axial compressor. However, the tornado vortex observed near the rotor tip region is a coherent vortex that travels circumferentially. As a result, more flow is pushed through beneath the tornado vortices due to the blockage. Note that the compressor is still at a stable operating condition indicated as point C in the compressor map given in Fig. 9.6.

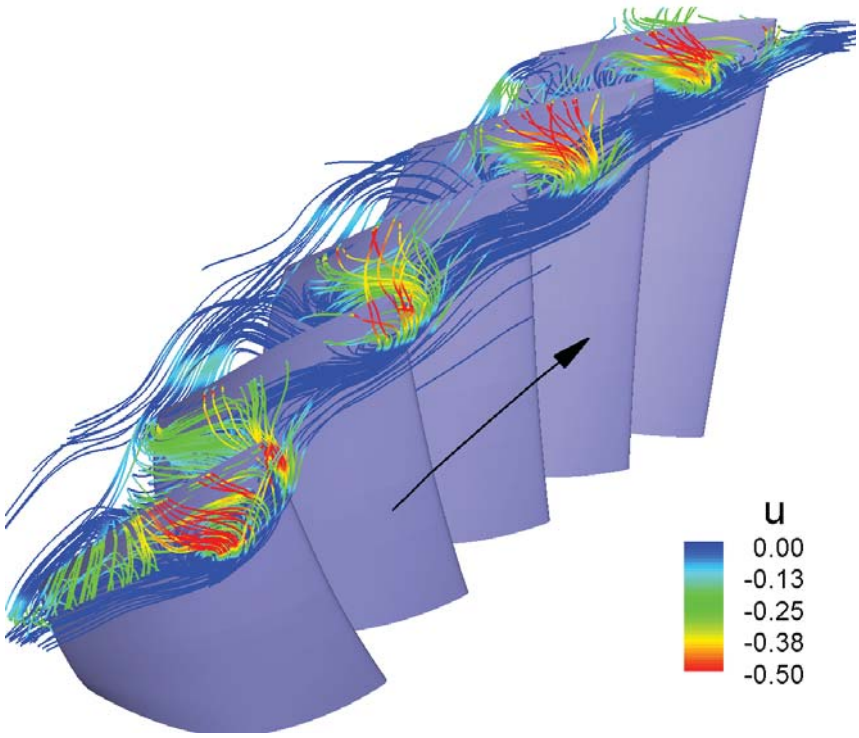

Figure 9.14: Tornado tip vortices in the blade passages colored with negative axial velocity for tip clearance 1

To understand the unsteadiness causing the NSV, Fig. 9.15 and Fig. 9.16 illustrate tornado vortex motion in one period observed from $\frac{0}{70}$ to $\frac{12}{70}$ Rev. In this study, $\frac{0}{70}$ Rev denotes the time instant at 3 rotor revolutions. The vortex motion Fig. 9.15 and Fig. 9.16 shows that the tornado vortex travels first to downstream in streamwise direction from 0/70 to 6/70. When it reaches the throat area formed by the aft part of the current blade and the leading edge region of the adjacent blade, the vortex quickly moves from the pressure side to the suction side of the adjacent blade in the leading edge region. At the same time, a tornado vortex travelling from the upstream blade appears on the suction surface side in the leading edge region of the current blade. However, the vortex travelling is stable without triggering the compressor to stall. The time period of the tip tornado vortex coming and departing on the suction surface leading edge region is about 6/70 to 7/70, which matches the NSV frequency of 2365 Hz. In other words, it is the circumferentially travelling tip tornado vortices that create the oscillating forcing and induce the NSV. The tip tornado vortex tube is most likely created because the tip region has too much designed loading and the incidence is too high. However, the whole blade load is still under the loading limit and pumps the flow stably. It is hence possible to remove this tip tornado vortex tube by unloading the rotor tip and increase the loading in the mid and lower span. This corresponds to the findings of Mailach et al. [15] who shows a traveling tip vortex in circumferential direction by the experiment of a multistage compressor as the main excitation source of the NSV with large amplitude. The experimental work of Marz et al. [2] also presents a tip passage vortex caused by the reversal flow near the rotor leading edge that interacts with incoming flow as a rotating instability for the non-engine order blade vibration.

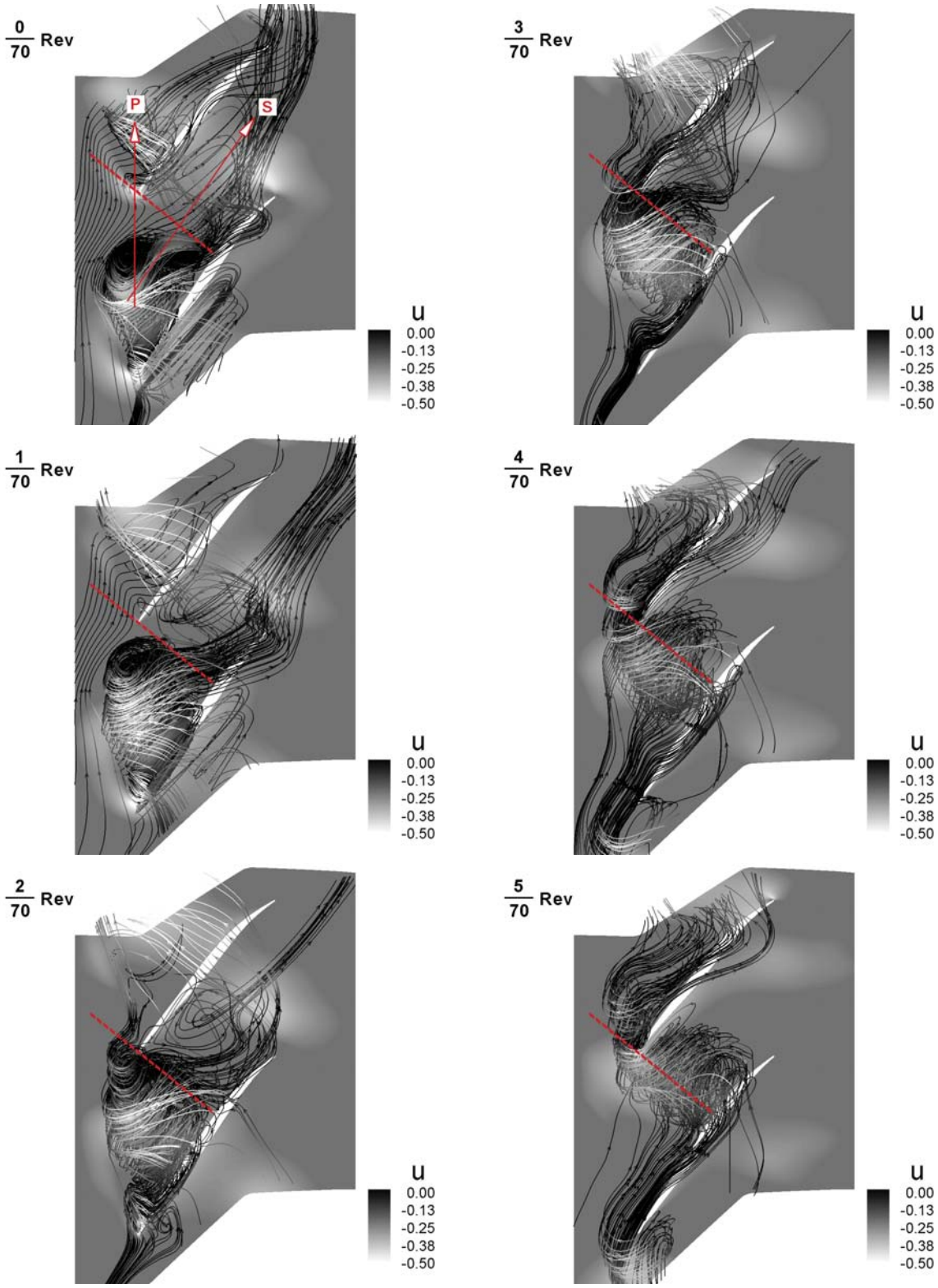

Figure 9.15: Instantaneous tip vortex trajectories at 0, 1/70, 2/70, 3/70, 4/70, 5/70 Rev colored by the negative axial velocity for tip clearance 1

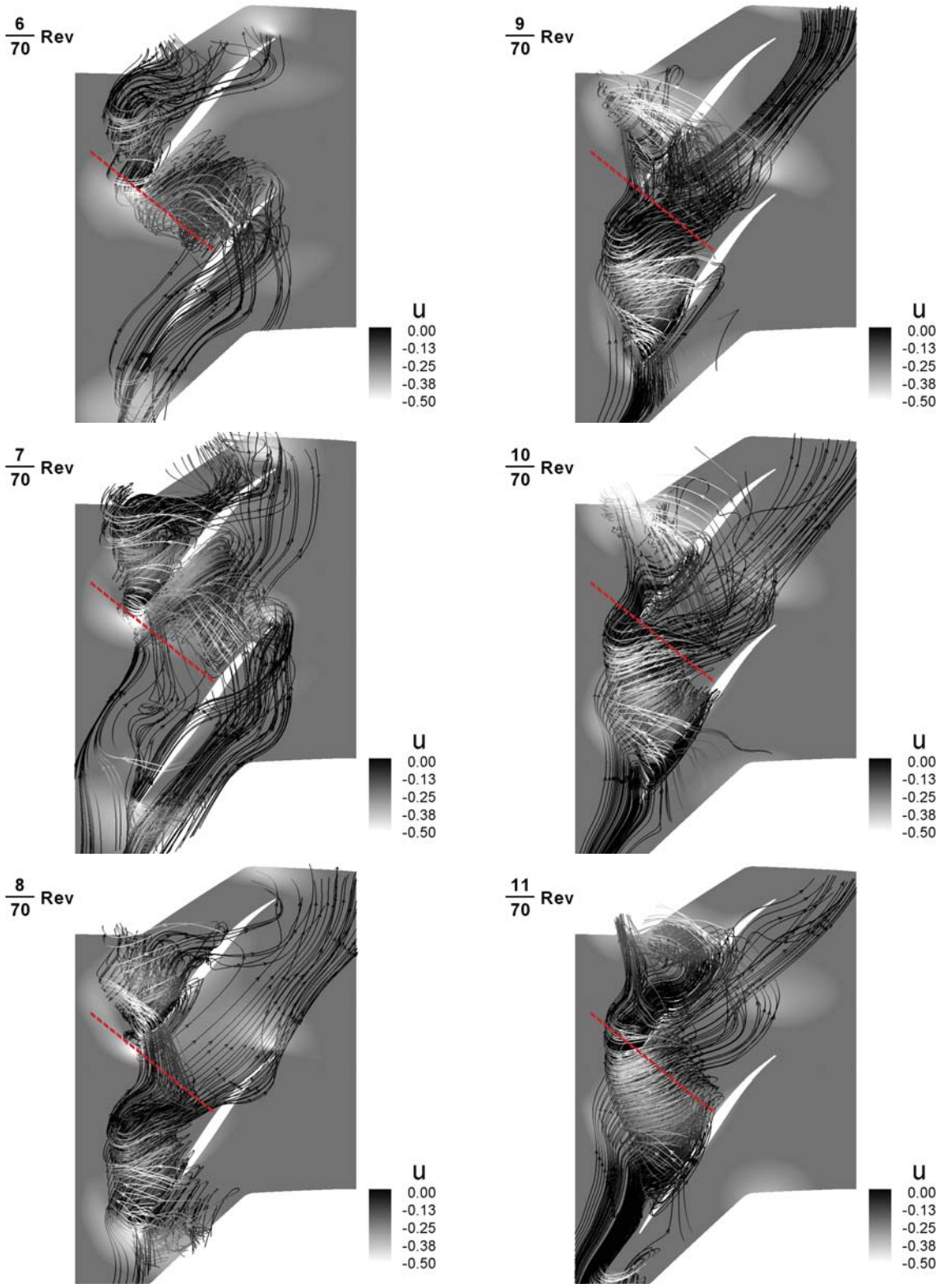

Figure 9.16: Instantaneous tip vortex trajectories at 6/70, 7/70, 8/70, 9/70, 10/70, 11/70 Rev colored by the negative axial velocity for tip clearance 1

The instantaneous axial velocity distributions along the normalized axial chord at the middle of tip clearance 1 are plotted in Fig. 9.17. The strong negative axial velocity appears at the tip clearance due to the tornado vortex. It is shown that the peak of the negative axial velocity varies according to the tornado vortex movement. For example, the peak at 0/70 Rev is observed below X_tip of 0.1, while that of 1/70 Rev is located at about X_tip of 0.1. At 2/70 Rev, the peak is then moved to around X_tip of 0.3. The velocity magnitude of the reverse flow increases up to about 15% axial chord due to the blockage by the tornado vortex and then decreases gradually such as a harmonic wave, which indicates that the tip flow instabilities are moving in the downstream of the blade passage during the NSV of the compressor.

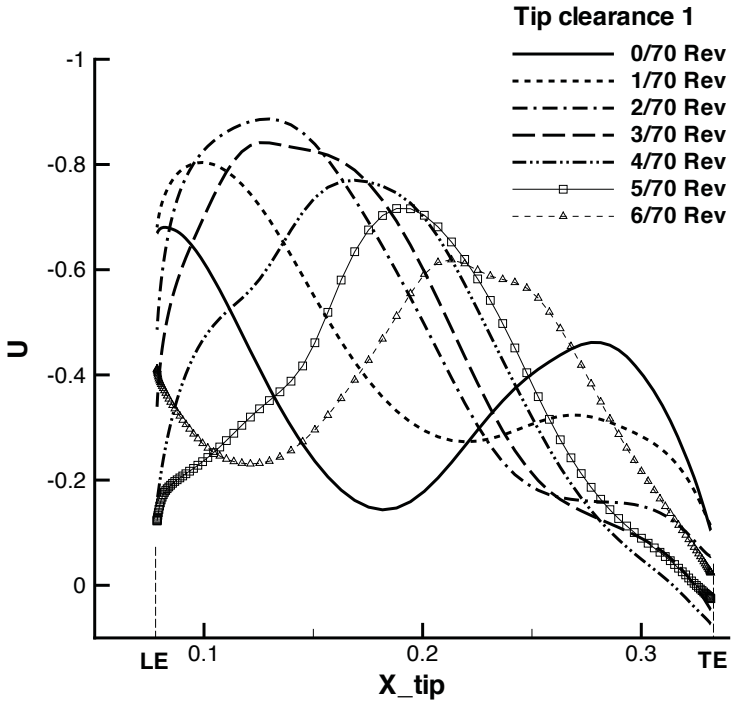

Figure 9.17: Instantaneous axial velocity (U) distributions at the middle of tip clearance 1

Fig. 9.18 shows the instantaneous vorticity contour around 80% span from $\frac{0}{70}$ to $\frac{6}{70}$ Rev. It is shown that the tornado like vortex is a type of coherent vortex structure and propagates to the next blade passage through rotor leading edge ahead. For instance, the tornado vortex on the blade 4 suction surface seen at $\frac{0}{70}$ moves to blade 5 suction surface, and at the same time another similar vortex is formed due to the vortex propagation from blade 3.

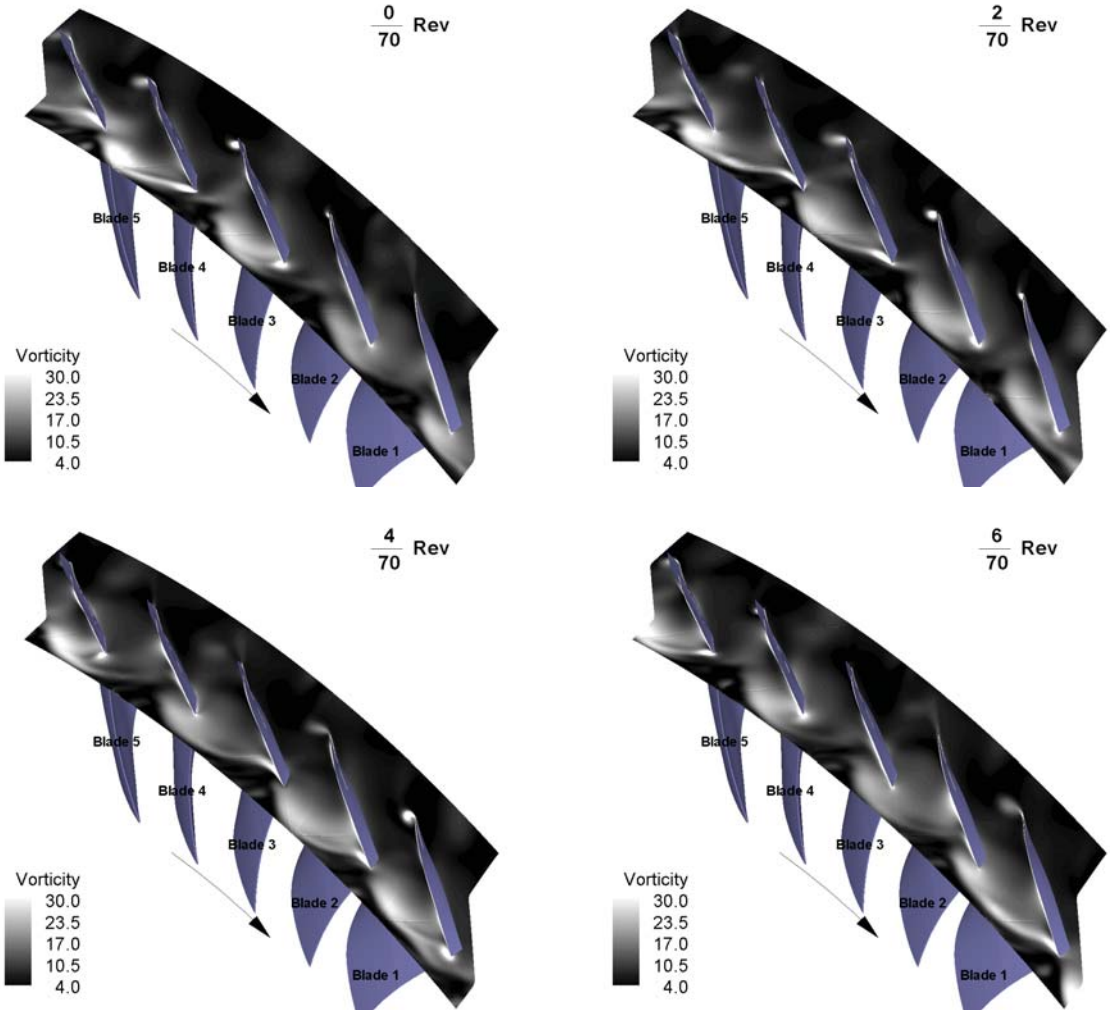

Figure 9.18: Instantaneous vorticity contour of about 80% span at 0, 2/70, 4/70, 6/70 Rev for tip clearance 1

Fig. 9.19 shows the instantaneous entropy contour at near the rotor leading edge axial plane. Entropy is significantly increased around the tornado vortices, which travels from one blade to the next inside the vortex tube, consumes a large amount of energy from the main flow, and generates a enormous entropy increase in that region.

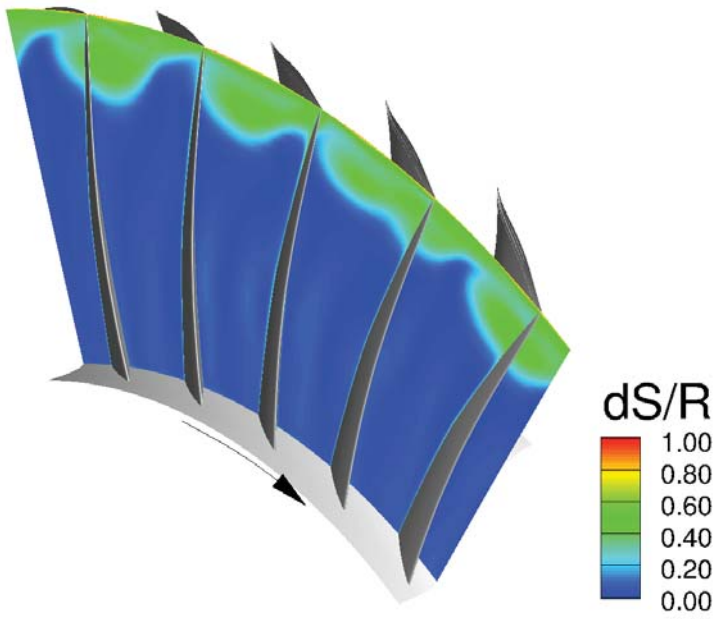

Figure 9.19: Instantaneous entropy contour at near the rotor leading edge axial plane for tip clearance 1

Effect of Rotor Tip Clearance on NSV

To study tip clearance effect on the NSV, tip clearance 2 with 1.1% tip chord(C_t) and tip clearance 3 with 1.1% C_t around tip center and 2.4% C_t near LE/TE as sketched in Fig. 9.20 are simulated at about the same mass flow where the dominant NSV of 2365 Hz is found for tip clearance 1.

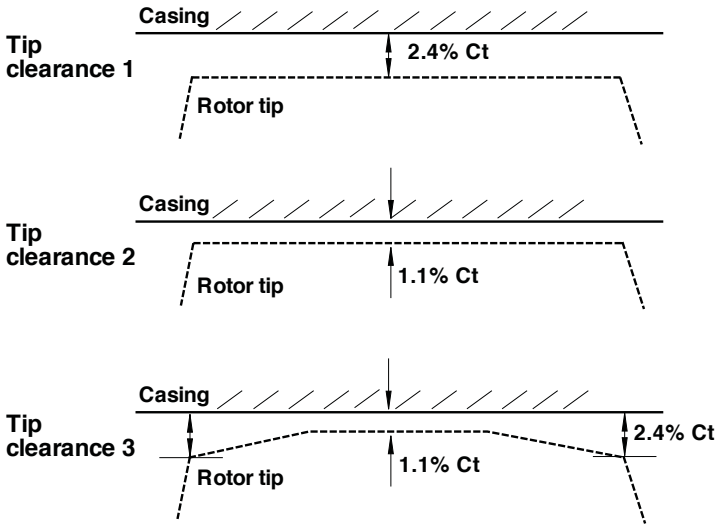

Figure 9.20: Sketch of rotor tip clearance shapes

Instantaneous blade surface pressures at 78% span near LE(probe 63) for tip clearance 1, 2 and 3 are plotted in Fig. 9.21. Oscillations in the surface pressures are different according to the rotor tip clearance shapes. The pressure signals for tip clearance 1, 2 and 3 show a periodical and phase-locked pattern but with different frequencies.

Fig. 9.22 shows the predicted NSV frequencies using the pressure signals in Fig. 9.21. It is found that the tip clearance of the compressor rotor changes the NSV frequency and the intensity as well. The dominant frequencies for tip clearance 1, 2 and 3 are 2365 Hz, 2513 Hz and 1774 Hz respectively. Those frequencies are not synchronous to the engine

rotor as presented in Fig. 9.5. The predicted NSV frequency from tip clearance 2 matches the measured value very well, only 3.3% lower. Tip clearance 2 is the one tested in the NSV experiment by GE [14]. Tip clearance 3 shows the peak NSV at 1774 Hz with a significant increase in amplitude by about 42% compared with tip clearance 2. It means that tip clearance 3 generates lower frequency and stronger NSV than tip 1 and 2. The straight rotor tip, which are tip clearance 1 and 2, shows smaller amplitude but higher frequency at about the same mass flow condition during the NSV caused by the tornado vortex instabilities. The NSV frequencies for tip clearance 1, 2 and 3 at the rotor tip LE are plotted in Fig. 9.23. The predicted frequencies are the same as those of 78% span near LE suction surface. Except for tip clearance 3, the intensity of the NSV are very weak. It is clear that a convex type of tip clearance 3 amplifies the intensity and reduces the frequency of the NSV.

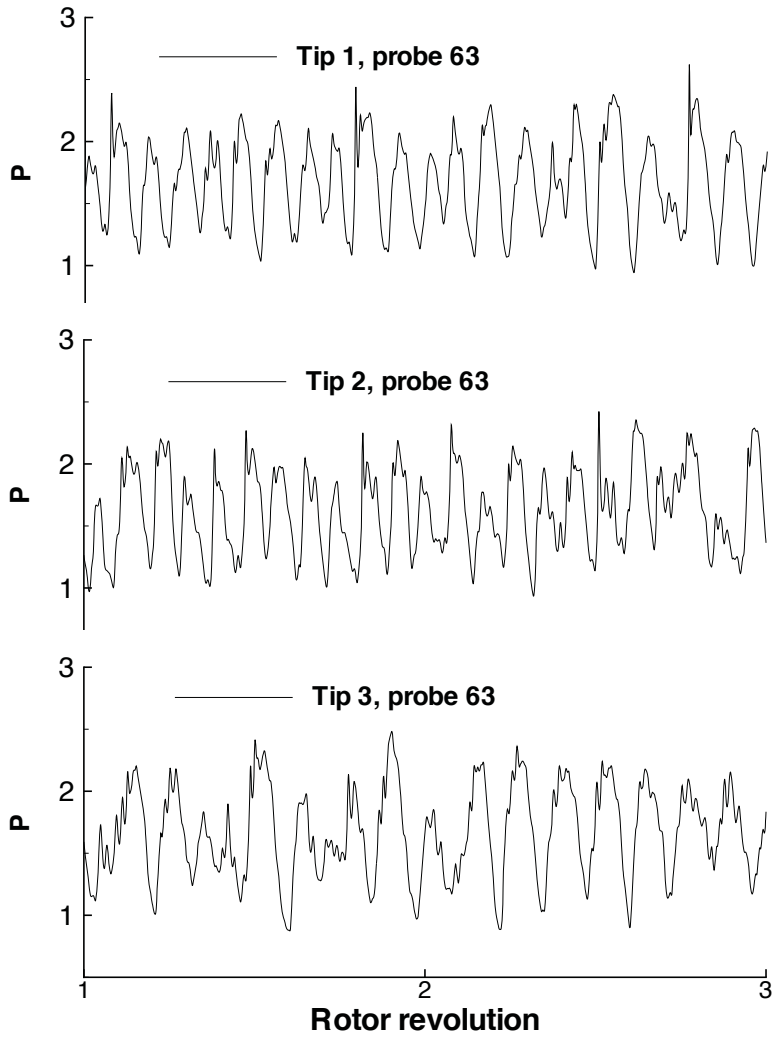

Figure 9.21: Instantaneous surface pressure signals acquired at blade 3 78% span near LE suction surface

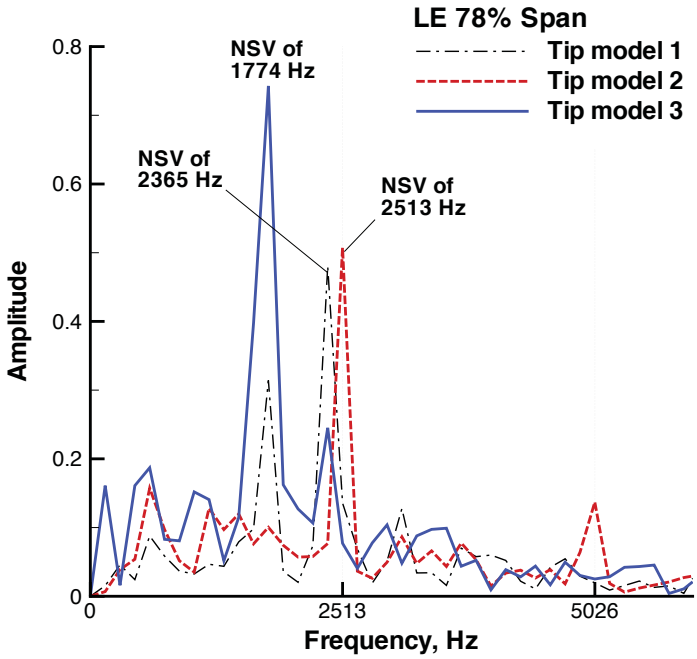

Figure 9.22: Predicted NSV frequencies for tip clearance 1, 2 and 3 at 78% span near LE

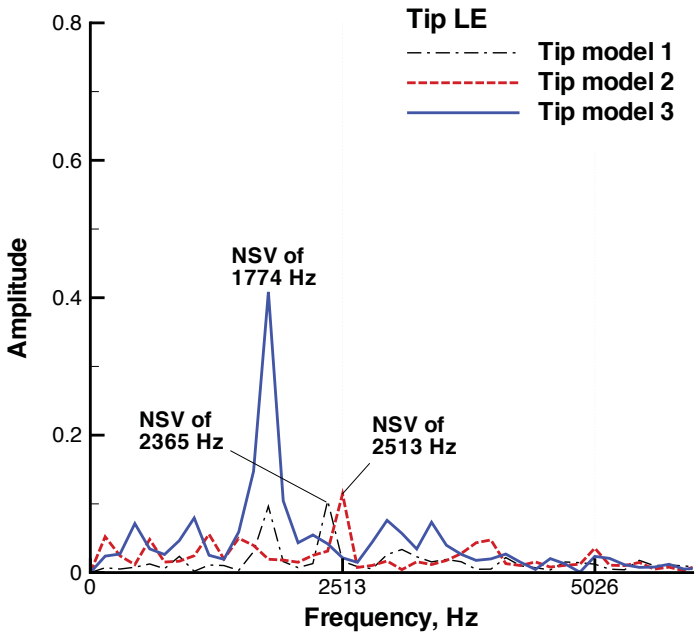

Figure 9.23: Predicted NSV frequencies for tip clearance 1, 2 and 3 at the rotor mid-tip clearance

For tip clearance 2 and 3, the tip tornado vortices similar to tip clearance 1 are also observed during the NSV. Fig. 9.24 shows entropy contours for tip clearance 1, 2 and 3 at the rotor tip span. The entropy jump due to interaction of the reverse flow with incoming flow is clearly captured between the IGV and rotor interface. The contours also show clearly the vortices rolling up and moving in circumferential direction. As a result, the reverse flow occurs in the vicinity of rotor tip and the tip leakage spillage to the next blade is also induced due to interaction with the tornado vortex as illustrated in Fig. 9.25.

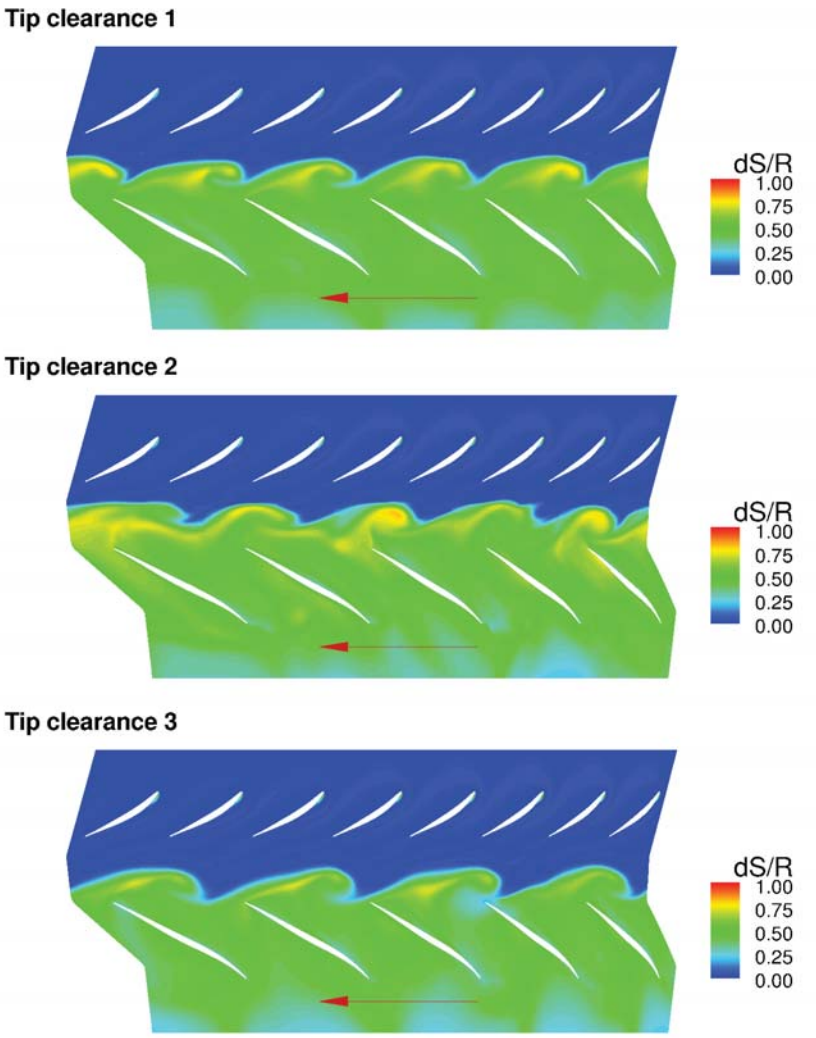

Figure 9.24: Contours of entropy at the rotor tip span; tip clearance 1(top), tip clearance 2(middle), tip clearance 3(bottom)

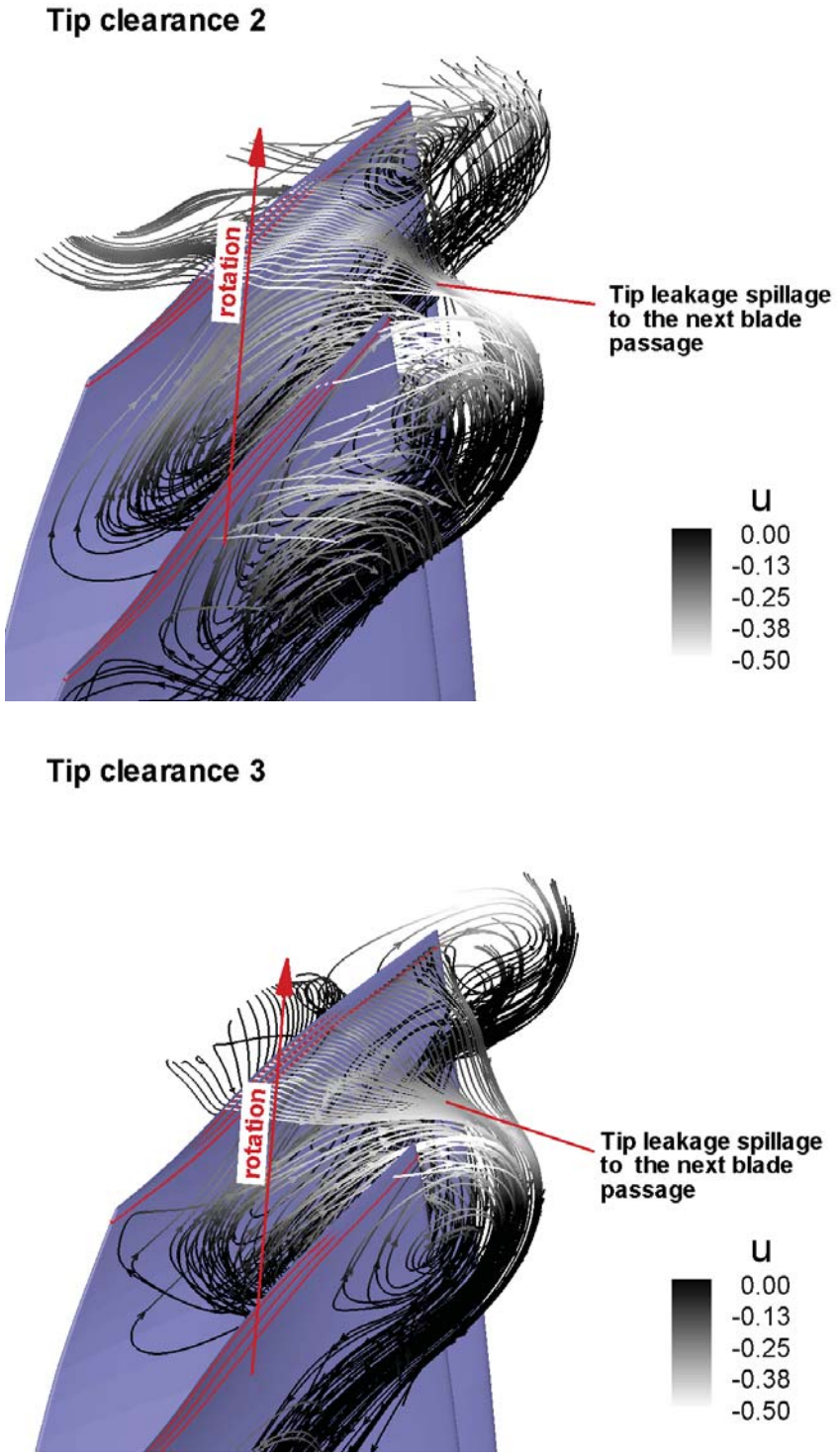

Figure 9.25: Tip leakage spillage to the next blade passage due to the tornado vortex colored with negative axial velocity for tip clearance 2

The instantaneous normalized static pressure distributions along the 1/7th sector rotor circumference of the tip section are plotted in Fig. 9.26. The pressure oscillation period in the rotor circumferential direction for tip clearance 3 is larger than tip clearance 1 and 2. For instance, tip clearance 3 has 4 cyclic pressure waves in the rotor circumferential direction, whereas tip clearance 2 shows more than 5. The fact is that a pressure spike usually in the rotor circumferential direction reflects the number of disturbances. In general the speed of rotating stall cell or rotating instability in the rotor annulus relies on the number of disturbance cells. As illustrated in Fig. 9.27, tip clearance 2 shows 5 disturbances (tornado vortices) in the 1/7th sector of annulus, whereas only 4 tornado vortices propagate in the opposite direction to the rotor rotation for tip clearance 3. This indicates why the NSV frequency for tip clearance 3 is lower than tip clearance 2.

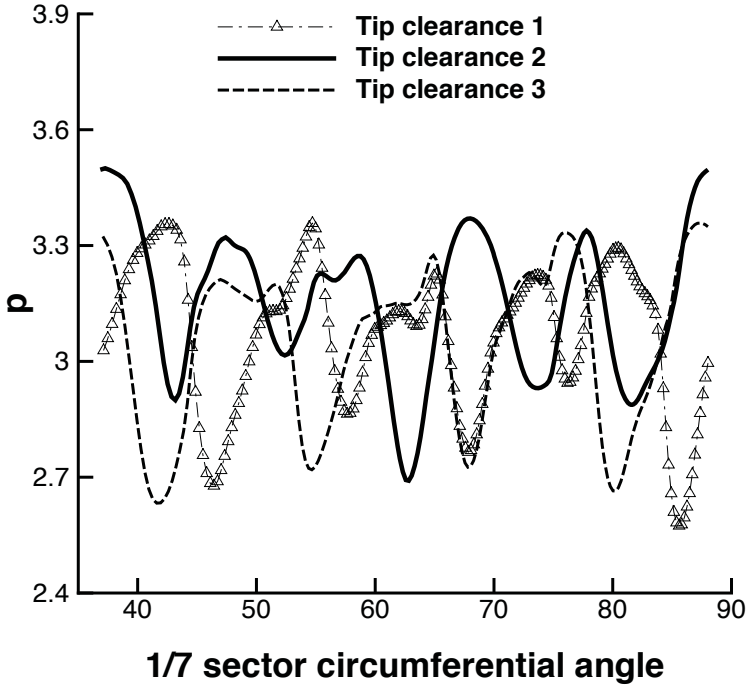

Figure 9.26: The normalized static pressure distributions of the rotor tip upstream by about 10% axial chord

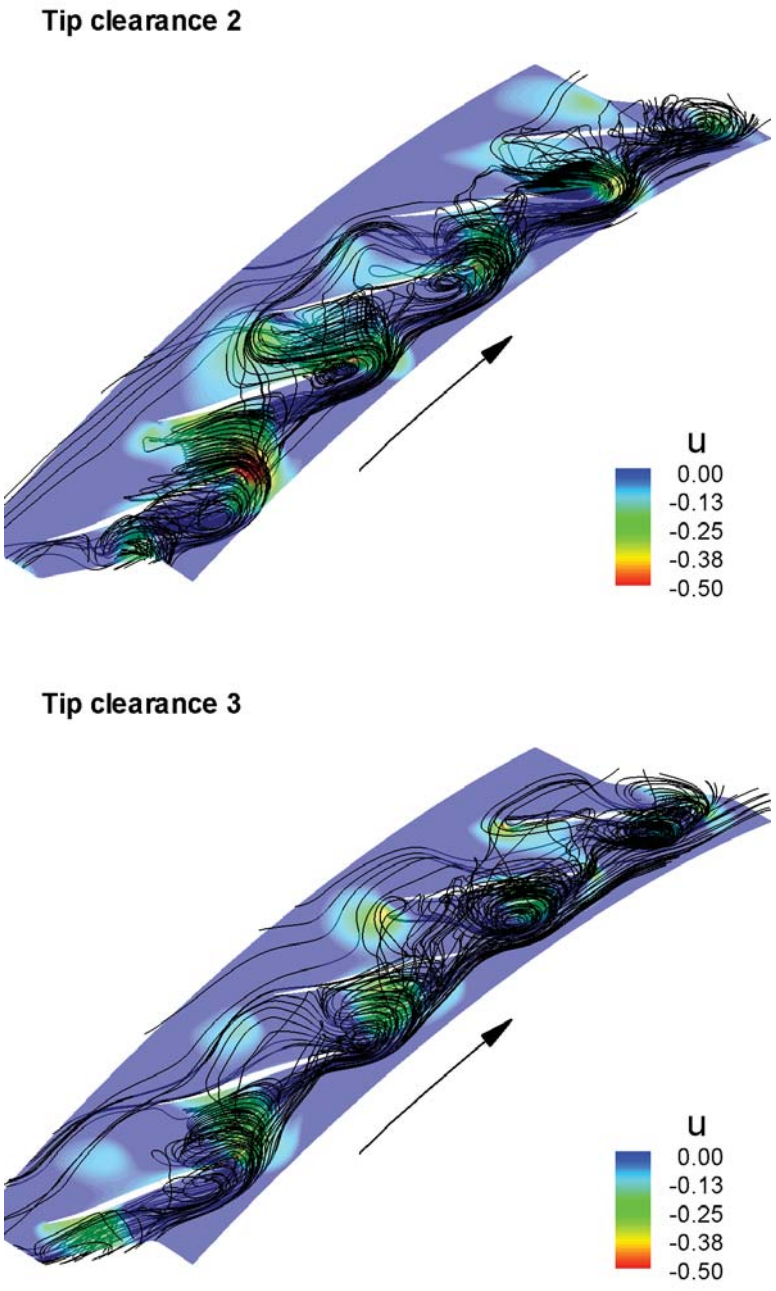

Figure 9.27: Tip tornado vortices of the 1/7th sector annulus

Fig. 9.28 shows the instant meridional flow pattern according to different tip clearances and shapes. The reversed flows are identified roughly above 70% span for all tip clearances studied. As aforementioned, these reversal flows are induced by the tornado vortex that causes NSV of the 1st stage rotor blades.

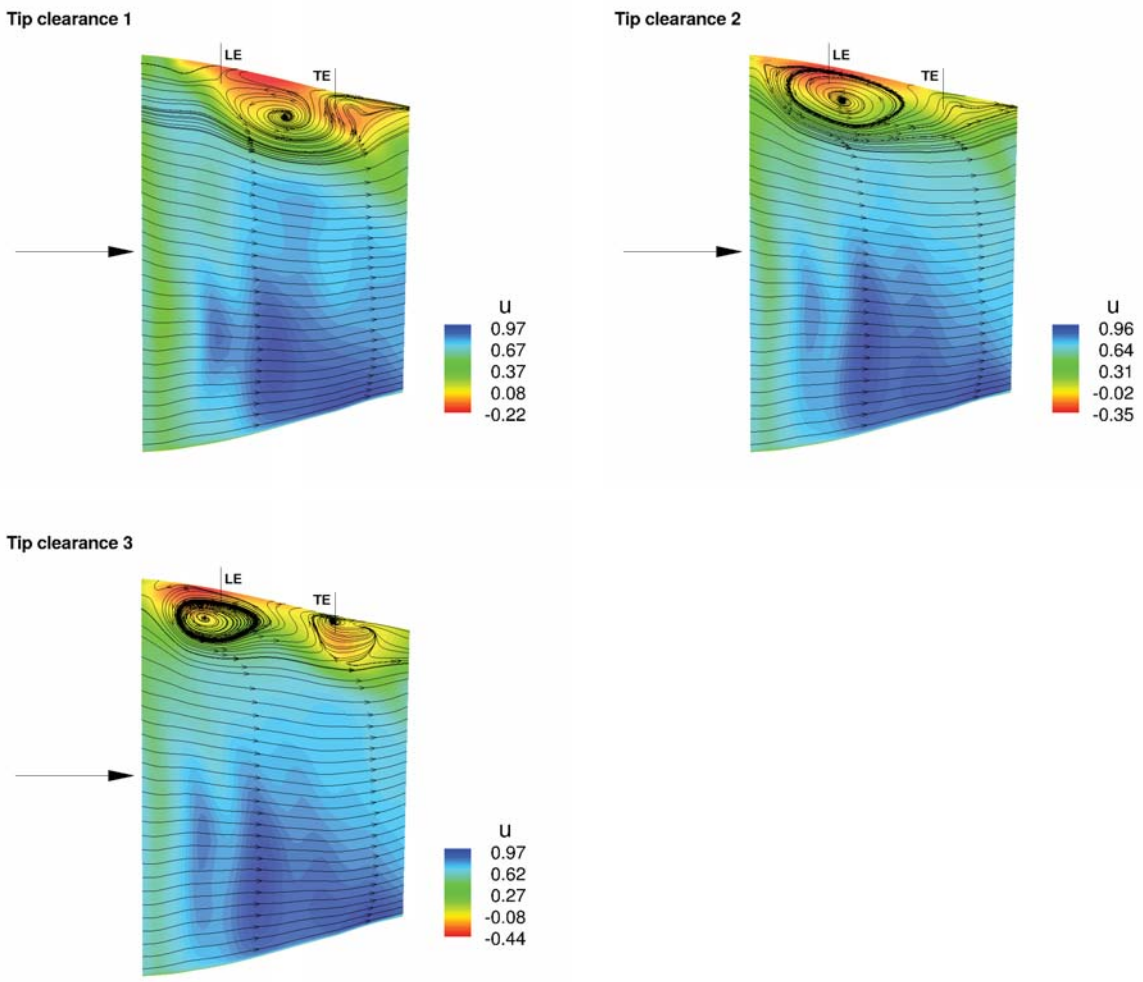

Figure 9.28: Time averaged negative axial velocity contour of a meridional plane

Fig. 9.29 explains the reason why NSV due to the tornado vortex occurs. At the rotor inlet, total pressure and temperature are uniform in the spanwise direction, whereas these roughly above 75% span are dramatically increased roughly above 75% span. The rotor

blade loading due to pumping work is too high near the rotor tip, which can induce the flow separation near the rotor leading edge suction surface because of high incidence. This may cause the tornado vortex above 75% span that causes NSV. Above 75% span the rotor adiabatic efficiency is significantly decreased due to the tornado vortex. The relative Mach number at the rotor outlet is very low due to the reversal flow.

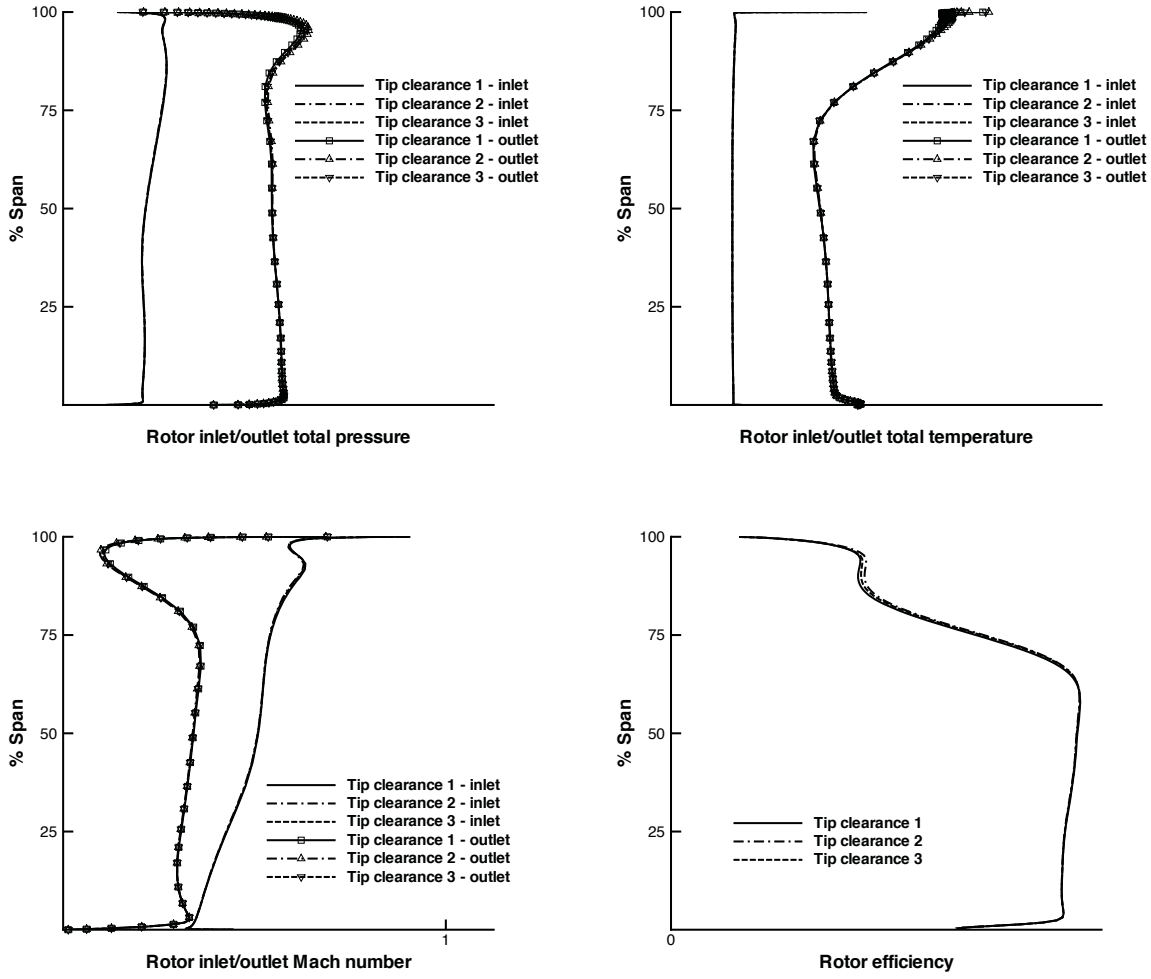

Figure 9.29: Time averaged radial profiles of tip clearance 1, 2 and 3 at the 1st stage rotor inlet and outlet; total pressure (top left), total temperature (top right), relative Mach number (bottom left), adiabatic efficiency (bottom right)

To investigate the effect of tip leakage impinging jet acoustic resonance on the NSV, the NSV critical tip velocity (Eq. 9.1) based on their impinging jet experiment suggested by Thomassin et al. [3, 16] is calculated.

$$U_{tipc} = 2(c - 2sf_b/n) \tag{9.1}$$

In the above equation, c is speed of sound at tip clearance, s the blade pitch, f_b the blade natural frequency and n the integer of harmonics for the acoustic feedback wave. The critical velocity(U_{tipc}) is estimated at tip clearance center(the probe 87).

For tip clearance 1, the blade natural frequency(f_b) near the NSV is about 2620 Hz, the local speed sound is about 349.5 m/s. The calculated U_{tipc} with $n = 1$ is 227.2 and with $n = 2$ is 463.1, while the blade tip velocity(U_{tip}) measured is about 340.5 m/s. The calculated NSV critical velocity(U_{tipc}) based on Eq.9.1 is about 33% lower than U_{tip}. For tip clearance 2, the local speed sound is about 355.3 m/s. U_{tipc} of 236.7 with $n = 1$ and of 473.7 with $n = 2$ are obtained, while U_{tip} is 341.4 m/s. The calculated value of U_{tipc} with $n = 1$ is roughly 30% lower than U_{tip}. Similar results are also obtained for tip clearance 3. Since the condition of the NSV driven by tip leakage acoustic resonance is $U_{tipc}/U_{tip} \approx 1$, it appears that the acoustic wave of tip leakage jet is not responsible for the NSV observed in this study.

9.7 Summary

Numerical simulation is conducted to investigate the tip flow instabilities potentially leading to the NSV in a GE axial compressor. A 1/7th annulus of a 1-1/2 stage is used with a fully conservative sliding BC at blade row interfaces and a time shift boundary condition at the lower/upper circumferential periodic boundaries. A 3D URANS solver with a low diffusion Riemann solver, 3rd Order WENO scheme and S-A turbulence model is used.

Three different tip clearances are studied. Tip clearance 1 and 2 are designed to have a straight tip clearance with the clearance size of 1.1% and 2.4% tip chord respectively, while tip clearance 3 has a convex type tip with clearance of 1.1% tip chord around tip center and 2.4% tip chord near LE/TE.

A tornado like tip vortex structure travelling in the circumferential direction with vortex axis normal to the blade suction surface is observed for all tip clearances studied. The frequencies of the tip flow instabilities near the rotor tip region are different for the different rotor tip clearance shapes. The present study accurately predicts the peak NSV of 2513 Hz for a straight tip of 1.1% tip clearance at about 78% span, which is about 3.3% lower than the experiment. As the rotor tip clearance is increased to 2.4% without shape change, the dominant NSV frequency is reduced by about 6% with the pressure oscillation amplitude slightly reduced. However, when the tip shape is changed to tip clearance 3, the peak NSV frequency is reduced by about 29% with a significant increase in pressure oscillation amplitude by about 42%.

The tip flow instabilities are caused by the circumferentially travelling tornado vortices whose frequency passing each blade is roughly equal to the NSV frequency.

Chapter 10

NSV Simulation Using Fully Coupled FSI

Non-synchronous vibration (NSV) of the $1/7$th annulus GE axial compressor is simulated using a fully coupled fluid/strcuture interaction (FSI) to study a relevant flow mechanism that causes NSV. A rotor tip with clearance size of 2.4% C_t is recommended by GE Aviation for investigation.

Time accurate Navier-Stokes equations are solved with a system of 5 decoupled structure modal equations in a fully coupled manner. A 3rd order WENO scheme for the inviscid flux and a 2nd order central differencing for the viscous terms are used to resolve nonlinear interaction between vibrating blades and fluid flow. The same boundary conditions applied to NSV tip clearance in chapter 9 are used including an accurate time shifted phase-lag (TSPL) boundary condition to reduce computational efforts and a fully conservative rotor/stator sliding boundary condition to accurately capture unsteady wake propagation between the rotor and stator blades. The computational mesh as illustrated in Fig. 9.3 is also used and the numerical probes as sketched in Fig. 9.4 are used to measure the unsteady variations of the normalized static pressure on the blade surface and at the tip clearance.

10.1 Blade Deforming Mesh

A CPU efficient deforming mesh technique is one of the requisites for FSI to accurately describe the vibration of the structure. The conventional method regenerates mesh inside domain with the fixed outer boundaries. However this may cause significant numerical instability due to the high mesh skewness when the vibrating structure is close to the boundaries like rotor tip clearance. In this study an advanced deforming mesh algorithm introduced in Chapter 7 is employed to improve mesh quality over rotor tip clearance. The basic idea is to reposition the casing grid points so as to keep high normality between the rotor tip and the casing. Once a blade-to-blade section is done, then 3D mesh is obtained by stacking each blade section from the hub to the tip. It has been shown that this algorithm for a blade-to-blade section works robustly for the large blade vibration.

10.2 Mode Shape of the 1st Stage Rotor Blade

The first five mode shapes used in this study are normalized by the generalized mass ($\sqrt{\phi^T m \phi}$) and provided by the manufacturer. The natural frequencies are 1041.42 Hz, 2658.02 Hz, 2988.68 Hz, 5180.21 Hz and 5890.47 Hz. The deflections of 1st and 2nd mode are displayed in Fig. 10.1. The blades are modeled as fixed at the rigid body rotor. Note that the NSV of the compressor under study is captured in the experiment close to the first torsional mode, which is mode 2 in Fig. 10.1.

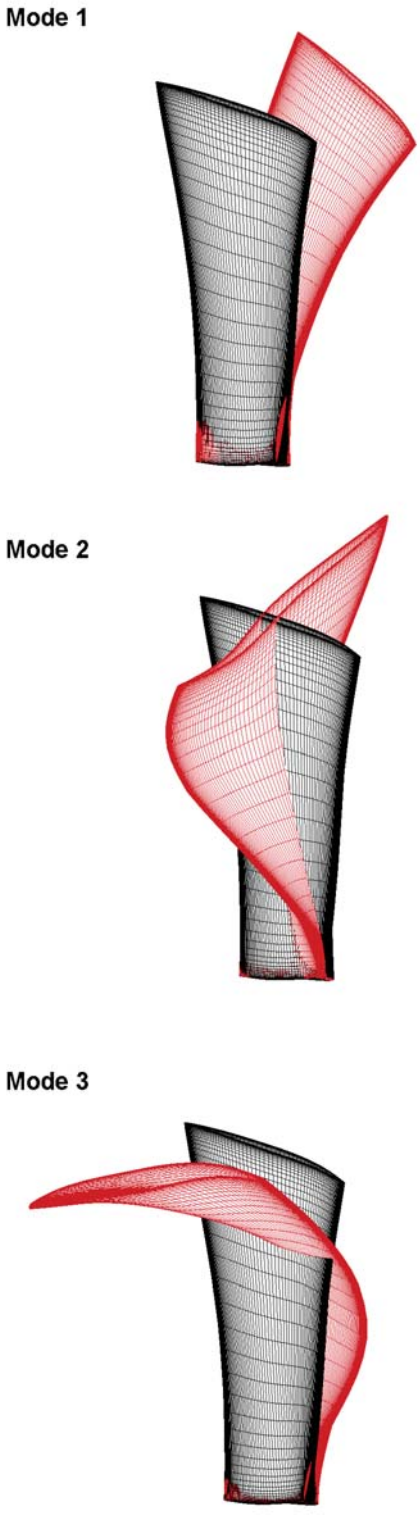

Figure 10.1: Rotor blade 1st and 2nd modal deflections

10.3 Results and Discussion

The rig testing of the full axial compressor with 1.1% tip clearance [14, 18] is shown to have the NSV frequency range of 2600 Hz to 2661 Hz, which is located between 12EOL to 13EOL and is near the first torsional mode (1T) as shown in the Campbell diagram in Fig. 10.2. The compressor operating point used for the present NSV simulations is 2600 Hz at 12880 RPM. Note that EOL(engine order line) in Campbell diagram is obtained by integer multiples of rotor shaft frequency with respect to RPM. The Campbell diagram can be used to evaluate whether a blade frequency including natural frequency is synchronous or not with engine shaft. The present FSI simulation with 2.4% tip clearance shows the dominant frequency of 2365 Hz, which is a NSV between 11EOL and 12EOL. Note that a large tip clearance size of 2.4% tip chord is recommended by the engine manufacturer. The

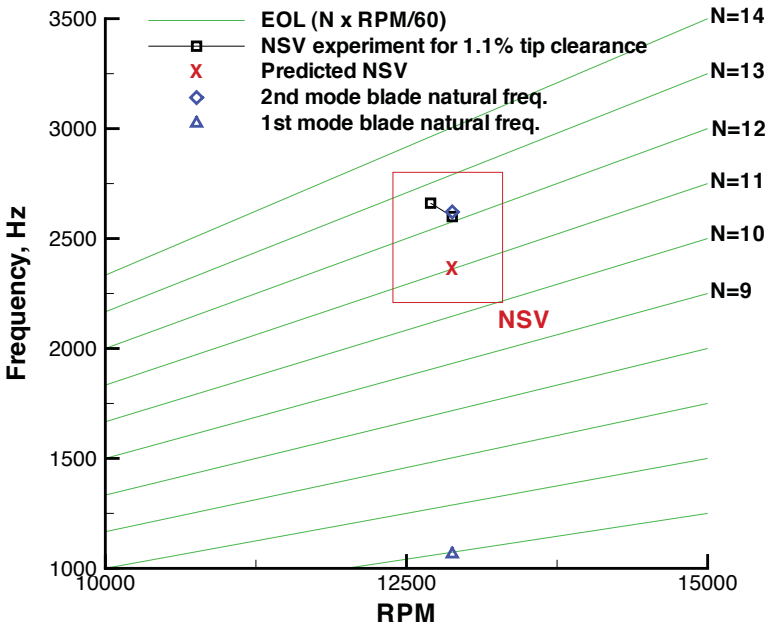

Figure 10.2: Campbell diagram of the compressor

residual is reduced by three orders of magnitude within each physical time step, which is usually achieved within 30 to 40 pseudo time step iterations. A non-dimensional time step of 0.005 is used.

The Speedline and NSV Location

Since NSV of axial compressors is typically observed in stable operation [1, 2, 14, 15], unsteady flow simulations are first conducted with rigid blades and no vibration using a finer mesh at different back pressure conditions to find the dominant region of NSV in the speedline.

Fig. 10.3 shows the predicted speedline of the 1-1/2 stage axial compressor. Note that the time averaged speedline data for the fine mesh and the baseline mesh are obtained with rigid blades for mesh refinement study by averaging final 2 rotor revolutions.

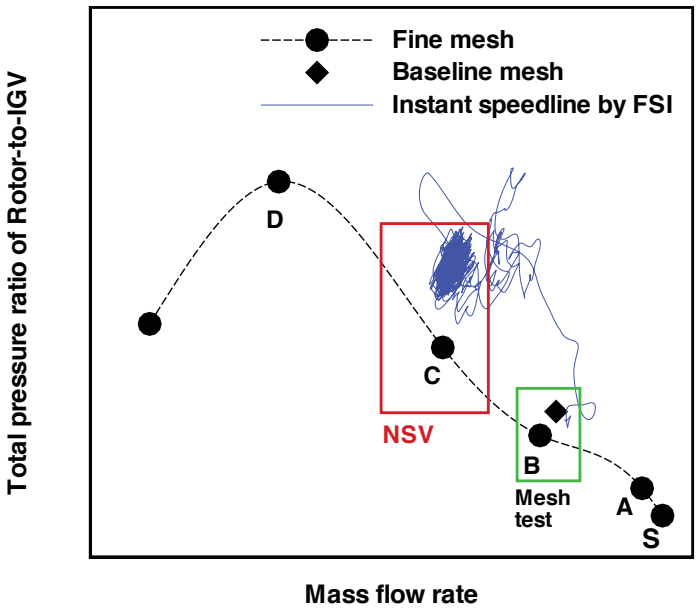

Figure 10.3: IGV-to-rotor speedline from the fully coupled FSI

The point A, B, C and D represent rotor-to-IGV total pressure characteristics. The back pressure is gradually increased from the point S to find the near stall point D. After the point D the compressor stalls. The point S is about maximum mass flow condition. No NSV events are found at point S. The mass flow rate obtained at the point C is about 6% higher than the near stall point D.

The unsteady FSI simulation is started from the solutions obtained at the point B. The back pressure used at the point B is slightly increased to obtain about the same mass flow near the point C. The NSV of 2365 Hz is obtained by the NSV simulation based on the fine mesh with rigid blades. As illustrated in Fig. 10.3, the instant speedline predicted by the FSI simulation with the baseline mesh converges well to the point C. The same NSV frequency of 2365 Hz is observed by the fully coupled FSI.

Fig. 10.4 shows time history of the rotor outlet mass flow rate during the NSV predicted by the fully coupled FSI. In this study the unsteady solutions between 0.5 and 2 rotor revolutions are used for the NSV frequency analysis since the predicted mass flow shows periodic oscillations after 0.5 revolution. It is clear that the compressor under the NSV operates without the mass flow breakdown as presented by the experimental studies [1, 2, 14, 15].

NSV Simulation Using a Fully Coupled FSI

As aforementioned, the flow instabilities around the rotor tip are the main causes of NSV [2, 14, 18]. The axial velocity contour at the blade tip span is shown in Fig. 10.5. There is a large area of the negative axial velocity near the rotor leading edge due to the tornado vor-

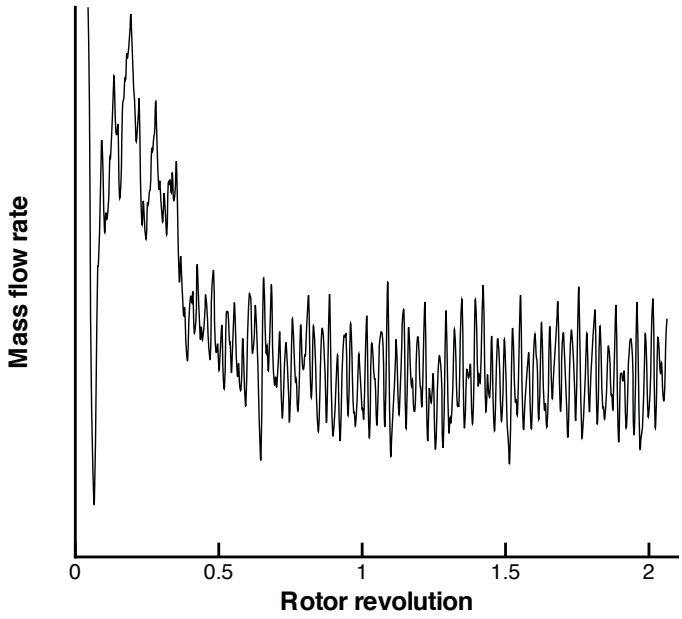

Figure 10.4: Instantaneous mass flow during NSV from the fully coupled FSI

tices during the NSV [18]. A strong interaction of the tornado-like vortices with incoming flow of the IGV downstream is observed near the rotor leading edge [18].

Fig. 10.6 shows entropy contour of the axial plane near rotor leading edge. Entropy stands for the degree of energy loss, hence high entropy reflects high disturbance due to the flow separation. Entropy is significantly increased for the flow field about 20% span from the casing, where the tornado vortex triggers the flow instabilities as the main cause of the NSV observed in this study [18]. The NSV of 2365 Hz with maximum amplitude is observed at roughly 78% span near leading edge of the rotor (probe 63 in Fig. 8.47). The boundary of the vortical flow dominant is around 78% span, where the strong interaction exits with entropy jump as shown in Fig. 10.6.

Instantaneous blade surface pressure acquired at 78% span and tip clearance are plotted in Fig. 10.7. The maximum amplitude of the pressure is observed at 78% span near the

rotor leading edge. As illustrated in Fig. 10.8, the tornado tip vortices propagate circumferentially roughly at the same frequency of the NSV [18]. The 3D tornado like tip vortex structure as the main cause of the NSV is different from the regular streamwise tip clearance vortex. It swirls strongly with vortex axis normal to the blade suction surface around the rotor leading edge and induces tip leakage spillage flows to the next blade passages. It should be emphasized by the NSV experiment of Baumgartner et al. [1] that the hot-film measurements of the 1st stage rotor blades show the radial dependency of the rotating instability as the main driver of the NSV observed for the 10 stage high pressure axial compressor. The NSV with high blade vibration amplitude is observed between 65% to 91% of the blade span, while the measurements close to the casing wall are very noisy without high fluctuations. The compressor investigated in this study is an aircraft engine high speed full compressor similar to the compressor used for the NSV experiment of Baumgartner et al. [1] and also exhibits the NSV in the 1st stage rotor blades.

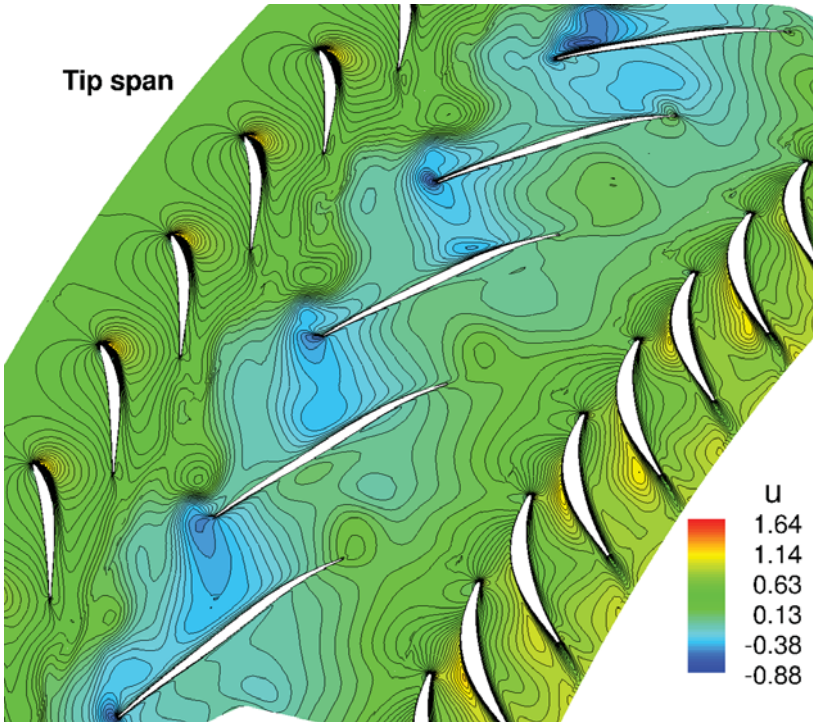

Figure 10.5: Axial velocity contour at tip span from the fully coupled FSI

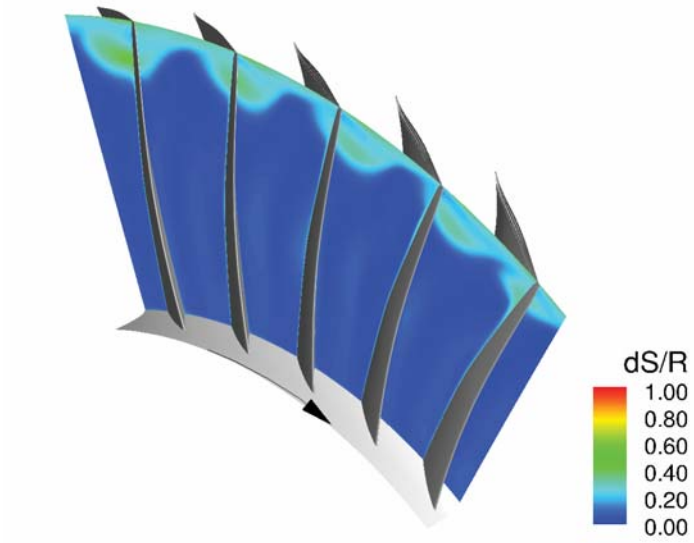

Figure 10.6: Entropy contour of the axial plane near the rotor leading edge from the fully coupled FSI

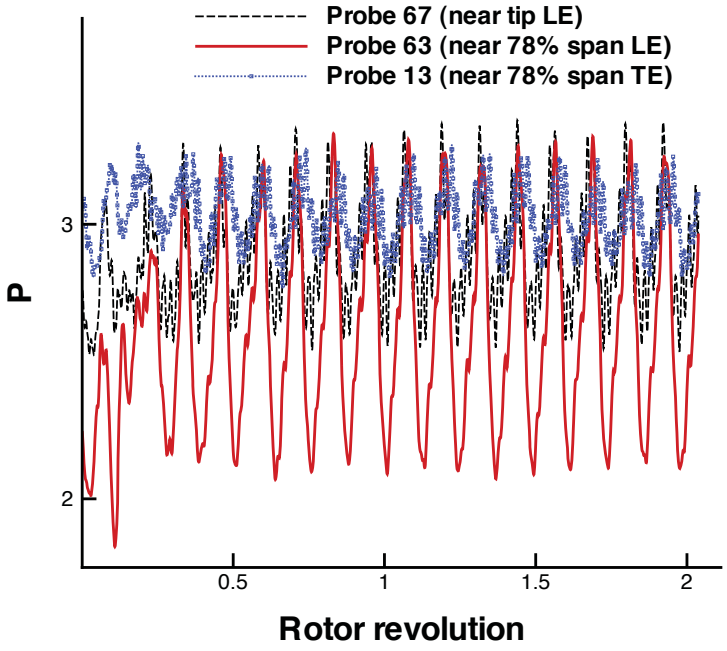

Figure 10.7: Instantaneous pressure acquired at the blade 3 during NSV from the fully coupled FSI

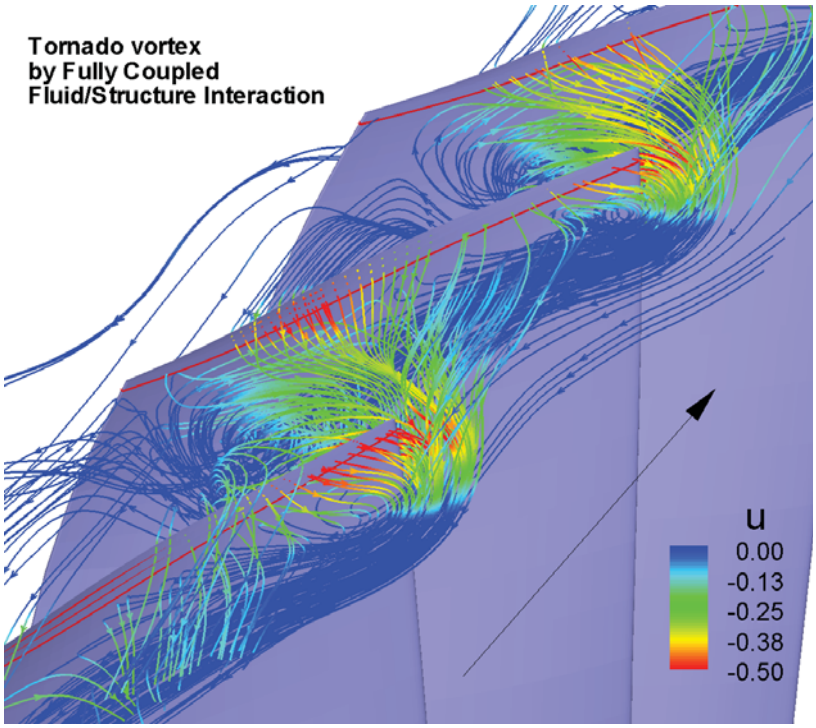

Figure 10.8: Tornado like tip vortices with static pressure contour around tip vortex center from the fully coupled FSI

It is clear that fluctuation level of the pressure is significantly amplified at78% span near the rotor leading edge. It is shown by the NSV experiments [1, 2, 15] that the blade sensor signals under the NSV have a strong periodic content due to the rotating instability near the rotor tip region. The present numerical simulation using a fully coupled FSI clearly demonstrates a strong periodic oscillation of the blade surface pressure during the NSV.

Fig. 10.9 shows the instantaneous flow structure of the meridional plane between the two blades. This indicates that the tip flow around the rotor blade leading edge where the blades vibrate at peak amplitude is largely disturbed due to the tip tornado vortex that travels in the opposite direction of the rotor rotation through the blade leading edge ahead above roughly 70% span.

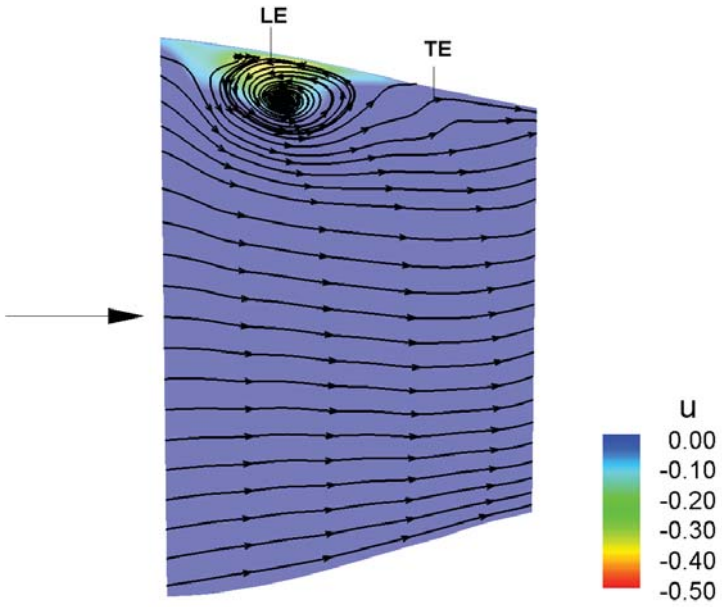

Figure 10.9: Flow structure of the meridional plane between the two blades from the fully coupled FSI

The modal force($\frac{\tilde{\phi}_j^{*T}}{m_j^*} \cdot \mathbf{F}^* \cdot {V_f}^2 \cdot \frac{b_s^2 L}{\bar{V}} \cdot \bar{m}$) acting on a blade is shown in Fig. 10.10. The fluctuation of the second modal force is much larger than that of the first mode and the third mode. The oscillating pattern is a phase-locked and periodic, which is very similar with the pressure signal acquired at 78% span near leading edge. The rotor blades are excited due to the highly oscillating aerodynamic force induced by the tornado vortex instability during the NSV. In this way, the first stage rotor blades vibrate with a high amplitude near the second mode.

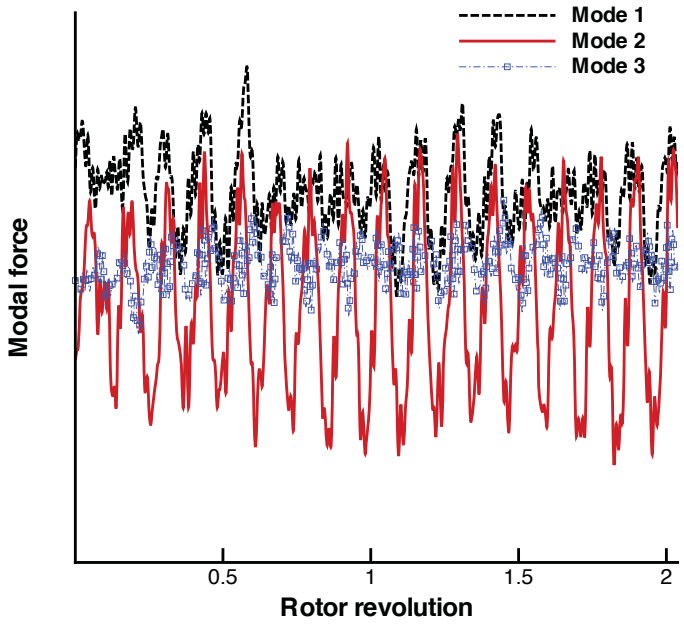

Figure 10.10: The blade modal force($\frac{\tilde{\phi}_j^{*T}}{m_j^*} \cdot \mathbf{F}^* \cdot {V_f}^2 \cdot \frac{b_s^2 L}{\bar{V}} \cdot \bar{m}$) during NSV from the fully coupled FSI

Fig. 10.11, Fig. 10.12 and Fig. 10.13 show the 1st, 2nd and 3rd modal displacements respectively during the NSV. The responses of the first mode are being damped out. While the displacements of the 2nd mode (torsion) do not diverge nor decay in time, which is the typical nonlinear vibration pattern of limited cycle oscillation (LCO). The 3rd mode responses also are damped out. If the NSV of the 1st stage rotor blades captured in this study is a blade aeroelastic instability like flutter, the blade responses then must be a kind of divergent response with increasing amplitude. However, the blade vibration predicted by the present FSI simulation clearly is a LCO that may cause high cycle fatigue(HCF) of the blade structure. Unfortunately no experimental measurement with regard to the unsteady pressure responses of the compressor blades is available. However, such an experiment of Baumgartner et al. [1] could be used as the qualitative comparison reference for the present study since both compressors are at high-speed regime with similar design specifications. The NSV experiments [1, 2, 15] show that the high amplitude blade signals under NSV oscillates in a periodic manner.

As shown in Fig. 10.12 and Fig. 10.14, a strong coupling between the pressure at 78% span of the blade and the second mode of the blade frequency exists during the NSV. Frequency analysis is carried out using the blade displacements and the static pressure signals acquired at the peak NSV point as presented in Fig. 10.15. The same NSV frequency of 2365 Hz is obtained at 78% span near the rotor leading edge using the blade displacement and the fluid pressure as plotted in Fig. 10.15. The predicted frequency ratio($\frac{\omega}{\omega_2}$) indicates no resonance with blade natural frequencies during the NSV. The frequency ratio of about 0.9 is the NSV frequency of 2365 Hz, which is about 9% lower than the frequency of the rig testing of the axial compressor with 1.1% tip clearance [14]. Therefore, it is obvious

that the blade pressure signal causes the second mode vibration during the NSV. In conclusion, the present FSI for the high-speed compressor demonstrates the reason why the NSV occurs near the second mode (or the first torsional mode) in the experiment [14].

Fig. 10.16 shows the modal displacements of blade 3. Since the first two modal displacements are dominant whereas the rest of higher modes are very small, use of first five mode shapes are reasonable to describe the blade vibration during the NSV.

It is meaningful to see the vibration at the blade tip leading edge where in general the largest displacement is observed. Fig. 10.17 shows the net tangential physical displacement at the rotor tip leading edge, where y_o, z_o denotes y-, z-coordinates of initial blade position. It is shown that the blade vibration is not a pure harmonic mode and at least two modes (bending and torsion) are combined within a cycle. Again, the 1st stage rotor blade vibration is not damped out but a limited cycle oscillation during the NSV.

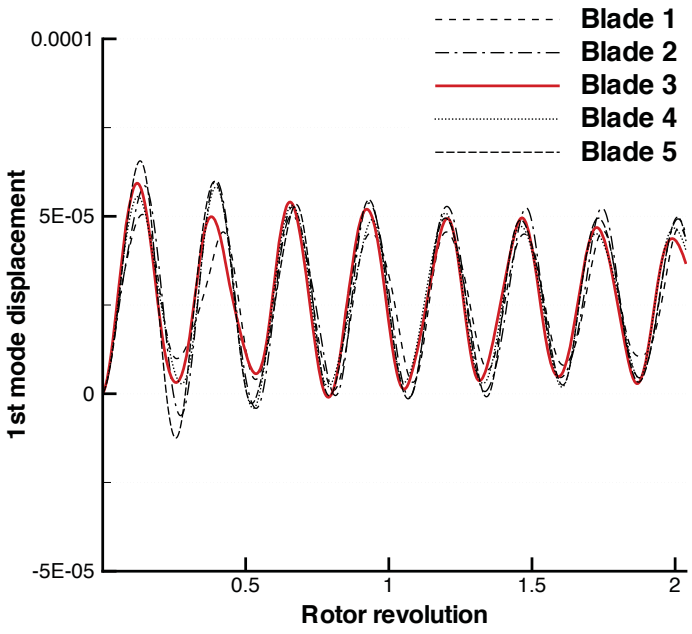

Figure 10.11: 1st mode displacements during NSV from the fully coupled FSI

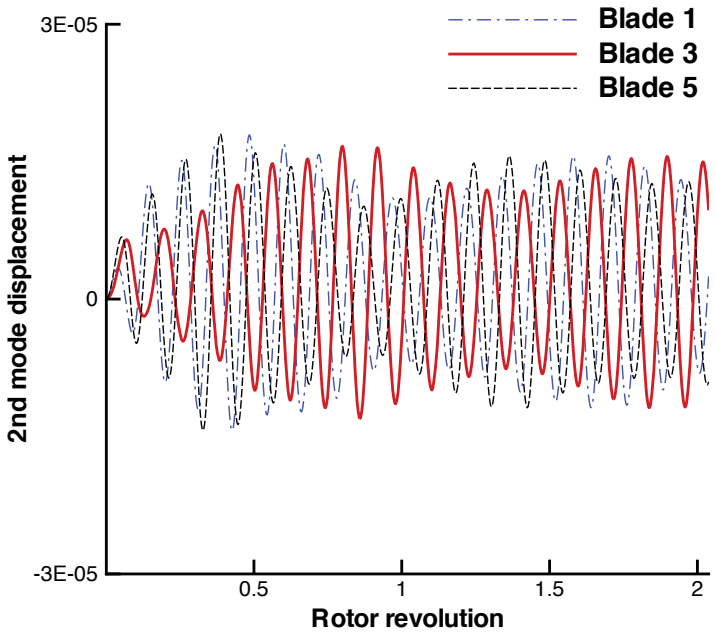

Figure 10.12: 2nd mode displacements during NSV from the fully coupled FSI

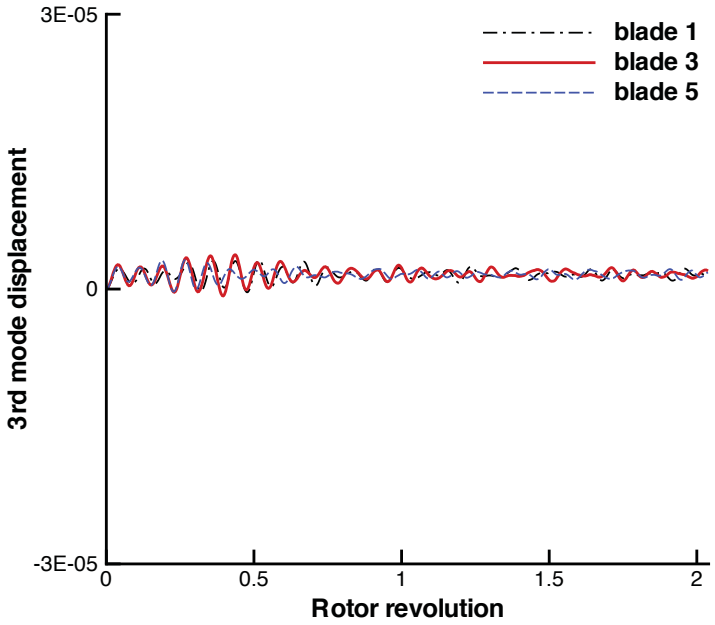

Figure 10.13: 3rd mode displacements during NSV from the fully coupled FSI

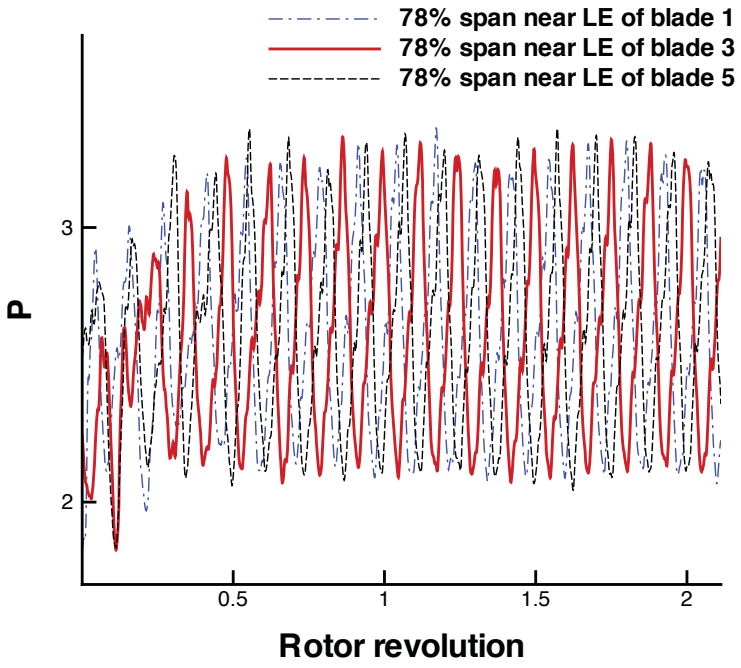

Figure 10.14: Instantaneous pressure acquired at 78% span near leading edge during NSV from the fully coupled FSI

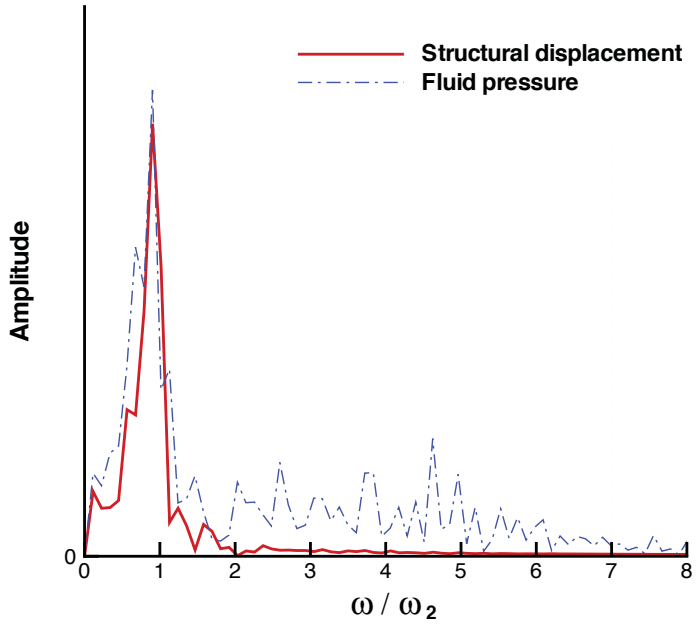

Figure 10.15: Comparison of frequencies using the structural displacement and the fluid pressure at 78% near LE suction surface during the NSV from the fully coupled FSI

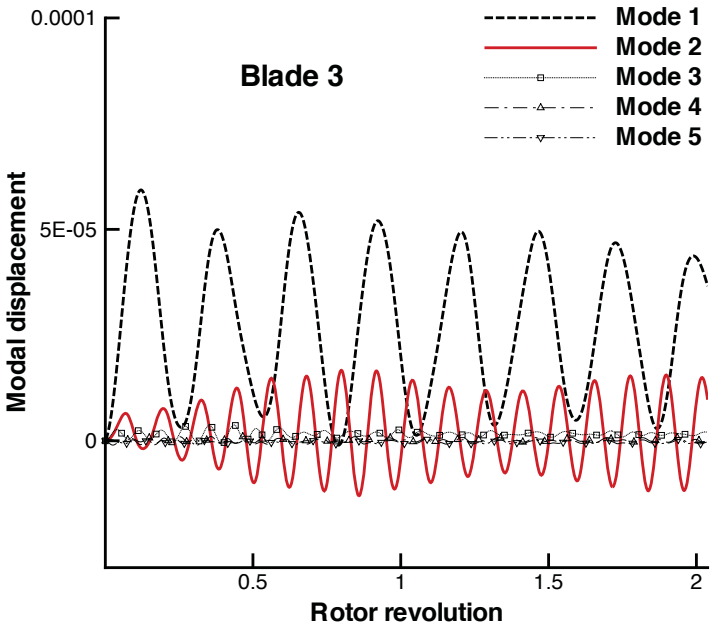

Figure 10.16: Five modal displacements of the blade 3 during NSV from the fully coupled FSI

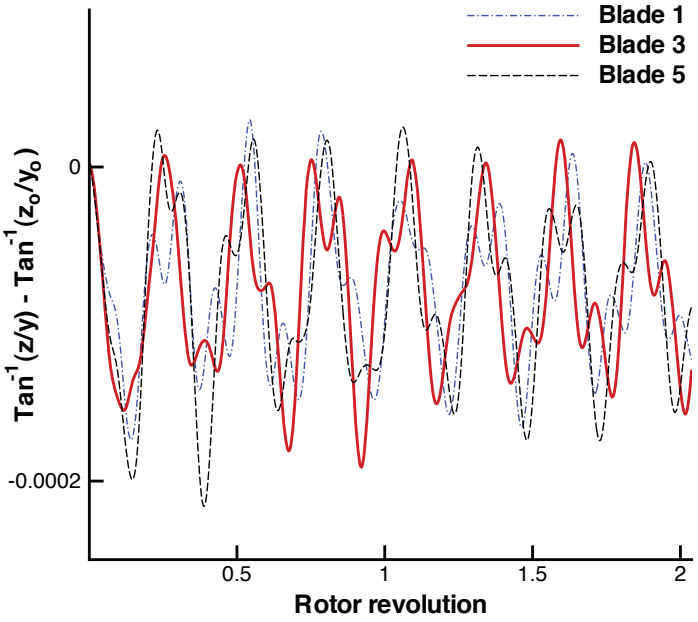

Figure 10.17: Normalized net tangential displacements at the rotor tip LE during NSV from the fully coupled FSI

10.4 Summary

The NSV is simulated using a fully coupled fluid-structural interaction for a GE axial compressor. A 1/7th sector of annulus for a 1-1/2 stage unsteady simulation is used with a fully conservative sliding BC and a time shifted boundary condition at the lower/upper circumferential periodic boundaries.

A tip clearance of 2.4% tip chord is used for the FSI simulation. The predicted NSV frequency of 2365 Hz is about 9% lower than the frequency of the rig testing with 1.1% tip clearance. The predicted NSV frequency is the same as the one predicted using rigid blades with no vibration.

The blade NSV is strongly coupled with unsteady aerodynamic pressure oscillation at 78% span near the rotor leading edge induced by the tip tornado vortex. The blades vibrate in a phase-locked manner without resonance to the blade natural frequencies.

The present numerical simulation indicates that the NSV of the compressor 1st stage rotor is caused by the tornado-like tip vortices travelling circumferentially.

Chapter 11

Investigation of Compressor NSV Using DDES

In this chapter, the delayed detached eddy simulation (DDES) of turbulence is used to investigate the mechanism of non-synchronous vibration (NSV) of a GE aircraft engine axial compressor. DDES is a hybrid model for turbulence simulation, which use RANS model within wall boundary layer and is automatically converted to large eddy simulation outside of the wall boundary layer. The DDES has been intensively validated with a NACA0012 airfoil at high angles of attack with massive flow separation. The drag is accurately predicted whereas the RANS model over predicts the drag by 33%. The DDES is also validated for AGARD wing subsonic/supersonic flutter boundary prediction and shows an excellent agreement with the experiment. Time accurate Navier-Stokes equations are solved with a 3rd order WENO scheme for inviscid flux and a 2nd order central differencing for viscous terms. The same boundary conditions and computational mesh used for the URANS NSV simulation in chapter 9 are used. DDES simulation is conducted for the tip clearance of 1.1% C_t, which is tip clearance 1 in chapter 9.

11.1 Results and Discussion

The rig testing of the axial compressor with 1.1% tip clearance [14] is shown to have the NSV frequency range of 2600 Hz to 2661 Hz, which is located between 12EOL(engine order line) to 13EOL as shown in the Campbell diagram in Fig. 11.1. The compressor NSV experiment is 2600 Hz at the present DDES simulation operating condition of 12880 RPM. The residual is reduced by three orders of magnitude within each physical time step, which is usually achieved within 30 to 40 pseudo time step iterations. A non-dimensional time step of about 0.005 is used. Note the Campbell diagram can be used to evaluate whether a blade frequency including natural frequency is synchronous or not with engine shaft. EOL in Campbell diagram is obtained by integer multiples of rotor shaft frequency with respect to RPM. The NSV predicted by DDES is 2217 Hz, which is underpredicted by about 14.7% compared to the experiment as shown in Fig. 11.1.

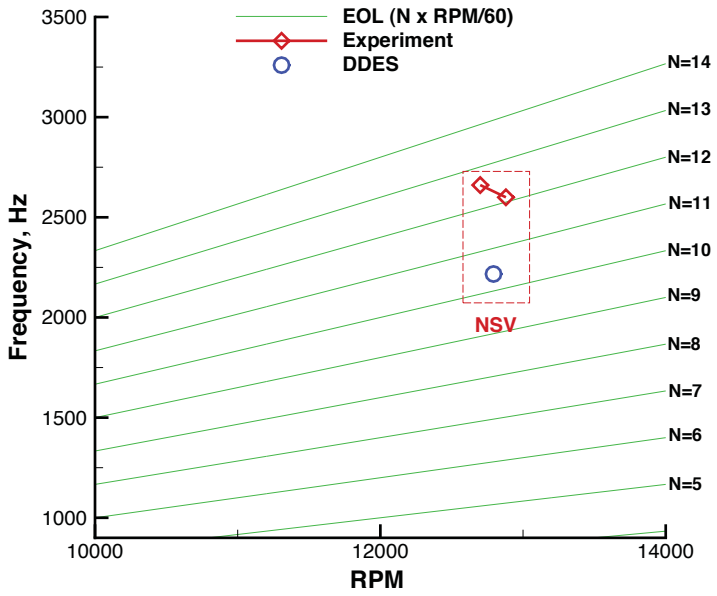

Figure 11.1: Campbell diagram

Tip Flow Instabilities

The present DDES demonstrates a rotating instability (RI) above 80% rotor span that causes NSV of the compressor stage 1 rotor. Fig. 11.2 shows entropy near the rotor leading edge axial plane. During the NSV of the compressor, entropy above 80% rotor span is significantly increased due to the RI that causes the NSV observed in this study as it travels circumferentially through the rotor leading edge ahead above 80% span.

As pointed out the NSV experiment [14, 18], the flow field of GE-C1 full compressor during the NSV event is not further developed in a form of rotating stall where the break-down of mass flow usually occurs. In the present simulation, the compressor runs without the mass flow decrease unlike rotating stall as presented in Fig. 11.3. The mass flow at the rotor outlet oscillates with a phase-locked manner. Roughly up to half rotor revolution, a transition behavior of the mass flow is observed because the present DDES simulation is started from the RANS solutions using a mixing plane [28]. Note that frequencies presented in this study are obtained based on the instantaneous pressure spectrum over 2 rotor revolutions after the transitional flow disappears.

The instantaneous flow field at about 88% span from 2 to 2+5/35 Rev is displayed in Fig. 11.4. The flow near the rotor is locally negative indicating axially reversal flow. There is the strong interaction of the reversal flow with the incoming healthy flow between the IGV and rotor. The flow in particular near the rotor leading edge is very unstable since the tornado vortex that causes the NSV travels circumferentially through the rotor leading edge ahead.

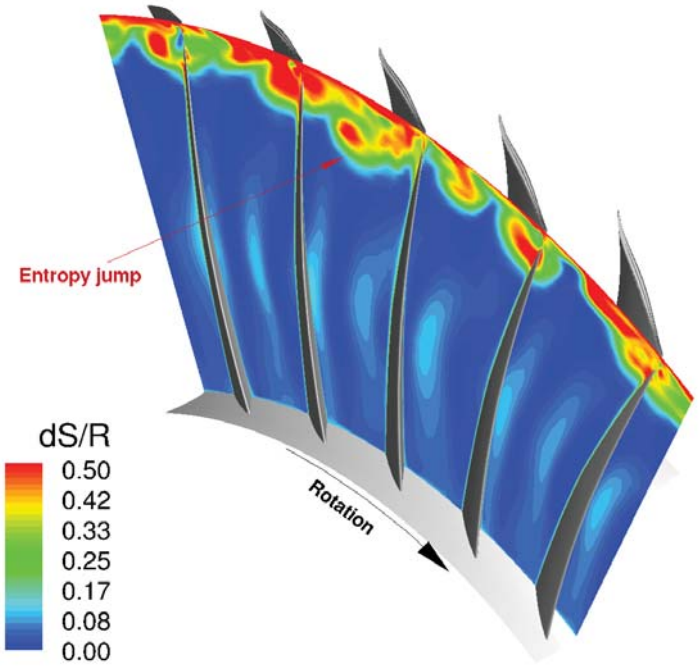

Figure 11.2: Entropy contour at leading edge axial plane predicted by DDES

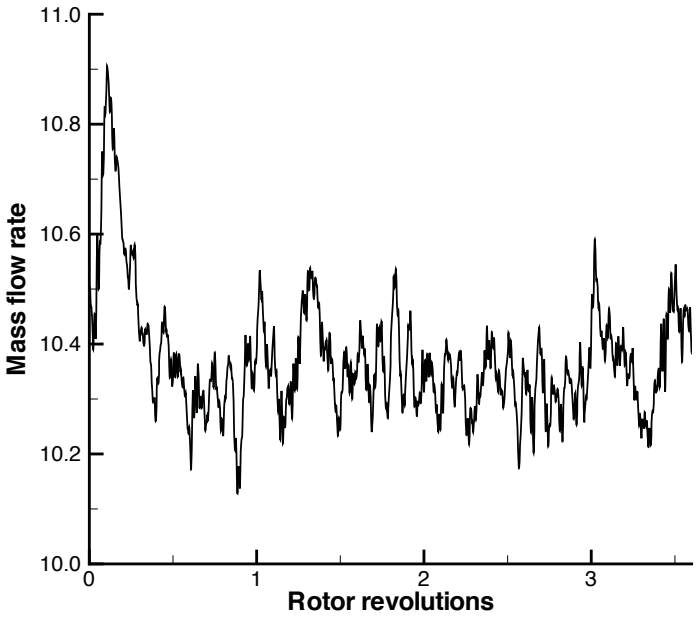

Figure 11.3: Instantaneous mass flow at the rotor outlet predicted by DDES

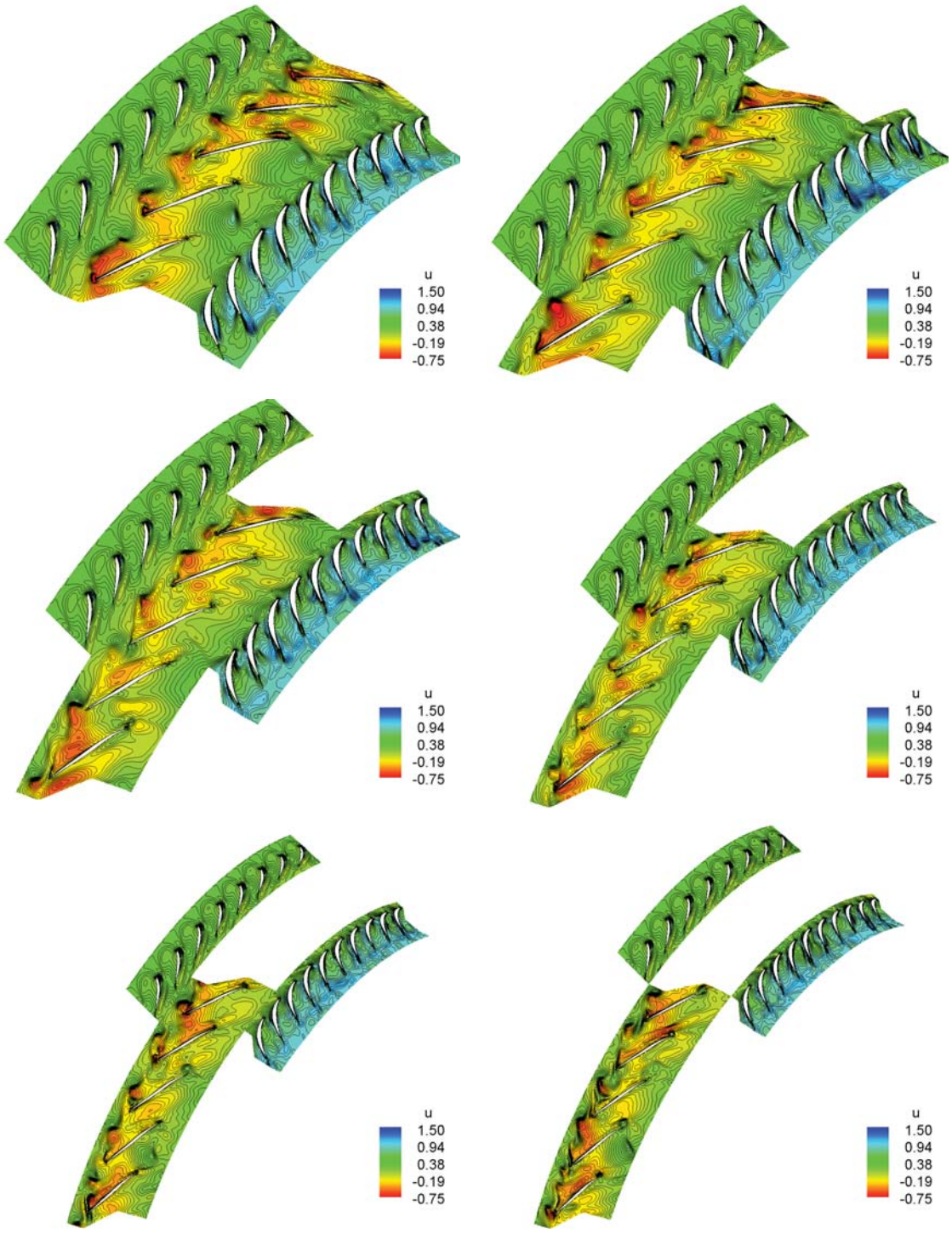

Figure 11.4: Instantaneous axial velocity contour at 88% span at 2 Rev(top left), 2+1/35 Rev(top right), 2+2/35 Rev(middle left), 2+3/35 Rev(middle right), 2+4/35 Rev(bottom left), 2+5/35 Rev(bottom right) predicted by DDES

Fig. 11.5 shows changes in the instantaneous circumferentially mass averaged radial profiles from 2 rotor revolutions including rotor total pressure ratio, mass flux at the rotor outlet, rotor adiabatic efficiency, and relative Mach number at the rotor outlet. The flow above roughly 75% span is very unstable. In particular, there is a large variation of the total pressure ratio around 80% to 90% rotor span, where the NSV of 2217 Hz is obtained with peak amplitude in this study.

The total pressure is decreased up to about 80% span, but it dramatically increases roughly above 80% span. The rotor blade loading for pumping work is too high near the rotor tip, which can induce the flow separation near the rotor leading edge suction surface because of high incidence. This may induce the tornado vortex above 80% span that causes NSV. Above 80% span the rotor adiabatic efficiency is significantly decreased due to the tornado vortex. Both the mass flux and relative Mach number at the rotor outlet are lower in the vicinity of the rotor tip during the NSV due to the reversal flow. It is indicated that the flow below roughly 70% span is stable during the NSV unlike rotating stall. As aforementioned in the introduction, the experiment for the 10 stage high pressure axial compressor [1] shows a NSV event due to a rotating instability with high amplitude vibration on the 1st stage rotor blades above 74% span. In their experiment, the NSV decays away from the RI center and eventually disappears below 65% blade span.

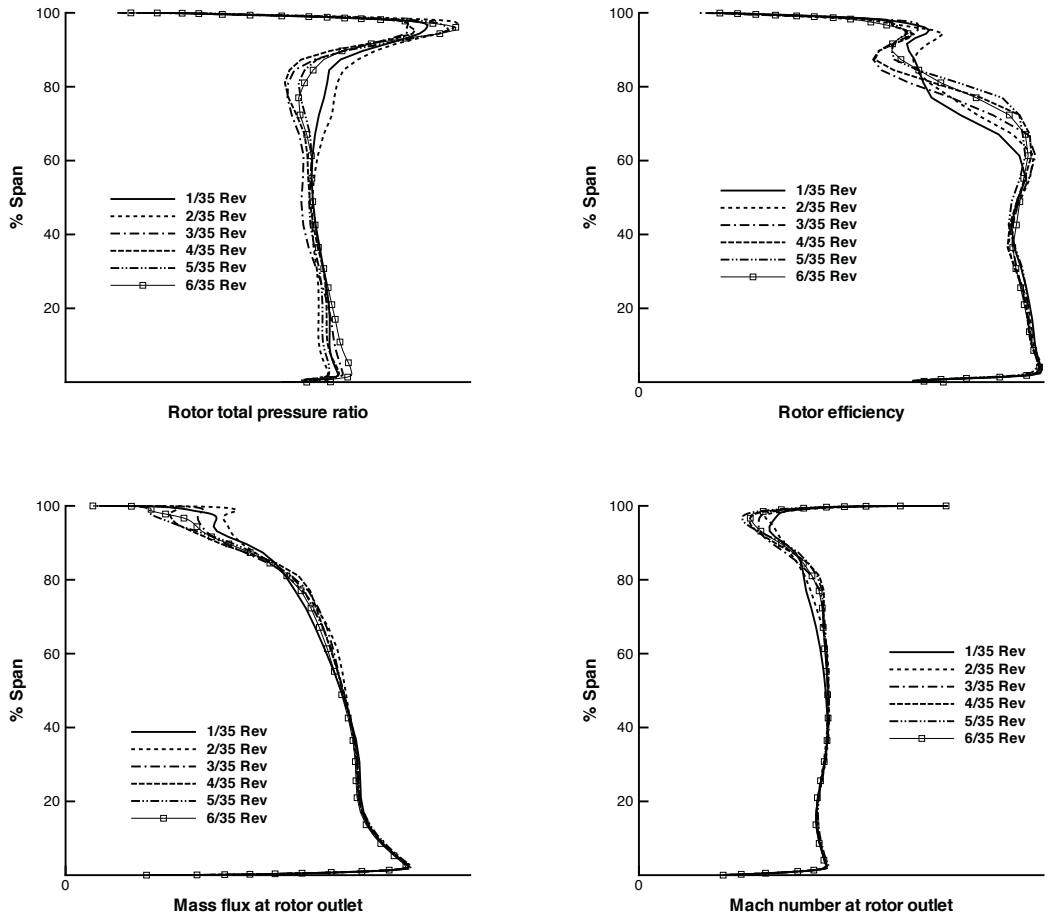

Figure 11.5: Circumferentially mass averaged radial profiles for the 1st stage rotor; rotor total pressure ratio (top left), rotor adiabatic efficiency (top left), mass flux at rotor outlet (bottom right), rotor outlet relative Mach number (bottom right)

Speedline Characteristics

In Fig. 11.6, the total pressure ratio of rotor-to-IGV is plotted in terms of the mass flow at RPM of 12880. The thick solid line represents the speedline predicted by GE URANS. The dashed line indicates possible NSV region obtained by the experiment [14, 18]. The symbol square is the speedline at the NSV of 2365 HZ predicted by GE CFD, while the solid circle denotes the NSV of 2217 Hz predicted by present DDES. Difference in the total pressure ratio at NSV between the DDES and GE CFD is about 0.8% and the mass flow difference between GE CFD and the DDES is about 4.7%. The DDES tends to predict the rotor stall earlier than the URANS and the NSV can be achieved only at higher mass flow rate, which generates a lower frequency.

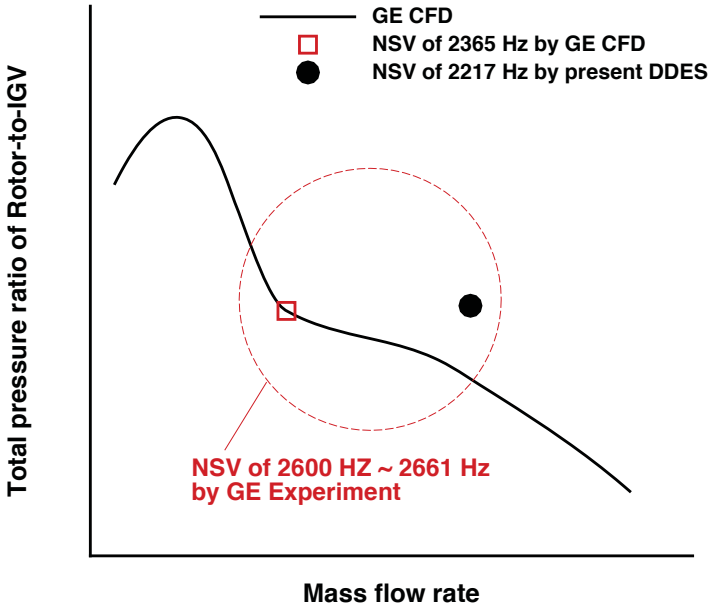

Figure 11.6: Speedline of GE 1-1/2 stage axial compressor predicted by DDES

It is emphasized that NSV of the compressor occurs at normal operating conditions

and its frequency varies due to the mass flow, operating speed and temperature [3, 18]. In addition, a URANS for the 1/7th rotor annulus with in-phase condition at circumferential periodic boundaries is used for GE NSV simulation [14]. Therefore, the effects of rotor/stator interaction and phase difference on NSV were neglected for GE NSV simulation. As shown by the earlier work of present authors [18], overall URANS predicts the NSV closer to the experiment than the DDES. However, the DDES resolves reasonably the rotating flow instabilities of tornado vortices that cause the NSV observed in this study, which will be presented in the rest of this paper.

Role of Tornado Vortex in NSV

Fig. 11.7 shows the instantaneous tornado vortex movement from 2 rotor revolutions. The present DDES simulates how the tornado vortex causes the NSV. The tornado vortex on the blade A suction surface at $\frac{1}{35}$ Rev is completely moved to the blade B at $\frac{3}{35}$ Rev in the opposite direction to the rotor rotation. Since the center of the tornado vortex is low pressure region, the blades undergo large pressure oscillations that causes NSV due to the tornado vortex propagation. It is shown in this study that the frequency of this tornado vortex propagation is roughly equal to the NSV frequency of the blade pressure signals. Most of NSV experiments [1, 15] for axial fan/compressor indicate that the flow instabilities in the vicinity of rotor tip rotates circumferentially and cause the NSV. However, the numerical studies on axial compressor NSV [2, 14] fail to capture the rotating instability. The URANS simulation by Kielb et al. [14] shows that the NSV is caused by the suction side vortex that does not go to the next blade passage but oscillates in a blade passage.

To inspect the NSV with peak amplitude, the numerical probes as sketched in Fig. 8.47 are used to acquire the unsteady pressure signal on the blade surface and at the tip clearance. Fig. 11.8 shows the normalized pressure signal on the blade pressure surface. It is shown that the pressure fluctuation at 88% span larger than those at tip clearance and 78% span. In this study, the peak NSV is found at 88% span (the center of the tornado vortex) near the rotor leading edge pressure surface where the largest pressure oscillation occurs due to the tornado vortex propagation. Note that the pressure signals acquired on the rotor leading edge suction surface also show the peak pressure fluctuations at 88% span in a phase-locked manner similar to those at the pressure surface near leading edge. The high amplitude of aerodynamic excitation during the NSV as observed in Fig. 11.8 can induce high cycle fatigue and damage the blade structure.

Fig. 11.9 shows the predicted frequencies for the normalized pressure signals on the blade suction (top) and pressure surface (bottom). It is clear that the peak frequency of 2217 Hz is obtained at 88% span near leading edge. The predicted NSV frequency of 2217 Hz is between 10EOL and 11EOL, which is a completely non-synchronous to the engine order. Note that the base engine order (or 1 EOL) frequency at 12888 RPM is 214.67 Hz. Like the NSV experiment of a high speed axial compressor [1], the present DDES also indicates that the intensity of NSV decreases away from the rotating instability.

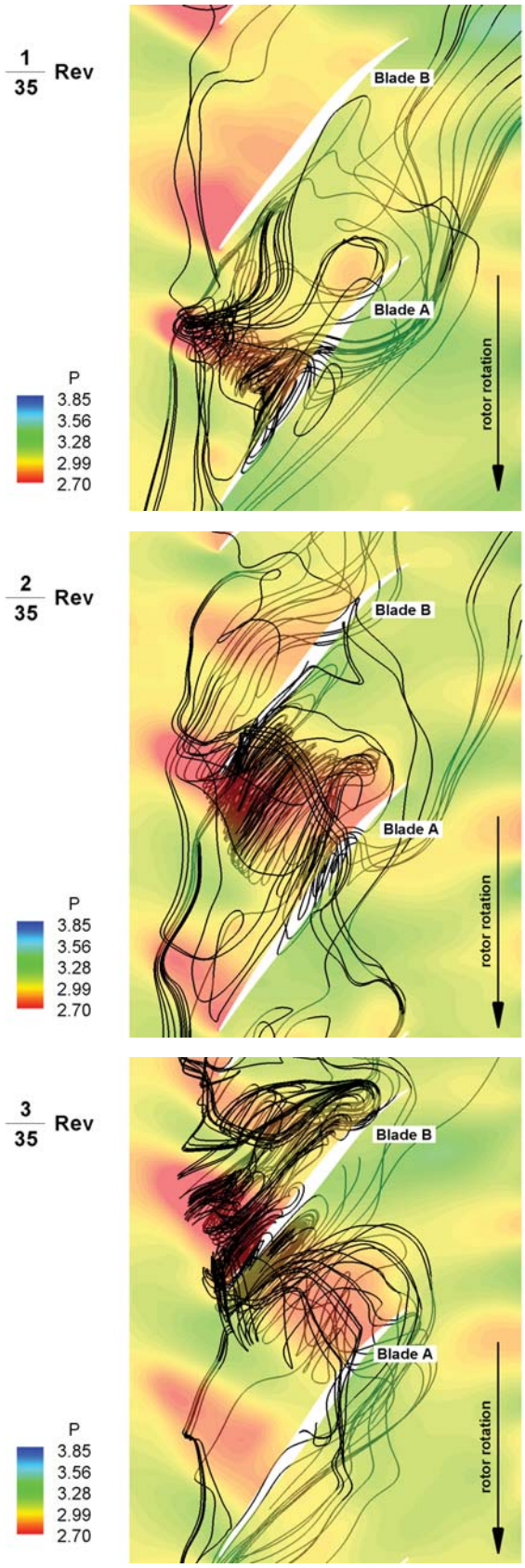

Figure 11.7: Instantaneous tornado vortex trajectories at 2+1/35, 2+2/35, 2+3/35 Rev colored by the normalized static pressure

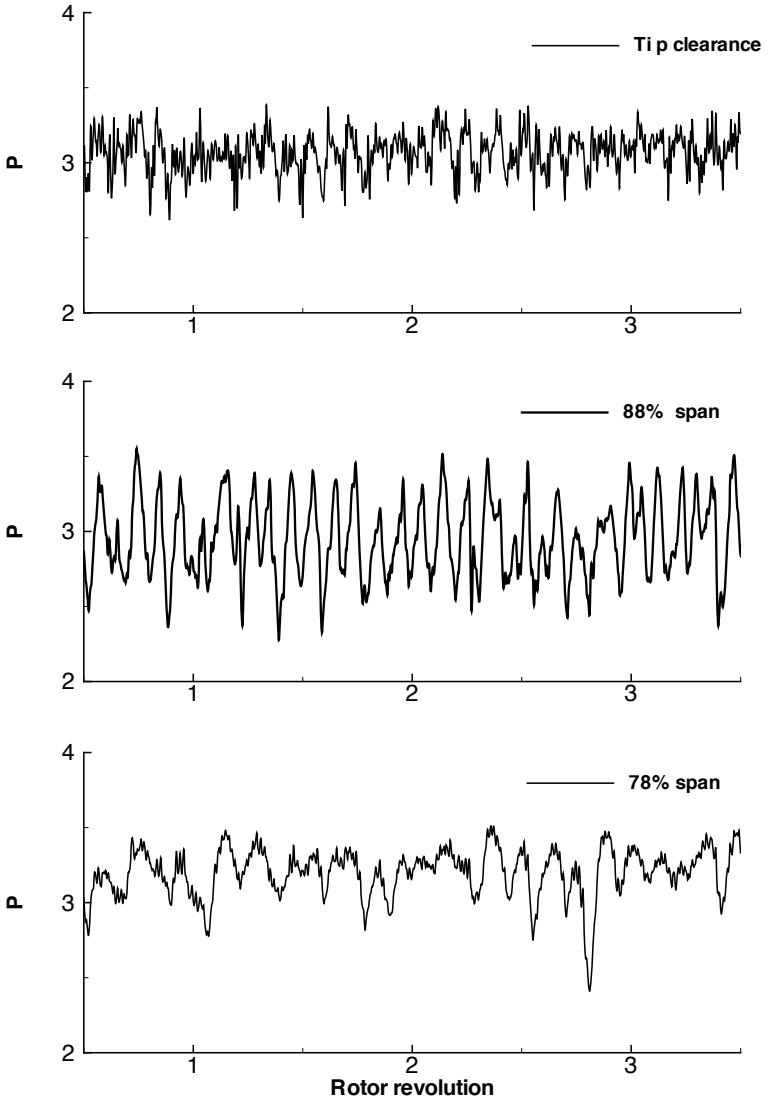

Figure 11.8: Instantaneous pressure signal on the rotor leading edge pressure surface during the NSV

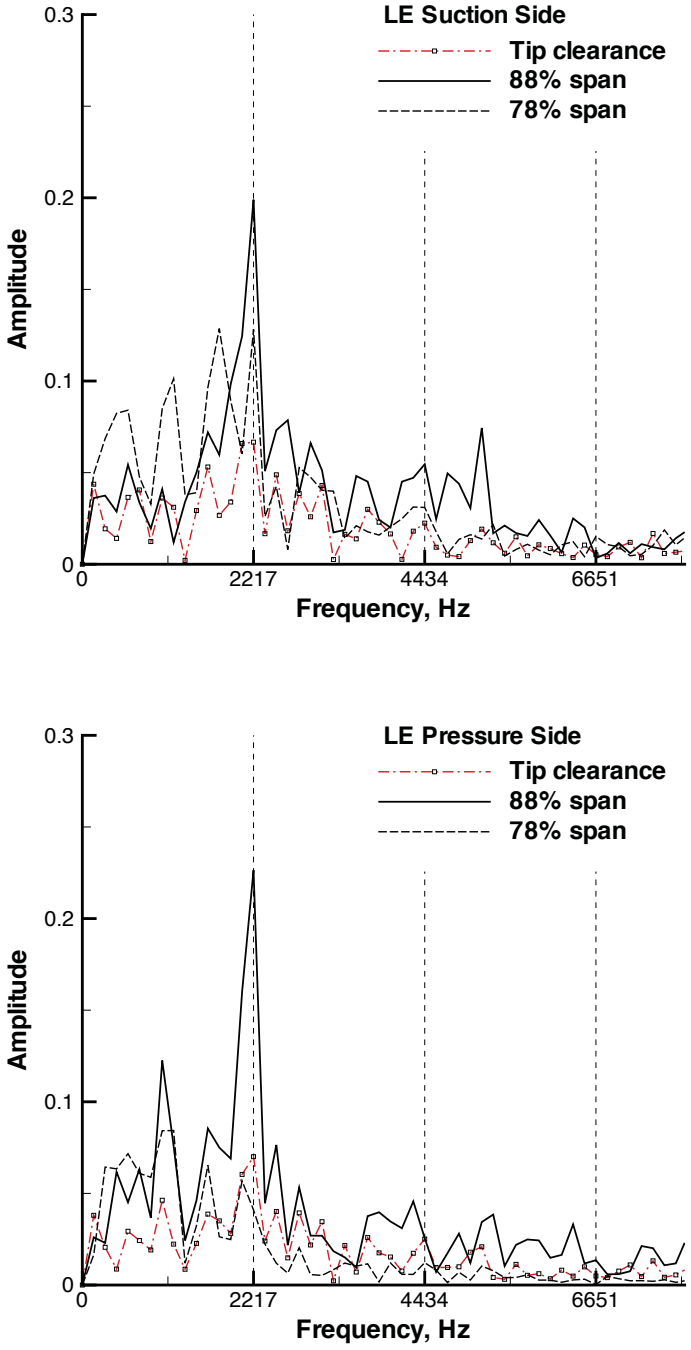

Figure 11.9: Predicted NSV frequencies for the blade pressure signals acquired at the rotor LE suction (top) and pressure surface (bottom)

Fig. 11.10 illustrates the 3D tornado like tip vortex structure as the main cause of the NSV observed in this study. Unlike the regular streamwise tip clearance vortex, it swirls strongly with vortex axis normal to the blade suction surface and induces the reversal flow near the rotor tip region. A similar vortical flow structure is detected by the experimental work of Inoue et al. [73], which is a separation vortex from the blade suction surface and ends up at the casing wall during the short length scale rotating stall of the multistage axial compressor. However, the present DDES demonstrates that the tornado vortex rotates circumferentially through the rotor leading edge ahead roughly above 80% span and causes the NSV of the compressor stage 1 rotor blades.

To investigate the effect of tip leakage impinging jet acoustics resonance on the NSV, the NSV critical tip velocity (Eq. 9.1) based on their impinging jet experiment suggested by Thomassin et al. [3, 16] is calculated at tip clearance center(the probe 87). The blade natural frequency(f_b) near NSV is about 2620 Hz, the local speed sound is about 346.23 m/s. The calculated U_{tipc} with $n = 1$ is 220.14 and with $n = 2$ is 440.28, while the blade tip velocity(U_{tip}) measured is about 341.4 m/s. The calculated NSV critical velocity(U_{tipc}) at $n = 1$ based on Eq.9.1 is about 36% lower than U_{tip}, and U_{tipc} at $n = 2$ is about 29% higher than U_{tipc}. Since the condition of the NSV driven by tip leakage acoustics resonance is $U_{tipc}/U_{tip} \approx 1$, it appears that the acoustic wave of tip leakage jet is not responsible for the NSV observed in this study.

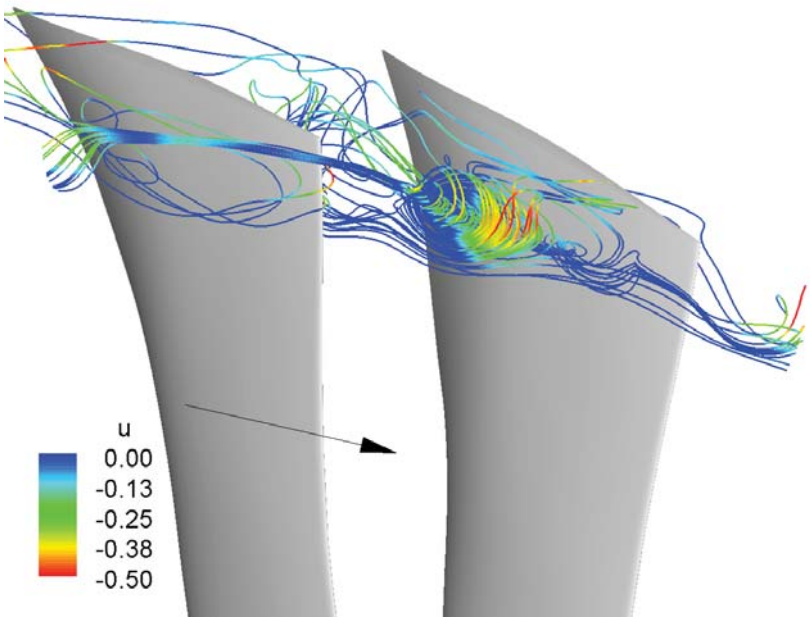

Figure 11.10: Tornado vortex during the NSV predicted by DDES

11.2 Summary

The delayed detached eddy simulation of turbulence is used with the low diffusion E-cusp scheme to investigate the mechanism of non-synchronous blade vibration of a GE high speed axial compressor. The fully conservative sliding BC is used for the 1-1/2 stage 1/7th sector annulus simulation with the time shifted phase lag BC (TSPL) at the lower/upper circumferential boundaries.

This paper appears to be the first time that a DDES is used to study compressor NSV problem. The measured NSV frequency by the GE full compressor rig test is 2600 Hz at the stage 1 rotor at 12880 RPM. The predicted NSV frequency by the present DES is 2217 Hz with its peak amplitude around 88% span near the rotor leading edge, which is under-predicted by about 14.7% compared to the experiment.

It is shown by the DDES that the tornado vortex formed in the vicinity of rotor tip causes the NSV of the compressor 1st stage rotor blades. The tornado vortex propagates at the speed of a non-engine order frequency to the next blade passage through the rotor leading edge ahead in the opposite to the rotor rotation, which results in the large aerodynamic excitation to the rotor blades that causes the NSV.

Chapter 12

Conclusions

In this thesis a high fidelity FSI methodology for axial turbomachinery aeromechanics simulation is developed using the low diffusion shock-capturing Riemann solver with the high order schemes, the delayed detached eddy simulation of turbulence, the fully coupled fluid-structure interaction with an advanced blade deforming mesh algorithm, the fully conservative unsteady sliding BC for rotor/stator interaction, and the phase lag boundary conditions. Thorough validation is achieved extensively to demonstrate high accuracy and robustness of the high fidelity FSI simulation methodology. The mechanism of non-synchronous vibration of aircraft engine axial fan/compressor is investigated using a GE high-speed axial compressor based on the high fidelity turbomachinery FSI methodology.

12.1 Contributions

The primary contributions achieved in this thesis include;

- Fully conservative sliding BC, interpolation sliding BC for rotor/stator interaction

- Mixing plane for steady multistage computation
- Phase lag BCs using the time shifted direct store approach and Fourier series
- Advanced blade deforming mesh for fully coupled turbomachinery FSI simulation
- Turbomachinery boundary conditions including the inlet BC, the outlet BC, the inflow perturbation BC for rotating stall simulation, and travelling wave BC to account for the effect of nodal diameter
- Detached eddy simulation capability for turbomachinery aeromechanics
- Non-synchronous vibration mechanism of aircraft engine axial fan/compressor

12.2 Validation Summary

The DDES is validated for a 3D flat plate turbulent boundary layer using a fine grid designed to generate Modeled-Stress Depletion of DES97. The DES shows 75% reduction of the eddy viscosity in the wall boundary layer, whereas the DDES preserves the eddy viscosity at the same level as the URANS.

Detached eddy simulations of NACA 0012 airfoil predict the drag and lift in excellent agreement with the experiment, whereas the URANS overpredicts the drag and lift by about 32% at AOA 45°. The comparison of the 5th and 3rd order WENO schemes indicates that the 5th order scheme predicts more accurately the lift and drag than the 3rd order scheme for the large angles of attack.

The fully coupled fluid/strcuture interaction with DDES is validated for the supersonic flutter of the 3D AGARD wing at a freestream Mach number of 1.141. The predicted

flutter boundary is only 0.9% lower than the experiment. It appears to be the first time that a numerical prediction of supersonic flutter boundary matches accurately with experiment.

The high fidelity turbomachinery methodology is validated using NASA Rotor 67. The predicted speedline and radial profiles at peak efficiency and near stall condition including total pressure ratio, total temperature ratio, absolute flow angle, and adiabatic efficiency agree very well with the experiment.

The NASA Stage 35 simulation, used to validate the mixing plane BC for multistage computation, indicates that the mixing plane method cuts off the shock propagation upstream and the wake propagation downstream. However, the accurate predictions of the measured total pressure ratio over entire mass flow conditions and the radial profiles demonstrate its efficiency and convenience for multistage compressor calculations.

The time shift phase lag (TSPL) BC and the Fourier series phase lag (FSPL) BC are validated using NASA Rotor 67 full annulus flutter simulation. The backward travelling wave for $N_D = 1$ is simulated using the fully coupled fluid/strcuture interaction with an advanced blade deforming mesh. The single blade passage flutter simulations with phase lag BCs indicate that the TSPL prediction agrees better with the full annulus FSI simulation.

The high performance of DES on fan/compressor rotating stall is demonstrated through the stall inception simulation of NASA Rotor 67 full annulus. The spikes observed for 6 to 7 blade passages at the rotor tip region propagate at 48% of the rotor speed counter to rotor rotation, which is the spike inception mechanism simulated by the DES. The spike stall cell extends to the full annulus roughly within 2 rotor revolutions.

The fully coupled stall flutter simulation of NASA Rotor 67 using 4 blade passages captures resonance of the flutter frequency to the blade's 1st mode as rotating stall develops.

12.3 Main Conclusions

A GE high speed axial compressor is used to investigate NSV mechanism of aircraft engine fan/compressor. The present high fidelity simulations reveal the mechanism behind aircraft engine axial compressor NSV that the tornado vortex formed near leading edge above roughly 78% rotor span cause the NSV of the compressor 1st stage rotor blades. The 1st stage rotor blades undergo the large aerodynamic excitation as the tornado vortex propagates at the speed of a non-engine order frequency to the next blade passage through the rotor leading edge ahead in the opposite to the rotor rotation.

The URANS simulation for the full compressor rig test model predicts the NSV frequency of 2513 Hz (2600 Hz by the experiment), which appears to be the first time that a numerical simulation predicts the measured NSV frequency accurately. The DDES underpredicts the NSV frequency by 14.7% because the NSV is captured only at higher mass flow rate by the DDES.

The NSV simulation using the fully coupled fluid/structure interaction shows that NSV of the 1st stage rotor blades is torsional vibration due to the travelling tornado vortex as the root cause of the NSV.

The NSV simulations with rigid blades and using the fully coupled fluid/structure interaction show the same dominant frequency, indicating that the primary cause of the NSV is due to rotating flow instabilities associated with tornado vortex of the 1st stage rotor blades not by an aeroelastic flutter-like instability.

Tip clearance study indicates that both tip clearance size and shape have a large impact on NSV characteristics. The straight rotor tip shows reduced NSV frequency as the rotor

tip clearance is increased, while the NSV frequency is reduced with significantly increased intensity for a convex type rotor tip.

The high fidelity FSI methodology developed for turbomachinery in this thesis demonstrates its excellency and robustness for aircraft engine fan/compressor NSV simulations.

12.4 Future Work

Singe Blade Passage Sliding BC

The present approach is shown to accurately capture non-synchronous blade vibration. By taking into account the efforts needed in the design process of new aircraft engine fan/compressor, it is highly desirable to resolve such a vexing and complex aeromechanical problems in more simple and easy way.

Use of single blade passage for multistage fan/compressor can remarkably reduce computational efforts. Since the accurate phase-lag boundary conditions are already developed through this research, which is necessary for the single passage as well, the key to success in this research eventually ends up with an idea to conserve the unsteadiness at non-matched rotor/stator interface. Note that rotor/stator interface is rarely matched to avoid resonance.

A direct store rotor/stator sliding BC is suggested. An imaginary layer is first constructed to meet geometry periodicity at each interface boundary, which is used to save primitive variables for exchange for one nodal diameter or a periodic cycle. Since no saved data are available for the first cycle, data exchange between the single blade passage rotor/stator interface is carried out using initially given (or assumed) data. After one cycle,

the imaginary periodic mesh layers are updated at every cycle and can be used for exchange. This direct store rotor/stator sliding approach can conserve flux and resolve the unsteadiness due to rotor/stator interaction in a phase-lagged manner.

Interpolation Circumferential Phase Lag BC

Most phase lag boundary conditions for turbomachinery use a matched grid at circumferential periodic boundaries. The fact is that in general it is very hard to achieve high quality blade-to-blade mesh if a matched grid at circumferential periodic boundaries is used. This can increase the numerical instability due to local high mesh skewness.

One way to cure this mesh problem is to use a non-matched grid at circumferential periodic boundaries and to use interpolation. The circumferential boundary mesh of a blade-to-blade section is distributed arbitrarily such that mesh quality of a blade-to-blade section can be significantly improved. This method can improve numerical stability, however like any interpolation this method can not satisfy the flux conservation at circumferential periodic boundaries.

DES of NSV Using NRBC

In chapter 11, the DDES underpredicts the NSV frequency because the DDES tends to predict the rotor stall earlier than the URANS and the NSV can be achieved only at higher mass flow rate, which generates a lower frequency. The possible reason for the DDES to predict the rotor stall early may be because DDES is more sensitive to wave reflection and a non-reflective boundary condition (NRBC) may be necessary.

Appendix A

Derivation of Structural Modal Equations

In this chapter, structural modal equations for turbomachinery blades are derived in detail. The undamped free vibration mode shapes are orthogonal with respect to the mass and stiffness matrices, however in general the undamped free vibration mode shapes are not orthogonal with respect to the damping matrix. Hence, equations of motion for damped systems cannot be uncoupled. However, we can choose damping matrix to be a linear combination of the mass and stiffness matrices, which is Rayleigh damping approach. Then, the mode shapes are orthogonal with respect to the damping matrix, and the equations of motion can be uncoupled using the orthogonality of eigenvectors.

$$\mathbf{C} = \alpha\mathbf{M} + \beta\mathbf{K} \tag{A.1}$$

The forced vibration system of equations (4.4) in a rating turbomachinery blade can be rewritten by using Rayleigh damping as

$$\begin{bmatrix} m & 0 & 0 \\ 0 & m & 0 \\ 0 & 0 & m \end{bmatrix} \begin{pmatrix} \ddot{x} \\ \ddot{y} \\ \ddot{z} \end{pmatrix} + \begin{bmatrix} \alpha m+\beta K_x & 0 & 0 \\ 0 & \alpha m+\beta K_y & -2m \\ 0 & 2m & \alpha m+\beta K_z \end{bmatrix} \begin{pmatrix} \dot{x} \\ \dot{y} \\ \dot{z} \end{pmatrix} + \begin{bmatrix} K_x & 0 & 0 \\ 0 & K_y & 0 \\ 0 & 0 & K_z \end{bmatrix} \begin{pmatrix} x \\ y \\ z \end{pmatrix} = \begin{pmatrix} F_x \\ F_y \\ F_z \end{pmatrix} \tag{A.2}$$

For the ith eigenvector, the normal mode equation for the ith mode is

$$\mathbf{K}\phi_i = \lambda_i \mathbf{M}\phi_i \tag{A.3}$$

Using modal superposition, the displacement vector can be written as a linear combination of the mode shape vectors

$$\begin{aligned} x_i(t) &= q_1(t)\phi_1(x_i) + q_2(t)\phi_2(x_i) + \cdots + q_n(t)\phi_n(x_n) \\ y_i(t) &= q_1(t)\phi_1(y_i) + q_2(t)\phi_2(y_i) + \cdots + q_n(t)\phi_n(y_n) \\ z_i(t) &= q_1(t)\phi_1(z_i) + q_2(t)\phi_2(z_i) + \cdots + q_n(t)\phi_n(z_n) \end{aligned} \tag{A.4}$$

The orthogonality of eigenvectors ensures the normal modes or the eigenvectors of the system to be orthogonal with respect to the mass and stiffness matrices.

$$\phi_j^T M \phi_i = 0; i \neq j \tag{A.5}$$

$$\phi_j^T K \phi_i = 0; i \neq j \tag{A.6}$$

$$\phi_i^T M \phi_i = M_{ii} \tag{A.7}$$

$$\phi_i^T K \phi_i = K_{ii} \tag{A.8}$$

where M_{ii} is the generalized mass and K_{ii} denotes the generalized stiffness. It can be proven by using notation ϕ_i for ith eigenvector.

$$K\phi_i = \lambda_i M\phi_i \tag{A.9}$$

$$\phi_j^T K\phi_i = \lambda_i \phi_j^T M\phi_i \tag{A.10}$$

$$\phi_i^T K\phi_j = \lambda_j \phi_i^T M\phi_j \tag{A.11}$$

Because K and M are symmetric matrices,

$$\begin{aligned} \phi_j^T K\phi_i &= \phi_i^T K\phi_j \\ \phi_j^T M\phi_i &= \phi_i^T M\phi_j \end{aligned} \tag{A.12}$$

By subtracting

$$\left(\lambda_i - \lambda_j\right) \phi_i^T M\phi_j = 0 \tag{A.13}$$

$$\left(\lambda_i - \lambda_j\right) \phi_i^T K\phi_j = 0 \tag{A.14}$$

If $\lambda_i \neq \lambda_j$, the foregoing equation require that

$$\phi_i^T M\phi_j = 0; i \neq j \tag{A.15}$$

$$\phi_i^T K \phi_j = 0; i \neq j \tag{A.16}$$

Eq. (A.15) and Eq. (A.16) define the orthogonal character of the normal modes. Finally, if $i = j, (\lambda_i - \lambda_j) = 0$ and Eq. (A.13) and Eq.(A.14) are satisfied for any finite value of the products given by Eq. (A.15) and Eq. (A.16). We therefore have

$$\phi_i^T M \phi_i = M_{ii} \tag{A.17}$$

$$\phi_i^T K \phi_i = K_{ii} \tag{A.18}$$

Let modal matrix P and its transpose matrix for the 1st 5-mode shapes as

$$P = \begin{bmatrix} \phi_1(x) & \phi_2(x) & \phi_3(x) & \phi_4(x) & \phi_5(x) \\ \phi_1(y) & \phi_2(y) & \phi_3(y) & \phi_4(y) & \phi_5(y) \\ \phi_1(z) & \phi_2(z) & \phi_3(z) & \phi_4(z) & \phi_5(z) \end{bmatrix} \tag{A.19}$$

$$P^T = \begin{bmatrix} \phi_1(x) & \phi_1(y) & \phi_1(z) \\ \phi_2(x) & \phi_2(y) & \phi_2(z) \\ \phi_3(x) & \phi_3(y) & \phi_3(z) \\ \phi_4(x) & \phi_4(y) & \phi_4(z) \\ \phi_5(x) & \phi_5(y) & \phi_5(z) \end{bmatrix} \tag{A.20}$$

Then, modal mass and stiffness matrix using orthogonality can be expressed as

$$\begin{aligned} P^T M P = & \begin{bmatrix} \phi_1(x) & \phi_1(y) & \phi_1(z) \\ \phi_2(x) & \phi_2(y) & \phi_2(z) \\ \phi_3(x) & \phi_3(y) & \phi_3(z) \\ \phi_4(x) & \phi_4(y) & \phi_4(z) \\ \phi_5(x) & \phi_5(y) & \phi_5(z) \end{bmatrix} \begin{bmatrix} m & 0 & 0 \\ 0 & m & 0 \\ 0 & 0 & m \end{bmatrix} \begin{bmatrix} \phi_1(x) & \phi_2(x) & \phi_3(x) & \phi_4(x) & \phi_5(x) \\ \phi_1(y) & \phi_2(y) & \phi_3(y) & \phi_4(y) & \phi_5(y) \\ \phi_1(z) & \phi_2(z) & \phi_3(z) & \phi_4(z) & \phi_5(z) \end{bmatrix} = \\ & \begin{bmatrix} M_{11} & 0 & 0 & 0 & 0 \\ 0 & M_{22} & 0 & 0 & 0 \\ 0 & 0 & M_{33} & 0 & 0 \\ 0 & 0 & 0 & M_{44} & 0 \\ 0 & 0 & 0 & 0 & M_{55} \end{bmatrix} = M_{ii} \end{aligned} \tag{A.21}$$

where

$$
\begin{aligned}
M_{11} &= \phi_1^T M \phi_1 = \phi_1(x) m \phi_1(x) + \phi_1(y) m \phi_1(y) + \phi_1(z) m \phi_1(z) = \textstyle\sum_j m \phi_1(x_j)^2 \\
M_{22} &= \phi_2^T M \phi_2 = \phi_2(x) m \phi_2(x) + \phi_2(y) m \phi_2(y) + \phi_2(z) m \phi_2(z) = \textstyle\sum_j m \phi_2(x_j)^2 \\
M_{33} &= \phi_3^T M \phi_3 = \phi_3(x) m \phi_3(x) + \phi_3(y) m \phi_3(y) + \phi_3(z) m \phi_3(z) = \textstyle\sum_j m \phi_3(x_j)^2 \\
M_{44} &= \phi_4^T M \phi_4 = \phi_4(x) m \phi_4(x) + \phi_4(y) m \phi_4(y) + \phi_4(z) m \phi_4(z) = \textstyle\sum_j m \phi_4(x_j)^2 \\
M_{55} &= \phi_5^T M \phi_5 = \phi_5(x) m \phi_5(x) + \phi_5(y) m \phi_5(y) + \phi_5(z) m \phi_5(z) = \textstyle\sum_j m \phi_5(x_j)^2
\end{aligned}
\tag{A.22}
$$

In the same fashion,

$$
\begin{aligned}
P^T K P = &\begin{bmatrix} \phi_1(x) & \phi_1(y) & \phi_1(z) \\ \phi_2(x) & \phi_2(y) & \phi_2(z) \\ \phi_3(x) & \phi_3(y) & \phi_3(z) \\ \phi_4(x) & \phi_4(y) & \phi_4(z) \\ \phi_5(x) & \phi_5(y) & \phi_5(z) \end{bmatrix} \begin{bmatrix} K_x & 0 & 0 \\ 0 & K_y & 0 \\ 0 & 0 & K_z \end{bmatrix} \begin{bmatrix} \phi_1(x) & \phi_2(x) & \phi_3(x) & \phi_4(x) & \phi_5(x) \\ \phi_1(y) & \phi_2(y) & \phi_3(y) & \phi_4(y) & \phi_5(y) \\ \phi_1(z) & \phi_2(z) & \phi_3(z) & \phi_4(z) & \phi_5(z) \end{bmatrix} = \\
&\begin{bmatrix} K_{11} & 0 & 0 & 0 & 0 \\ 0 & K_{22} & 0 & 0 & 0 \\ 0 & 0 & K_{33} & 0 & 0 \\ 0 & 0 & 0 & K_{44} & 0 \\ 0 & 0 & 0 & 0 & K_{55} \end{bmatrix} = K_{ii}
\end{aligned}
\tag{A.23}
$$

where

$$
\begin{aligned}
K_{11} &= \phi_1^T K \phi_1 = \phi_1(x) K_x \phi_1(x) + \phi_1(y) K_y \phi_1(y) + \phi_1(z) K_z \phi_1(z) = \textstyle\sum_j K_j \phi_1(x_j)^2 \\
K_{22} &= \phi_2^T K \phi_2 = \phi_2(x) K_x \phi_2(x) + \phi_2(y) K_y \phi_2(y) + \phi_2(z) K_z \phi_2(z) = \textstyle\sum_j K_j \phi_1(x_j)^2 \\
K_{33} &= \phi_3^T K \phi_3 = \phi_3(x) K_x \phi_3(x) + \phi_3(y) K_y \phi_3(y) + \phi_3(z) K_z \phi_3(z) = \textstyle\sum_j K_j \phi_1(x_j)^2 \\
K_{44} &= \phi_4^T K \phi_4 = \phi_4(x) K_x \phi_4(x) + \phi_4(y) K_y \phi_4(y) + \phi_4(z) K_z \phi_4(z) = \textstyle\sum_j K_j \phi_1(x_j)^2 \\
K_{55} &= \phi_5^T K \phi_5 = \phi_5(x) K_x \phi_5(x) + \phi_5(y) K_y \phi_5(y) + \phi_5(z) K_z \phi_5(z) = \textstyle\sum_j K_j \phi_1(x_j)^2
\end{aligned}
\tag{A.24}
$$

Rayleigh damping can be diagonalized in the linear fashion

$$
C = \alpha M + \beta K \tag{A.25}
$$

where, α and β are constants. The application of modal matrix P results in

$$\begin{aligned} P^T CP &= \alpha P^T MP + \beta P^T KP \\ &= \alpha M_{ii} + \beta K_{ii} \end{aligned} \tag{A.26}$$

Using modal superposition(or normal mode summation) Eq. (A.4), Eq. (A.2) can be expressed as follows

$$\begin{gathered} \begin{bmatrix} m & 0 & 0 \\ 0 & m & 0 \\ 0 & 0 & m \end{bmatrix} \begin{bmatrix} \phi_1(x) & \phi_2(x) & \phi_3(x) & \phi_4(x) & \phi_5(x) \\ \phi_1(y) & \phi_2(y) & \phi_3(y) & \phi_4(y) & \phi_5(y) \\ \phi_1(z) & \phi_2(z) & \phi_3(z) & \phi_4(z) & \phi_5(z) \end{bmatrix} \begin{pmatrix} \ddot{q}_1 \\ \ddot{q}_2 \\ \ddot{q}_3 \\ \ddot{q}_4 \\ \ddot{q}_5 \end{pmatrix} + \\ \begin{bmatrix} \alpha m+\beta K_x & 0 & 0 \\ 0 & \alpha m+\beta K_y & -2m \\ 0 & 2m & \alpha m+\beta K_z \end{bmatrix} \begin{bmatrix} \phi_1(x) & \phi_2(x) & \phi_3(x) & \phi_4(x) & \phi_5(x) \\ \phi_1(y) & \phi_2(y) & \phi_3(y) & \phi_4(y) & \phi_5(y) \\ \phi_1(z) & \phi_2(z) & \phi_3(z) & \phi_4(z) & \phi_5(z) \end{bmatrix} \begin{pmatrix} \dot{q}_1 \\ \dot{q}_2 \\ \dot{q}_3 \\ \dot{q}_4 \\ \dot{q}_5 \end{pmatrix} + \\ \begin{bmatrix} K_x & 0 & 0 \\ 0 & K_y & 0 \\ 0 & 0 & K_z \end{bmatrix} \begin{bmatrix} \phi_1(x) & \phi_2(x) & \phi_3(x) & \phi_4(x) & \phi_5(x) \\ \phi_1(y) & \phi_2(y) & \phi_3(y) & \phi_4(y) & \phi_5(y) \\ \phi_1(z) & \phi_2(z) & \phi_3(z) & \phi_4(z) & \phi_5(z) \end{bmatrix} \begin{pmatrix} q_1 \\ q_2 \\ q_3 \\ q_4 \\ q_5 \end{pmatrix} = \begin{pmatrix} F_x \\ F_y \\ F_z \end{pmatrix} \end{gathered} \tag{A.27}$$

Eq. (A.27) can be rearranged as follows by multiplying transpose modal matrix P^T

$$\begin{bmatrix} \phi_1(x) & \phi_1(y) & \phi_1(z) \\ \phi_2(x) & \phi_2(y) & \phi_2(z) \\ \phi_3(x) & \phi_3(y) & \phi_3(z) \\ \phi_4(x) & \phi_4(y) & \phi_4(z) \\ \phi_5(x) & \phi_5(y) & \phi_5(z) \end{bmatrix} \begin{bmatrix} m & 0 & 0 \\ 0 & m & 0 \\ 0 & 0 & m \end{bmatrix} \begin{bmatrix} \phi_1(x) & \phi_2(x) & \phi_3(x) & \phi_4(x) & \phi_5(x) \\ \phi_1(y) & \phi_2(y) & \phi_3(y) & \phi_4(y) & \phi_5(y) \\ \phi_1(z) & \phi_2(z) & \phi_3(z) & \phi_4(z) & \phi_5(z) \end{bmatrix} \begin{pmatrix} \ddot{q}_1 \\ \ddot{q}_2 \\ \ddot{q}_3 \\ \ddot{q}_4 \\ \ddot{q}_5 \end{pmatrix} +$$

$$\begin{bmatrix} \phi_1(x) & \phi_1(y) & \phi_1(z) \\ \phi_2(x) & \phi_2(y) & \phi_2(z) \\ \phi_3(x) & \phi_3(y) & \phi_3(z) \\ \phi_4(x) & \phi_4(y) & \phi_4(z) \\ \phi_5(x) & \phi_5(y) & \phi_5(z) \end{bmatrix} \begin{bmatrix} \alpha m+\beta K_1 & 0 & 0 \\ 0 & \alpha m+\beta K_2 & -2m \\ 0 & 2m & \alpha m+\beta K_3 \end{bmatrix} \begin{bmatrix} \phi_1(x) & \phi_2(x) & \phi_3(x) & \phi_4(x) & \phi_5(x) \\ \phi_1(y) & \phi_2(y) & \phi_3(y) & \phi_4(y) & \phi_5(y) \\ \phi_1(z) & \phi_2(z) & \phi_3(z) & \phi_4(z) & \phi_5(z) \end{bmatrix} \begin{pmatrix} \dot{q}_1 \\ \dot{q}_2 \\ \dot{q}_3 \\ \dot{q}_4 \\ \dot{q}_5 \end{pmatrix} +$$

$$\begin{bmatrix} \phi_1(x) & \phi_1(y) & \phi_1(z) \\ \phi_2(x) & \phi_2(y) & \phi_2(z) \\ \phi_3(x) & \phi_3(y) & \phi_3(z) \\ \phi_4(x) & \phi_4(y) & \phi_4(z) \\ \phi_5(x) & \phi_5(y) & \phi_5(z) \end{bmatrix} \begin{bmatrix} K_1 & 0 & 0 \\ 0 & K_2 & 0 \\ 0 & 0 & K_3 \end{bmatrix} \begin{bmatrix} \phi_1(x) & \phi_2(x) & \phi_3(x) & \phi_4(x) & \phi_5(x) \\ \phi_1(y) & \phi_2(y) & \phi_3(y) & \phi_4(y) & \phi_5(y) \\ \phi_1(z) & \phi_2(z) & \phi_3(z) & \phi_4(z) & \phi_5(z) \end{bmatrix} \begin{pmatrix} q_1 \\ q_2 \\ q_3 \\ q_4 \\ q_5 \end{pmatrix} = \begin{bmatrix} \phi_1(x) & \phi_1(y) & \phi_1(z) \\ \phi_2(x) & \phi_2(y) & \phi_2(z) \\ \phi_3(x) & \phi_3(y) & \phi_3(z) \\ \phi_4(x) & \phi_4(y) & \phi_4(z) \\ \phi_5(x) & \phi_5(y) & \phi_5(z) \end{bmatrix} \begin{pmatrix} F_x \\ F_y \\ F_z \end{pmatrix} \tag{A.28}$$

or

$$P^T MP\ddot{q}_i + P^T CP\dot{q}_i + P^T KPq_i = P^T F : i = 1,2,...5 \tag{A.29}$$

Applying orthogonality of mass and stiffness modal matrix

$$\begin{bmatrix} M_{11} & 0 & 0 & 0 & 0 \\ 0 & M_{22} & 0 & 0 & 0 \\ 0 & 0 & M_{33} & 0 & 0 \\ 0 & 0 & 0 & M_{44} & 0 \\ 0 & 0 & 0 & 0 & M_{55} \end{bmatrix} \begin{pmatrix} \ddot{q_1} \\ \ddot{q_2} \\ \ddot{q_3} \\ \ddot{q_4} \\ \ddot{q_5} \end{pmatrix} +$$

$$\begin{bmatrix} (\alpha M_{11}+\beta K_{11}) & 0 & 0 & 0 & 0 \\ 0 & (\alpha M_{22}+\beta K_{22}) & 0 & 0 & 0 \\ 0 & 0 & (\alpha M_{33}+\beta K_{33}) & 0 & 0 \\ 0 & 0 & 0 & (\alpha M_{44}+\beta K_{44}) & 0 \\ 0 & 0 & 0 & 0 & (\alpha M_{55}+\beta K_{55}) \end{bmatrix} \begin{pmatrix} \dot{q_1} \\ \dot{q_2} \\ \dot{q_3} \\ \dot{q_4} \\ \dot{q_5} \end{pmatrix} + \tag{A.30}$$

$$\begin{bmatrix} K_{11} & 0 & 0 & 0 & 0 \\ 0 & K_{22} & 0 & 0 & 0 \\ 0 & 0 & K_{33} & 0 & 0 \\ 0 & 0 & 0 & K_{44} & 0 \\ 0 & 0 & 0 & 0 & K_{55} \end{bmatrix} \begin{pmatrix} q_1 \\ q_2 \\ q_3 \\ q_4 \\ q_5 \end{pmatrix} = \begin{pmatrix} \phi_1(x)F_x+\phi_1(y)F_y+\phi_1(z)F_z \\ \phi_2(x)F_x+\phi_2(y)F_y+\phi_2(z)F_z \\ \phi_3(x)F_x+\phi_3(y)F_y+\phi_3(z)F_z \\ \phi_4(x)F_x+\phi_4(y)F_y+\phi_4(z)F_z \\ \phi_5(x)F_x+\phi_5(y)F_y+\phi_5(z)F_z \end{pmatrix}$$

or

$$M_{ii}\ddot{q}_i + (\alpha M_{ii} + \beta K_{ii})\dot{q}_i + K_{ii}q_i = P^T \boldsymbol{F} : i = 1,2,...5 \tag{A.31}$$

Dividing equation (A.30) by M_{ii} yields the following

$$\begin{pmatrix} \ddot{q_1} \\ \ddot{q_2} \\ \ddot{q_3} \\ \ddot{q_4} \\ \ddot{q_5} \end{pmatrix} + \begin{bmatrix} (\alpha+\beta\omega_1^2) & 0 & 0 & 0 & 0 \\ 0 & (\alpha+\beta\omega_2^2) & 0 & 0 & 0 \\ 0 & 0 & (\alpha+\beta\omega_3^2) & 0 & 0 \\ 0 & 0 & 0 & (\alpha+\beta\omega_4^2) & 0 \\ 0 & 0 & 0 & 0 & (\alpha+\beta\omega_5^2) \end{bmatrix} \begin{pmatrix} \dot{q_1} \\ \dot{q_2} \\ \dot{q_3} \\ \dot{q_4} \\ \dot{q_5} \end{pmatrix} + \begin{bmatrix} \omega_1^2 & 0 & 0 & 0 & 0 \\ 0 & \omega_2^2 & 0 & 0 & 0 \\ 0 & 0 & \omega_3^2 & 0 & 0 \\ 0 & 0 & 0 & \omega_4^2 & 0 \\ 0 & 0 & 0 & 0 & \omega_5^2 \end{bmatrix} \begin{pmatrix} q_1 \\ q_2 \\ q_3 \\ q_4 \\ q_5 \end{pmatrix}$$

$$= \begin{pmatrix} \frac{\phi_1(x)F_x+\phi_1(y)F_y+\phi_1(z)F_z}{M_{11}} \\ \frac{\phi_2(x)F_x+\phi_2(y)F_y+\phi_2(z)F_z}{M_{22}} \\ \frac{\phi_3(x)F_x+\phi_3(y)F_y+\phi_3(z)F_z}{M_{33}} \\ \frac{\phi_4(x)F_x+\phi_4(y)F_y+\phi_4(z)F_z}{M_{44}} \\ \frac{\phi_5(x)F_x+\phi_5(y)F_y+\phi_5(z)F_z}{M_{55}} \end{pmatrix} \tag{A.32}$$

or

$$\ddot{q}_i + (\alpha + \beta\omega_i^2)\dot{q}_i + \omega_i^2 q_i = \frac{P^T \boldsymbol{F}}{M_{ii}} : i = 1,2,...5 \tag{A.33}$$

The modal damping can be defined by the equation

$$2\varsigma_i\omega_i = \alpha + \beta\omega_i^2 \tag{A.34}$$

and using the definition considering the whole N-mass block

$$P^T\boldsymbol{F} = \sum_j (\phi_i(x)F_x + \phi_i(y)F_y + \phi_i(z)F_z) \tag{A.35}$$

$$M_{ii} = \sum_j m_j\phi_i^2(x_j) \tag{A.36}$$

We then obtain for the ith modal equation

$$\ddot{q}_i + 2\varsigma_i\omega_i\dot{q}_i + \omega_i^2 q_i = \frac{\sum_j (\phi_i(x)F_x + \phi_i(y)F_y + \phi_i(z)F_z)}{\sum_j m_j\phi_i^2(x_j)} = \frac{P^T\boldsymbol{F}}{M_{ii}} \tag{A.37}$$

where $i(=1,2,3,4,5)$ and $j(=1,2,....,N)$ represent the number of mode shapes considered and the whole number of mass block respectively. Note that above equation (A.37) can be further simplified by use of mass normalized mode shape, $\tilde{\phi}$ that results in $M_{ii} = 1$.

Appendix B

Cell Volume Calculation

The volume (V) of a hexahedron cell with six faces as seen in Fig. B.1 can be calculated as

$$V = \frac{1}{3}(\vec{S}_{4321} + \vec{S}_{6512} + \vec{S}_{8415}) \bullet \vec{d}_{71} \tag{B.1}$$

where $\vec{d}_{17}$ is the vector between point 1 and 7, and the area vector $\vec{S}$ are defined as follows.

$$\vec{d}_{71} = (x_7 - x_1)\mathbf{i} + (y_7 - y_1)\mathbf{j} + (z_7 - z_1)\mathbf{k} \tag{B.2}$$

$$\vec{S}_{4321} = \frac{1}{2}(\vec{d}_{42} \times \vec{d}_{31}) \tag{B.3}$$

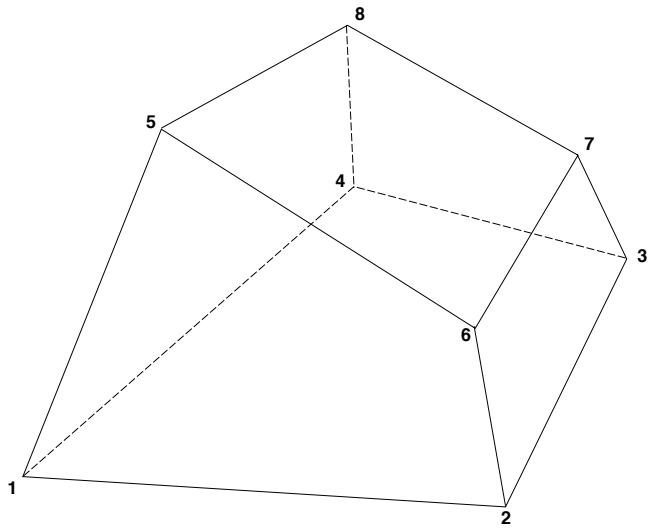

Figure B.1: A hexahedron cell with six faces

The area vector $\vec{S}_{4321}$ is calculated as

$$\vec{S}_{4321} = \frac{1}{2}(\vec{d}_{42} \times \vec{d}_{31}) = \frac{1}{2}\begin{vmatrix} \mathbf{i} & \mathbf{j} & \mathbf{k} \\ (x_2 - x_4) & (y_2 - y_4) & (z_2 - z_4) \\ (x_1 - x_3) & (y_1 - y_3) & (z_1 - z_3) \end{vmatrix} \tag{B.4}$$

References

[1] M. Baumgartner, F. Kameier, and J. Hourmouziadis, "Non-Engine Order Blade Vibration in a High Pressure Compressor," ISABE, Twelfth International Symposium on Airbreathing Engines, Melbourne, Australia, 10-15, 1995.

[2] J. Marz, C. Hah, and W. Neise, "An Experimental and Numerical Investigation Into the Mechanisms of Rotating Instability," *Journal of Turbomachinery*, Vol. 124, 2002, pp. 367–375.

[3] J. Thomassin, H. Vo, and N. Mureithi, "Blade Tip Clearance Flow and Compressor Nonsynchronous Vibrations: The Jet Core Feedback Theory as the Coupling Mechanism," *Journal of Turbomachinery*, Vol. 131, 2009, pp. 11013–1–11013–9.

[4] E.C. Yates Jr., "AGARD Standard Aeroelastic Configurations for Dynamic Response. Candidate Configuration I.-Wing 445.6," NASA-TM-1000492, 1987.

[5] L. Reid, and R.D. Moore, "Performance of Single-Stage Axial-Flow Transonic Compressor With Rotor and Stator Aspect Ratios of 1.19 and 1.26, Respectively, and With Design Pressure Ratio of 1.82," NASA TP-1338, 1978.

[6] A.J. Sanders, K.K. Hassan, and D.C. Rabe, "Experimental and Numerical Study of Stall Flutter in a Transonic Low-Aspect Ratio Fan Blisk," *Journal of Turbomachinery*, Vol. 126, 2004, pp. 166–174.

[7] H.-S. Im, X.-Y. Chen, and G.-C. Zha, " Detached Eddy Simulation of Transonic Rotor Stall Flutter Using a Fully Coupled Fluid-Structure Interaction," ASME GT2011-45437, ASME Turbo Expo 2011, Vancouver, Canada, June 2011, 2011.

[8] R. Srivastava, and T.G. Keith Jr., "Influence of Shock Wave on Turbomachinery Blade Row Flutter," *Journal of Propulsion and Power*, Vol. 21, 2011, pp. 167–174.

[9] R. Srivastava, J. Panovsky, R. Kielb, L. Virgin, and K. Ekici, "Nonlinear Flutter in Fan Stator Vanes With Time Dependent Fixity," *Journal of Turbomachinery*, Vol. 134, 2012, pp. 021009–1–021009–8.

[10] M. Vahdati, A.I. Sayma, C. Bread, and M. Imregun, "Computational Study of Intake Duct Effects on Fan Flutter Stability," *AIAA Journal*, Vol. 40, 2002, pp. 408–418.

[11] M. Vahdati, G. Simpson, and M. Imregun, "Mechanisms for Wide-Chord Fan Blade Flutter," *Journal of Turbomachinery*, Vol. 133, 2011, pp. 041029–1–041029–7.

[12] J.W. Chew, R.J. Hamby, J.G. Marshall, and M. Vahdati, " Part Speed Flutter of Transonic Fan," RTO AVT Symposium on Design Principles and Methods for Aircraft Gas Turbine Engines, Toulouse, France, May 1998, 1998.

[13] A.V. Srinivasan, "Flutter and Resonant Vibration Characteristics of Engine Blades," ASME 97-GT-533, October 1997.

[14] R. Kielb, J. Thomas, P. barter, and K. Hall, "Blade Excitation by Aerodynamic Instabilites - A Compressor Blade Study," ASME Paper No. GT-2003-38634, 2003.

[15] R. Mailach, I. Lehmann, and K. Vogeler, "Rotating Instabilites in an Axial Compressor Originating From the Fluctuating Blade Tip Vortex," ASME Paper No. GT-2003-38634, 2003.

[16] J. Thomassin, H. Vo, and N. Mureithi, "The Tip Clearance Flow Resonance Behind Axial Compressor Nonsynchronous Vibration," *Journal of Turbomachinery*, Vol. 133, 2011, doi:10.1115/1.4001368, pp. 041030–1–041030–10.

[17] H.S. Im, and G.C. Zha, "Simulation of Non-Synchronous Blade Vibration of an Axial Compressor Using a Fully Coupled Fluid/Strcuture Interaction," ASME GT2012-68150, 2012.

[18] H.S. Im, and G.C. Zha, "Effects of Rotor Tip Clearance on Non-Synchronous Blade Vibration for an Axial Compressor," ASME GT2012-68148, 2012.

[19] R. Kamakoti, and W. Shyy, "Fluid-Structure Interaction for Aeroelastic Applications," *Progress in Aerospace Sciences*, Vol. 40, 2004, pp. 535–558.

[20] H. Doi, and J.J. Alonso, "Fluid/Structure Coupled Aeroelastic Computations for Transonic Flows in Turbomachinery," GT2002-30313,Proceedings of ASME Turbo Expo 2002, 2002.

[21] V. Gnesin, and R. Rzadkowski, "A Coupled Fluid-Structure Analysis for 3-D Inviscid Flutter of IV Standard Configuration," *Journal of Sound and Vibration*, Vol. 251, 2002, pp. 315–327.

[22] V. Carstens, R. Kemme, and S. Schmitt, "Coupled Simulation of Flow-Structrue Interaction in Turbomachinery," *Aerospace Science and Technology*, Vol. 7, June 2003, pp. 298–306.

[23] A.I. Sayma, M.V. Vahdati, and M. Imregun, "Turbine Forced Response Prediction Using an Integrated Non-Linear Analysis," *Proceedings of the Institution of Mechanical Engineers, Part K: Journal of Multi-body Dynamics*, Vol. 214, 2000, pp. 45–60.

[24] X.Y. Chen, G.-C. Zha, M.-T. Yang, "Numerical Simulation of 3-D Wing Flutter with Fully Coupled Fluid-Structural Interaction," *Journal of Computers & Fluids*, Vol. 36, 2007, doi:10.1016/j.compfluid.2006.08.005, pp. 856–867.

[25] B.Y. Wang, and G.C. Zha, "Detached Eddy Simulation of Transonic Limit Cycle Oscillations Using High Order Schemes," *To appear in Journal of Computer & Fluids*, 2011.

[26] B.Y. Wang, and G.C. Zha, "Numerical simulation of transonic limit cycle oscillations using high-order low-diffusion schemes," *Journal of Fluids and Structures*, Vol. doi:10.1016/j.jfluidstructs.2010.02.003, 2010.

[27] H. Im, X. Chen, and G. Zha, "Prediction of a Supersonic Flutter Boundary Using a High Fidelity Delayed Detached Eddy Simulation," 50th AIAA Aerospace Sciences Meeting, Nashville, Tennessee, Jan. 2012, 2012.

[28] H.S. Im, X.Y. Chen, and G.C. Zha, "Simulation of 3D Multistage Axial Compressor Using a Fully Conservative Sliding Boundary Condition," ASME IMECE2011-62049, International Mechanical Engineering Congress & Exposition, Denver, November 2011, 2011.

[29] H.S. Im, X.Y. Chen, and G.C. Zha, "Detached Eddy Simulation of Stall Inception for a Full Annulus Transonic Rotor," Journal of Propulsion and Power, to appear.

[30] Horlock, J., *Axial Flow Compressors - Fluid Mechanics and Thermodynamics*, Krieger Pub Co, 1982.

[31] I.J. Day, "Stall Inception in Axial Flow Compressors," *AMSE J. of Turbomach.*, Vol. 115, 1993, pp. 1–9, doi:10.1115/1.2929209.

[32] C.S. Tan, I. Day, S. Morris, and A. Wadia, "Spike-Type Compressor Stall Inception, Detection, and Control," ANRV400-FL42-13, 2009, doi: 10.1146/annurev-fluid-121108-145603.

[33] J.I. Erods, E. Alzner, and W. McNally, "Numerical Solution of Periodic Transonic Flow Through a Fan Stage," *AIAA Journal*, Vol. 15, Nov. 2004, pp. 1559–68.

[34] L. He, and J.D. Denton, "Three-Dimensional Time Marching Inviscid and Viscous Solutions for Unsteady Flows Around Vibrating Blades," *Journal of Turbomachinery*, Vol. 116, 1994, pp. 469–476.

[35] H.S. Im, and G.C. Zha, "Delayed Detached Eddy Simulation of a Stalled Flows Over NACA0012 Airfoil Using Higher Order Schemes," AIAA Paper 2011-1297, Jan. 2011.

[36] P.R. Spalart, W.H. Jou, M. Strelets, and S.R. Allmaras, "Comments on the Feasibility of LES for Wings, and on a Hybrid RANS/LES Approach," Advances in DNS/LES, 1st AFOSR Int. Conf. on DNS/LES, Greyden Press, Columbus, H., Aug. 4-8, 1997.

[37] P.R. Spalart, S. Deck, M. Shur, and K.D. Squires, "A New Version of Detached Eddy Simulation, Resistant to Ambiguous Grid Densities," *Theoritical and Computational Fluid Dynamics*, Vol. 20, 2006, pp. 181–195.

[38] F.R. Menter, and M. Kuntz, "Adaptation of Eddy-Viscosity Turbulence Models to Unsteady Separated Flow Behind Vehilces, *The Aerodynamics of Heavy Vehicles: Trucks, Buses and Trains, Edited by McCallen, R. Browand, F. and Ross, J.* ," *Springer, Berlin Heidelberg New York, 2004*, 2-6 Dec. 2002.

[39] Vo, H.D., "Role of Tip Clearance Flow in Rotating Instabilities and Nonsynchronous Vibrations," *Journal of Propulsion and Power*, Vol. 26, 2010, pp. 556–561, doi: 10.2514/1.26709.

[40] A. Sanders, "Nonsynchronous Vibration(NSV) due to a Flow-Induced Aerodynamic Instability in a Composite Fan Stator," *Journal of Turbomachinery*, Vol. 127, 2005, pp. 412–421.

[41] A. Carter, and D. Kilpatrick, "Self-Excited Vibration of Axial-Flow Compressor Blades," *Proceedings of the Institution of Mechanical Engineers 1847-1996*, Vol. 171, 1957, DOI:10.1243/PIME_PROC_1957_171_030_02, pp. 245–281.

[42] F.O. Carta, and A.O. Hilaire, "Effect of Interblade Phase Angle and Incidence Angle on Cascade Pitching Stability," *Journal of Engineering for Power*, Vol. 102, 1980, pp. 391–396.

[43] D.G. Halliwell, "Fan Supersonic Flutter: Prediction and Test Analysis," Aeronautical Research Councel R.&M. No. 3789, 1977.

[44] F. Sisto, S. Thangam, and A. Abdel-Rahim, "Computational Prediction of Stall Flutter in Cascade Airfoils," *AIAA Journal*, Vol. 29, 1991, pp. 1161–1167.

[45] B. Gruber, and V. Carstens, "The impact of Viscous Effects on the Aerodynamic Damping of Vibrating Transonic Compressor Blades - A Numerical Study," *Journal of Turbomachinery*, Vol. 123, 2001, pp. 409–417.

[46] X.Y. Chen, and G.-C. Zha, "Fully Coupled Fluid-Structural Interactions Using an Efficient High Solution Upwind Scheme," *Journal of Fluid and Structure*, Vol. 20, 2005, pp. 1105–1125.

[47] E. M. Lee-Rausch, and J.T. Batina, "Calculation of AGARD Wing 445.6 Flutter Using Navier-Stokes Aerodynamics," AIAA Paper 1993-3476, August 9-11, 1993.

[48] J. Xiao, and C. Gu, "Wing Flutter Simulations Using an Aeroelastic Solver Based on the Predictor-Corrector Scheme," *Proceedings of the Institution of Mechanical Engineers, Part G: Journal of Aerospace Engineering*, Vol. 224, 2009, doi:10.1243/09544100JAERO756, pp. 1193–1210.

[49] G. Yang, S. Obayashi, and J. Nakamichi, "Aileron Flutter Calculation for a Supersonic Fuselage-Wing Configuration," ICAS 2002 Congress, 2002.

[50] F. Liu, J. Cai, and Y. Zhu, "Calculation of Wing Flutter by a Coupled CFD-CSD method," AIAA-2000-0907, 2000.

[51] L. Cavagna, , G. Quaranta, and P. Mantegazzaa, "Application of Navier-Stokes Simulations for Aeroelastic Stability Assessment in Transonic Regime ," *Journal of Computer and Fluids*, Vol. 85, 2007, doi:10.1016/j.compstruc.2007.01.005, pp. 818–832.

[52] P. Chen, and D. Liu, "A Harmonic Gradient Method for Unsteady Supersonic Flow Calculations," *Journal of Aircraft*, Vol. 22, 1985, doi: 10.2514/3.45134, pp. 371–379.

[53] J. Alonso, and A. Jameson, "Fully-Implicit Time Maraching Aeroelastic Solutions," AIAA Paper 94-0056, 1994.

[54] Z. Yang, and D.J. Mavriplis, "Higher-order Time Integration Schemes for Aeroelastic Applications on Unstructured Meshes," 44th AIAA Aerospace Science Meeting, AIAA, Washington, DC, January 2006, 2006.

[55] H. D. Li, and L. He, "Blade Aerodynamic Damping Varaition With Rotor-Stator Gap: A Computational Study Using Single-Passage Approach," *Journal of Turbomachinery*, Vol. 127, Jul. 2005, pp. 573–578.

[56] R. Srivastava, M.A. bakhle, T.G. Keith Jr, and G.L. Stefko, "Aeroelastic Analysis of Turbomachinery: Part I-Phase Lagged Boundary Condition Methods," *International Journal of Numerical Methods for Heat & Fluid Flow*, Vol. 14, Nov. 2004, pp. 366–381.

[57] S. Ji, and F. Liu, "Flutter Computation of Turbomachinery Cascades Using a Parallel Unsteady Navier-Stokes Code," *AIAA Journal*, Vol. 37, 1999, pp. 320–327.

[58] J.D. Denton, "The Calculation of 3-D Viscous Flow Through Multistage Turbomachines," *Journal of Turbomachinery*, Vol. 114, 1992, pp. 18–26.

[59] W.N. Dawes, "Toward Improved Throughflow Capability: the Use of 3-D Viscous Flow Solvers in a Multistage Environment," *Journal of Turbomachinery*, Vol. 114, 1992, pp. 8–17.

[60] U.K. Singh, "A Computation and Comparison With Measurements of Transonic Flow in an Axial Compressor Stage With Shock and Boundary-Layer Interaction," *Journal of Engineering Gas Turbine Power*, Vol. 104, 1982, pp. 510–515.

[61] J.W. Barter, P.H. Vitt, and J.P. Chen, "Interaction Effects in a Transonic Turbine Stage," ASME paper 2000-GT-0376, Proceedings of ASME Turboexpo 2000, May 8-11 2000, Munich Germany, 2000.

[62] G.A. Gerolymos and C. Hanisch, "Multistage Three-Dimensional Navier-Stokes Computation of Off-Design Operation of a Four-Stage Turbine," Proc Instn Mech Engrs Vol 213 Part A, Third European Conference on Turbomachinery, March 1999, London UK.

[63] G. Fritch and M.B. Giles, "An Asymptotic Analysis of Mixing Loss," ASME paper 93-GT-345, 1993.

[64] M. Rai, "Three-dimensional Navier-Stokes Simulations of Turbine Rotor-Stator Interaction. I - Methodology ," *AIAA Journal of Propulsion and Power*, Vol. 5, 1989, pp. 305–311.

[65] M.B. Giles, "Stator/Rotor Interaction in a Transonic Turbine," *AIAA Journal of Propulsion and Power*, Vol. 6, 1990, pp. 621–627.

[66] L. He, "Three-Dimensional Unsteady Navier-Stokes Analysis of Stator-Rotor Interaction in Axial Flow Turbines," *Proceedings of the Institution of mechanical Engineers, Part A: Journal of Power and Energy*, Vol. 214, 2000, pp. 13–22.

[67] A. Ruprecht, C. Bauer, C. Gentner, and G. Lein, "Parallel Computation of Stator-Rotor Interaction in an Axial Turbine," ASME PVP Conference, CFD Symposium, Boston, 1999.

[68] J.P. Chen, and J.W. Barter, " Comparison of Time-Accurate Calculations for the Unsteady Interaction in Turbomachinery Stage," AIAA Paper 98-3292, 1998.

[69] T.R. Camp, and I.J. Day, "A Study of Spike and Modal Stall Phenomena in a Low Speed Axial Compressor," *AMSE J. of Turbomach.*, Vol. 120, 1998, pp. 393–401, doi:10.1115/1.2841730.

[70] N.M. McDougall, N.A. Cumpsty, and T.P. Hynes, "Stall Inception in Axial Compressors," *AMSE J. of Turbomach.*, Vol. 112, 1990, pp. 116–123, doi:10.1115/1.2927406.

[71] I.J. Day, T. Breuer, J. Escuret, M. Cherrett, and A. Wilson, "Stall Inception and the Prospects for Active Control in Four High-Speed Compressors," *AMSE J. of Turbomach.*, Vol. 121, 1999, pp. 18–27, doi:10.1115/1.2841229.

[72] P.D. Silkowski, "Measurements of Rotor Stalling in a Matched and Mismatched Multistage Compressor," GTL Report No. 221, Gas Turbine Laboratory, Mass. InsT. Technol., Cambridge, 1995.

[73] M. Inoue, M. Kuroumaru, S. Yoshida, and M. Furukawa, "Short and Long Length-Scale Disturbances Leading to Rotating Stall in an Axial Compressor Stage With Different Stator/Rotor Gaps ," *AMSE J. of Turbomach.*, Vol. 124, 2002, doi:10.1115/1.1458022, pp. 376–385.

[74] N. Reuss, and C. Mundt, "Experimental Investigations of Pressure Distortions on the High-Pressure Compressor Operating Behavior," *Journal of Propulsion and Power*, Vol. 25, 2009, pp. 653–667, doi: 10.2514/1.37412.

[75] C. Hah, J. Bergner, and H. Schifer, "Short Length Scale Rotating Stall Inception in a Transonic Axial Compressors : Criteria and Mechanisms," GT2006-90045, ASME Turbo Expo, 2006, doi:10.1115/GT2006-90045.

[76] M. Zake, L. Sankar, and S. Menon, "Hybrid Reynolds-Averaged Navier-Stokes/Kinetic-Eddy Simulation of Stall Inception in Axial Compressors," *Journal of Propulsion and Power*, Vol. 26, 2010, pp. 1276–1282, doi: 10.2514/1.50195.

[77] L. He, "Computational Study of Rotating-Stall Inception in Axial Compressors," *Journal of Propulsion and Power*, Vol. 13, 1997, pp. 31–38, doi: 10.2514/2.5147.

[78] R. Davis, and J. Yao, "Computational Approach for Predicting Stall Inception in Multistage Axial Compressor," *Journal of Propulsion and Power*, Vol. 23, 2007, doi: 10.2514/1.18442, pp. 257–265, doi: 10.2514/1.50195.

[79] D.A. Hoying, C.S. Tan, H.D. Vo, and E.M. Greitzer, "Role of Blade Passage Flow Structures in Axial Compressor Rotating Stall Inception," *AMSE J. of Turbomach.*, Vol. 121, 1999, pp. 735–742, doi:10.1115/1.2836727.

[80] H.D. Vo, C.S. Tan, and E.M. Greitzer, "Criteria for Spike Initiated Rotating Stall," *AMSE J. of Turbomach.*, Vol. 130, 2008, pp. 1–8, doi:10.1115/1.2750674.

[81] H. Khaleghi, M. Boroomand, A.M. Tousi, and J.A. Teixeira, "Stall Inception in a Transonic Axial Fan," *Journal of Power and Energy*, Vol. 222, 2008, pp. 199–208, doi:10.1243/09576509JPE407.

[82] H. Khaleghi, J. Teixeira, A. Tousi, and M. Boroomand, "Parametric Study of Injection Angle Effects on Stability Enhancement of Transonic Axial Compressors," *Journal of Propulsion and Power*, Vol. 24, 2009, pp. 1100–1107, doi: 10.2514/1.34817.

[83] J. Chen, B. Johnson, M. Hathaway, and R. Webster, "Flow Characteristics of Tip Injection on Compressor Rotating Spike via Time-Accurate Simulation," *Journal of Propulsion and Power*, Vol. 25, 2009, pp. 678–687, doi: 10.2514/1.41428.

[84] J. Chen, M. Hathaway, and G. Herrick, "Prestall Behavior of a Transonic Axial Compressor Stage via Time-Accurate Numerical Simulation," *AMSE J. of Turbomach.*, Vol. 130, 2008, pp. 1–12, doi:10.1115/1.2812968.

[85] F. Lin, J. Zhang, J. Chen, and C. Nie, "Flow Structure of Short-Length-Scale Disturbance in an Axial-Flow Compressor," *Journal of Propulsion and Power*, Vol. 24, 2008, pp. 1301–1308, doi: 10.2514/1.36525.

[86] S.A. Orszag, "Analytical Theories of Turbulence," *Journal of Fluid Mechanics*, Vol. 41, 1970, pp. 363–386.

[87] I. Mary, "Large Eddy Simulation of Vortex Breakdown Behind a Delta Wing," *Int. J. of Heat and Fluid Flow*, Vol. 24, 2003, pp. 596–605.

[88] S. Eisenbach, and R. Friedrich, "Large Eddy Simulation of Flow Separation on an Airfoil at a High Angle of Attack and $Re = 10^5$ Using Cartesian Grids," *Theor. Comput. Fluid Dyn.*, Vol. 22, 2008, pp. 213–225.

[89] S. Moreau, J. Christopher, M. Roger, "LES of the Trailingedge Flow and Noise of a NACA0012 Airfoil Near Stall," Proceedings of the Summer Program 2008, Center for Turbulence Research, 2008.

[90] R.B. Melville,and S.A. Morton, "Fully Implicit Aeroelasticity on Overset Grid Systems," AIAA Paper-98-0521, 1998.

[91] G. Martinat, M. Braza, Y. Hoarau, G. Harran, "Turbulence Modelling of the Flow Past a Pitching NACA0012 Airfoil at $10^5$and 10^7 Reynolds Numbers," *J. of Fluids and Structures*, Vol. 24, 2008, pp. 1294–1303.

[92] Travin, A.K., Shur, M.L., Spalart, P.R., and Strelets, M.K., "Improvement of Delayed Detached Eddy Simulation for LES With Wall Modelling," European Conference on Computational Fluid Dynamics, ECCOMAS CFD 2006, 2006.

[93] M. Shur, P.R. Spalart, M. Strelets, and A. Travin, "Detached Eddy Simulation of an Airfoil at High Angle of Attack", 4th Int. Symp. Eng. Turb. Modeling and Measurements, Corsica," May 24-26, 1999.

[94] P.R. Spalart, "Detached Eddy Simulation," *Annual Review Fluid Mechanics*, Vol. 41, 2009, pp. 181–202, doi: 10.1146/annurev.fluid.010908.165130.

[95] X.D. Liu, S. Osher, T. Chan, "Weighted Essentially Non-Oscillatory Schemes," *J.Comput.Phys.*, Vol. 115, 1994, pp. 200–212.

[96] G.S. Jiang, C.W. Shu, "Efficient Implementation of Weighted ENO Schemes," *J.Comput.Phys.*, Vol. 126, 1996, pp. 202–228.

[97] C.W. Shu, "Essentially Non-Oscillatory and Weighted Essentially Schemesfor Hyperbolic Conservation Laws," NASA/CR-97-206253, 1997.

[98] B. Van Leer, "Towards the Ultimate Convservative Difference Scheme, V: A Second-Order Sequel to Godunov's Method," *J. of Computational Physics*, Vol. 32, 1979, pp. 101–136.

[99] S.H. Zhang, C.W. Shu, "A New Smoothness Indicator for the WENO Schemes and its Effect on the Convergence to Steady State Solutions," *Journal of Scientific Computing*, Vol. 31, 2007, pp. 273–305.

[100] A.K. Henrick, T.D. Aslam, J.M. Powers, "Mapped Weighted Essentially Non-Oscillatory Schemes:Achiving Optimal Order Near Critical Points," *J.Comput.Phys.*, Vol. 208, 2005, pp. 206–227.

[101] Y.Q. Shen, and G.C. Zha, "Improvement of the WENO Scheme Smoothness Estimator," *International Journal for Numerical Methods in Fluids*, Vol. 64,, 2009, pp. 653–675, DOI:10.1002/fld.2186.

[102] Y.Q. Shen, G.C. Zha, and B.Y. Wang, "Improvement of Stability and Accuracy of Implicit WENO Scheme," *AIAA Journal*, Vol. 47, 2009, pp. 331–334, DOI:10.2514/1.37697.

[103] Y.Q. Shen, G.C. Zha, and X. Chen, "High Order Conservative Differencing for Viscous Terms and the Application to Vortex-Induced Vibration Flows," *Journal of Computational Physics*, Vol. 228(2), 2009, pp. 8283–8300, doi:10.1016/j.jcp.2009.08.004.

[104] P. Roe, "Approximate Riemann Solvers, Parameter Vectors, and Difference Schemes," *Journal of Computational Physics*, Vol. 43, 1981, pp. 357–372, doi:10.1016/0021–9991(81)90128–5.

[105] B. Van Leer, J.L. Thomas, P.L. Roe, and R.W. Newsome, "A Comparison of Numerical Flux Formulas for the Euler and Navier-Stokes Equations," AIAA paper 87-1104, 1987.

[106] M.S. Liou, and C.J. Steffen, "A New Flux Splitting Scheme," *Journal of Computational Physics*, Vol. 107, 1993, pp. 1–23.

[107] A. Jameson, "Analysis and Design of Numerical Schemes for Gas Dynamics I: Artificial Diffusion, Upwind Biasing, Limiters and Their Effect on Accuracy and Multigrid Convergence in Transonic and Hypersonic Flow," *Journal of Computational Fluid Dynamics*, Vol. 4, 1995, pp. 171–218.

[108] A. Jameson, "Analysis and Design of Numerical Schemes for Gas Dynamics II: Artificial Diffusion and Discrete Shock Structure," *Journal of Computational Fluid Dynamics*, Vol. 5, 1995, pp. 1–38.

[109] G.C. Zha, Y.Q. Shen, and B.Y. Wang, "An Improved Low Diffusion E-CUSP Upwind Scheme ," *Journal of Computer and Fluids*, Vol. 48, 2011, doi:10.1016/j.compfluid.2011.03.012, pp. 214–220.

[110] J.R. Edwards, "A Low-Diffusion Flux-Splitting Scheme for Navier-Stokes Calculations," AIAA Paper 95-1703-CP, June, 1995.

[111] J.R. Edwards, "A Low-Diffusion Flux-Splitting Scheme for Navier-Stokes Calculations," *Computer & Fluids*, Vol. 6, 1997, pp. 635–659, doi:10.1016/S0045–7930(97)00014–5.

[112] I.H. Shames, "Engineering Mechanics : Dynamics," Prentice-Hall, Englewood Cliffs, New Jersey, 1980.

[113] G. Erlebacher, M. Y. Hussaini, C. G. Speziale, and T. A. Zang, "Toward the Large Eddy Simulation of Compressible Turbulent Flows," *Journal of Fluid Mechanics*, Vol. 238, 1992, DOI:10.1017/S0022112092001678, pp. 155–185.

[114] P.R. Spalart, and S.R. Allmaras, "A One-equation Turbulence Model for Aerodynamic Flows," AIAA-92-0439, 1992.

[115] C. Lawrence, R. A. Aiello, and M. A. Earnst, "A Nastran Primer for the Analysis of Rotating flexible Blades," NASA Lewis Research center, E-3528-1.

[116] J. Szwedowicz, R. Visser, W. Sextro, and P. A. Masserey, "On Nonlinear Forced Vibration of Shrouded Turbine Blades," *J. Turbomach.*, Vol. 130, 2008, pp. 011002–011010, doi:10.1115/1.2218889.

[117] Y.Q. Shen, B.Y. Wang, and G.C. Zha, "Implicit WENO Scheme and High Order Viscous Formulas for Compressible Flows ," AIAA Paper 2007-4431, 2007.

[118] R.V. Goggett, R.V. Rainey, and H.G. Morgan, "An experimental Investigsation of Aerodynamic Effects of Airfoil Thickness on Transonic Flutter Characteristics," NASA TMX-79, 1959.

[119] M.A. Bakhle, T.S.R. Reddy, and T.G. Keith Jr., "Time Domain Flutter Analysis of Cascades Using a Full-Potnetial Solver," *AIAA Journal*, Vol. 30, 1992, pp. 163–169.

[120] Y.Q. Shen, and G.C. Zha, "Large Eddy Simulation Using a New Set of Sixth Order Schemes for Compressible Viscous Terms," *Journal of Computational Physics*, Vol. 229, 2010, pp. 8296–8312, doi:10.1016/j.jcp.2010.07.017.

[121] G.-C. Zha, and E. Bilgen, "Numerical Study of Three-Dimensional Transonic Flows Using Unfactored Upwind-Relaxation Sweeping Algorithm," *Journal of Computational Physics*, Vol. 125, May 1996, pp. 425–433.

[122] Y.Q. Shen, B. Wang, and G.C. Zha, "Comparison Study of Implicit Gauss-Seidel Line Iteration Method for Transonic Flows," AIAA Paper 2007-4332, 2007.

[123] B. Van Leer, "Flux Vector Splitting for the Euler Equations," *Eighth International Conference on Numerical Methods in Fluid Dynamics: Lecture Notes in Physics*, Vol. 170, 1982, pp. 507–512.

[124] J. L Steger, and R.F Warming, "Flux Vector Pplitting of the Inviscid Gasdynamic Equations With Application to Finite Difference Methods," *Journal of Computational Physics*, Vol. 40, 1981, pp. 263–293.

[125] Zha, G.C., Shen, Y.Q., and Wang, B.Y., "Calculation of Transonic Flows Using WENO Method with a Low Diffusion E-CUSP Upwind Scheme," AIAA Paper 2008-0745, 46th AIAA Aerospace Sciences Meeting, Reno, NV, Jan. 2008.

[126] S. De Rango, and D. W. Zingg, "Aerodynamic Computations Using a Higher Order Algorithm," AIAA 99-0167, 1999.

[127] D. W. Zingg, S. De Rango, M. Nemec, T. H. Pulliam, "Comparison of Several Spatial Discretizations for the Navier-Stokes Equations," *Journal of Computational Physics*, Vol. 160, 2000, pp. 683–704.

[128] A. Jameson, "Time Dependent Calculations Using Multigrid with Applications to Unsteady Flows Past Airfoils and Wings," AIAA Paper 91-1596, 1991.

[129] J. Alonso, L. Martinelli, and A. Jameson, "Multigrid Unsteady Navier-Stokes Calculations with Aeroelastic Applications," AIAA Paper 95-0048, 1995.

[130] A.J. Strazisar, J.R. Wood, M.D. Hathaway, and K.L. Suder, "Laser Anemometer Measurements in a Transonic Axial-Flow Fan Rotor," NASA Technical Paper 2879, November, 1989.

[131] J.D. Denton, "Lessons from Rotor 37," *Journal of Thermal Science*, Vol. 6, 1996, pp. 1–13, doi: 10.1007/s11630–997–0010–9.

[132] J. Dunham, "CFD Validation for Propulsion System Components," AGARD-AR-355, 1998.

[133] H.D. Vo, "Rotating Stall Suppression in Axial Compressors with Casing Plasma Actuation," *Journal of Propulsion and Power*, Vol. 26, 2010, pp. 808–818, doi: 10.2514/1.36910.

[134] H.D. Vo, "Role of Tip Clearance Flow on Axial Compressor Stability," Ph.D. Thesis, MIT, 2002.

[135] H.-S. Im, and G.-C. Zha, " Flutter Prediction of a Transonic Rotor Using a Phase-lagged Boundary Condition," Proceedings of 50th AIAA Aerospace Sciences Meeting including the New Horizons Forum and Aerospace Exposition, Nashville, Tennessee, Jan 2012, 2012.

[136] H. Schlichting, "Boundary Layer Theory," McGRAW-Hill, 1979.

[137] L.K. Loftin, "Airfoil Section Characteristics at High Angles of Attack," NASA TM 100019, October 1987.

[138] W.J. McCroskey, "A Critical Assessment of Wind Tunnel Results for the NACA0012 Airfoil," NACA TN 3241, August, 1954.

[139] B.Y. Wang, and G.C. Zha, "Detached Eddy Simulation of a Co-Flow Jet Airfoil at High Angle of Attack ," *To appear in AIAA Journal of Aircraft, 2011*, 2011.

[140] H.S. Im, and G.C. Zha, "Delayed Detached Eddy Simulation of a Stall Flow Over NACA0012 Airfoil Using High Order Schemes," AIAA Paper 2011-1297, 49th AIAA Aerospace Sciences Meeting including the New Horizons Forum and Aerospace Exposition 4 - 7 January 2011, Orlando, Florida, submitted to AIAA Journal, 2011.

[141] B. Wang, Z. Hu, and G. Zha, "A General Sub-Domain Boundary Mapping Procedure For Structured Grid CFD Parallel Computation," *AIAA Journal of Aerospace Computing, Information, and Communication*, Vol. 5, 2008, pp. 425–447.

[142] R. V. Chima, "Calculation of Tip Clearance Effects in a Transonic Compressor," *AMSE J. of Turbomach.*, Vol. 120, 1998, pp. 131–140.

[143] T. Arima, T. Sonda, M. Shirotori, A. Tamura, and K. Kikuchi, "A numerical Investigation of Transonic Axial Compressor Rotor Flow Using a Low-Reynolds-Number k-e Turbulence Model," *AMSE J. of Turbomach.*, Vol. 121, 1999, pp. 44–58, doi:10.1115/1.2841233.

[144] I.K. Jennions, and M.G. Turner, "Three-Dimensional Navier-Stokes Computations of Transonic Fan Flow Using an Explicit Flow Solver and an Implicit $k-\varepsilon$ Solver," *AMSE J. of Turbomach.*, Vol. 115, 1993, pp. 261–272, doi:10.1115/1.2929232.

[145] L. Reid, and R.D. Moore, "Design and Overall Performance of Four Highly-Loaded, High Speed Inlet Stages for an Advanced, High Pressure Ratio Core Compressor," NASA TP.1337, 1978.

[146] I.J. Day, and C. Freeman, "The Unstable Behavior of Low and High-Speed Compressors," *AMSE J. of Turbomach.*, Vol. 116, 1994, pp. 194–201, doi:10.1115/1.2928353.

[147] W.W Copenhaver, S.L. Puterbaugh, and C. Hah, "Unsteady Flow and Shock Motion in a Transonic Compressor Rotor," *Journal of Propulsion and Power*, Vol. 13, 1997, pp. 17–23.

[148] C. Hah, D.C. Rabe, and A.R. Wadia, "Role of Tip-Leakage Vortices and Passage Shock in Stall Inception in a Swept Transonic Compressor Rotor," GT2004-53867, Proceedings of ASME Turbo Expo 2004, 2004.

[149] H. Im, X. Chen, and G. Zha, "Detached Eddy Simulation of Unsteady Stall Flows of a Full Annulus Transonic Rotor," ASME GT2010-23465, 2010.

[150] Y. Gong, "A Computational Model for Rotating Stall and Inlet Distortions in Multistage Compressors," Ph.D. Thesis, Massachusetts Institute of Technology, Feb. 1999.

[151] M. Inoue, M. Kuroumaru, T. Tanino, S. Yoshida, and M. Furukawa, "Comparative Studies on Short and Long Length-Scale Stall Cell Propagating in an Axial Compressor Rotor," *AMSE J. of Turbomach.*, Vol. 123, 2001, pp. 24–31.

[152] F. Lane, "System Mode Shapes in the Flutter of Compressor Blade Rows," *Journal of the Aeronautical Science*, Vol. 23, 1956, pp. 54–66.

[153] A. Arone, "Viscous Analysis of Three Dimensional Rotor Flow Using a Multigrid Method," *AMSE J. of Turbomach.*, Vol. 116, 1994, pp. 435–445.

[154] G. Herrick, M. Hathaway and J. Chen, "Unsteady Full Annulus Simulations of a Transonic Axial Compressor Stage," NASA/TM-2009-215604, 2009.

[155] R. Chima, "SWIFT Code Assesment for Two Similar Transonic Compressors," NASA/TM-2009-215520, 2009.